



EDITE ED 130

**Doctorat ParisTech**

**T H È S E**

pour obtenir le grade de docteur délivré par

**Télécom ParisTech**

**Spécialité “ Communications & Electronique ”**

*présentée et soutenue publiquement par*

**Heming Huang**

le 13 mars 2017

**Optical nonlinearities in quantum dot lasers for high-speed  
communications**

Directeur de thèse : **Frédéric GRILLOT**  
Co-encadrement de la thèse : **Didier ERASME**

**Jury**

**M. Christophe LABBE**, École Nationale Supérieure d'Ingénieurs de Caen  
**M. Ammar SHARAIHA**, École Nationale d'Ingénieurs de Brest  
**M. Dieter BIMBERG**, Technische Universität Berlin  
**M. Olivier DURAND**, Institut National des Sciences Appliquées de Rennes  
**M. Fan-Yi LIN**, National Tsing Hua University  
**M. Philip POOLE**, National Research Council Canada  
**M. Frédéric GRILLOT**, Télécom ParisTech  
**M. Didier ERASME**, Télécom ParisTech

Rapporteur  
Rapporteur  
Examineur  
Examineur  
Examineur  
Examineur  
Directeur de thèse  
Co-directeur de thèse

**T  
H  
È  
S  
E**



# Acknowledgements

First of all, I would like to express my sincere gratitude and appreciation to my supervisors, Prof. Frédéric Grillot and Prof. Didier Erasme, for their excellent patient guidance and vive support all along my Ph.D. study. I have learned a lot from their constant knowledge, professional approach, and rigorous attitude towards scientific research. I thank them for offering me international exchanges in different countries with multiple leading groups in the field, as well as for supporting me on various international conferences that help me to catch the most recent research topics and technology advances in industrial area. Working with them is a great experience which will be without doubt invaluable beneficial to my future career.

I would like to thank Prof. Dieter Bimberg from Technische Universität Berlin, Germany, and Dr. Philip Poole from National Research Center, Canada, Prof. Fan-Yi Lin from National Tsing Hua University, Taiwan and Dr. Jean-Guy Provost from III-V Lab, France for providing me all the experimental matters that made this work possible. Their high-quality laser samples and unique platform allowed me to achieve a rich variety of results sustaining the comprehension of underlying physics. I would thank equally Dr. Kathy Lüdge from Technische Universität Berlin, Germany, Dr. Paolo Bardella, Dr. Mariangela Gioannini, and Prof. Ivo Montrosset from Politecnico di Torino, Italy for hosting me in their renowned groups. Their thorough and enlightening understanding in optoelectronics granted me important guidance on my research work.

A special thank for Dr. Kevin Schires from Telecom ParisTech, France and Dr. Cheng Wang from ShanghaiTech University, China. They aid and support me tremendously to build up the experimental abilities and theoretical background in my Ph.D. work.

I would also thank Dejan Arsenijević, Tagir Sadeev, Holger Schmeckeber, Christoph Redlich from Technische Universität Berlin, Germany, Lu-Chih Lin, Chih-Ying Chen from National Tsing Hua University, Taiwan, Dr. Mohamed Chaibi from Télécom ParisTech, France and Dr. Ravi Raghunathan from Virginia Tech, USA for the collaborations which pulled off significant results.

I appreciate all our collaborators Prof. Yves Jaouen, Dr. Renaud Gabet, Dr. Louise Jumpertz, Damien Maraval, Dr. Xin You, Dr. Mengdi Song from Télécom ParisTech, France, Prof. Marek Osiński from University of New Mexico, USA, Wei Wei, Prof. Lilin Yi from Shanghai Jiaotong University for meaningful scientific discussions.

I would like to thank all the professors, all my colleagues and all the friends in GTO group, Télécom ParisTech who aid me in work and in life.

I acknowledge the Institut Mines-Telecom for supporting my Ph.D. work via Futur & Rupture funding.

Last but not least, I am very grateful to my wife and my parents for their persistent support and encouragement.



# Table of content

Acknowledgements .....	1
Table of content .....	3
List of acronyms .....	7
List of figures .....	9
List of tables.....	19
Chapter I. Introduction .....	21
I. Optical networks .....	21
II. Quantum dot lasers .....	25
1. Development history.....	25
2. GaAs-based QD lasers .....	27
3. InP-based QD lasers .....	30
III. Motivations of the dissertation .....	33
1. Narrow linewidth QD lasers for coherent communications.....	35
2. QD lasers-based optical wavelength converters .....	35
3. Feedback resistant QD lasers .....	37
IV. Organization of the dissertation .....	39
Chapter II. Fundamentals of quantum dot lasers .....	41
I. Electronic structure .....	41
II. Carrier dynamics.....	44
1. Carrier capture .....	45
2. Carrier relaxation .....	45
III. Gain broadening mechanisms .....	46
IV. Gain dynamics .....	49
1. Linewidth broadening factor.....	49
2. Stability analysis, relaxation oscillations and damping .....	52
3. Nonlinear carrier dynamics.....	55
4. Gain compression.....	57

5. Optical spectral linewidth .....	59
V. Summary .....	60
Chapter III. Advanced characterizations of quantum dot lasers .....	61
I. Investigated QD laser devices.....	61
1. InAs/GaAs QD lasers.....	61
2. InAs/InP QD lasers.....	67
II. Linewidth broadening factor .....	71
1. Below-threshold measurements.....	72
2. Above-threshold measurements .....	76
III. Optical spectral linewidth.....	86
1. Self-heterodyne method .....	86
1. Experimental results .....	87
2. Spectral linewidth reduction under external control.....	93
IV. Summary .....	94
Chapter IV Nonlinear conversion in optically-injected QD lasers.....	97
I. Introduction.....	97
II. Four-Wave Mixing.....	99
1. Phase conjugation generation.....	99
2. NDFWM in semiconductor gain medium.....	101
3. Extraction of the third-order nonlinear susceptibility .....	106
4. Optical injection-locking .....	108
III. Experimental investigation of four-wave mixing in injection-locked QD lasers .....	112
1. Experimental setup .....	112
2. Static conversion in InAs/InP FP QD lasers.....	113
2.2. Influence of the pump wavelength .....	120
3. Nonlinear conversion with InAs/GaAs QD lasers .....	127
4. Summary .....	134
IV. Dynamic conversion .....	137
1. Experimental setup .....	137
2. Conversion optimization .....	138

3. Conversion performance characterization .....	139
V. Conclusions.....	140
Chapter V. Delay dynamics in quantum dot Lasers .....	141
I. Introduction.....	141
1. Principle of optical feedback.....	141
2. Fundamentals of optical feedback .....	142
II. Theoretical analysis of external optical feedback .....	145
1. Lang & Kobayashi equations .....	145
2. Light-current characteristics with optical feedback .....	147
3. Phase conditions .....	149
4. Critical level boundary .....	152
5. Low-frequency fluctuations .....	156
6. Regular pulse package.....	158
III. Experimental analysis of the long-delay feedback dynamics of QD lasers.....	160
1. Experimental setup .....	160
2. Identification of the feedback regimes .....	161
3. InAs/GaAs QD FP lasers.....	164
4. GS chaotic dynamics .....	168
IV. Experimental analysis of the short-delay dynamics of QD lasers.....	169
1. Experimental Setup.....	169
2. GS vs. ES feedback dynamics.....	170
2.3. Analysis of the excited periodic oscillations.....	174
2.4. Self-pulsating dynamics.....	177
V. Summary .....	182
Chapter VI. Conclusions and perspectives.....	183
Appendix 1: Synthèse en français.....	189
I. Introduction.....	189
II. Conversion nonlinéaire en longueur d'onde dans les lasers QD.....	190
1. Principe du mélange à quatre-ondes .....	190
2. Mélange à quatre-ondes dans les lasers QD.....	191

3. Configurations expérimentales .....	194
4. Conversion statique.....	195
5. Extraction de la susceptibilité nonlinéaire de troisième-ordre $\chi(3)$ .....	198
6. Conversion dynamique dans les lasers QD .....	199
7. Résumé.....	201
III. Dynamiques nonlinéaires des lasers QD sous retour optique externe .....	202
1. Principe de la rétroaction optique .....	202
2. Rétroaction optique dans les lasers QD .....	204
3. Configuration expérimentale .....	206
4. Dynamiques nonlinéaire des lasers QD rétroactionnés dans les cavités longues	208
5. Dynamiques nonlinéaire des lasers QD rétroactionnés dans les cavités courtes	211
6. Résumé.....	213
IV. Réduction de la Largeur de raie dans les lasers QD .....	214
1. Largeur de optique des lasers QD .....	214
2. Configuration expérimentale .....	214
3. Réduction de la largeur de raie par rétroaction optique .....	216
4. Résumé.....	217
Appendix 2: List of Publications.....	219
Journal Papers .....	219
Conference Papers.....	219
References .....	223

## List of acronyms

Abbreviation	Stand for
AOM	Acousto-Optical Modulator
ASE	Amplified Spontaneous Emission
CDP	Carrier Density Pulsation
CE	Conversion Efficiency
CH	Carrier Heating
DFB	Distributed FeedBack laser
DOS	Density Of States
DWELL	Dot-in-WELL structure
ES	Excited-State
ESA	Electrical Spectrum Analyzer
FM/AM	Frequency Modulation / Amplitude Modulation
FP	Fabry-Perot
FSR	Free Spectral Range
FWM	Four-Wave Mixing
GS	Ground-State
LEF	Linewidth Enhancement Factor
LIV	Light-current-Voltage
LI	Light-current
NCE	Normalized Conversion Efficiency
NDFWM	NonDegenerate Four-Wave Mixing
OIL	Optical Injection Locking
OSA	Optical Spectrum Analyzer
OSNR	Optical Signal-to-Noise Ratio
PD	PhotoDiode
QW	Quantum Well
QWire	Quantum Wire
QD	Quantum Dot
RS	Reservoir State
RWG	Ridge WaveGuide
SCH	Separate Confinement Heterostructure
SHB	Spectral Hole Burning

TL	Tunable Laser
WDM	Wavelength Division Multiplexing
WL	Wetting Layer
WPE	Wall-Plug Efficiency
XGM	cross-Gain Modulation
XPM	cross-Phase Modulation

## List of figures

Figure 1.1. IP traffic compound annual growth rate (CAGR) in exabyte per month, after [2].	21
Figure 1.2. Schematic of the current optical network infrastructure.....	22
Figure 1.3. Evolution of the density of states (DOS) for (a) bulk material, (b) quantum well (QW), (c) quantum wire (QWire) and (d) quantum dots (QD), after [37].	26
Figure 1.4. Chronological progress of the threshold current density for semiconductor lasers. The last data set to the right shows the evolution of the threshold current density per layer for GaAs-based QD lasers as compare to bulk and QW laser structures, after [38].	27
Figure 1.5. Plan-view transmission electron microscopy image of a single QD layer with nanostructures formed by (a) 2.5 monolayers InAs deposition followed by GaAs overgrowth and (b) 2.5 monolayers InAs deposition followed by overgrowth with a 5-nm-thick $\text{In}_{0.15}\text{Ga}_{0.85}\text{As}$ layer prior to GaAs deposition, after [49].	28
Figure 1.6. Light-Current-Voltage (LIV) characteristics of an InAs/GaAs QD laser grown by hetero-epitaxy on silicon, after [22].	30
Figure 1.7. The formation of InAs nanostructures on InP (001) as a function of trimethylindium (TMIn) flow and growth temperature, after [75].	31
Figure 1.8. Cross-section scanning-electron-microscopy (X-SEM) image of an InAs/InP QDash laser grown by MBE at the National Research Council (NRC) Canada (courtesy of Dr. Philip Poole)	31
Figure 1.9. Chronological progress of the threshold current density per layer for InAs/InP QD and QDash lasers, after [77].	32
Figure 2.1. (a) 3-D schematic of a QD p-i-n-doped semiconductor laser diode. The yellow region is the undoped active region, and the black triangles represent the dots. (b) Cross-section of the schematic in (a), showing the material composition and thickness of each layer. (c) Energy band alignment of the heterostructure along the x-axis, after [142].	42
Figure 2.2. Schematic of a QD laser electronic structure with electrons and holes, after [146].	43
Figure 2.3. Illustration of the carrier capture and relaxation processes: a) multi-phonon	

processes under low excitation density, b) single Auger process, and c) sequential Auger processes under high injection current density, after [152]. .....	44
Figure 2.4. The capture rate as a function of the carrier density, after [159]. .....	45
Figure 2.5. Representation of the inhomogeneous broadening illustrating dots with different sizes, and leading to an energy state distribution, after [168]. .....	47
Figure 2.6. Photoluminescence spectrum as a function of temperature from a single InAs/GaAs dot, after [177]. .....	48
Figure 2.7. Lasing and electroluminescence spectra under pulsed injection mode for different bias level at two different temperatures: (a) 110K and (b) 253 K, after [178]. .....	48
Figure 2.8. (a) Schematic of gain $g$ and refractive index $n$ profiles variation with the carrier density changes for QW and symmetric QD ensemble, after [194]; (b) gain ( $g$ ) and refractive index ( $n$ ) profiles versus $\alpha_H$ -factor in symmetric QD ensemble, which is compared to asymmetric QD ensemble, after [43]. .....	51
Figure 2.9. Modulation response of a semiconductor laser. The blue arrow indicates the increase of the bias current, after [192]. .....	55
Figure 2.10. Representation of the carrier energy distributions $\eta(E)$ after propagation of an optical pulse within the semiconductor medium pumped in the gain regime, after [142]. ...	56
Figure 2.11. Gain recovery dynamics for (a) a QD-SOA and (b) a QW-SOA as a function of different pump currents. The pump pulse duration is (a) 12 ps and (b) $\sim 20$ ps. The input pump pulse energy: (a) $\sim 40$ fJ and (b) $\sim 300$ fJ, after [204]. .....	57
Figure 2.12. The evolution of $n_{sp}(1 + \alpha_H^2)$ as a function of modal gain in bulk, single QW (SQW), multi-QW (MQW) material as compared to a six-layer InAs/GaAs QD DFB laser (6QD), after [217], [218]. .....	60
Figure 3.1. Epi-layer structure of the InAs/GaAs QD lasers (courtesy of Prof. Dieter Bimberg). .....	62
Figure 3.2. InAs/GaAs QD FP laser bar with 1-mm long lasers. ....	62
Figure 3.3. (a) Typical laser VI curve and extraction method for $R_s$ and $V_{th}$ values; (b) output power and WPE as a function of bias current for QD laser GaFP4. ....	64
Figure 3.4. LIV curves (left) and optical spectrum (right) of the InAs/GaAs QD laser GaFP1. .	65
Figure 3.5. LIV curves (left) and optical spectrum (right) of the InAs/GaAs QD laser GaFP2. .	65



Figure 3.6. LIV curves (left) and optical spectrum (right) of the InAs/GaAs QD laser GaFP3..	65
Figure 3.7. LIV curves (left) and optical spectrum (right) of the InAs/GaAs QD laser GaFP4..	66
Figure 3.8. LIV curves (left) and optical spectrum (right) of the InAs/GaAs QD laser GaFP5..	66
Figure 3.9. PL spectrum at 8 K from an InAs/GaAs QD sample grown by the same technology than the InAs/GaAs QD lasers studied in this thesis, after [223]. The GS-ES separation is 65 meV [174].	67
Figure 3.10. (a) Schematic diagram of the InAs QD structure, after [38]; (b) An atomic-force microscopy image of one QD layer ( $1\ \mu\text{m} \times 1\ \mu\text{m}$ ) (courtesy of Dr. Philip Poole).	67
Figure 3.11. (a) InAs/InP QD laser PDFB2 (Scale: $500\ \mu\text{m}$ ); (b) cross-section view of the DFB structure.	68
Figure 3.12. PL spectrum from a five-layer InAs/InP QD sample grown by the same CBE technology, after [53].	69
Figure 3.13. Output power and WPE as a function of the bias current in QD laser PFP1.	69
Figure 3.14. LIV curves (left) and optical spectrum (right) of InAs/InP QD laser PFP1.	70
Figure 3.15. LIV curves (left) and optical spectrum (right) of InAs/InP QD laser PDFB1.	70
Figure 3.16. LIV curves (left) and optical spectrum (right) of the InAs/InP QD laser PDFB2.	71
Figure 3.17. Sub-threshold optical spectra of QD laser PFP1 for different bias currents.	73
Figure 3.18. Net modal gain spectra of QD laser PFP1 for various bias current conditions.	74
Figure 3.19. The net gain and refractive index variations of the mode around 1543.3 nm (see in Figure 3.17) in QD laser PFP1. Red solid lines: linear fitting below threshold; Green solid lines: linear fitting above threshold.	74
Figure 3.20. The measured $\alpha_H$ -factor spectral dependence for QD laser PFP1.	75
Figure 3.21. The measured $\alpha_H$ -factor for the GS QD laser GaFP1 and ES QD laser GaFP2.	76
Figure 3.22. Free-space experimental setup used for the FWM analysis. TL: tunable laser; LD: QD laser diode; FR: Faraday rotator; HW: half-wave plate; PBS: polarizing beam splitter; PD: photodiode; SA: electric spectrum analyzer; VA: variable attenuator; AOM: acousto-optic modulator; B: beam block; FC: 50/50 fiber coupler, after [232].	78
Figure 3.23. Measured (a) normalized regenerated signals intensity and (b) normalized beating intensity of the 100 MHz shifted probe and wave mixing QD laser PDFB1 under FWM at $3 \times I_{th}$ (red dots). Blue solid curves represent the fitting calculated from the analytical model.	79

Figure 3.24. The retrieved $\alpha_H$ -factor of QD laser PDFB1 as a function of the bias current. ....	80
Figure 3.25. Schematic of the experimental setup used for FM/AM measurements, after [227]. .....	81
Figure 3.26. Transfer function of the MZ interferometer [37]......	82
Figure 3.27. (a) The measured $2\beta/m$ ratio of QD laser PFP1 at 298K under $2 \times I_{th}$ bias, the red solid line gives the $\alpha_H$ -factor value $\sim 6$ ; (b) the measured $\alpha_H$ -factor as a function of the bias current. ....	84
Figure 3.28. Numerical simulation of carrier variations at $I = 1.2 \times I_{th}$ . The carrier variations are normalized to the value $\delta N_{GS}$ of 0.01 GHz at lasing threshold $I_{th}$ , after [37]. ....	85
Figure 3.29. The measured $\alpha_H$ -factor of QD laser PDFB2. The red line is the fitting from Eq. 2.34. .....	86
Figure 3.30. Self-heterodyne experimental setup used for the optical linewidth measurement. .....	87
Figure 3.31. RF spectrum of QD DFB laser PDFB2 recorded at 95 mA (298K). ....	88
Figure 3.32. Normalized RF spectrum from Figure 3.31 (blue dots) and the corresponding Voigt fitted spectrum (red solid line). ....	89
Figure 3.33. The measured optical spectral linewidth as a function of the total output power of QD laser PDFB2. ....	90
Figure 3.34. The measured optical spectral linewidth as a function of the total output power for QD laser PDFB1. ....	91
Figure 3.35. The measured optical spectral linewidth as a function of the total output power for a packaged QW DFB laser from Nokia. ....	92
Figure 3.36. Feedback arm inserted at the upstream of the linewidth measurement setup shown in Figure 3.30. ....	93
Figure 3.37. Measured spectral optical linewidth of QD laser PDFB1 under external optical feedback. The blue triangles correspond to five different measurements done in sequence; the black dotted line represents the spectral linewidth of the free-running laser. ....	94
Figure 4.1. Illustration of the NDFWM process, the interaction of fields $E_1$ and $E_2$ at the frequencies of $\omega_1$ and $\omega_2$ leads to the generation of fields $E_3$ and $E_4$ at $\omega_3$ and $\omega_4$ . ....	97
Figure 4.2. Schematic illustration of the NDFWM in a semiconductor gain medium. ....	101

Figure 4.3. The contributions of the CDP, CH and SHB mechanisms to the nonlinear conversion efficiency in a QD SOA device, after [118].	102
Figure 4.4. Directions of $\chi^{(3)}$ of CDP and SHB for bulk, QW and QD, after [116].	104
Figure 4.5. Comparison of the measured CE between a bulk and a QD SOA, after [102].	105
Figure 4.6. Scheme illustrating the optical injection-locking.	109
Figure 4.7. Optical spectra of the free-running FP laser (blue) and of the injection-locked laser (red).	110
Figure 4.8. Illustration of the injection-locking boundaries in terms of injection detuning and injection strength, after [276]. SL: stable locking; NL: nonlinear dynamics area.	112
Figure 4.9. Experimental setup for NDFWM investigation, the pump signal originates from tunable laser TL1, whose beam is seeded into the QD laser and injection-locked it.	112
Figure 4.10. Measured CE (a), NCE (b) and OSNR (c) of FWM in the QD laser PFP1 as a function of the pump-probe frequency detuning.	115
Figure 4.11. Intensity mode profile in the x and y directions (left) and corresponding distribution in the waveguide cross-section (right).	116
Figure 4.12. The normalized third-order nonlinear susceptibility $\chi^{(3)}/g_0$ as a function of the pump-probe frequency detuning.	117
Figure 4.13. Numerical simulations showing the output power as a function of the injection detuning for an injection-locked QD FP laser. Green: $P_{out}$ from the same facet (left); Red: $P_{out}$ of the slave laser only from the left facet; Pink: $P_{out}$ from the right facet of the laser; Dashed line: reflected pump alone.	118
Figure 4.14. Experimental results illustrating the impact the injection ratio on the output power measured at the two facets of a QD FP laser. The pump is injected from the left facet.	119
Figure 4.15 NDFWM spectra of the QD FP laser measured in reflection and transmission configurations for a pump-probe frequency detuning of 340 GHz (down-conversion).	119
Figure 4.16. Measured CE versus frequency detuning for different pump wavelengths for (a) down-conversion and (b) up-conversion. The red, blue and green curves represent the results obtained for 1538, 1543 and 1548 nm respectively.	120
Figure 4.17. The normalized $\chi^{(3)}/g_0$ as a function of the pump-probe frequency detuning and	

for different injected pump wavelengths. The red, green and blue colors represent the results obtained when the pump mode is at 1538, 1543 and 1548 nm, respectively. ....	121
Figure 4.18. The measured CE as a function of the pump-probe frequency detuning for down-conversion (a) and up-conversion (b) for the two TL1 under study. ....	122
Figure 4.19. $\chi^{(3)}/g_0$ as a function of the pump-probe frequency detuning for the two TL1 under study.....	122
Figure 4.20 The LIV characteristics of the (a) QD FP laser PFP2 and (c) QDash FP laser PFP3; the optical spectrum of (b) PFP2 and (d) PFP3 is measured at $2.5 \times I_{th}$ . ....	123
Figure 4.21 (a) Net gain and (b) $\alpha_H$ -factor spectral dependence for both QD FP laser PFP2 and QDash FP laser PFP3. ....	124
Figure 4.22 NCE of QD PFP2 and QDash PFP3 measured using the same setup and experimental conditions as for PFP1. The inset represents the corresponding OSNR. ....	125
Figure 4.23. The $\alpha_H$ -factor spectral dependence for QD lasers GaFP3 and GaFP4 measured by the ASE method. The gain peaks are around 1309 nm for both lasers. ....	128
Figure 4.24 The measured CE as a function of the pump-probe frequency detuning for QD lasers (a) GaFP3 and (b) GaFP4 under $2.4 \times I_{th}$ and 1 dB pump injection strength. Filled (resp. empty) triangles represent up (resp. down) conversion. The figures in inset show the corresponding OSNR of QD lasers GaFP3 and GaFP4.....	129
Figure 4.25 (a) CE as a function of the pump-probe wavelength detuning; (b) CE within an SOA made with the same material, after [112]. ....	130
Figure 4.26. (a) CE and (b) OSNR in QD laser GAFP5 (2 mm) and QD laser GAFP3 (1.5 mm).131	
Figure 4.27. (a) CE and (b) OSNR in the 1.5 mm $\times$ 2 $\mu$ m QD GaFP3 laser at two different bias currents.....	131
Figure 4.28. Schematic of injection-locking map, red dot marks the same injection conditions for the three pump wavelengths used in section III.2.2, and the blue arrows indicate the local tuning of the injection conditions with respect to the stable-locking (SL) area.....	132
Figure 4.29. (a) CE and (b) OSNR in QD laser GaFP3 at two different pump injection ratios; (c) CE and (d) OSNR in GaFP3 at two different pump master-slave injection detunings. ....	133
Figure 4.30. Pump optical spectra at different injection frequency detunings. ....	134
Figure 4.31. Schematic of the experimental setup dedicated for dynamical conversion. MZM:	

Mach-Zehnder modulator; PPG: pulse pattern generator; TBPF: thin band-pass filter; SMF: single mode fiber; EDFA: Erbium-doped fiber amplifier; Osc.: oscilloscope; BERT: bit error rate test.....	138
Figure 4.32. Back-to-back eye diagram of the converted signal with a modulation of 2.5 Gbps PRBS sequence of length of $2^7-1$ by using (a) Yenista T100 (1550 nm) and (b) Tunics as the TL2. ....	138
Figure 4.33. BER curves as a function of the receiving power by the detector for the probe before injection, the converted signal on back-to-back (Conv.) and after the transmission within 25 km SMF coil. The horizontal dotted black line corresponds to the conventional error-free boundary ( $BER = 10^{-9}$ ). ....	139
Figure 5.1. Schematic representing a semiconductor laser subjected to conventional optical feedback (COF). ....	141
Figure 5.2. Feedback regimes in a semiconductor DFB laser (center), after Ref. [304]. The optical spectra on both sides illustrate the laser dynamics under optical feedback, after [323]. ....	143
Figure 5.3. (a) LI curves of a QD FP laser under free-running operation (black) and for three different amounts of feedback ( $r_{ext} = 1.7\%$ , $3.4\%$ and $6.7\%$ ); (b) Extracted threshold current $I_{th}$ from (a) as a function of $r_{ext}$ , the red triangle is the free-running value ( $r_{ext} = 0$ ).....	148
Figure 5.4. Interaction between the ECM $M_i$ and the laser cavity modes $N_j$ , after [303]. ....	148
Figure 5.5. Hysteresis effect in the LI a QD FP laser operating under optical feedback ( $r_{ext}=6.7\%$ ) while increasing and decreasing the bias current. ....	148
Figure 5.6. Solutions of Eq. 5.18 in the $(C, \varphi_0)$ space. The roman numbers represent the number of solutions, after [294]. ....	149
Figure 5.7. Steady-state solutions with respect to parameter $C$ . Solid and dashed lines are obtained for $C = 0.76$ and $C = 9.50$ , respectively. The black circle corresponds to the single solution for $C < 1$ and white circles represent the various solutions for $C > 1$ , after [294]. .	150
Figure 5.8. Carrier density $\Delta N$ variation versus the phase difference $\Delta\omega\tau_{ext}$ . Crossing points between solid and dashed sine waves give the locations of the modes. The red dot is the free-running mode, while black dots/circles correspond to ECM and antimodes respectively [294]. ....	151

Figure 5.9. Optical spectral linewidth as a function of the feedback strength. The markers represent different feedback phase conditions, after [330].	152
Figure 5.10. The critical feedback level $r_{crit}$ as a function of the external round-trip time $\tau_{ext}$ (solid line). The dashed line marks $C = 1$ , and the vertical line indicates is $f_{RO} \times \tau_{ext} = 1$ , after [305].	153
Figure 5.11. Sub-boundaries of regime IV as a function of the external cavity length $L_{ext}$ and feedback strength $r_{ext}$ . Fixed: stable state, P1, P2: periodic oscillations, QP: quasi-periodic oscillations, after [294].	153
Figure 5.12. Excited periodic oscillation frequencies as a function of $L_{ext}$ (black dots), the horizontal line is the free-running ROF ( $r_{ext} = 0$ ), after [335].	156
Figure 5.13. Mapping of the LFF dynamic as a function of the injection current and optical feedback strength. The LFF regime is depicted in light gray. In the dark-gray region stable emission and LFF dynamic coexist. In the undashed region LFF and fully developed coherence collapse coexist, after [339].	157
Figure 5.14. (a) Trajectory of the modes in the $(\Delta N, \Delta\omega\tau_{ext})$ plane; (b) Corresponding LFF waveform, after [336].	158
Figure 5.15. The RF spectrum and the corresponding temporal waveform of a semiconductor laser operating under the RPP regime, after [340].	158
Figure 5.16. Trajectory of the modes in the phase domain illustrating the RPP dynamic and the corresponding temporal waveform.	159
Figure 5.17. Experimental setup used for the long-delay feedback dynamics.	161
Figure 5.18. The optical (a) and RF (b) spectra of QD DFB laser PDFB1 under external feedback with $r_{ext}$ ranging from 0 to 1%. The vertical lines in red allow to distinguish the different feedback regimes. Green dashed lines correspond to the measured operation points of optical ((c), (e), (g), (i)) and RF spectra ((d), (f), (h), (j)).	162
Figure 5.19. Optical and spectral mappings of QD DFB laser PDFB1 under external optical feedback at different bias conditions of $1.5 \times ((a), (b))$ , $2 \times ((c), (d))$ and $3 \times I_{th}$ ((e), (f)).	163
Figure 5.20. The critical feedback level $r_{crit}$ as a function of the normalized bias level $I/I_{th}$ .	164
Figure 5.21. (a) Optical and (b) RF spectra of the GS QD laser GaFP1 measured at $3 \times I_{th}$ without	

feedback ( $r_{ext} = 0$ ) and for the maximal feedback strength.....	165
Figure 5.22. Optical (left) and RF (right) spectral mappings for ES QD laser GaFP2 at (a-b) $1.5 \times I_{th}$ , and (c-d) $2 \times I_{th}$ .....	166
Figure 5.23. ES QD laser GaFP2 at $1.5 \times I_{th}$ bias level: (a) optical and (b) RF spectra of the free-running laser, at 0.6% and 4.3% optical feedback; GaFP2 at $2 \times I_{th}$ bias level: (c) optical and (d) RF spectra of the free-running laser, at 0.1% and 4.6% optical feedback. ....	167
Figure 5.24. (a) Optical and (b) RF spectral mapping of GS QD laser GaFP3 at $2.5 \times I_{th}$ with optical feedback. ....	168
Figure 5.25. Experimental setup used for the short-delay feedback investigation. ....	169
Figure 5.26. LI characteristics of the QD ES laser GaFP2 measured at 293 K. ....	170
Figure 5.27. Optical and RF spectral mappings of GS QD laser GaFP1. The external cavity length is 2 cm long. The bias currents are at $1.5 \times I_{th}$ ((a) and (b)) and $1.7 \times I_{th}$ ((c) and (d)). The green and the orange horizontal solid lines mark the frequencies $f_{ext}$ and $f_{RO}$ respectively. ....	171
Figure 5.28. RF spectral mappings ((a), (c)) and RF spectra under free-running ( $r_{ext}=0$ ) and for the maximal optical feedback strength ( $r_{ext} = 76\%$ ) ((b), (d)) of GS QD laser GaFP1. The external cavity length is 50 cm long. Bias currents are at $1.5 \times I_{th}$ ((a), (b)) and $1.7 \times I_{th}$ ((c), (d)). The green and the orange horizontal solid lines mark the frequencies $f_{ext}$ and $f_{RO}$ respectively.....	172
Figure 5.29. RF spectral mappings of ES QD laser GaFP2 biased at $1.5 \times I_{th}$ under free-running ( $r_{ext}=0$ ) and for the maximal optical feedback strength ( $r_{ext}=55\%$ ) considering 2 and 50 cm long external cavity ((a) and (c)); RF spectra under free-running ( $r_{ext}=0$ ) and for the maximal optical feedback strength ( $r_{ext}=55\%$ ) ((b) and (d)). ....	173
Figure 5.30 Excited periodic oscillation frequency $f_p$ as a function of external cavity length for QD lasers GaFP1 and GaFP2 at $1.5 \times I_{th}$ ((a), (c)) and at $2 \times I_{th}$ ((b), (d)). The vertical solid lines in orange mark the boundaries between the short- and long-delay feedback regime, and the horizontal one in black gives the ROF $f_{RO}$ of the free-running laser. ....	175
Figure 5.31. Boundaries of excited periodic and chaotic oscillations as a function of the external cavity length for QD GS laser GaFP1 and QD ES laser GaFP2 at $1.5 \times I_{th}$ ((a), (c)) and $1.7 \times I_{th}$ ((b), (d)). The vertical solid lines in orange mark the boundaries between short- and long-delay feedback regimes.....	176

---

Figure 5.32. (a) Temporal waveform and (b) RF spectrum of QD laser GaFP2 cavity at $1.5 \times I_{th}$ under 8.5% optical feedback in 20 cm long external cavity at $1.5 \times I_{th}$ .....	178
Figure 5.33. (a) Temporal waveform and (b) RF spectrum of QD laser GaFP2 under 29% optical feedback in 6 cm long external cavity at $1.5 \times I_{th}$ .....	179
Figure 5.34. (a) RF spectrum and (b) temporal waveforms of QD laser GaFP2 for a phase $\varphi_0$ ; (c) RF spectrum and (d) temporal waveform of GaFP2 for a phase of $\varphi_0 + 10\pi/3$ .....	180
Figure 5.35. Mapping of the dynamical transitions with respect to the feedback strength $r_{ext}$ and the external cavity length $L_{ext}$ (a) $1.5 \times$ and (b) $1.7 \times I_{th}$ . In blue and red, the periodic and chaotic oscillation boundaries; the black contours show the windows of self-pulsations. ..	181
Figure 5.36. Measured self-pulsation frequency for ES QD laser GaFP2 as a function of the external cavity length at two bias currents. ....	181



## List of tables

Table 3.1. Measured intrinsic parameters of the InAs/GaAs QD FP lasers.....	63
Table 3.2. Measured intrinsic parameters of the InAs/InP QD FP and DFB lasers.....	70
Table 3.3. The measured $\alpha_H$ -factor (gain peak) for GaAs-based QD FP lasers.....	76
Table 3.4. Extraction procedure of $n_{sp}(1 + \alpha_H^2)$ for QD DFB laser PDFB2.....	90
Table 4.1. Summary of the state-of-the-art of the NDFWM achievements in QD SOAs and lasers. QW laser results are included for comparison. ....	106
Table 4.2. Experimental conditions used for testing PFP1. ....	114
Table 4.3. Parameters used in Eq. (4.10). ....	117
Table 4.4. Experimental conditions used in InAs/GaAs QD FP laser GaFP1. ....	127
Table 4.5. Impact of the type of nanostructures on the conversion performance (results from InP-based nanostructures). ....	135
Table 4.6. Impact of the $\alpha_H$ -factor on the conversion performance (results from InP-based QD). .....	135
Table 4.7. Impact of the cavity dimensions on the conversion performance (results from GaAs- based nanostructures).....	136
Table 4.8. Impact of the bias current on the conversion performance (results from GaAs-based nanostructures). ....	136
Table 4.9. Impact of the injection strength on the conversion performance (results from GaAs- based nanostructures).....	136
Table 4.10. Impact of the injection frequency detuning on the conversion performance (results from GaAs-based nanostructures). ....	137
Table 4.11. Impact of the pump linewidth on the conversion performance (results from InP- based nanostructures).....	137
Table 5.1. Main differences between the RPP and LFF dynamics. ....	159
Table 5.2. ROFs measured at both bias levels for GS laser GaFP1 and ES laser GaFP2. ....	170



# Chapter I. Introduction

The introduction sets the context and the motivations of the thesis. First, key-features and current challenges of fiber-optics communication networks are described. Then, a brief history of quantum dot lasers (QD) is recalled as well as their potentials for optical communications. Both GaAs- and InAs-based QD lasers are introduced along with the main breakthroughs. Exploiting the nonlinear properties of QDs is the central point of the thesis. To this end, QD lasers operating with external control are introduced with the view to propose novel integrated photonics solutions either for the realization of all-optical wavelength converters, isolator-free transmitters and low phase noise oscillators. Finally, the overall organization of the manuscript will be detailed at the end of this introduction chapter.

## I. Optical networks

Nowadays, semiconductor lasers contribute fundamentally to modern optical communication networks. Every year, several millions of new semiconductor laser devices are used in communication systems, generating several billion dollars of annual revenue at the component level [1].

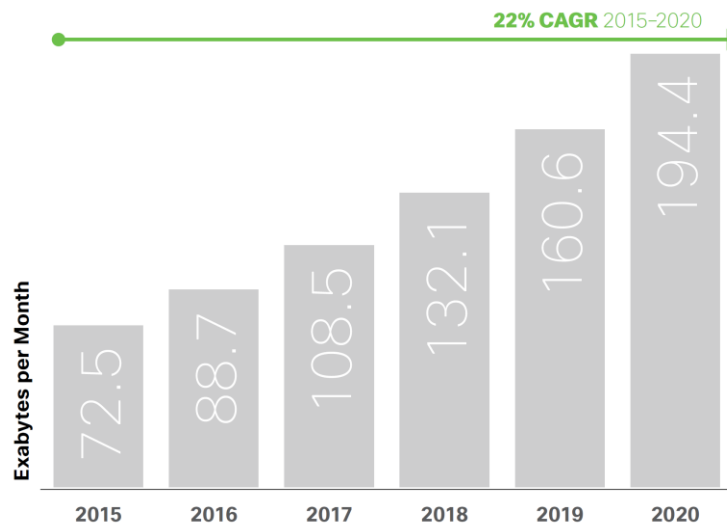


**Figure 1.1.** IP traffic compound annual growth rate (CAGR) in exabyte per month, after [2].

With the exponentially growing telecom market, the annual global IP (Internet Protocol) traffic in the optical network will increase threefold in the next five years with a prediction for

2020 of 200 exabytes per month (EB, 1 EB =  $10^{18}$  GB), as illustrated in Figure 1.1 [2]. In addition, with the wide spread of smartphones and smart devices, these terminals will occupy two third of the total IP traffic by the end of 2020 [2]. Therefore, faster optical sources are on demand to ensure the cost-effective information transmission, which pushes forward the development of novel semiconductor laser technologies. In fiber telecommunications, the C-band (1530-1565 nm) has been widely exploited. At 1550 nm, the loss of single-mode optical fibers (e.g. SMF G. 652) is as low as 0.2 dB/km that is of first importance for long-haul communications. Indeed, low loss means that the distance between repeaters and erbium fiber doped amplifiers (EDFA) is long. A second important parameter of the optical fiber is the chromatic dispersion, which contributes to broaden the pulse light during the propagation. With standard SMF optical fibers, the dispersion is null at 1310 nm, which makes the O-band (1260-1360 nm) very suitable for short distances hence avoiding costly dispersion compensating techniques. In today's networks, the O-band is typically used for up-streaming the data from the customer premises to the central office. Using the O-band for down-streaming data is also considered but this will be expanded in the future.

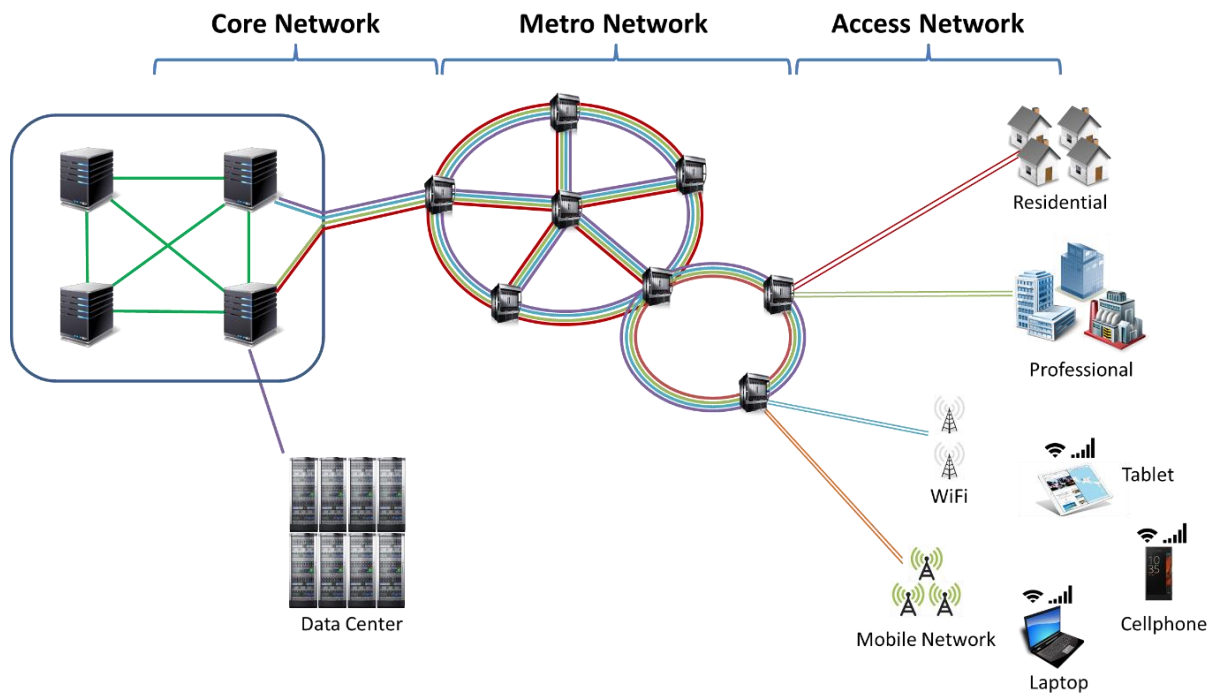


**Figure 1.2.** Schematic of the current optical network infrastructure.

As illustrated in Figure 1.2, the current topology of optical networks is as follows [3]:

- 1) The access network connects the individual endpoints to the local exchanges, the interlinks are usually of a few km;
- 2) The metro network is usually considered in two parts – area network that links the access network in a city, and regional network that connects to other cities, the interlinks varies from a few tens of km up to 1000 km scale;
- 3) The core network performs all the necessary routing and also serves as the gateway to neighboring core nodes [4], the interlinks are usually several thousands of km and includes the inter-continental connections, as well as the hyperscale data center interconnections.

In particular, numerous short-reach applications requiring high data throughputs are emerging, not only in access networks, where upgrades of the bit rate of passive FTTx (Fiber To The x endpoint) systems need to be anticipated, but also in data center networks, where huge amounts of information may need to be exchanged between servers, in part triggered by the rise of “Big Data” applications. In addition, due the increase of the data traffic, the energy consumption is also becoming very problematic with the substantial growth of global IP traffic. Therefore, fast and low-cost transmitters with low energy consumption are absolutely required, especially for short-reach communication links such as access and data center optical networks. Typically for a few hundred meters to a few km transmission distances, direct modulation with on-off keying (OOK) remains the simplest optical transmitter and receiver architecture and it is thus preferred from investment cost point of view. However, although the fiber dispersion is not a limiting factor in the O-band, a weak frequency-chirped operation is demanded from the laser sources in particular to avoid signal distortion and cross-talk problems.

However, as the link distance increases (from a few km to 1000 km scale), direct modulation is no longer the most effective way to support the transmission rate and reach [5]. Coherent communications have been introduced to increase the long-haul transmission efficiency, especially in metro and core networks [6]. In order to reduce the noise in the detection part, local oscillators with low phase noise is required [7]. Indeed, although the frequency drift of the transmitter can be minimized, the carrier phase still fluctuates randomly

because of the phase noise induced from the lasers. Therefore, local oscillator with narrow spectral linewidth is a crucial requirement for realizing stable heterodyne detection. Commercial QW lasers usually exhibit spectral linewidth of a few MHz, in order to reach kHz-spectral linewidth, continuous efforts have been made to decrease the spontaneous emission rate into the lasing mode or to increase the number of photons stored in the cavity. In the latter, high-Q resonator with Q the quality factor defined as the ratio of the energy stored by a cavity to the power lost can lead to a narrow spectral linewidth [8]–[11]. On this stage, different designs of single-mode devices have been proposed to achieve narrow linewidths in the order of 100 kHz or below, such as external cavity [12], chirped grating [13], and discrete mode DFB lasers [9], [10]. In particular, one recent solution was obtained from a proper modal engineering of a DFB laser in which light is generated in the III-V material and stored in the low-loss silicon material. Fabricated lasers using modal engineering to concentrate light in silicon demonstrate spectral linewidths at least 5 times smaller than any other semiconductor lasers [11].

In addition, advanced modulation formats like pulse amplitude modulation (PAM) and phase-shift keying (PSK) and digital signal processing (DSP) would be needed particularly for datacenter interconnects, also leveraging off previous work done for long-haul transmission. Nevertheless, although recently developed DSPs can reach fast operating speed, it has been proved that the long latency introduced by the electronic processing results in a severe communication bottleneck for short-reach communication links [14]. Therefore, direct detection through direct modulation still provides a simple, low cost and compact solution for short reach communication links without suffering from the electronics [5], [7]. However, direct modulation can make the output light strongly dependent on nonlinear laser characteristics. Up to now, external modulators are well-known and commonly used to overcome these problems by providing a larger bandwidth and lower chirp but external modulation still suffers from a higher cost and power consumption [15]. With direct detection, the modulation bandwidth of the laser is the most important feature that determines the maximum data rate achievable. The best performers to date, edge-emitting lasers have achieved modulation bandwidths up to 55 GHz [16], [17]. For very short reach interconnects up to a few hundred meters, inexpensive vertical-cavity surface-emitting lasers (VCSELs) with

ultra-low threshold are generally used for communications at 10 Gbps within the data centers. Nevertheless, combined with the multimode fiber dispersion, it turns out that VCSELs are not good candidates when the link speed exceeds 20 Gbps. To overcome such a limitation, distributed-feedback (DFB) lasers and single-mode fiber are preferred within the data centers to cover transmissions above 20 Gbps. Numerous results have been published in the literature showing the advantages of various complex DFB structures with higher-power, better temperature performance, and higher speeds [18]–[21]. Although the DFB technology is more expensive, it does provide a higher bandwidth and a relatively narrow spectral linewidth to increase interconnect bandwidth and reach, while maintaining low power consumption and relatively low cost. Overall the development of energy saving quantum-confined devices still constitutes an active field of research [2]. Over the last past years, tremendous efforts have been carried out towards the improvement of semiconductor lasers. All these achievements are actually related to the invention of novel in plane semiconductor materials like those based on QD technology. Such self-organized nanostructures are one of the best practical examples of emerging nanotechnologies. Indeed, due to the atom-like discrete energy levels, QDs exhibit various properties resulting from the three-dimensional confinement of carriers, like a high stability against temperature variation and a low-threshold lasing operation, which are in favor for the reduction of the energy consumptions. Very recently, it was also proved that QDs have a high potential to overcome the inherent problems related to standard diode lasers integrated on silicon in the context of large-scale and low-cost photonic integration [22]–[25]. In addition, QD lasers display an intrinsic narrow spectral linewidth [26], which can also make them good candidates for the implementation of local oscillator in coherent detection systems. To this end, narrow linewidth lasers together with the precisely controlled center frequency have accelerated the development of studies of coherent communication systems.

## **II. Quantum dot lasers**

### **1. Development history**

Since the first demonstration of the semiconductor laser in 1962, significant achievements have been reported including but not limited to, the development of the

heterojunction and the quantum well (QW) laser structure. In 1970s, the bulk heterostructure (3D system) semiconductor laser was developed to provide an efficient carrier confinement within the active region [27]. In particular, the double heterostructure (DH), which also yields optical confinement, has transformed semiconductor lasers from laboratories into industries [28]. The quantum confinement of electrical carriers occurs when one or more spatial dimensions of the nanocrystal approach the de Broglie wavelength of the carrier, i.e. on the order of 10 nm. Such confinement leads to a quantification of the density of states (DOS), and splits the energy band of bulk semiconductors into discrete energy levels [29]. The QW structure relies on the use of an ultra-thin film with a thickness of a few nanometer (nm), where the carriers are confined in one dimension [30]. In 1975, the first QW laser (2D system) was demonstrated exhibiting multiple advantages over bulk DH lasers, like lower threshold currents [31]. Owing to the spectacular development of crystal growth technology, a wide range of accessible wavelengths can be achieved by varying the QW thickness [32]. As such, QW lasers have been considered as one major step forward in semiconductor laser technology hence making them by far the best transmitters available nowadays on the market. Over the last 20 years, further decrease of the degree of freedom have kept attracting a lot of attention in order to realize quantum confined devices with improved performances [33]–[36].

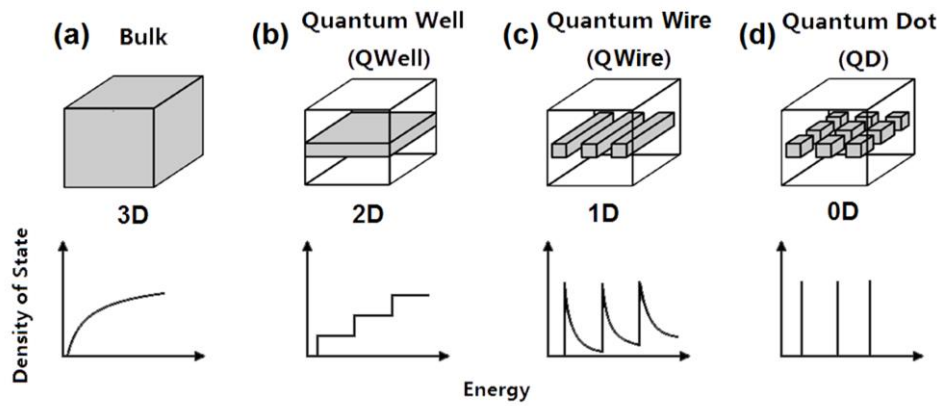


**Figure 1.3.** Evolution of the density of states (DOS) for (a) bulk material, (b) quantum well (QW), (c) quantum wire (QWire) and (d) quantum dots (QD), after [37].

As shown in Figure 1.3, decreasing the degree of freedom of carriers leads to the formation of low dimensional nanostructures such as quantum wire (1D) and QD structures (0D). Ideally, 0D systems exhibit an atom-like DOS hence providing an ultimate carrier



confinement. The concept of QD laser was originally introduced in 1982 by Arakawa and Sakaki [33]. Multiple theoretical works have shown that owing to the ultimate carrier confinement, QD lasers would display outstanding properties like a temperature insensitive operation with ultra-low threshold current, a high spectral purity and enhanced modulation capabilities [33], [35]. For instance, Figure 1.4 shows the evolution of the threshold current density for semiconductor lasers over time [38], [39]. The last data set to the right depicts the evolution of the threshold current density per QD layer for GaAs-based lasers. From DH to QW then to QD, it is straightforward that significant breakthroughs have been reported proving that the ultimate carrier confinement can lead to ultra-low threshold currents.

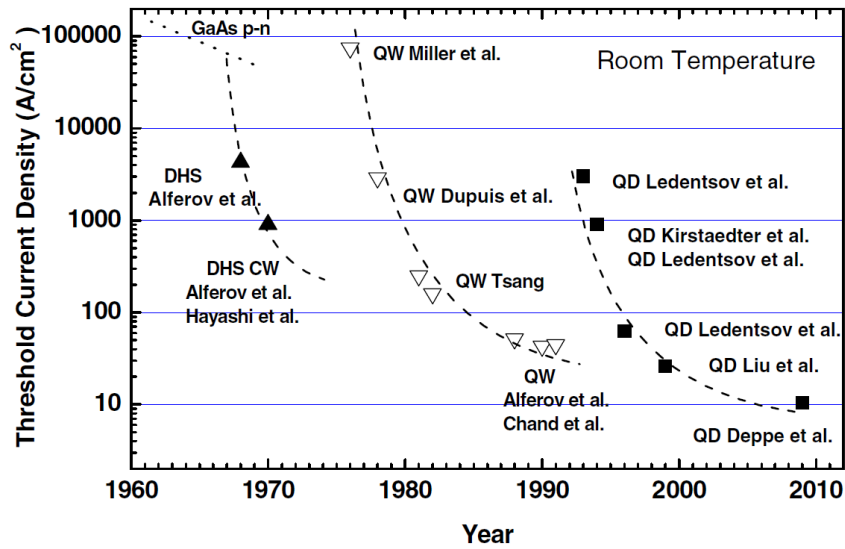


**Figure 1.4.** Chronological progress of the threshold current density for semiconductor lasers. The last data set to the right shows the evolution of the threshold current density per layer for GaAs-based QD lasers as compare to bulk and QW laser structures, after [39].

## 2. GaAs-based QD lasers

One initial approach used to obtain arrays of QDs was to apply patterned mesa-etched QWs grown by metal-organic chemical vapor deposit (MOCVD) or Molecular beam Epitaxy (MBE) [38], [40]. Although radiative recombinations were observed [41], etched QW layers still produce nonradiative defects hence altering the material quality of the nanostructure matrix. In order to eliminate nonradiative defects, other solutions like selective growth [42] and self-assembled growth technique [43] were introduced in the 1990's. In particular, the Stranski-

Krastanov (SK) growth has been very successful for GaAs-based systems [43]–[45], where InAs QDs are formed via a trade-off between the growing film strain energy and the dot surface free energy [30]. In practice, several parameters are involved during the growth, making the dot formations more difficult to control leading to a QD size dispersion i.e. to an inhomogeneously broadened gain medium (will be further discussed chapter II) [46]. The first QD laser realized in 1994 was emitting at 77 K from a single QD layer [47]. Two years later, lasing operation was unveiled at room temperature with a threshold current density of 950 A/cm<sup>2</sup> [48]. Fabrication of QD lasers usually require growing multiple stacks of dots in the active region to increase the material gain [48]. However, in doing so, careful optimization of the growth process is mandatory, because as the number of stacks increases, the strain also accumulates in each dot layer hence necessitating to use a thicker spacer in the structure, which will in turn reduce the contribution to the gain and slow down the carrier dynamics [49]. For InAs/GaAs QD lasers, the maximum number of dot layers is usually limited to 10 ~ 15 [46], [49]. Figure 1.5 represents the plan-view transmission electron microscopy images of a single QD layer [49], showing nanostructures with 5 nm in height and a 15 – 20 nm lateral extension. Several self-assembled growth techniques, such as solid-state MBE [50], gas source MBE (GSMBE) [51], metal-organic vapor phase epitaxy (MOVPE) [52], and chemical-beam epitaxy (CBE) [53], have been improved and successfully used to properly grow GaAs-based QD materials.

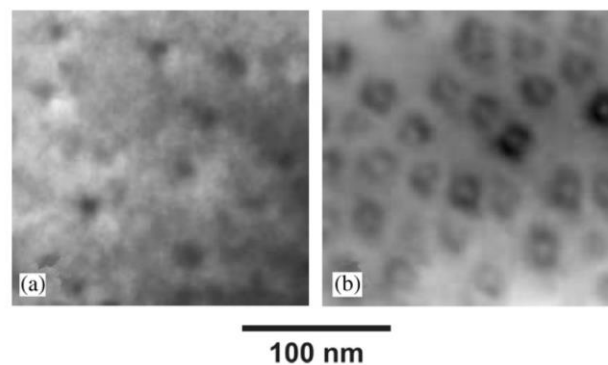


**Figure 1.5.** Plan-view transmission electron microscopy image of a single QD layer with nanostructures formed by (a) 2.5 monolayers InAs deposition followed by GaAs overgrowth and (b) 2.5 monolayers InAs deposition followed by overgrowth with a 5-nm-thick In<sub>0.15</sub>Ga<sub>0.85</sub>As layer prior to GaAs deposition, after [49].

Since the birth of QD lasers, the development of GaAs-based QD lasers has been extensively pursued [54]. For instance, in 1997, a better optimized structure was demonstrated with three dot layers and a very low threshold current density ( $\sim 21 \text{ A/cm}^2$ ), a characteristic temperature  $T_0$  of 385 K up to 300 K, and a large material gain of  $\sim 10^5 \text{ cm}^{-1}$ . Two years later, further breakthrough has been unveiled owing to the development of the "Dot-in-a-well" (DWELL) structure [55]. Such structure, in which the QDs are embedded into QWs allows to a better capture and localization of electrons into the QDs and to speed-up the carrier dynamic as well as to improve the material gain owing to a larger dot density up to  $7.5 \times 10^{10} \text{ cm}^{-2}$ . Over time, more improvements have been further obtained in InAs/GaAs QD lasers, [47], [56]–[59], with for instance threshold current densities down to  $\sim 17 \text{ A/cm}^2$  [60], negative characteristic temperature [61], as well as high output power of 16 W [62]. The lowest threshold current density ever reported for a QD laser is as low as  $8.8 \text{ A/cm}^2$  [63]. In order to keep enhancing the lasing performance, recent research has suggested using a strain-compensation technique inside the multi-stack structure from which a modulation bandwidth up to 11 GHz has been reported [64].

As compared to commercial QW lasers, QD transmitters are much better candidates to reduce the power consumption both of the electrical pumping and the thermoelectric cooling in butterfly-packaged devices [39]. In the current market, mature commercialized GaAs-based QD laser products are already provided for telecommunication applications by different companies such as QD Laser Inc. and Innolume GmbH [43], [65]–[67]. In addition, silicon photonics is anticipated to be a disruptive optical technology for communication system applications, such as intra-chip or inter-chip interconnects [68], short reach communications in datacenters [69] and supercomputers [70], as well as all-optical signal processing [68]. In this context, it was shown that QD lasers display a lower sensitivity to the crystalline defects than QW ones due to the carrier localization and reduced interaction with defects [22], hence constituting better source candidates for silicon integration like in photonics integrated circuits (PICs) [22]. For instance, a very recent work by Chen et al. has successfully demonstrated a 5-layer GaAs-based QD laser directly grown by hetero-epitaxy on silicon, as shown in Figure 1.6, a threshold current density of  $62.5 \text{ A/cm}^2$  and a high output power up to 100 mW is reported at room temperature [11] for a lifetime performance over 3100 hours. From the end-user point

of view, Ranovus Inc. has also recently launched a 200 Gbps QD-laser-based datacenter interconnect platform, and plans to achieve a 400 Gbps one in the future [71].

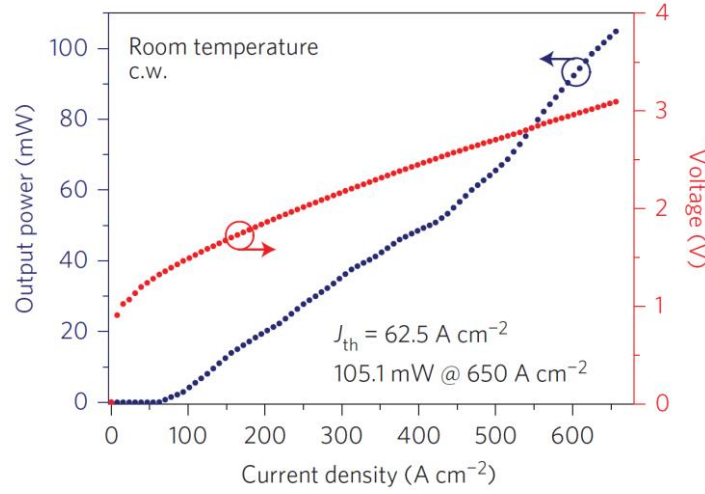


**Figure 1.6.** Light-Current-Voltage (LIV) characteristics of an InAs/GaAs QD laser grown by hetero-epitaxy on silicon, after [25].

### 3. InP-based QD lasers

The SK growth has been proved to be very efficient for the realization of GaAs-based QD laser devices, with an emitting wavelength in the O-band (1260 – 1360 nm) that is ideal for short-reach communication links. On the other hand, InAs QDs grown on InP substrates can also be used for the realization of quantum confined devices operating in the C-band. The first InAs/InP QD laser was demonstrated in 1998, first with a lasing operation limited to 77 K [72] and then at room temperature [73]. Although the InAs/InP and InAs/GaAs systems share the same material in the dots, they remain quite different from each other, mostly because the lattice mismatch in InAs/InP (3 %) is smaller than that in InAs/GaAs (7 %) [62]. Therefore, the challenge regarding the dot formation on InP substrates is to deal with the lattice mismatch and the complex strain distribution which tends to produce elongated dots, i.e. quantum dash (QDash), a new class of self-assembled nanostructures that exhibits mixed characteristics in between the quantum wire (QWire) and QD [74].

As an example, Figure 1.7 shows the impact of the trimethylindium (TMIn,  $\text{In}(\text{CH}_3)_3$ ) flow and of the growth temperature on the formation of the InAs nanostructures on InP(001) substrate. At 500 °C, the InAs tends to form in dashes with the increase of the quantity of TMIn

flow, as well as decreasing the temperature with TMIn fixed at 13 sccm.

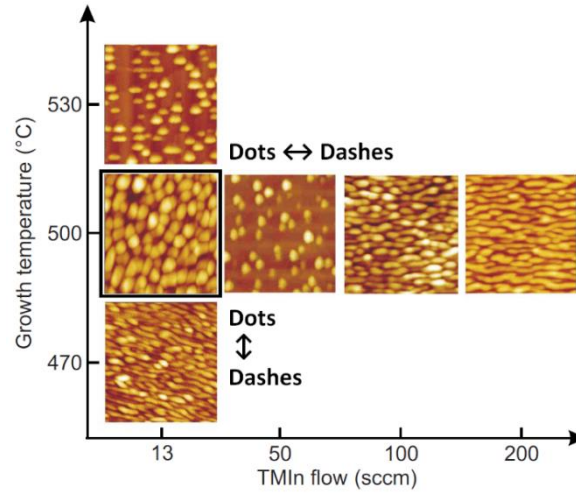


**Figure 1.7.** The formation of InAs nanostructures on InP (001) as a function of trimethylindium (TMIn) flow and growth temperature, after [75].

Figure 1.8 illustrates the cross-section scanning electronic microscopy (X-SEM) image of a QDash laser grown by MBE at the National Research Council (NRC) Canada (courtesy of Dr. Philip Poole). The layers from top to bottom are respectively: InGaAs p-type contact layer, p-type InP, InGaAsP etch stop layer, p-type InP spacer, InGaAsP core containing the QDashes near the top of the core, and the n-type InP layer.

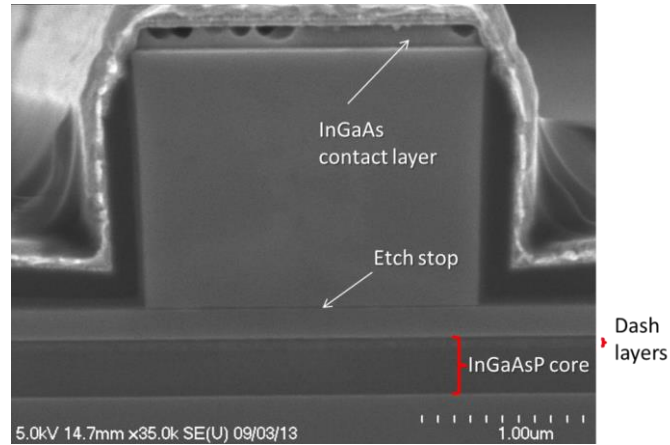


**Figure 1.8.** Cross-section scanning-electron-microscopy (X-SEM) image of an InAs/InP QDash laser grown by MBE at the National Research Council (NRC) Canada (courtesy of Dr. Philip Poole).

The dashes are strongly anisotropic nanostructures and exhibit electronic properties rather close to QWires [76]. Thus, the fabrication of real InAs/InP QDs requires careful

procedures in order to avoid the formation of QDash, e.g. utilizing miscut InP(100) or InP(311)B misoriented substrates [77].

The formation of nanostructures (dashes or dots) on InP(100) substrate strongly depends on the growth conditions and on the thickness of the InAs layer, hence lots of efforts have been devoted to improve the growth with views of enhancing the dot density [78]. By employing chemical beam epitaxy (CBE), Allen et al. reported an InAs/InGaAsP grating coupled external cavity QD lasers with an increased dot density of  $3\text{-}6 \times 10^{10} \text{ cm}^{-2}$  and a wavelength tuning range of 110 nm [79]. On the other hand, using MBE in conjunction with MOCVD p-doped cladding and contact layers, Lelarge et al. has obtained a very high modal gain up to  $10.7 \text{ cm}^{-1}$  per layer by stacking six QD dot in the active region [80]. Very recently, using solid source MBE (SSMBE) technique, the inhomogeneous broadening was substantially reduced down to 26 meV, allowing a modulation bandwidth of 15 GHz and modulation capabilities up to 36 Gbps [81], [82]. Same as GaAs-based QD lasers, InP-based QD lasers can exhibit reduced threshold currents.

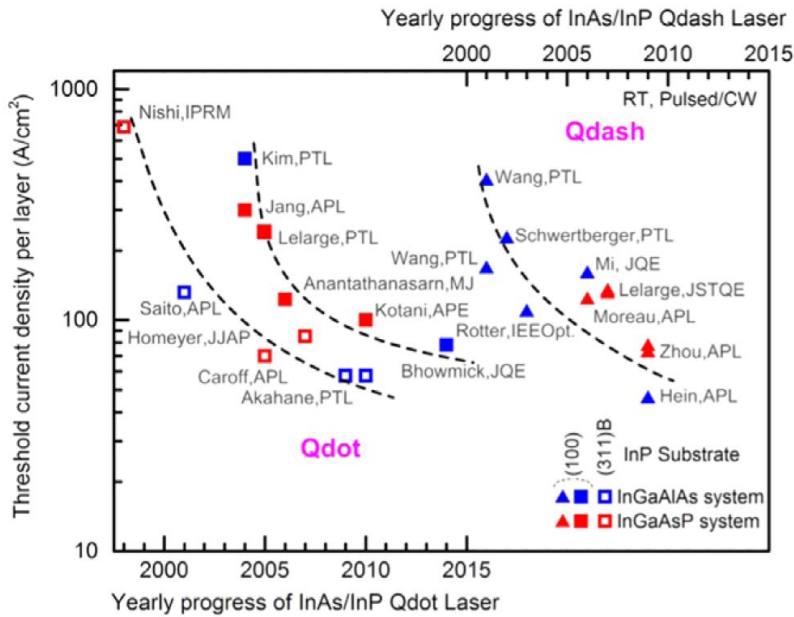


**Figure 1.9.** Chronological progress of the threshold current density per layer for InAs/InP QD and QDash lasers, after [77].

Figure 1.9 represents the evolution of the threshold current density per layer in both InAs/InP QD and QDash lasers [77]. Although the lowest value of  $78 \text{ A/cm}^2$  [83] is still higher

than in GaAs-based QD ( $8.8 \text{ A/cm}^2$ ) [63], InAs/InP QD lasers show a similar trend than the one displayed in Figure 1.4. Overall, although the performance of InAs/InP QD lasers are still far from those reported on GaAs-based substrate, progress has been made over the years towards demonstrating good performance for optical communications [77].

As compared to InP(100) substrate, it has to be noted that high indexed InP(311)B substrates can provide higher nucleation point density, hence strongly reducing the surface migration effects and allowing the formation of more symmetrical QDs in the planar direction. Moreover, a higher dot density with a smaller dispersion in size can also be obtained. For instance, dot density of  $2$  to  $7.5 \times 10^{10} \text{ cm}^{-2}$  [84], [85], with dot sizes of  $3 \text{ nm}$  in high and  $30$  to  $50 \text{ nm}$  in wide have been reported. Using an InAs/InGaAsP active region, the first InP(311)B based QD laser was obtained including  $7$  stack layers grown by MBE and with a dot density of  $2 \times 10^{10} \text{ cm}^{-2}$ , displaying a lasing operation at  $1400 \text{ nm}$  and at  $77 \text{ K}$  [73]. Then, using a double capped technique, Caroff et al. achieved a significant improvement in the dot density up to  $1.1 \times 10^{11} \text{ cm}^{-2}$  leading to a threshold current density of  $23 \text{ A/cm}^2$  per layer [86]. One year later, by optimizing the InAs deposition process, small QDs ( $\sim 20 \text{ nm}$ ) with very high density ( $\sim 1.3 \times 10^{11} \text{ cm}^{-2}$ ) have been reported by the same group [87]. Using a strain compensation technique, Akahane et al. have recently demonstrated an InP(311)B-based QD laser with  $20$  QD stacks in the active region, and a high characteristic temperature  $T_0$  of  $148 \text{ K}$  at  $298 \text{ K}$  [88]. Unfortunately, applications of InAs/InP(311)B QD lasers are still limited since the fabrication requires a more complex technological process that is not always compatible with the industrial standards.

In the following, we will be concentrated on the InAs/GaAs and InAs/InP QD materials, other configurations such as InP/GaP [89], (In, Ga)As/GaP [90], [91] are beyond the scope of this thesis.

### **III. Motivations of the dissertation**

As aforementioned, the recent evolution of optical communication systems is such that the transfer of massive amounts of information is no longer limited to long-distance transoceanic links or backbone networks. Numerous short-reach applications requiring high

data throughputs are emerging, not only in access networks, where upgrades of the bit rate of fiber-to-the-home systems need to be anticipated, but also in data center networks where huge amounts of information may need to be exchanged between servers, in part triggered by the rise of “Big Data” applications. In the future, high throughput interconnects will also be required within servers. However, the technological solutions developed over the years for long-distance and high-capacity systems are ill-suited for those emerging applications. The use of direct modulation in telecommunication core networks has been ruled out since the 1990’s when systems have been upgraded to 2.5 Gbps or 10 Gbps operation. The new requirements in terms of cost and energy consumption set by novel short-reach applications therefore need to be considered in the design and operation of a new generation of semiconductor laser sources, which is the main topic of the present dissertation. The evolution of the requirements on new optical transmitters takes two forms. First, energy efficiency has recently become a major concern in the tele- and data-communication world. With a global energy consumption already accounting for more than 2% of the world total and rapidly rising, information and communication technology must take drastic measures to improve the efficiency of its infrastructure. This is precisely one of the targets of using QD lasers. Besides, exploiting the nonlinear properties of QDs is the central point of the thesis with the view of developing novel optical functionalities like all-optical wavelength-converters with improved efficiency as well as optical feedback-resistant transmitters. This last point is even more critical since it is expected that short-reach links making use of directly modulated sources will experience massive deployment in the near future, in contrast to conventional backbone links where the number of required optoelectronic interfaces remains relatively modest. Regarding the long-haul applications, we have seen that the massive deployment of coherent systems does require the implementation of optical sources with narrow linewidth otherwise the sensitivity to the phase noise of both transmitters and local oscillators can strongly affect the bit error rates at the receiver. This is another objective to be addressed in the thesis where, we believe that the opportunities offered by the QD technology may be able to address this challenge. The experimental demonstration of the benefits of QD lasers in the context of the foreseen applications would therefore have a major impact.



## 1. Narrow linewidth QD lasers for coherent communications

The combination of advanced modulation formats and coherent detection are the key technologies in coherent communication systems to overcome the limitations in capacity of the currently fiber infrastructure by increasing the spectral efficiency [92]. Over the past years, the DSP technology has been successfully implemented in the fiber transmission system, in particular, coherent detection can benefit from these novel abilities: the electronic distortion equalization can effectively compensate the impairments over the transmission, and carrier synchronization can be performed by digital phase estimation, thus the optical phase locked loop can be removed and free running lasers can be directly used as local oscillators [92]. However, for high-order modulations, narrow linewidth lasers are still demanded for coherent detection. As an example, for 16-ary quadrature amplitude modulation (16QAM), a 120 kHz linewidth is necessary to ensure a maximal receiver sensitivity with a power penalty less than 2 dB at a  $10^{-4}$  bit-error rate [92]. Aside from the linewidth, the laser devices must be single-frequency, low cost and low power consumption. To further reduce the cost and power consumption, future candidate will consider hybrid III-V/Silicon technology where devices can be monolithically integrated on one single chip [93]. QD lasers are promising candidates for coherent communication systems, as previously discussed, they fulfill all these criteria: narrow spectral linewidth, low cost, low power consumption, and suitable for monolithic integration. Theoretically, narrow linewidth from a free-running laser can be obtained at high output power, however, the minimum achievable linewidth is limited by the rebroadening effect due to thermal and nonlinear effects [13], [94]–[98]. Nevertheless, the output power from the local oscillator is crucial in the coherent detection, thus the nonlinear effects must be reduced to achieve a narrow spectral linewidth and a high power lasing operation. In this work, results will show that QD DFB lasers with an optimized design can display a narrow spectral linewidth compatible for coherent systems.

## 2. QD lasers-based optical wavelength converters

All-optical wavelength converters are the building block for optical signal processing, such as optical routing and logical operations. In this context, four-wave mixing (FWM) is a

wavelength conversion technique, which has the great advantage to be transparent to both, intensity- and phase-modulated signals [99]–[101]. From a general viewpoint, the wave-mixing has been widely exploited in wavelength-division multiplexing (WDM) based systems [102] as well as for negative frequency chirping, fiber dispersion compensation [103], [104], optical nonlinear distortion compensation [105] and all-optical signal processing [106], [107]. With the emergence of commercial coherent systems, efficient FWM-based SOA wavelength converters are envisioned for advanced modulation format signals with wideband wavelength conversion over the whole C-band [72],[75]. Most published works have shown that FWM can be generated within different nonlinear media such as nonlinear silica and photonic crystal fibers [108], [109], silicon based micro-rings [110]–[112], and semiconductor optical amplifiers (SOAs) [113], [114]. Although the use of highly nonlinear optical fibers allows very efficient conversion, it usually requires an interaction length of several meters and a large pump power, which are not suitable for monolithic integration. Another important issue with optical fibers is that the required fiber length combined with an operation away from the zero-dispersion wavelength strongly affects the wave mixing and can alter conversion efficiency. On the other hand, recent works have reported efficient FWM with relatively low power consumption in micro-ring resonators. However such resonators usually require sophisticated low-loss bus waveguides design, and fabrication costs may thus be an issue as compared to a simple SOA. In the latter, FWM is obtained from the beating between the incident pump and probe beams and phase-matching is ensured owing to the hetero-structure confinement. Additional nonlinear effects occurring in SOAs like cross-gain modulation (XGM), and cross-phase modulation (XPM) can be used for optical wavelength conversion, however these do not usually provide the same modulation format transparency as does FWM [115].

In forward biased semiconductor devices, the wave mixing is essentially piloted by the carrier density pulsation (CDP) that enhances the static conversion, but with a slow response speed inherently limited by the carrier recombination lifetime (nanosecond timescale) [116]. In contrast, carrier heating (CH) and spectral hole burning (SHB), occurring within picosecond timescales, allow pushing the dynamic frequency conversion over much larger bandwidths, enabling conversion of high rate modulated signals. Although both SHB and CH contribute to increase the bandwidth, their efficiency is also reduced with respect to CDP meaning that a

tradeoff between efficiency and bandwidth is to be considered. Another detrimental effect that must be avoided for practical applications is the asymmetry of the conversion efficiency i.e. between up- and down-converted signals [103], [117]. For instance, it has been shown that a symmetric conversion allows to convert 40 Gbps non-return-to-zero (NRZ) modulated signal with similar BER penalties in up- and down-conversion in QD SOAs [118]. In this context, QDs constitute a class of nanostructures exhibiting larger optical nonlinearities with faster response speed [117], [119], [120]. As compared to bulk/QW semiconductors, the QD gain material exhibits a spectrally broader and improved conversion efficiency due to faster carrier dynamic and a lower linewidth broadening factor ( $\alpha_H$ -factor) [117]. Up to now, experimental studies have mainly focused on QD SOAs, taking advantage of their large linear gain and long interaction length [113], [114], [121], [122]. Instead, this thesis aims at investigating the capabilities of QD oscillators for FWM generation. Taking advantage of both the cavity resonances and reduced amplified spontaneous emission (ASE) noise [123], QD lasers can produce efficient FWM with improved amplitude and bandwidth, and more compact dimensions. In order to further compress the ASE noise, QD lasers using optical-injection-locking (OIL) are considered as originally reported for InGaAs/InP DFB QW lasers [124], [125]. In the dissertation, it will be shown that under proper OIL conditions, nonlinear dynamic of QD lasers allow faster modulation of the converted signals. In this context, an exhaustive comparison between InAs/GaAs and InAs/InP OIL lasers with either QD or QDash nanostructures will be performed. At the end, key-parameters ruling out the conversion performances will be proposed as manufacturing guidelines for future QD-based all-optical wavelength converters.

### **3. Feedback resistant QD lasers**

In order to meet the requirements of the explosive growth in data traffic, fast and low-cost transmitters with low energy consumption are required [5], [126]. Commonly, QD lasers are engineered to operate on the ground-state (GS) transition because of its low threshold current density. In addition, because of the strong damping of the relaxation oscillations, it is also known that QD lasers operating on the GS transition exhibit a larger resistance to external optical feedback which is of primal importance for isolator-free applications i.e. without the

integration of optical isolators [127], [128]. This enhanced robustness to optical perturbations combined to the large gain compression however sets the limit of modulation capabilities of QD lasers operating on the GS transition to a few GHz at room temperature [31], [128], [129].

In order to increase both speed and reach, prior studies have proposed to take advantage of the stimulated emission originating from the ESs transitions [130]. Owing to the faster carrier capture from the surrounding carrier reservoir as well as a higher saturated gain, ES QD transmitters have been touted to be a promising solution for high-speed applications [131]. The larger degeneracy of the ES translates into a larger differential gain and smaller nonlinear gain compression than those of the GS. The first successful investigation at the link level was realized with 1.3- $\mu\text{m}$  InAs/GaAs QD lasers emitting on the first ES transition, for which modulation capabilities up to 25 Gbps (OOK) and 35 Gbps (PAM) have been reported [132], [133]. Prior studies have also unveiled that taking advantage of the ES can be useful for ultra-short pulse generation [134], [135] and that the dynamics of ES QD mode-locked lasers in presence of optical feedback is more stable owing to a smaller linewidth broadening factor [136]. Very recent theoretical and experimental works have proved that ES QD lasers can indeed exhibit a near-zero  $\alpha_H$ -factor in comparison with the GS ones, which is of first importance for the making of chirp-free transmitters as well as crucial regarding the laser coherence and the modal stability [130], [137]. Lastly, various studies have investigated the two-state lasing dynamics where ES and GS lasing can take place simultaneously either with or without external optical feedback [136], [138]–[140]. Lastly, recent numerical studies investigating the two-state lasing regime, where both GS and ES emissions are simultaneously observed. In particular, it was recently unveiled that the two-state lasing can produce a large GS modulation enhancement [141], [142]. In order to further evaluate the impact of QD lasers in a communication link, the dissertation also unveils an in-depth comparison of the optical feedback dynamics of InAs/GaAs QD FP lasers emitting on different lasing states. As opposed to GS-emitting devices, nonlinear dynamic experiments reveal various differences between the lasing states as far as the route to chaos is concerned. Besides, it is shown that the ES QD laser exhibit regular pulse packaged pulsations, which can be used for the development of self-pulsating lasers with tunable repetition rates. These investigations also give realistic guidelines for the fabrication of feedback resistant QD lasers.

## IV. Organization of the dissertation

The dissertation is organized as follows:

Chapter II reminds the fundamentals of QD lasers including the electronic structure, the relaxation oscillations and damping, the linewidth broadening factor, the optical spectral linewidth, the nonlinear susceptibility, as well as the gain broadening mechanisms. This introduction constitutes a substrate for the understanding of the various experimental and theoretical investigations conducted throughout the thesis.

Chapter III describes the QD laser devices realized at the Technische Universität Berlin and the National Research Council of Canada as well as their fundamental characteristics. A focus is performed on the linewidth broadening factor and the optical spectral linewidth. The former strongly affects the nonlinear dynamics under OIL and external optical feedback, therefore experimental investigations of such parameter are performed both below and above the threshold and with three different methods (Amplified Spontaneous Emission, FWM, and modulation). Particularly, it is shown that the modulation technique does not properly characterize the linewidth broadening factor of QD lasers. The spectral linewidth is crucial to describe the lasing performance, and therefore is of first importance for the realization of narrow linewidth local oscillators in future coherent communication systems [7]. In this thesis, record values of the optical spectral linewidth below 200 kHz are also reported in InAs/InP QD lasers. In addition, using a controlled optical feedback loop, it will be shown that the latter can be further reduced down to about 100 kHz, which is also important for applications related to chip atomic clocks where both narrow linewidth operation and low frequency drift are mandatory.

In chapter IV, optically-injected resonant oscillators using QDs as a non-linear gain medium are studied both for InAs/InP and InAs/GaAs QD material systems. Large FWM conversion efficiencies with large optical signal-to-noise ratios are unveiled. The static conversion bandwidth is extended far in the terahertz window with a quasi-symmetrical response between up- and down-converted signals. Impact of operating parameters (bias conditions, pump wavelength, etc.), external conditions (injection strength and detuning), and cavity dimensions (length and ridge waveguide) are considered. A semi-analytical model based

on a travelling-wave approach is also presented to extract the third-order nonlinear susceptibility while the impact of the reflected field on the conversion efficiency is also discussed from simulations based on a multi-population rate approach.

Chapter V is then devoted to study the optical feedback dynamics of InAs/GaAs QD lasers. To further evaluate the potential impact of such transmitters in the view of their inclusions into a fiber-pigtailed telecom module, this part aims at characterizing the nonlinear dynamics of such lasers emitting on different lasing states. Comprehensive characterizations are performed, unveiling different complex dynamics. Chaos boundaries are extracted for the different lasing states both under long and short external cavity regimes. In addition, self-pulsating behaviors are unveiled in the ES QD laser, with a repetition rate tunable with the external cavity length. This last study is of first importance for the development of feedback resistant high-speed transmitters for short-reach communication links.

Finally, chapter VI gives a general conclusion and the perspectives to this work.

## Chapter II. Fundamentals of quantum dot lasers

The objective of this chapter is to recall the basic features of QD lasers. In the first place, the electronic structure will be introduced, then the carrier dynamics including capture and relaxation processes will be presented. In the second place, fundamental properties of QD lasers will be considered, such as linewidth broadening factor, optical spectral linewidth, nonlinear gain, damping factor, as well as gain broadening mechanisms.

### I. Electronic structure

In semiconductor physics, the discretization of the carrier mobility is achieved when the crystal dimension becomes lower or equal than the de Broglie wavelength of carriers. To this end, it is shown that the critical diameter  $D_{\min}$  of discretization is defined as a function of the material band offset  $\Delta E_c$  (see for instance Figure 2.2) [43]:

$$D_{\min} = \frac{\pi \hbar}{\sqrt{2m_e^* \Delta E_c}} \quad (2.1)$$

where  $m_e^*$  is the electron effective mass. In the case of self-assembled QDs, the typical critical diameter value is 3 to 5 nm, of the same order of magnitude of the dot dimension, thus the carrier is confined in all 3 space-dimensions hence the electronic structure can be approximately represented in the form of a three-dimensional potential well, with discretized energy levels. As an example, Figure 2.1 (a) represents of a classical p-i-n doped QD laser from [143]. The gain media is sandwiched between the AlGaAs separate confinement heterostructures (SCHs) and the GaAs barriers, the dots are interconnected with a wetting layers (WL), and each dot layer is separated by a spacer made of the same material than the barriers. Figure 2.1 (b) shows the material composition and thickness of each layer in Figure 2.1 (a). Figure 2.1 (c) depicts the space energy diagram aligned to the x-axis, Carriers transport from the three-dimensional SCH to the barrier then into the two-dimensional WL before being captured into the dots. It should be stressed out that such diagram is not exclusive and depends on the nature of the epi-structure. For instance, for a dot-in-a-well (DWELL) configuration [144], each dot layers are embedded in a QW, thus the dot energy levels are confined in the surrounding well, and the WL is absent.

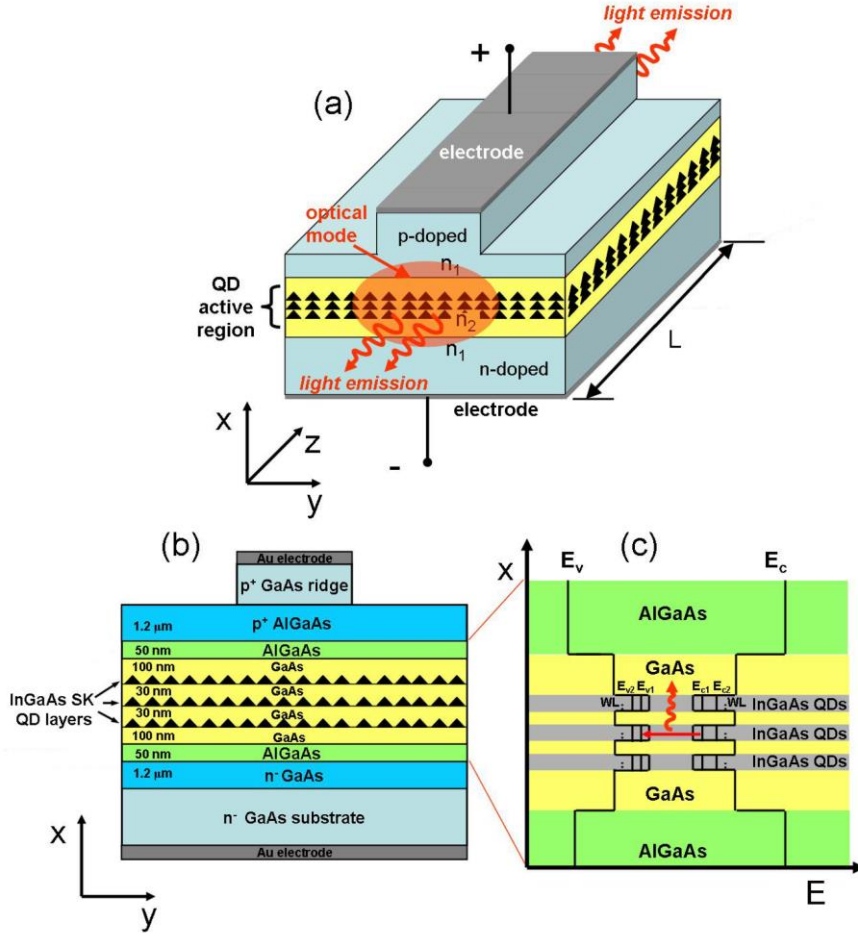


**Figure 2.1.** (a) 3-D schematic of a QD p-i-n-doped semiconductor laser diode. The yellow region is the undoped active region, and the black triangles represent the dots. (b) Cross-section of the schematic in (a), showing the material composition and thickness of each layer. (c) Energy band alignment of the heterostructure along the x-axis, after [143].

Figure 2.2 illustrates the typical QD laser electronic structure including a 3D barrier, a 2D reservoir state (RS) corresponding to the WL, and the zero-dimensional QD. Within the 3D and the RS, carriers are usually treated as quasi-free particles. Using the effective mass theory, the DOS of the electrons in the conduction band for both the barrier and RS can be expressed as follows [145]:

$$\rho_{\text{barrier}}(E) = d_{\text{barrier}} (2m_e^*/2\pi^2\hbar)^{2/3} \sqrt{E - E_{\text{barrier}}} \quad (2.2)$$

$$\rho_{\text{RS}}(E) = \frac{1}{d_{\text{RS}}} (m_{e,\text{RS}}^*/\pi\hbar^2) u(E - E_{\text{RS}}) \quad (2.3)$$

where  $m_e^*$  is the effective mass for electron,  $d_{\text{barrier}}$  and  $d_{\text{RS}}$  the thickness of the barrier and the WL,  $\hbar = h/2\pi$  the reduced Plank constant,  $E_{\text{barrier}}$  and  $E_{\text{RS}}$  the recombination energy



from the barrier and the RS, and  $u(E - E_{RS})$  is the step like function. Similar expressions for the holes can be obtained from the valence band [145]. By solving the Schrödinger's equation within the dot and by using a 3D finite box approximation, a series of delta functions can be obtained at the quantized energy solutions representing the GS and the higher ES transitions respectively. The quasi-continuum carrier reservoir coupling with the localized energy states of the dots results in smaller energy separations and thus state overlapping at higher energies [146]. While at lower energies, the discrete states are separated of a few tens of meV in the conduction band (CB), such a separation is much smaller in the valence band (VB) due to the heavier hole effective masses.

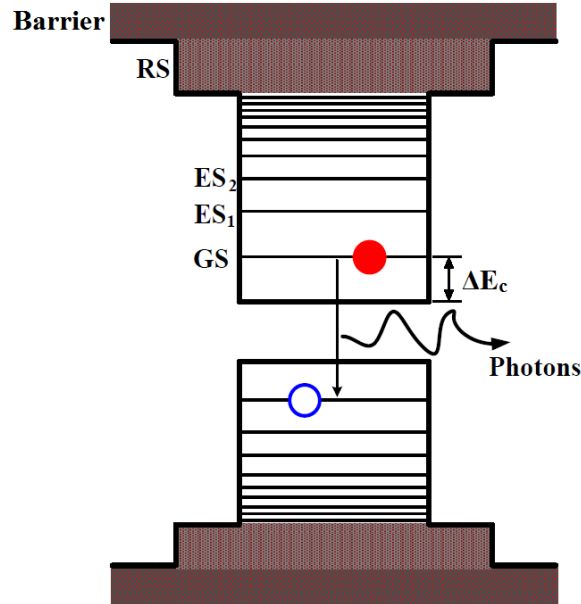


**Figure 2.2.** Schematic of a QD laser electronic structure with electrons and holes, after [147].

In the semiconductor active region, electrons and holes are bounded into excitons (electron-hole pairs) due to the Coulomb interaction, and the distance between them is referred as the Bohr radius, which is typically of a few nanometers [148]. The exciton nature can be modified by the confinement structure and thus exhibits different optical properties. Assuming the excitonic approach, semi-empirical models have been developed in which the vertical coupling is taken into account from two discrete states in QDs: a two-fold degenerate GS and a four-fold degenerate first ES. The lateral coupling among the QD nanostructures is ensured through the 2D RS. This configuration has been used with a great success to reproduce

the time resolved photoluminescence (TRPL) experiments as well as for predicting the modulation dynamics of QD semiconductor lasers [37], [149]. However, the excitonic approach has some limitations in predicting behaviors such as the GS quenching which, occurs when QD lasers exhibit simultaneous GS and ES lasing, which is attributed to the asymmetry between electrons and holes [150].

## II. Carrier dynamics

The QD carrier dynamics is driven by the carrier capture and the carrier relaxation processes. Generally, while injecting current into a QD device, a high density carrier plasma is activated in the barrier [151], the carriers then travel across it before reaching the 2D RS. Depending on the thickness of the barrier, the carrier transportation time can be of several picoseconds (1~5 ps) [152]. Finally, once carriers are captured into the dots, they will relax through the higher energetic ES levels down to the GS, where the lasing operation will be activated owing the recombination between electrons and holes. The mechanisms that mainly contribute to the carrier capture and relaxation are carrier-phonon and carrier-carrier scatterings involving Auger effect, as illustrated in Figure 2.3 [153].

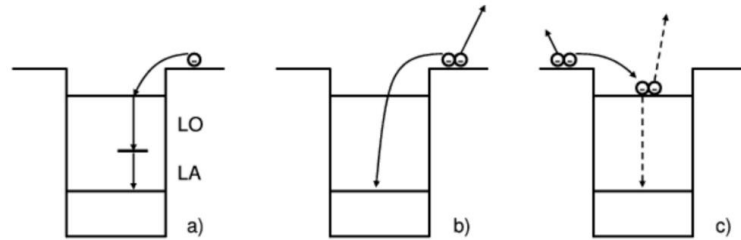


**Figure 2.3.** Illustration of the carrier capture and relaxation processes: a) multi-phonon processes under low excitation density, b) single Auger process, and c) sequential Auger processes under high injection current density, after [153].

On the other hand, it has been shown that carriers can also be directly captured from the RS to the GS. This direct relaxation channel contributes to accelerate the carrier dynamics. In addition, it has been shown that this direct capture plays an important role on the dual-state lasing operation from which GS and ES can turn on simultaneously [154]. Finally, let us stress that lateral coupling among the dots and defects assistance are also alternative ways for enhancing the carrier dynamics through carrier scattering [146], [155], [156].

## 1. Carrier capture

Carrier capture in QD is driven by Auger process and longitudinal optical (LO) phonon-carrier scattering [157]. In QW structures, the latter is dominant for its efficient energy dissipation. However, in QDs, the capture process is more complicated since the carrier scattering depends on the carrier density. Figure 2.4 provides a direct comparison of capture rates between the two mechanisms. As represented, carrier-carrier scattering (e-e and h-e) from the RS into the dots is the dominant contribution at high carrier density [158] (see also figure 2.3 (b) and (c)), while at lower carrier density, the LO phonon-assisted capture that is temperature dependent is more efficient. Generally, scattering by electrons has been found to be more efficient than scattering by holes because of their smaller effective mass. In addition, the capture rate is strongly dependent on the energy separation between the RS and the QD states. With the increased separation, the Auger coefficients for all types of Auger process (e-e, e-h, h-h, h-e) decrease. This indicates that in QDs with multiple levels, carrier capture into the highest excited states is the most efficient [157], [159].

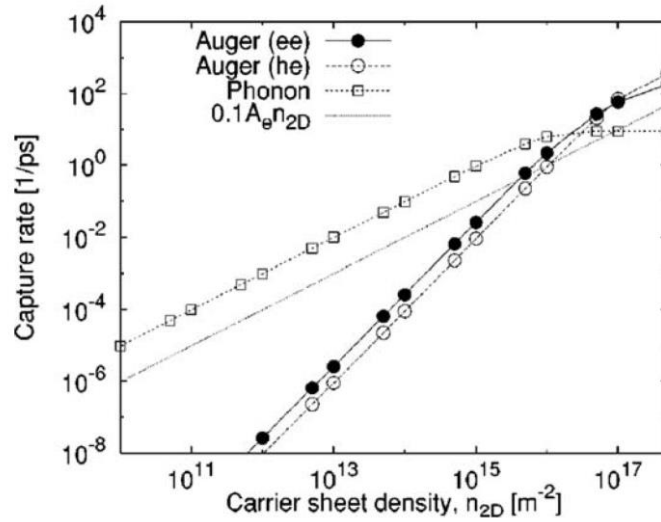


**Figure 2.4.** The capture rate as a function of the carrier density, after [160].

## 2. Carrier relaxation

Early studies have pointed out that, in zero-dimensional QD systems, relaxation occurs through carrier-phonon interactions [157], [161]–[163]. Although the large energy separation of the QD states does not usually match the LO phonon energy, thus the carriers will interact

with multi-phonons, i.e. LO phonons and longitudinal acoustic (LA) phonons (Figure 2.3 (a)). As such, the phonon-assisted relaxation process slowing down the relaxation dynamic is often referred as "phonon bottleneck" [38], [161]. However, it has to be stressed out that in some experimental observations, a fast relaxation have been observed, indicating that additional mechanisms are involved [163]. By including the anharmonic decay of LO phonons into bulk acoustic phonons, Li et al. pointed out that carrier lifetime of 2.5 to 7 ps allows LO phonon emission to extend up to tens of meV, hence opening an efficient carrier relaxation window [164], [165]. On the other hand, Uskov et al. [166] suggest that the Auger process is also involved in the relaxation process. For carrier densities of  $10^{11} - 10^{12} \text{ cm}^{-2}$ , the relaxation time is calculated from 1 to 10 ps. A comprehensive comparison between the LO phonon-carrier and carrier-carrier scattering has been performed by Nielsen et al. [151]. By including the population effects and the in- and out-scattering, relaxation time as low as 1 ps has been identified. Besides, the carrier relaxation was found to be faster than the capture, and processes involving holes were faster than the corresponding effects for electrons. An alternative relaxation channel is the defect-assisted carrier relaxation, suggesting that a carrier at higher dot energy state can relax down to lower states with multi-phonon emission [155], [156], [167]. The calculations carried out a relaxation time of about 1 ps, hence indicating that the defect-assisted relaxation can be an efficient process.

### III. Gain broadening mechanisms

As aforementioned, ideal QDs exhibit atom-like discrete energy levels which would ideally lead to QD lasers with outstanding properties [35]. However, these theoretical predictions hold under the assumptions of identical dots and single energy levels, that were rapidly disproved in real devices [168]. In a real QD laser both homogeneous and inhomogeneous gain broadening mechanisms must be considered. The latter comes from the QD size dispersion that leads to an energy state distribution as depicted in Figure 2.5. [169]. As a consequence of that, the lasing operation is only supported by a limited population of dots meaning that the optical gain is reduced and the lasing performances altered [170]. A smaller value of the FWHM of the inhomogeneous broadening is required to maximize the optical gain and the

dynamical properties of a QD laser. A typical value of inhomogeneous broadening is a few tens of meV (30 – 60 meV) in GaAs- and InP-based QD lasers [77], [171].

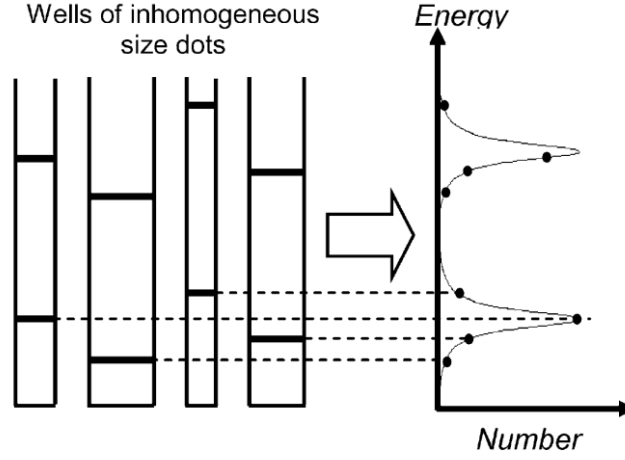


**Figure 2.5.** Representation of the inhomogeneous broadening illustrating dots with different sizes, and leading to an energy state distribution, after [169].

As for the homogeneous broadening, it is proportional to the polarization dephasing rate, which corresponds to the decay time of the optical polarization associated with an interband transition [172]. For a quasi-equilibrium carrier system, the dephasing time  $T_2$  can be considered as twice of the total carrier scattering time constant [173], and the full-width-at-half maximum (FWHM) of the homogeneous broadening for a confined QD lasing state can be expressed as [174]:

$$2\hbar\Gamma_{hom} = \frac{2\hbar}{T_2} = \hbar \left( \frac{1}{\tau_{hh}} + \frac{1}{\tau_{he}} + \frac{1}{\tau_{ee}} + \frac{1}{\tau_{eh}} \right) + \hbar \frac{1}{\tau_{phon}} + \hbar \frac{1}{\tau_{recom}} \quad (2.4)$$

Eq. 2.4 specifies the mechanisms that contribute to the finite carrier lifetime: the Auger scattering processes (hh, he, ee, eh), carrier-phonon and carrier-carrier scatterings as well as the finite carrier lifetime related to the radiative recombinations [120], [175]–[177]. The homogeneous broadening is strongly temperature-dependent as illustrated in Figure 2.6 from the photoluminescence (PL) spectra of a single InAs/GaAs QD [178]. As observed, increasing the temperature from 77 K to 300 K broadens the PL spectrum and so the homogeneous broadening from a few micro-eV to a few meV.

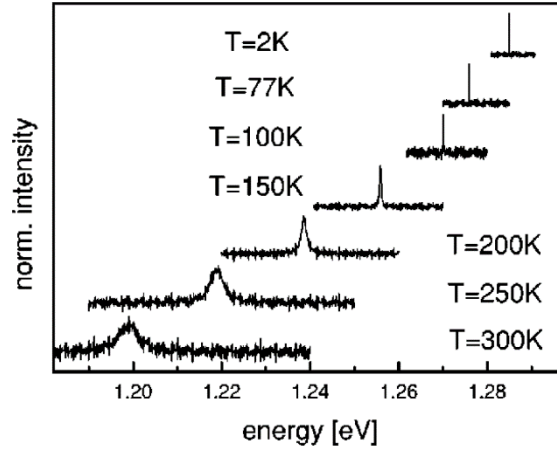


**Figure 2.6.** Photoluminescence spectrum as a function of temperature from a single InAs/GaAs dot, after [178].

In a real QD laser, while the homogeneous broadening is much smaller than the inhomogeneous broadening, i.e. at low temperature, due to the carrier localization, all dots that have an optical gain above the lasing threshold start lasing independently, leading to a broadband lasing emission, as illustrated in Figure 2.7 (a). Then, as the temperature rises, the homogeneous broadening become comparable to the inhomogeneous broadening, lasing mode photons are emitted not only from energetically resonant dots but also from other non-resonant dots hence leading to an emission with a narrow line of a dot ensemble, which explains the narrow emission spectra observed close to room temperature as depicted in Figure 2.7 (b) [175], [179]–[181].

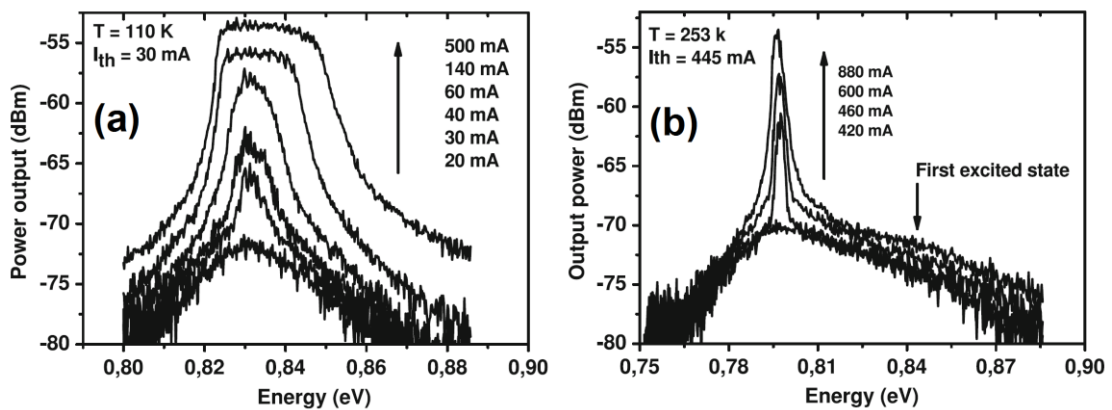


**Figure 2.7.** Lasing and electroluminescence spectra under pulsed injection mode for different bias level at two different temperatures: (a) 110K and (b) 253 K, after [179].

## IV. Gain dynamics

### 1. Linewidth broadening factor

In semiconductor lasers, the gain and the refractive index are coupled via the Kramers-Kronig relations [182] through the carrier injection. Theoretical investigation of the Kramers-Kronig relations require the use of microscopic equations in which the Hamiltonian of the system includes contributions from the kinetic energies, the many-body Coulomb interactions, the electric-dipole interaction between the carriers and the laser field, the carrier-phonon interactions, as well as the effects of the injection current [183]. From a general viewpoint, the macroscopic polarization  $P$  can be expressed as the sum of the microscopic polarizations  $p_i$  related to all interband transitions:

$$P = \frac{1}{V} \sum_i \mu_i p_i \quad (2.5)$$

where  $V$  is the active region volume and  $\mu_i$  is the dipole matrix element for the GS, ES and RS transitions in dots. Assuming the medium isotropic, the complex optical susceptibility can be written as:

$$\chi = \frac{1}{\epsilon_0 n_0^2} \frac{P}{E} \quad (2.6)$$

with  $\epsilon_0$  is the vacuum permittivity and  $E$  the electric field amplitude. The laser's electric field propagating throughout the active region is coupled via the gain  $g$  and the carrier-induced refractive index  $\delta n$  as follows:

$$\frac{d}{dt} E(t) = \Gamma \frac{cg}{2n_0} E(t) + j \frac{\omega \delta n}{n_0} E(t) \quad (2.7)$$

Where  $\Gamma$  the confinement factor,  $c$  the velocity of light, and  $\omega$  the lasing angular frequency. From Eq. 2.7, the gain and the carrier-induced refractive index is expressed as:

$$g = -\frac{\omega n_0}{c} \text{Im}\{\chi\} = -\frac{\omega}{\epsilon_0 n_0 c} \frac{\text{Im}\{P\}}{E} \quad (2.8)$$

$$\delta n = \frac{n_0}{2} \text{Re}\{\chi\} = \frac{1}{2\epsilon_0 n_0} \frac{\text{Re}\{P\}}{E} \quad (2.9)$$

The gain is then described assuming a linear carrier density dependence such as:

$$g = a(N - N_{tr}) \quad (2.10)$$

In Eq. 2.10,  $N$  is the carrier density injected into the laser,  $N_{tr}$  is the carrier density at the transparency where the gain compensates totally the absorption and  $a = \partial g / \partial N$  is the differential gain (i.e. dynamic gain).

From Eq. 2.8 and 2.9, the  $\alpha_H$ -factor is further introduced to describe the coupling between the gain and the refractive index [182], [184]:

$$\alpha_H = \frac{\partial \text{Re}\{\chi\} / \partial N}{\partial \text{Im}\{\chi\} / \partial N} = -2 \frac{\omega}{c} \frac{dn/dN}{dg/dN} = -\frac{4\pi}{\lambda} \frac{dn/dN}{dg/dN} \quad (2.11)$$

where  $\lambda$  is the lasing wavelength, and  $dn/dN$  the differential index.

The  $\alpha_H$ -factor is a vital parameter in the description of semiconductor laser physics that influences many characteristics and performances, for instance the optical spectral linewidth [182], [185], the frequency chirp [186], the mode stability [187] as well as the nonlinear dynamics under optical injection [188] or optical feedback [54], [189], [190]. In the latter cases, a positive  $\alpha_H$  is required to generate complex nonlinear dynamics within a semiconductor laser. Historically the  $\alpha_H$ -factor was first introduced simultaneously in 1967 by Lax [191] and Haug & Haken [192]. Using either quantum calculations from the density matrix equations or a semi-classical theory, both have introduced a factor of  $(1 + \alpha_H^2)$  to describe the noise-induced phase fluctuations that also appear in the equation setting the spectral linewidth. However, the former did not further exploit the spectral linewidth equation, whereas the latter did not consider the  $\alpha_H$ -factor since it was too small as compared to the unity. In 1982, Henry [182] reintroduced the  $\alpha_H$ -factor and fully theorized the spectral linewidth of semiconductor lasers. Typical values of the  $\alpha_H$ -factor range between 2 to 5 for bulk and QW materials.

Figure 2.8 (a) depicts the evolution of the material Kramer-Kronig related gain and refractive index versus the lasing photon energy. In a QW laser, the zero point of the refractive index is dislocated from the gain peak both for low and high carrier density, hence the  $\alpha_H$ -factor always deviates from 0 [193]. In the case of an ideal QD laser, i.e. for a QD ensemble with symmetric gain, the gain arises from the carrier population in the resonant GS, hence the



differential refractive index change is exactly zero at the lasing photon-energy  $h\nu_0$  (i.e. position of gain peak), as indicated in Figure 2.8 (b). Therefore, in QD lasers having a symmetric gain, the  $\alpha_H$ -factor is null at the lasing frequency. However, it has been shown multiple times that the  $\alpha_H$ -factor of QD lasers is widely dispersed with values ranging from zero up to more than 10, including a giant one as high as 60 [194].

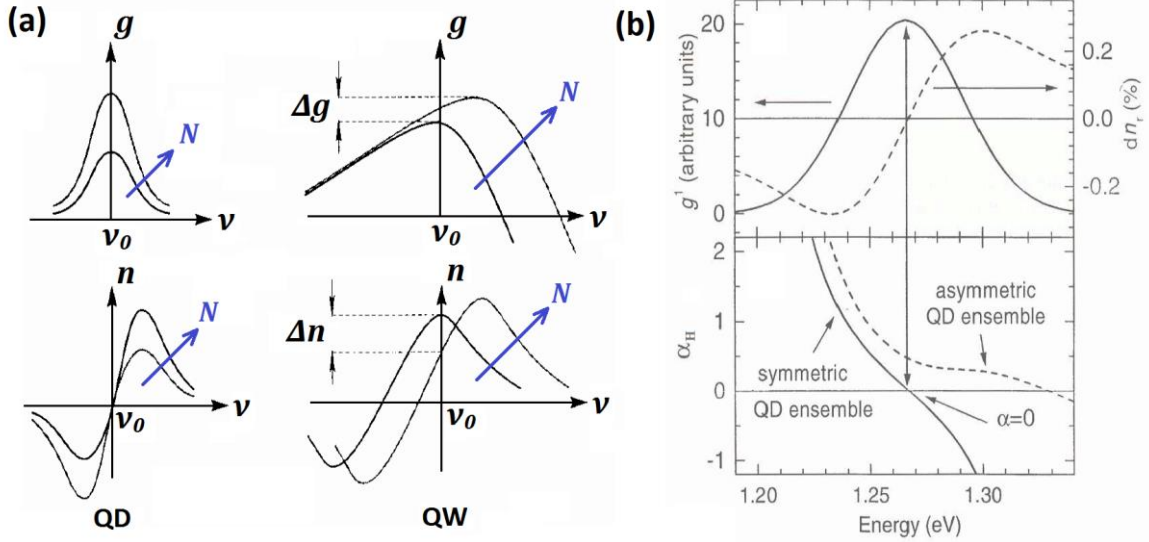


**Figure 2.8.** (a) Schematic of gain  $g$  and refractive index  $n$  profiles variation with the carrier density changes for QW and symmetric QD ensemble, after [195]; (b) gain ( $g$ ) and refractive index ( $n$ ) profiles versus  $\alpha_H$ -factor in symmetric QD ensemble, which is compared to asymmetric QD ensemble, after [43].

In QD lasers, the non-zero  $\alpha_H$ -factor is attributed to the large inhomogeneous broadening, the off-resonant states (i.e. higher energy levels) as well as the free carrier plasma. Indeed as the injection current increases, the lower energy states are saturated and the carrier filling into the higher energy levels significantly alters the symmetry of the gain spectrum hence ballooning the  $\alpha_H$ -factor to larger values [58], [194], [196]. Lingnau et al. have even pointed out that, while the GS resonant state contributes the most to the gain change, the off-resonant states impact mostly on the refractive index variation [197], [198], therefore the real and imaginary parts of the optical susceptibility  $\chi$  are “desynchronized”, and the  $\alpha_H$ -factor is strongly altered. As regards the carrier plasma effect it originates from intraband transitions [199]. In QW lasers, the carrier plasma effect is described by the Drude model [200]:

$$\delta n_{FC} = -\frac{\Gamma_p e^2 N}{2n_b \epsilon_0 m^* \omega^2} \quad (2.12)$$

where  $\delta n_{FC}$  is the carrier plasma induced refractive index change,  $e$  the electron charge. Analog transitions in QD lasers can be envisaged between the bound states and the continuum levels of the RS and the barrier. It has been shown that the Drude formula can also be applied to the case of QD lasers when carriers are not tightly confined into the QDs and for photon energies within 0.8-1.0 eV [199]. Prior works have shown that carrier plasma effect contributes to almost to half of the overall refractive index changes [199], [200].

## 2. Stability analysis, relaxation oscillations and damping

Relaxation oscillations are inherent to class B semiconductor lasers like bulk, QW and QD lasers for which the photon lifetime  $\tau_p$  is much smaller than the carrier lifetime  $\tau_c$  [201]. In a semiconductor laser, the lasing field  $\tilde{E}(t)$  can be described as [202]:

$$\frac{d\tilde{E}(t)}{dt} = \left\{ \frac{1+i\alpha_H}{2} \left[ \Gamma G_N(N(t) - N_{tr}) - \frac{1}{\tau_p} \right] + i\omega \right\} \tilde{E}(t) \quad (2.13)$$

where  $N(t)$  is the carrier density,  $G_N = v_g dg/dN$  is the linear gain with  $v_g$  and  $g$  being the group velocity and the optical gain,  $N_{tr}$  the transparency carrier intensity, and  $\omega$  the lasing angular frequency.

Assuming the lasing field is in the form  $\tilde{E}(t) = A(t)\exp(i\omega t + i\phi(t))$ , thus by separating the real part and the imaginary part of Eq. 2.13, we obtain the following rate equations:

$$\frac{dA(t)}{dt} = \frac{1}{2} \left[ \Gamma G_N(N(t) - N_{tr}) - \frac{1}{\tau_p} \right] A(t) \quad (2.14)$$

$$\frac{d\phi(t)}{dt} = \frac{\alpha_H}{2} \left[ \Gamma G_N(N(t) - N_{tr}) - \frac{1}{\tau_p} \right] \quad (2.15)$$

In addition, the rate equation for  $N(t)$  is given by [202]:

$$\frac{dN(t)}{dt} = \frac{\eta_i I}{qV} - \frac{N(t)}{\tau_c} - G_N[N(t) - N_{tr}]A^2(t) \quad (2.16)$$

where  $\eta_i$  is the injection efficiency characterizing the fraction of bias current that generates

carriers in the active region,  $I$  the injection current,  $q$  the electron charge,  $V$  the active region volume,  $\tau_c$  the carrier lifetime,  $v_g$  the group velocity. In Eq. 2.16, the first term on the right hand represents the injected carriers into the laser active region; the second and the last terms correspond to the carrier decay and photon generation respectively.

The steady-state solutions  $A_s$ ,  $\phi_s$  and  $N_s$  of Eq. 2.14 to 2.16 are given by:

$$A_s^2 = \frac{\eta_i I / qV - N_s / \tau_c}{G_N(N_s - N_{th})} \quad (2.17)$$

$$\phi_s = 0 \text{ with } \omega_s = \omega \quad (2.18)$$

$$N_s = N_{tr} + \frac{1}{\Gamma G_N \tau_p} = N_{th} \quad (2.19)$$

with  $N_{th}$  is the threshold carrier density.

Let us assume now small perturbations around the steady-state solutions such that:

$$A(t) = A_s + \delta A(t) \quad (2.20)$$

$$\phi(t) = (\omega_s - \omega_0)t + \delta \phi(t) \quad (2.21)$$

$$N(t) = N_s + \delta N(t) \quad (2.22)$$

By injecting Eq. 2.17 to 2.22 into Eq. 2.14 and 2.16, one gets:

$$\frac{d\delta A(t)}{dt} = \frac{1}{2} \Gamma G_N A_s \delta N(t) \quad (2.23)$$

$$\frac{d\delta \phi(t)}{dt} = \frac{\alpha_H}{2} \Gamma G_N \delta N(t) \quad (2.24)$$

$$\frac{d\delta N(t)}{dt} = -\frac{2A_s}{\Gamma \tau_p} \delta A(t) - \frac{1}{\tau_c} \delta N(t) - G_N A_s^2 \delta N(t) \quad (2.25)$$

Rearranging Eq. 2.23 to 2.25 yields:

$$\begin{bmatrix} \frac{d\delta A(t)}{dt} \\ \frac{d\delta \phi(t)}{dt} \\ \frac{d\delta N(t)}{dt} \end{bmatrix} = \begin{bmatrix} 0 & 0 & \frac{1}{2} \Gamma G_N A_s \\ 0 & 0 & \frac{\alpha_H}{2} \Gamma G_N \\ -\frac{2A_s}{\Gamma \tau_p} & 0 & -\frac{1}{\tau_c} - G_N A_s^2 \end{bmatrix} \begin{bmatrix} \delta A(t) \\ \delta \phi(t) \\ \delta N(t) \end{bmatrix} = M_J \begin{bmatrix} \delta A(t) \\ \delta \phi(t) \\ \delta N(t) \end{bmatrix} \quad (2.26)$$

Thus the solutions of Eq. 2.23 to 2.25 can be obtained from the eigenvalues of the Jacobian

Matrix  $M_J$ . The characteristics equation solving the eigenvalue  $\xi$  is given by  $|M_J - \lambda I| = 0$ :

$$|M_J - \lambda I| = -\xi \left[ \xi^2 + \left( \frac{1}{\tau_c} + G_N A_s^2 \right) \xi + \frac{G_N A_s^2}{\tau_p} \right] = 0 \quad (2.27)$$

where the trivial solution is  $\xi = 0$ , and the two other solutions are given by:

$$\xi = -\frac{1}{2} \left( \frac{1}{\tau_c} + G_N A_s^2 \right) \pm \sqrt{\frac{1}{4} \left( \frac{1}{\tau_c} + G_N A_s^2 \right)^2 - \frac{G_N A_s^2}{\tau_p}} \quad (2.28)$$

As previously mentioned, for class B laser,  $\tau_p \ll \tau_c$ , therefore the term inside the square root is negative, and the solution becomes complex with:

$$\xi = -\frac{1}{2} \left( \frac{1}{\tau_c} + G_N A_s^2 \right) \pm i \sqrt{\frac{G_N A_s^2}{\tau_p} - \frac{1}{4} \left( \frac{1}{\tau_c} + G_N A_s^2 \right)^2} = \xi_{Re} + i \xi_{Im} \quad (2.29)$$

where the relaxation oscillation  $f_{RO}$  and the damping factor  $\gamma$  are defined from the real part  $\xi_{Re}$  and the imaginary part  $\xi_{Im}$  such as [202]:

$$f_{RO} = \frac{1}{2\pi} \sqrt{\frac{G_N A_s^2}{\tau_p}} \quad (2.30)$$

$$\gamma = \frac{1}{2} \left( \frac{1}{\tau_c} + G_N A_s^2 \right) \quad (2.31)$$

In Eq. 2.29, as  $\tau_c$ ,  $G_N$  and  $A_s$  are positive meaning that  $\xi_{Re} < 0$ , thus the steady solutions are always stable. In Eq. 2.30, the steady-state field amplitude  $A_s$  increases with the bias current, leading to the increase of the relaxation oscillation frequency, as well as the damping.

The impact of the relaxation oscillation frequency and the damping rate can be further analyzed from the modulation response of a semiconductor laser which can be extracted via a small signal analysis of the rate equations, i.e. by using a time-varying current  $I(t) = I_0 + \delta I \exp(i\omega t)$ , where  $I_0$  is the bias current and  $\delta I \ll I_0$  the modulation current. Figure 2.9 shows the evolution of the modulation response of the laser while increasing the bias current. The resonant peak with a magnitude of  $\sim (f_{RO}/\gamma)^2$  is induced by the relaxation oscillation and the -3 dB frequency  $f_{-3dB}$  gives the small-signal modulation bandwidth of the laser. As compare

to QW lasers, the modulation dynamics of QD lasers is strongly limited by the carrier capture and relaxation processes as well as by the Pauli blocking (direct consequence of Pauli exclusion principle), which are responsible for the large damping factor [203]. Besides, due to the inhomogeneous broadening and the high gain compression effects that will be discussed later on, the relaxation oscillation frequency is further reduced as well as the 3-dB modulation bandwidth [193].

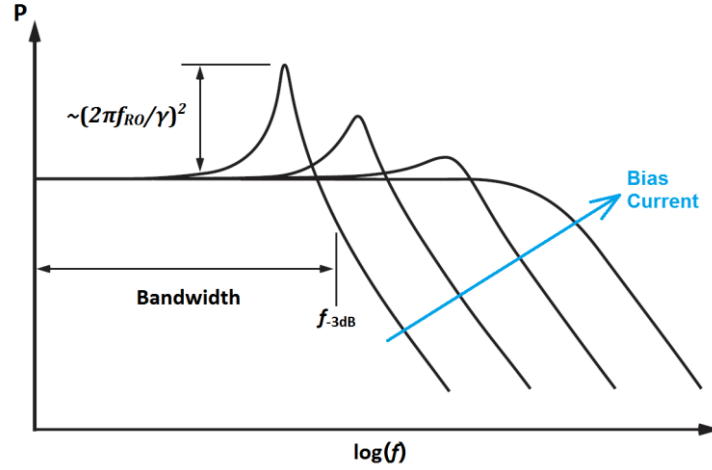


**Figure 2.9.** Modulation response of a semiconductor laser. The blue arrow indicates the increase of the bias current, after [193].

### 3. Nonlinear carrier dynamics

When the semiconductor gain medium is perturbed by an optical pulse, the physical mechanisms governing the recovery of the carrier population are related to inter-band and intra-band dynamics whose typical time constants are of the order and below 100 ns and 1 ps respectively. Figure 2.10 illustrates the evolution of the carrier energy distributions after the propagation of an optical pulse at frequency  $\omega_0$  within the semiconductor material pumped in the gain regime. The blue solid line (0) represents the carrier distribution under thermal equilibrium (following Fermi distribution) before the perturbation. The black dotted horizontal line corresponds to the quasi Fermi level  $E_f$ .

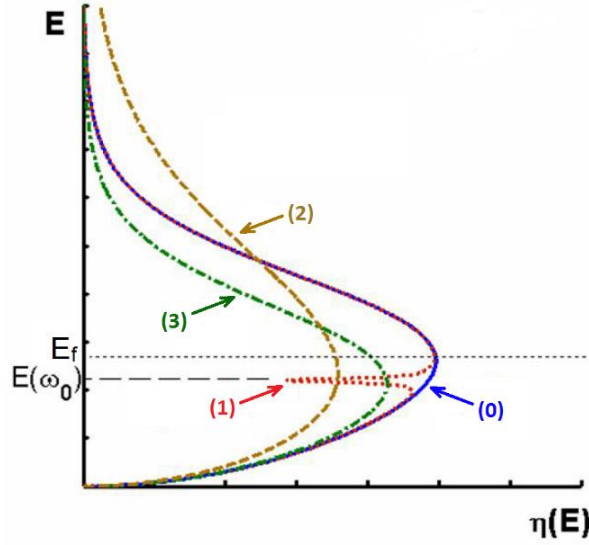


**Figure 2.10.** Representation of the carrier energy distributions  $\eta(E)$  after propagation of an optical pulse within the semiconductor medium pumped in the gain regime, after [143].

The following sequence of event occurs:

- From (0) to (1): when an optical pulse penetrates the semiconductor material, the photons participate in stimulated emission, and carriers are “burned”. Such phenomenon is referred to as the spectral hole burning (SHB) which reduces the carrier distribution at a specific energy related to the injected photon energy (and consequently the laser’s gain for frequencies around that of the injected photons  $\omega_0$  (red dotted line (1)).
- From (1) to (2): after the light pulse exits, the carriers thermalize to recover and the spectral hole vanishes via intraband carrier-carrier scattering. However, the new distribution is different from the initial one. It has a higher temperature than the original carrier temperature set up by the lattice acting as a thermostat. The carrier heating (CH) mechanisms involved is attributed to the carrier consumption by stimulated emission following the perturbation that removes “cold carriers” whose energy is below the average energy. In addition to that, free-carrier absorption can also play a role since, instead of participating to the stimulated transitions, photons may also be absorbed by a free-electron already in the conduction band. The energy of the photon transfers to the free electron, causing the electron to be excited to a higher energy state increases the total energy of the carriers’ population.
- From (2) to (3) the distribution cools down to the lattice temperature via carrier

redistribution occurring through carrier-phonon scattering.

- to (0): The total carrier population recovers the steady-state population through carrier replenishing with the injection current.

As for the SHB, Borri et al. have measured a characteristic time as low as  $\sim 100$  fs in InAs/GaAs QDs by pump-probe spectroscopy [204]. Such a fast response that dominates the phonon-bottleneck can be attributed to the strong Coulomb interaction in QDs [203]. On the other hand, the CH recovery mechanism is slowed down in QDs ( $\sim 0.7$  ps, [204]) as compared to QW or bulk materials, since the energy discretization restricts the carrier population on each energy state. Figure 2.11 illustrates the pump-probe measurements in a six-layer InAs/GaAs QD SOA device [17]. As compared to a conventional QW SOA, it can be noticed that, the gain recovery dynamics is faster in QDs and ruled out by two time constants. It has been mentioned that the fastest time constant can be due to the relaxation bottleneck while the other comes from the carrier population recovery.

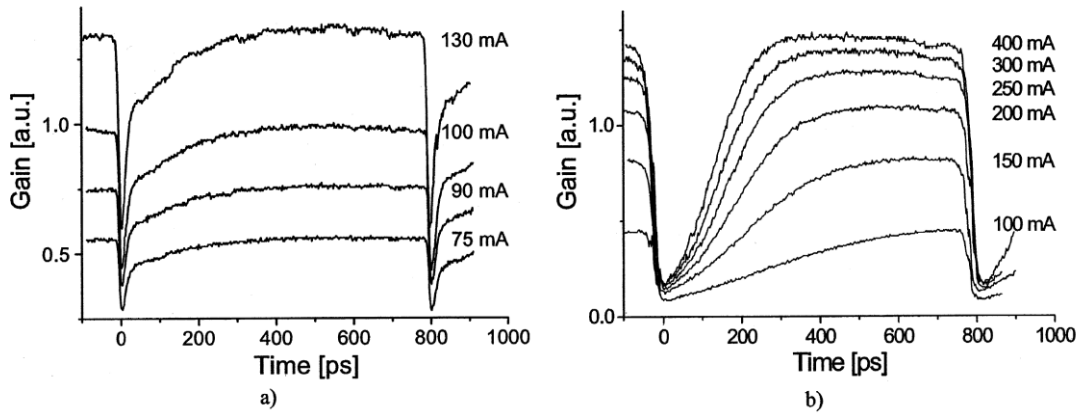


**Figure 2.11.** Gain recovery dynamics for (a) a QD-SOA and (b) a QW-SOA as a function of different pump currents. The pump pulse duration is (a) 12 ps and (b)  $\sim 20$  ps. The input pump pulse energy: (a)  $\sim 40$  fJ and (b)  $\sim 300$  fJ, after [205].

#### 4. Gain compression

The gain compression in interband semiconductor lasers corresponds to the decrease of the gain coefficient with optical intensity. Processes such as CH, SHB, as well as spatial hole burning (SpaHB) [206]–[208] contribute to the gain compression in semiconductors. The latter comes from the spatial dependence of photon and carrier densities along the cavity [209]–[211].

The nonlinear gain  $g_{nl}$  can be expressed following the expression:

$$g_{nl} = \frac{g}{1 + \epsilon_P P} \quad (2.32)$$

where  $g$  is the uncompressed material gain,  $P$  the output power, and  $\epsilon_P$  the gain compression factor related to the output power. In QD lasers, the gain compression factor related to the power is typically in the order of  $0.2 \text{ mW}^{-1}$ , corresponding to a value related to the photon density in the range of  $10^{-16} \text{ cm}^3$  to  $5 \times 10^{-15} \text{ cm}^3$ , one or two order of magnitude higher than in QW lasers [212].

The gain compression has a direct impact on the above-threshold  $\alpha_H$ -factor. For instance, in QW lasers, which are made from a nearly homogeneously-broadened gain medium, the carrier density is clamped at threshold. As a result, the change of the  $\alpha_H$ -factor that is mostly due to the gain compression can be expressed as follows:

$$\alpha_H(P) = \alpha_{H0}(1 + \epsilon_P P) \quad (2.33)$$

where  $\alpha_{H0}$  is the  $\alpha_H$ -factor at threshold.

In QD lasers, the impact of the gain compression on the  $\alpha_H$ -factor of the GS lasing transition can be described analytically by the following equation [212]:

$$\alpha_H(P) = \alpha_0(1 + \epsilon_P P) + \alpha_1 / \left(1 - \frac{g_{th}}{g_{max} - g_{th}} \epsilon_P P\right) \quad (2.34)$$

In Eq. 2.34,  $g_{th}$  is the threshold gain,  $g_{max}$  the maximum gain for the GS lasing and  $\alpha_0$   $\alpha_1$  are pre-factors whose expressions can be found in [227]. The first term in Eq. 2.34 denotes the gain compression effect at the GS while the second term is the direct contribution from the carrier filling in the ES that is related to the gain saturation in the GS. A high gain compression effect has an impact on different aspects of the QD laser performance. For instance, for large signal modulation applications, according to Eq. 2.31, a high value of  $\epsilon_P$  leads to a larger damping rate, hence strongly reducing both the 3-dB bandwidth and the modulation efficiency. Besides, since the gain is reduced, the  $\alpha_H$ -factor is enhanced and a larger output signal frequency chirp is observed under direct modulation [212].



## 5. Optical spectral linewidth

With the increasing demand for transmission capacity in optical communication systems, coherent communication technology has been attracting intensive studies [213]. The coherent system can restore both the amplitude and phase information of optical signals, while it is sensitive to the phase noise of both transmitters and local oscillators, which strongly affects the bit error rates at the receiver [6], [214]. The phase noise in semiconductor lasers arises from the spontaneous emission and is at the origin of the Schawlow-Townes linewidth. Additionally, the optical linewidth is broadened by the phase-amplitude coupling effect characterized by the  $\alpha_H$ -factor. The optical spectral linewidth  $\Delta\nu$  of the semiconductor laser can be expressed as:

$$\Delta\nu = \frac{\Gamma g_{th} v_g^2 \alpha_m h\nu}{4\pi P_0} n_{sp} (1 + \alpha_H^2) \quad (2.35)$$

where  $\Gamma g_{th}$  is the threshold modal gain,  $\alpha_m$  the cavity mirror loss,  $h\nu$  the photon energy, and  $P_0$  the optical output power. The population inversion factor  $n_{sp}$  is given by [193]:

$$n_{sp} = \frac{1}{1 - \exp(E_{21} - \Delta E_F / k_B T)} \quad (2.36)$$

where  $E_{21}$  and  $\Delta E_F$  are the energy separation between the bands and between their corresponding quasi-Fermi levels respectively. For QW structures, the typical value of  $n_{sp}$  is between 1.5 to 2.5 [215]. As compared to QW lasers, QD lasers have a lower  $n_{sp}$  around or below the unity due to the abrupt DOS [216], [217]. From Eq. 2.35, one figure of merits of a narrow spectral linewidth is the amount  $n_{sp}(1 + \alpha_H^2)$ . As illustrated in Figure 2.12, this value is strongly dependent on the material and structure of the active region.

From Eq. 2.35, the optical linewidth is reduced at higher output power. However, in practical devices, the minimum achievable value is limited because of modal instability [94], existence of side-modes [95], spatial hole burning [13], and gain compression [97], [98]. The former three are mostly related to the design of the laser thus they can be eliminated through a careful optimization of the design geometry. On the other, as seen above, the gain compression is larger in QD devices, and can substantially broaden the spectral linewidth at

higher bias currents. This last point will be discussed later in the manuscript.

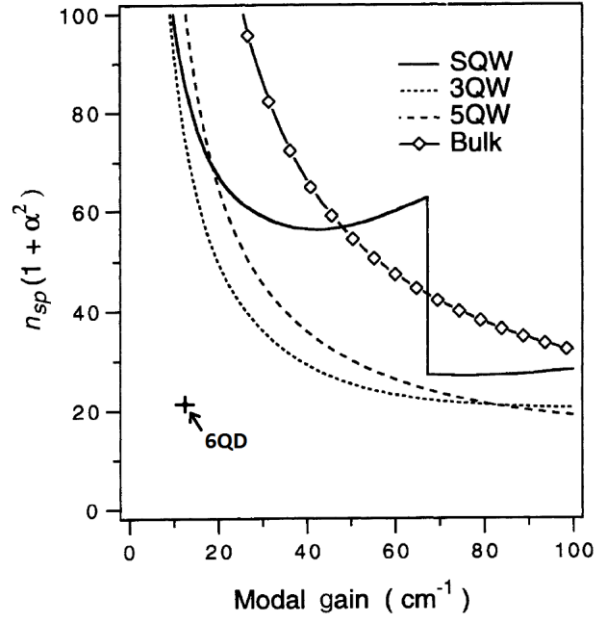


**Figure 2.12.** The evolution of  $n_{sp}(1 + \alpha_H^2)$  as a function of modal gain in bulk, single QW (SQW), multi-QW (MQW) material as compared to a six-layer InAs/GaAs QD DFB laser (6QD), after [218], [219].

## V. Summary

In summary, this chapter has introduced the fundamental features of QD lasers, including the electronic structure, the carrier dynamics, the linewidth broadening factor, the optical spectral linewidth, the nonlinear gain, as well as the gain broadening mechanisms. All these elements are essential for understanding the results presented in the following chapters. For instance, analyzing the gain dynamics is crucial for optimizing the performance of FWM based wavelength converters. As QD material exhibits a faster gain recovery than QW structures, better conversion performance in terms of amplitude and bandwidth can be expected, which will be demonstrated in chapter IV. In addition, the  $\alpha_H$ -factor strongly impacts the spectral linewidth and the nonlinear dynamics of semiconductor lasers. A large  $\alpha_H$ -factor will enhance the laser stability against external optical feedback. Further discussion and experimental demonstrations will be performed in chapter V.

## Chapter III. Advanced characterizations of quantum dot lasers

This chapter presents the InAs/GaAs and InAs/InP QD lasers studied in this thesis. After a description of their continuous wave behaviors, the chapter investigates the  $\alpha_H$ -factor with different methods. Particularly, it will be shown that the applicability of the modulation technique to structures with multiple electronic states is limited when the phase noise needs to be properly characterized like in coherent systems. To this end, narrow phase noise InAs/InP QD lasers will be unveiled with spectral linewidth around 160 kHz.

### I. Investigated QD laser devices

#### 1. InAs/GaAs QD lasers

The GaAs-based QD laser devices have been fabricated within the group of Professor Dieter Bimberg at Technische Universität Berlin. The QD active region was grown in a DWELL structure by solid source MBE on an n+ (100) GaAs substrate. Growth conditions including growth temperature and depositing rate, V–III ratio, layer thickness, and indium content of the InGaAs layer have been carefully optimized in order to improve the quality of the self-assembled QDs [220], [221]. The dot formation was directly achieved on the GaAs matrix at 485°C by 2.5 ML (monolayer) of InAs at the growth rate of 0.083 ML/s and then covered with a 5-nm thick  $\text{In}_{0.15}\text{Ga}_{0.85}\text{As}$  layer [49]. Ten dot sheets were stacked with 33 nm GaAs spacers, the thickness of which was optimized through a trade-off between the reduction of the strain degradation while multiplying the number of stack, which demands thicker spacers, and the preservation of a modal gain contribution from side layers, which requires thinner layer. The resulting dot size is 5 nm high and 15 to 20 nm wide, with a surface density of  $3\sim 5 \times 10^{10} \text{ cm}^{-2}$ . The transmission electron microscopy images of a dot layer can be found in Figure 1.5. Vertical waveguiding is achieved by sandwiching the active region between two 1.5  $\mu\text{m}$  thick AlGaAs cladding layers [114]. The epi-layer structure with detailed doping profile is represented in Figure 3.1. An inhomogeneous broadening of 51 meV for the GS transition was retrieved from photoluminescence measurements. Further details can be found in [49].

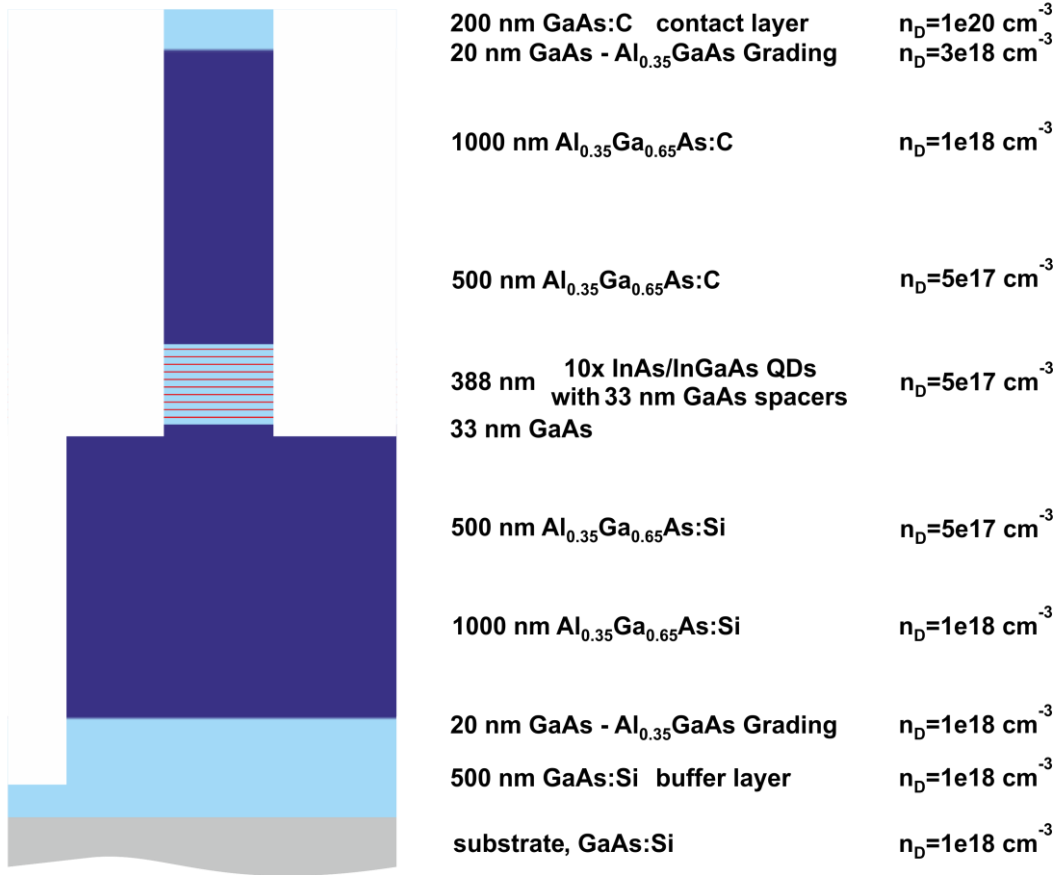


**Figure 3.1.** Epi-layer structure of the InAs/GaAs QD lasers (courtesy of Prof. Dieter Bimberg).

The studied devices are cleaved Fabry-Perot (FP) lasers, with 3 different cavity lengths: 1, 1.5 and 2 mm. As an example, Figure 3.2 shows a bar including several 1-mm long QD FP lasers. The vertical gold lines on the laser bar indicate the location of the optical waveguides (red circle), the letters next to them refer to the ridge waveguide (RWG) width  $W_{RWG}$  (A/b: 4  $\mu\text{m}$ ; C/d: 2  $\mu\text{m}$ ), the gold pads are used for electrical contact, while the isolated pads are connected to ground. The bar is fixed on a copper sub-mount with one side aligned with the edge in order to collect the light.

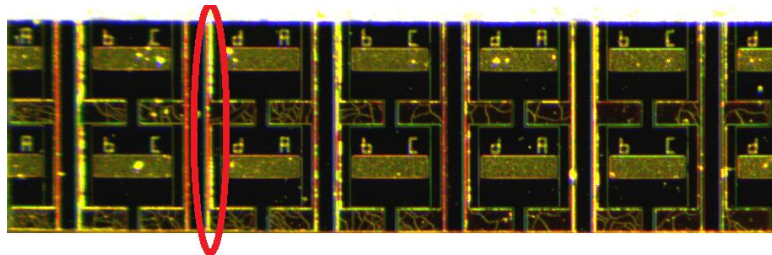


**Figure 3.2.** InAs/GaAs QD FP laser bar with 1-mm long lasers.

Table 3.1 gives the most important parameters of the QD lasers under study, including the lasing state, the cavity length  $L_c$ , and  $W_{RWG}$ . Other laser parameters measured at room temperature (298K) are the threshold current  $I_{th}$ , the threshold current density per QD layer  $J_{th}$ , the lasing wavelength at the gain peak  $\lambda_c$ , the external differential quantum efficiency  $\eta_D$ , the series resistance  $R_s$  and the turn-on voltage  $V_{th}$ . The threshold current  $I_{th}$  corresponds to the clamping condition for which gain equals the loss. The threshold current density  $J_{th}$ , is obtained by dividing the threshold current value  $I_{th}$  by the surface area of the active region. A low threshold current density gives a direct indication of the quality of the active region.

Laser Device		GaFP1	GaFP2	GaFP3	GaFP4	GaFP5
Lasing State	-	GS	ES	GS	GS	GS
Cavity length	$L_c$ (mm)	1	1	1.5	1.5	2
Ridge width	$W_{RWG}$ ( $\mu\text{m}$ )	2	2	2	4	2
Threshold current	$I_{th}$ (mA)	16.5	88.5	29	36	31
Threshold current Density	$J_{th}$ (A/cm <sup>2</sup> per layer)	82.5	442.5	97	60	77.5
Gain peak wavelength	$\lambda_c$ (nm)	1302	1221	1308	1309	1307
External efficiency	$\eta_D$	21%	11%	18%	27%	21%
Series resistance	$R_s$ ( $\Omega$ )	8.6	5.5	3.5	2.3	2.5
Turn-on voltage	$V_{th}$ (V)	1.1	1.4	1.2	1.1	1.2

**Table 3.1.** Measured intrinsic parameters of the InAs/GaAs QD FP lasers.

In Table 3.1,  $V_{th}$  is the threshold voltage expressed as:

$$V = V_{th} + IR_s \quad (3.1)$$

with  $I$  the bias current and  $R_s$  the series resistance. Both  $V_{th}$  and  $R_s$  can be extracted from the V-I curve. As shown in Figure 3.3(a), using a linear regression (red) above the threshold voltage allows retrieving  $V_{th}$  from the interception with the y-axis and  $R_s$  from the slope of the fitted line.

We can further estimate the power efficiency of the laser by investigating the wall-plug efficiency (WPE)  $\eta_{WPE}$ , that is defined as the ratio between the output optical power to the

injected electrical power:

$$\eta_{WPE} = P_{out}/VI = \left[ \eta_{ext} \frac{h\nu}{q} \left( 1 - \frac{I_{th}}{I} \right) \right] / (V_{th} + IR_s) \quad (3.2)$$

As an example, the evolution of the WPE versus bias current is depicted in Figure 3.3 (b) for QD laser GaFP4. A maximum WPE of 14% is achieved while the curve tends to saturate. However, if the current increases further, the WPE will start decreasing, which can be attributed to the gain saturation and the gain compression in the active region, as well as the increasing thermal effects. Previous work have demonstrated WPE greater than 70% for specific laser diodes [222]. The  $\eta_{WPE}$  from GaFP4 is still low, however, as the bias stage is not optimized, the electric power loss from the source to the laser active region may not be negligible.

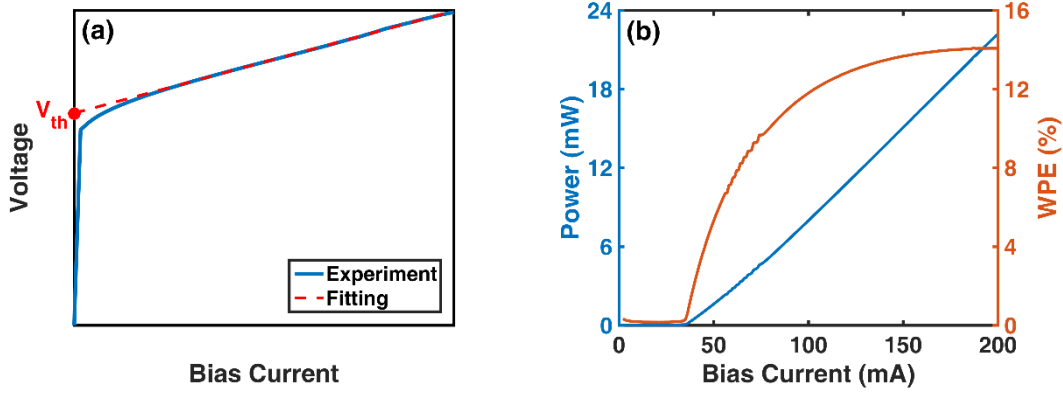


**Figure 3.3.** (a) Typical laser VI curve and extraction method for  $R_s$  and  $V_{th}$  values; (b) output power and WPE as a function of bias current for QD laser GaFP4.

Then,  $I_{th}$  is extracted from the light-current characteristics (LI) response, plotting the emitted optical power versus bias current.  $\lambda_c$  is measured from the OSA and  $\eta_D$  is determined from the slope  $dP/dI$  of the linear part of the light-current characteristic:

$$\eta_D = \frac{q}{h\nu} \frac{dP}{dI} \quad (3.3)$$

where  $q$  is the electron charge, and  $h\nu$  the emitted photon energy.

As a summary, the light-current-voltage characteristics (LIV) and the optical spectra measured for the five different devices (GaFP1 to GaFP5) can be found in Figures 3.4 to 3.8.

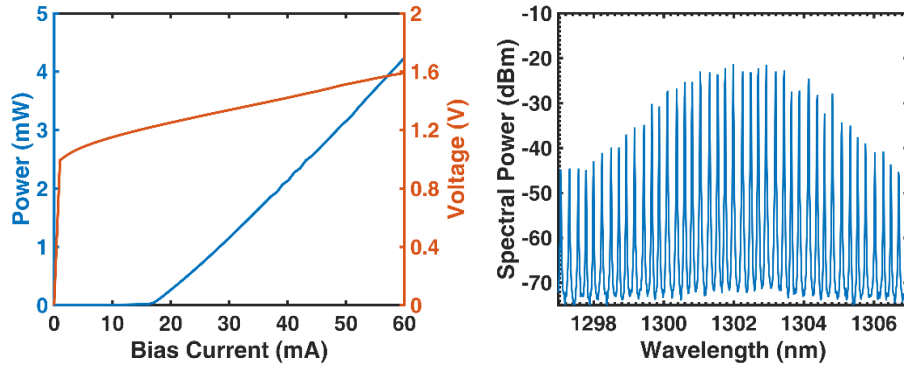


**Figure 3.4.** LIV curves (left) and optical spectrum (right) of the InAs/GaAs QD laser GaFP1.

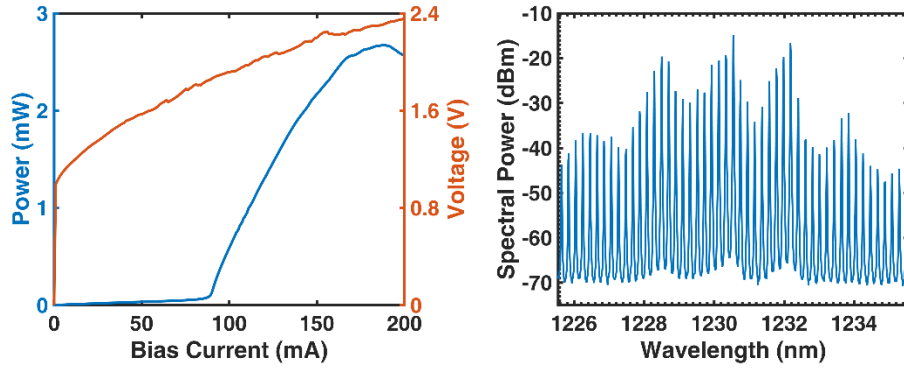


**Figure 3.5.** LIV curves (left) and optical spectrum (right) of the InAs/GaAs QD laser GaFP2.

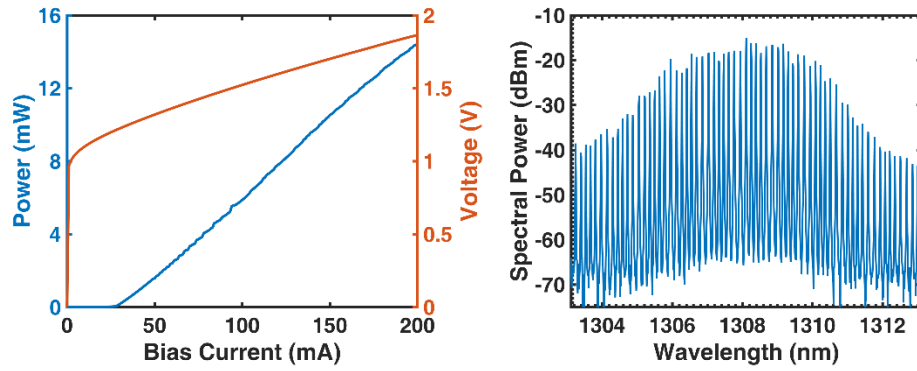


**Figure 3.6.** LIV curves (left) and optical spectrum (right) of the InAs/GaAs QD laser GaFP3.

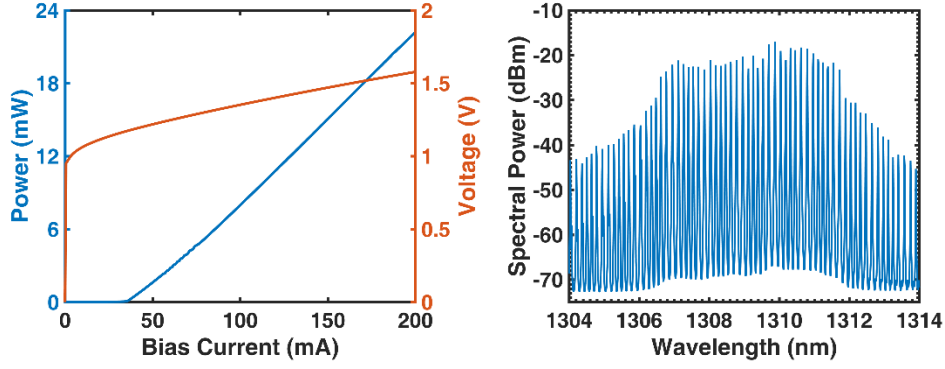


**Figure 3.7.** LIV curves (left) and optical spectrum (right) of the InAs/GaAs QD laser GaFP4.

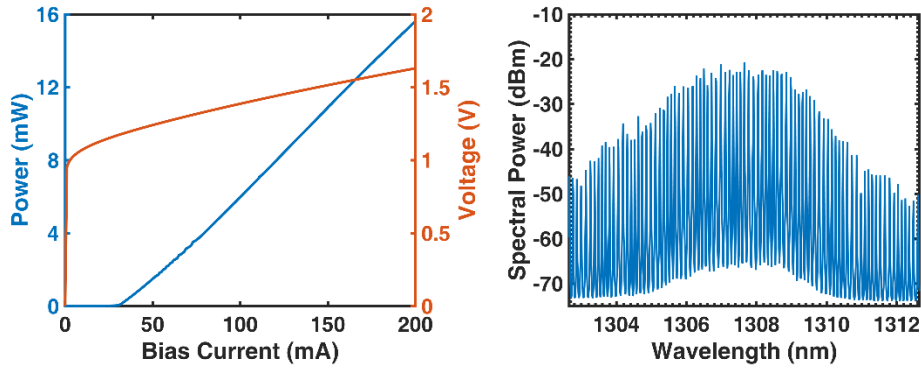


**Figure 3.8.** LIV curves (left) and optical spectrum (right) of the InAs/GaAs QD laser GaFP5.

Let us point out that, although QD devices GaFP1 and GaFP2 have identical cavity, the latter operates exclusively on the ES at 1221 nm, hence the GS emission at 1300 nm is fully inhibited. In this work, the selection between the lasing states has been obtained by exploiting the natural wavelength dispersion of the PL peak across the wafer. It is known that both the thickness and the composition of the epitaxial layers are sensitive to growth conditions (flow, pressure, temperature, etc.) hence inducing a residual dispersion on wafer [223]. As an example, Figure 3.9 shows a PL spectrum of an InAs/GaAs QD sample grown by the same technology as the InAs/GaAs QD lasers studied in this thesis [224]. Typically, the ES-GS separation in GaAs-based QD is around 65 meV [176], i.e. the ES gain peak wavelength should be about 70 nm shorter than that of GS, thus the lasing operation on ES transition of QD laser GaFP2 is confirmed.



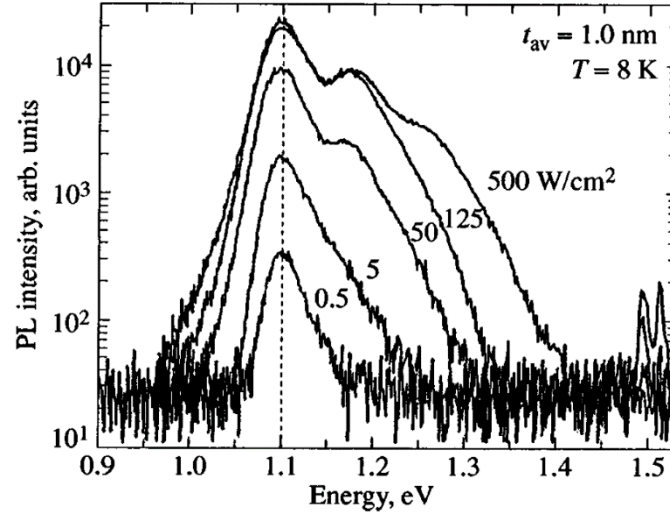


**Figure 3.9.** PL spectrum at 8 K from an InAs/GaAs QD sample grown by the same technology than the InAs/GaAs QD lasers studied in this thesis, after [224]. The GS-ES separation is 65 meV [176].

## 2. InAs/InP QD lasers

The InP-based QD laser devices have been fabricated within the group of Dr. Philip Poole at the National Research Council (Canada). The undoped QD active region was grown using Riber 32P CBE growth system on a n-type InP(100) substrate. Five dot sheets are stacked with 30 nm  $\text{In}_{0.816}\text{Ga}_{0.184}\text{As}_{0.392}\text{P}_{0.608}$  (1.15Q) barriers. The double cap growth procedure [86] and a GaP sublayer were employed to tune the QDs in order to achieve desirable lasing operating wavelength range. A schematic diagram of the structure can be found in Figure 3.10 (a).

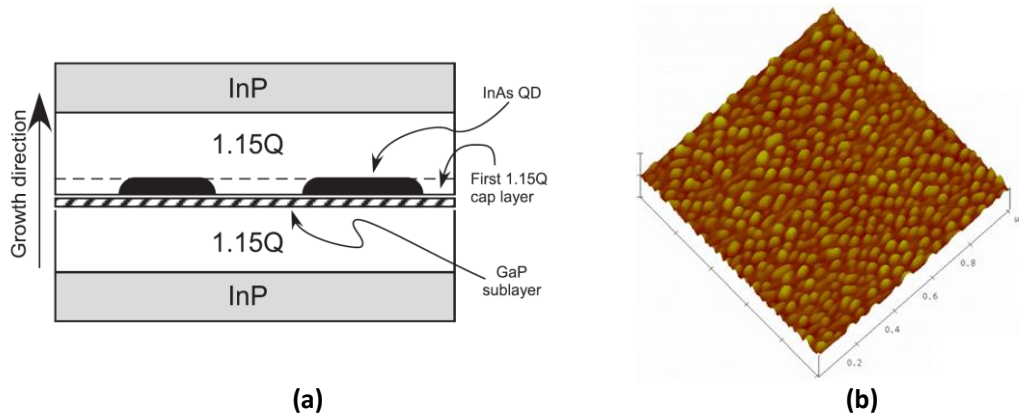


**Figure 3.10.** (a) Schematic diagram of the InAs QD structure, after [39]; (b) An atomic-force microscopy image of one QD layer ( $1\ \mu\text{m} \times 1\ \mu\text{m}$ ) (courtesy of Dr. Philip Poole).

The role of the thin GaP sublayer is to improve the dot density and uniformity while

stacking multiple layers. This active layer was embedded in a 350 nm-thick 1.15Q waveguide core, providing both carrier and optical confinement. The dots are about 1.6 nm high and 50 nm wide, with a surface density of approximately  $4 \times 10^{10} \text{ cm}^{-2}$  per layer according to atomic force microscopy (AFM) measurements on uncapped stacked dot samples. An AFM image is shown in Figure 3.10 (b). More details can be found in ref. [39].

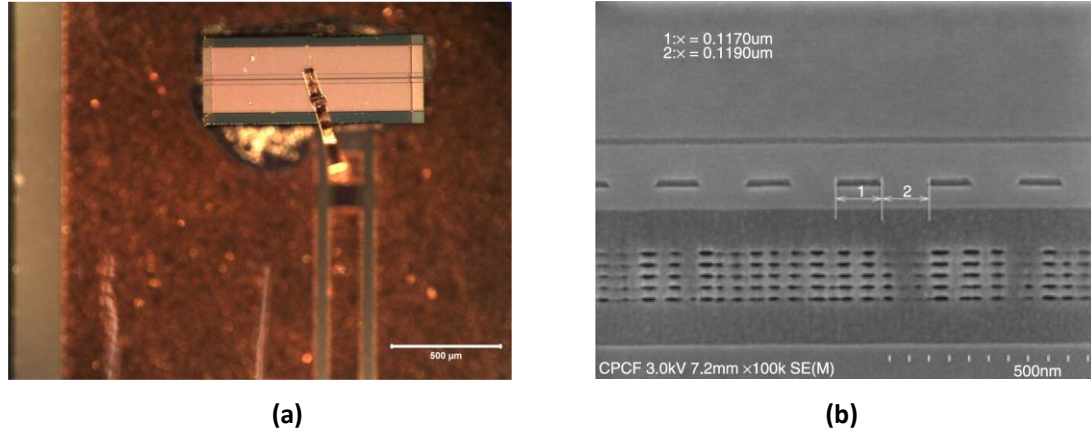


**Figure 3.11.** (a) InAs/InP QD laser PDFB2 (Scale: 500 μm); (b) cross-section view of the DFB structure.

The InP-based QD devices studied include FP and distributed feedback (DFB) lasers. The QD FP laser PFP1 has a 1 mm long cleaved cavity consisting in a 3 μm wide ridge, mounted on a sapphire chip, where a resistance of 50 Ω is buried for direct modulation purpose. The DFB lasers are also 1 mm long and 3 μm wide. The period of the etched Bragg grating is 236 nm, and the coupling coefficient is  $25 \text{ cm}^{-1}$ . The first DFB laser PDFB1 has anti-reflection coatings on both facets (AR/AR) without a phase-shift in the grating. The cavity is mounted on a ceramic holder. Generally such laser cavity implies a dual-mode lasing operation, since none of the two modes around the stopband are preferentially selected by the grating [225]. In order to obtain a single mode operation, the laser cavity must have some asymmetry between the two possible modes. This can be achieved by using an AR/HR coating (HR: high-reflection), a phase shift or multi-section devices [225]. However, in our case we suspect that the single mode behavior results from spatial hole burning which causes a small wavelength shift in the stopband in the facet region relative to the center of the device. This creates preferential lasing for the short wavelength mode. The second DFB laser PDFB2 is AR/HR coated, the same mount is used as for PFP1. Figure 3.11 (a) and (b) show the QD laser PDFB2 and the cross-section of

the total structure.

Figure 3.12 depicts a PL spectrum of a five-layer InAs/InP QD sample grown by the same CBE technology at NRC [13]. At 300 K, the full width at half maximum (FWHM) is about 107 meV. For the InAs/InP QD lasers under study, an inhomogeneous broadening around 32 meV is measured at 4 K. Typically, the GS-ES separation in InP-based QD material system is around 20 meV (40 nm in wavelength).

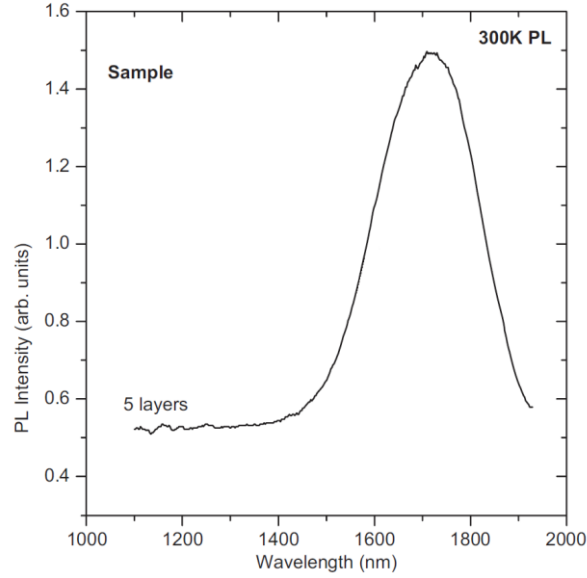


**Figure 3.12.** PL spectrum from a five-layer InAs/InP QD sample grown by the same CBE technology, after [53].

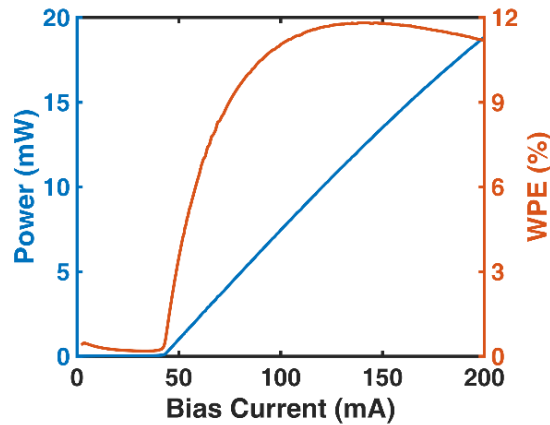


**Figure 3.13.** Output power and WPE as a function of the bias current in QD laser PFP1.

The WPE of QD laser PFP1 is represented in Figure 3.13. The WPE reaches a maximum level of 11.5% at bias current of 145 mA. The LIV curves, the optical spectra and the most

relevant intrinsic parameters of the three QD lasers are presented in Table 3.2 and Figure 3.14 to 3.16.

Laser Device		PFP1	PDFB1	PDFB2
Lasing State	-	GS	GS	GS
Cavity length	$L_c$ (mm)	1	1	1
Ridge width	$W_{RWG}$ ( $\mu\text{m}$ )	3	3	3
Threshold current	$I_{th}$ (mA)	39	46	47.5
Threshold current Density	$J_{th}$ ( $\text{A}/\text{cm}^2$ per layer)	260	307	317
Gain peak wavelength	$\lambda_c$ (nm)	1543	1521	1520
External efficiency	$\eta_D$	26%	11%	14%
Series resistance	$R_s$ ( $\Omega$ )	3.3	3.2	8
Turn-on voltage	$V_{th}$ (V)	1	1.3	1

**Table 3.2.** Measured intrinsic parameters of the InAs/InP QD FP and DFB lasers.

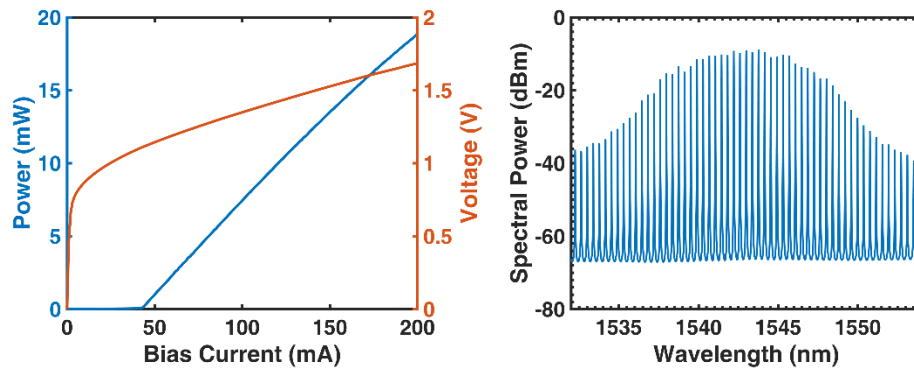


**Figure 3.14.** LIV curves (left) and optical spectrum (right) of InAs/InP QD laser PFP1.

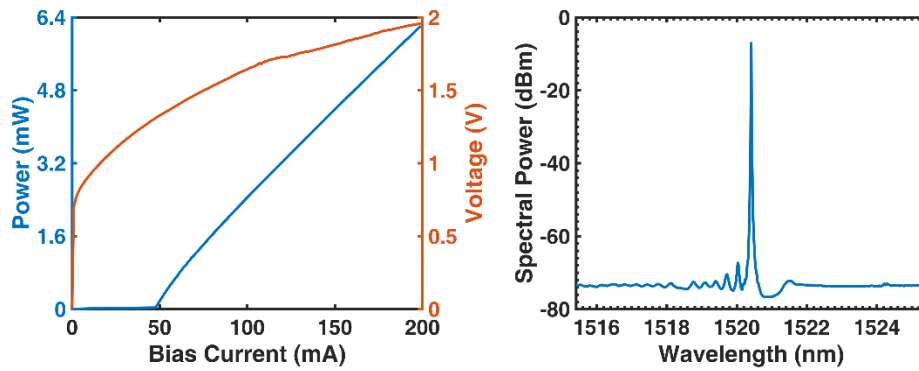


**Figure 3.15.** LIV curves (left) and optical spectrum (right) of InAs/InP QD laser PDFB1.

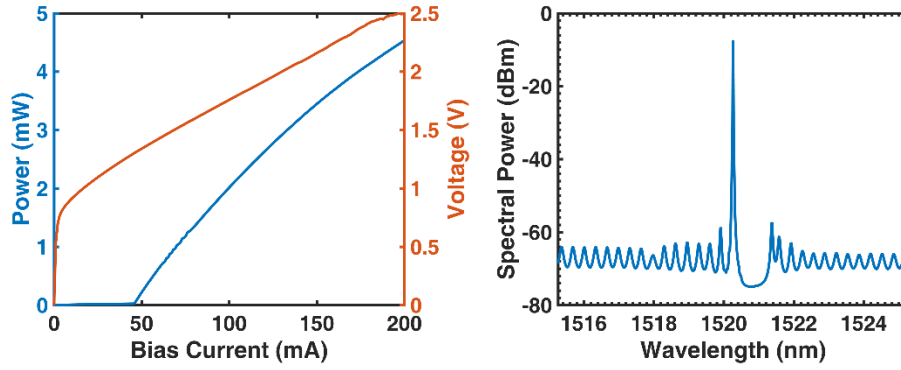


**Figure 3.16.** LIV curves (left) and optical spectrum (right) of the InAs/InP QD laser PDFB2.

## II. Linewidth broadening factor

The  $\alpha_H$ -factor is a fundamental feature in semiconductor lasers, and is responsible amongst other consequences for a large spectral linewidth broadening. In contrast to the fundamental quantum limit originally proposed by Schawlow and Townes [226] taking into account the spontaneous emission, the spectral linewidth in a semiconductor laser is multiplied by a factor of  $(1 + \alpha_H^2)$ . Since its first introduction in the early 1980's, multiple measurement techniques have been proposed to assess the  $\alpha_H$ -factor that can be classified into three types:

1. Analysis of the optical spectrum, including the optical linewidth method [182] and the amplified spontaneous emission (ASE) method, relying on simultaneous observation of the longitudinal mode wavelength shift and the modal gain changes with varying current below the lasing threshold [227].
2. High-frequency modulation, such as the FM/AM method [228], [229] and the Fiber Transfer Function method [230].
3. External optical control, including optical injection [231], optical feedback [232], and four-wave mixing methods [233].

All these methods for measuring  $\alpha_H$  are indirect and require some modeling to connect  $\alpha_H$  to the measured parameters. The complexity of the laser structure and operating principle makes these models always dependent on approximation. To this end, the extracted values are somewhat dependent on the measurement method. On the other hand, the measured parameter may end up being the important one for practical applications (linewidth,

modulation, etc.). Although all the above-threshold techniques can be used under the exactly controlled operating conditions of the device, the extracted  $\alpha_H$ -factor results from a complex combination of multiple effects. In particular, above the lasing threshold, the  $\alpha_H$ -factor depends on the optical power [212], [234], the type of the cavity (DFB, FP) [235], [236], and gain nonlinearities (spectral and spatial hole burnings, carrier-heating) [187], [237], [238]. As a consequence, extraction of the  $\alpha_H$ -factor above the laser threshold may mask some basic features of the semiconductor material. Therefore, it is still of interest to access asymptotic values of the  $\alpha_H$ -factor close to threshold, in particular to probe its dependence on carrier concentration and photon energy that cannot be varied in the real operating conditions above threshold. In this section, a careful extraction of the  $\alpha_H$ -factor is performed below the threshold using the ASE method and then the extracted values are compared with the above-threshold measurements from FM/AM and FWM methods.

## 1. Below-threshold measurements

### a) Amplified spontaneous emission

This ASE method is based on the analysis of the ASE spectrum [30]. Eq. 2.11 indicates that the  $\alpha_H$ -factor also requires the measurement of the refractive index from the carrier induced wavelength variation. The free-spectral range  $\delta\lambda$  in a laser cavity is expressed as:

$$\delta\lambda = \frac{\lambda_m}{2nL} \quad (3.4)$$

with  $\lambda_m$  the modal wavelength. The change in the refractive index within the active layer  $dn$  is then related to the modal wavelength shift  $d\lambda_m$  through:

$$\frac{d\lambda_m}{\lambda} = \Gamma \frac{dn}{n} \quad (3.5)$$

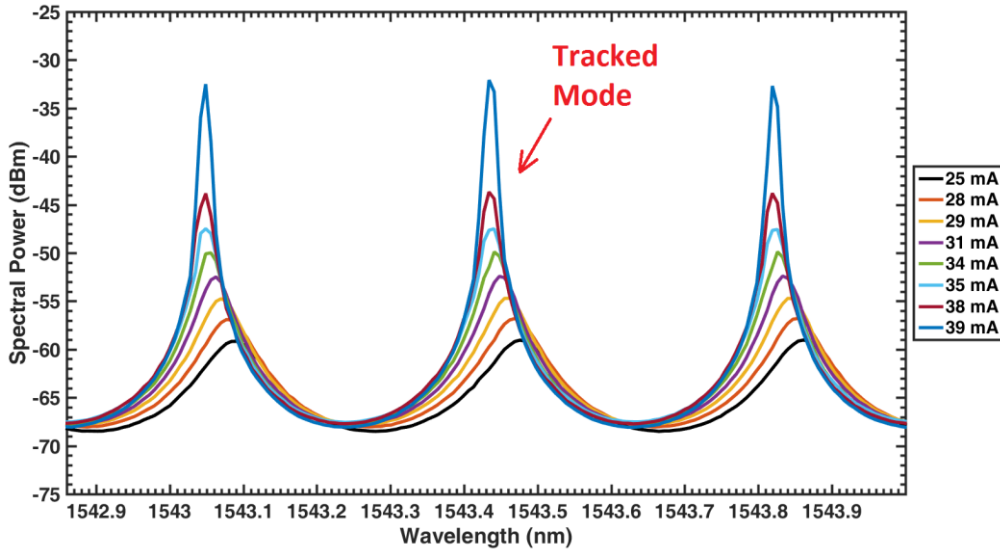
On the other hand, the variation of gain  $g$  is equivalent to the variation of net modal gain  $G_{net}$ , which can be extracted from the relationship [80]:

$$G_{net} = \Gamma g - \alpha_i = \alpha_m = \frac{1}{L_c} \ln \left( \frac{1}{\sqrt{R_1 R_2}} \frac{\sqrt{x}-1}{\sqrt{x}+1} \right) \quad (3.6)$$

where  $\Gamma$  is the confinement factor,  $R_1$  and  $R_2$  the reflection coefficients of the laser cavity, and  $x$  the modal peak-to-valley ratio. Injecting Eqs. 3.5 and 3.6 into Eq. 2.11, the  $\alpha_H$ -factor can be retrieved from the following expression

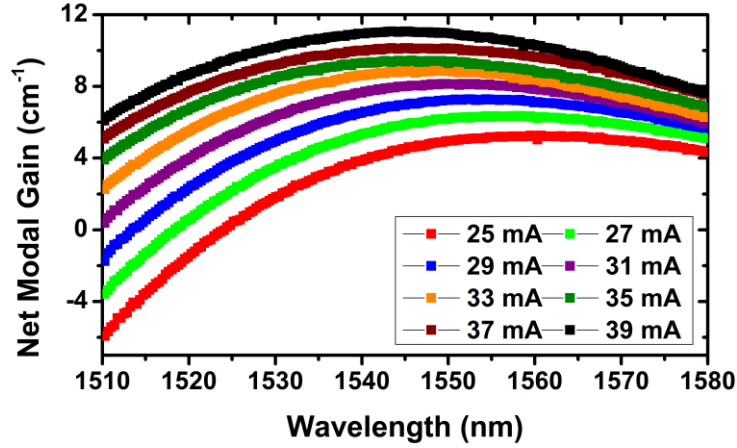
$$\alpha_H = -\frac{2\pi}{L\delta\lambda} \frac{d\lambda_m/dN}{dG_{net}/dN} = -\frac{2\pi}{L\delta\lambda} \frac{d\lambda_m/dI}{dG_{net}/dI} \quad (3.7)$$

In principle, the method is only applicable for FP cavities, as for DFB lasers, the grating makes the gain extraction more complicated leading to complex piecewise functions [239]. In order to get rid of the thermal effect, it is possible to use a pulsed current source with a low duty cycle at a sub-microsecond rate, however, this usually results in a very low signal-to-noise ratio and even irregular optical spectral line shape, which can hinder the extraction of the  $\alpha_H$ -factor. In our case, the lasers are biased under continuous waves (CW), the lasing emission is coupled by an AR coated lens-ended fiber, isolated by an optical isolator to prevent any external optical feedback, then measured with a 10 pm-resolution OSA. The experimental procedure details hereinafter allow to properly eliminate the thermal effects and to access to very precise values of the  $\alpha_H$ -factor.



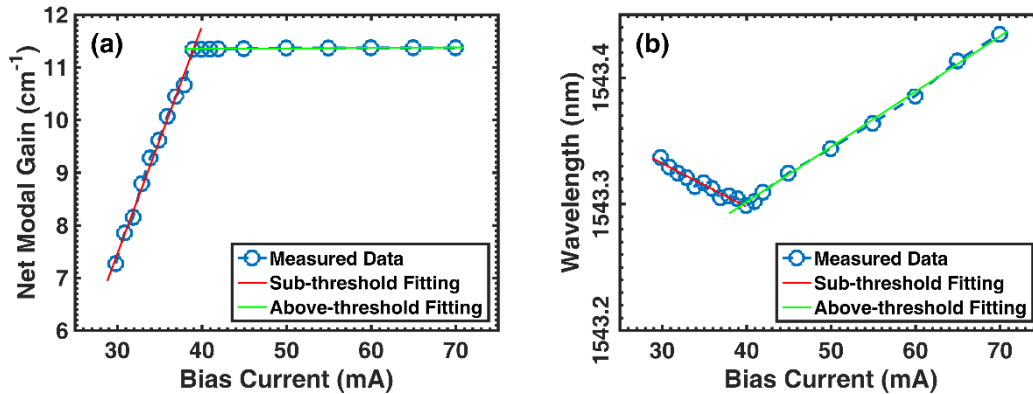
**Figure 3.17.** Sub-threshold optical spectra of QD laser PFP1 for different bias currents.

Figure 3.17 shows the sub-threshold optical spectra of QD laser PFP1 assuming variation of the bias current from  $0.75 \times I_{th}$  to  $I_{th}$ . In order to properly locate the mode peaks a third-order interpolation has been used. The extracted gain spectra are represented in Figure 3.18 for various bias current conditions.



**Figure 3.18.** Net modal gain spectra of QD laser PFP1 for various bias current conditions.

Therefore, by following the central longitudinal mode that has a wavelength of about 1543.3 nm in Figure 3.17, we can track both the modal gain and refractive index variations. Figure 3.19 depicts the evolutions of the net modal gain and the modal wavelength as a function of the bias current.



**Figure 3.19.** The net modal gain and modal wavelength variations of the mode around 1543.3 nm (see in Figure 3.17) in QD laser PFP1. Red solid lines: linear fitting below threshold; Green solid lines: linear fitting above threshold.

Since the measurements are done under CW conditions, the wavelength shift caused by thermal effects must be carefully taken into account. By fitting the below threshold part, the terms  $d\lambda_m/dI$  and  $dG_{net}/dI$  are obtained. Because of the CW operation, thermal effects induced wavelength red-shift must be considered and eliminated so as to only account the net carrier-induced effects. To overcome such an issue, we have followed the procedure of ref. [80]. To this end, the wavelength red-shift due to thermal effects, measured by varying the



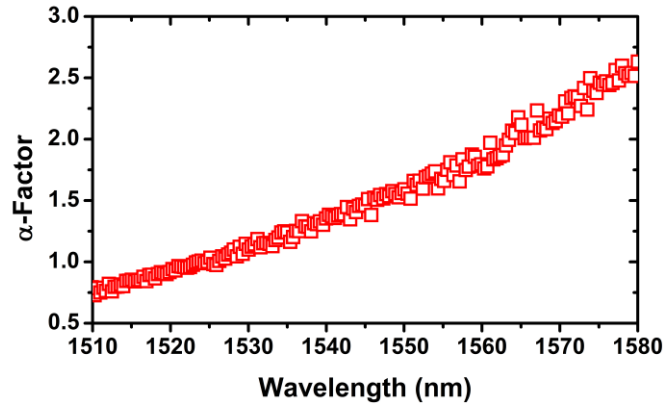
pump current right above threshold, is subtracted from the wavelength blue-shift measured below threshold. Thus, the  $\alpha_H$ -factor can be re-expressed as:

$$\alpha_H = -\frac{2\pi}{L\delta\lambda} \frac{(d\lambda_m - \Delta\lambda)/dI}{dG_{net}/dI} \quad (3.8)$$

Following this protocol, the fitting error is estimated below 0.2%, which means that the extraction of the  $\alpha_H$ -factor is very accurate. However, the thermal correction holds under the assumption that thermal effects in QD lasers are unchanged below and above threshold and that the carriers are clamped above threshold. The latter assumption is somewhat disputable for QD lasers, as the carrier population in resonant states keeps increasing with the bias current, which will continue to enhance the gain and change the refractive index.

## b) Experimental results

From Eq. 3.8, the spectral dependence of the  $\alpha_H$ -factor is retrieved. An example is presented in Figure 3.20 for the InAs/InP QD laser PFP1. The  $\alpha_H$ -factor varies from 0.75 to 2.5 over a span of 80 nm, and the gain peak, it is around 1.4.



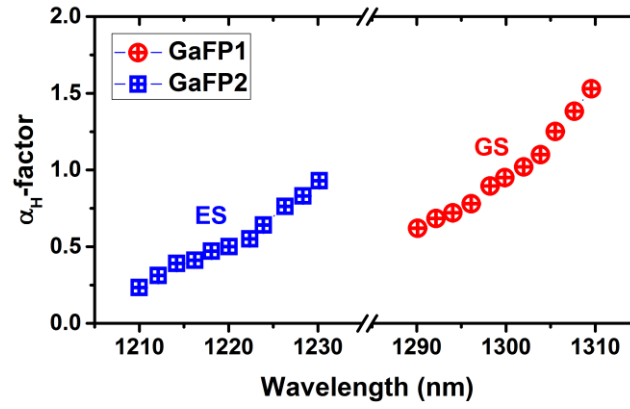
**Figure 3.20.** The measured  $\alpha_H$ -factor spectral dependence for QD laser PFP1.

Table 3.3 gives the values of the measured  $\alpha_H$ -factor at the gain peak for the GaAs-based QD FP lasers. Overall the results show that the  $\alpha_H$ -factor of InAs/GaAs QD lasers are relatively small which is in agreement with prior works [130], [137]. Besides, let us remember that QD laser GaFP2 emits exclusively on the ES transition, and accordingly, a lower  $\alpha_H$ -factor is clearly observed. Such a reduced  $\alpha_H$ -factor in ES QD lasers has been recently observed [137] and is

mostly attributed to smaller index changes. Indeed in a QD laser emitting on the GS transition, it is important to take into account the changes of the GS refractive index caused by both the GS and ES gain variations.

Laser	$\alpha_H$ -factor (gain peak)
GaFP1	1
GaFP2	0.5
GaFP3	2.1
GaFP4	0.9
GaFP5	2

**Table 3.3.** The measured  $\alpha_H$ -factor (gain peak) for GaAs-based QD FP lasers.



**Figure 3.21.** The measured  $\alpha_H$ -factor for the GS QD laser GaFP1 and ES QD laser GaFP2.

## 2. Above-threshold measurements

### a) Four-wave mixing

Here we present a novel method for measuring the above-threshold  $\alpha_H$ -factor using the FWM generated in an optically-injected semiconductor laser [233]. Further details and explanations regarding the principle of OIL and the associated nonlinear dynamics are given in chapter IV. The optically-injected QD laser can be described by the following rate equations including the electric field  $E$ , the occupancy probability of dots  $\rho$ , and the carrier density in the surrounding QW  $N_W$  such as [233]:

$$\begin{cases} \frac{dE}{dt} = \frac{1}{2} v_g g_0 \left( \frac{2\rho-1}{1+\epsilon|E|^2} - \frac{\gamma_s}{v_g g_0} \right) (1 - i\alpha_H) E + \gamma_s E_i \exp(-i\Delta t) \\ \frac{d\rho}{dt} = -\gamma_d \rho + C N_W (1 - \rho) - v_g \zeta \left( \frac{2\rho-1}{1+\epsilon|E|^2} \right) |E|^2 \\ \frac{dN_W}{dt} = -\gamma_N N_W + \frac{I}{q} - 2C N_W (1 - \rho) \end{cases} \quad (3.9)$$

where  $\gamma_s$  is the photon decay rate in the cavity,  $\gamma_N$  and  $\gamma_d$  the carrier decay rates in the QW and QD,  $C$  the capture rate from the wells into the dots,  $J$  the bias current per dot,  $\varsigma$  the interaction cross-section of the carriers in the dots,  $g_0$  the differential gain,  $\epsilon$  the gain compression coefficient,  $E_i$  the effective complex amplitude and  $\Delta$  the detuning frequency of the injected field. In Eq. 3.9, the presence of the higher ES energy levels is neglected. In the degenerate FWM states, the electrical field consists of three components:

- the original laser field  $E_0$ ,
- the injected laser field (probe) that undergoes parametric amplification through FWM within the cavity that will be called regenerated field  $E_r$  and
- the FWM generated field also called converted signal  $E_f$ .

Hence the steady-state solution of  $E$  is given by [233]:

$$E(t) = E_0 + E_r \exp(-i\Delta t) + E_f \exp(-i\Delta t) \quad (3.10)$$

While the field  $E_r$  and  $E_f$  are much smaller than  $E$ , Eq. 3.10 can be approximated as:

$$|E|^2 \approx |E_0|^2 (1 + \sigma \exp(-i\Delta t) + \sigma^* \exp(-i\Delta t)) \quad (3.11)$$

where  $\sigma$  is the amplitude of the modulation on  $E$ , and

$$\frac{1}{1 + \epsilon_P |E|^2} \approx \frac{1}{1 + \epsilon |E_0|^2} \quad (3.12)$$

The beating between these signals will optically modulate the field at the detuning frequency and also the carrier probability of occupancy  $\rho$ :

$$\rho(t) = \rho_0 + \rho_1 \exp(-i\Delta t) + \rho_1^* \exp(i\Delta t) \quad (3.13)$$

where  $\rho_0$  is the steady-state occupancy of dots and  $\rho_1$  is the modulation amplitude contribution.

Assuming that the carrier capture  $C$  rate is much larger than the carrier decay rates in the well, the steady-state solution of  $N_W$  is given by:

$$N_W = \frac{J/q}{2C(1-\rho)} \quad (3.14)$$

By injecting Eq. 3.11, 3.12 and 3.14 into 3.9, the following expressions can be deduced:

$$\frac{E_r}{E_0} = \frac{1\rho_1 G(1-i\alpha_H)}{\Delta} - K \quad (3.15)$$

$$\frac{E_f}{E_0} = \frac{1\rho_1^* G(1-i\alpha_H)}{\Delta} - K \quad (3.16)$$

$$\sigma = \rho_1 Z \quad (3.17)$$

where

$$\rho_1 = -\frac{K}{Z+W}, G = \frac{v_g g_0}{1+\epsilon|E|^2}, K = -\frac{i\gamma_s E_i}{\Delta E_0}, W = -\frac{i2G}{\Delta},$$

$$Z = \left[ \frac{2v_g \zeta |E_0|^2}{1+\epsilon|E_0|^2} - i\Delta + \gamma_d \right] / \left[ \frac{-v_g \zeta |E_0|^2 (2\rho_0 - 1)}{1+\epsilon|E_0|^2} \right] \quad (3.18)$$

Eq. 3.15 and 3.16 will be used to retrieve the  $\alpha_H$ -factor. The experiments have been performed on QD laser PDFB1 within Prof. Fan-Yi Lin's group at the National Tsing Hua University (NTHU) in Taiwan. The experiments cannot be easily performed on a FP laser since the FWM generation would require a more complex configuration while it is straightforward with an optically-injected DFB laser. The free-space experimental setup is represented in Figure 3.22.

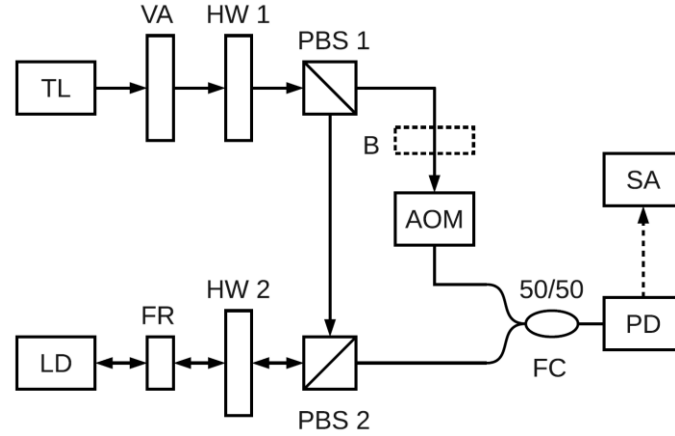


**Figure 3.22.** Free-space experimental setup used for the FWM analysis. TL: tunable laser; LD: QD laser diode; FR: Faraday rotator; HW: half-wave plate; PBS: polarizing beam splitter; PD: photodiode; SA: electric spectrum analyzer; VA: variable attenuator; AOM: acousto-optic modulator; B: beam block; FC: 50/50 fiber coupler, after [233].

The tunable laser (TL) probe wave is splitted into two parts by PBS1, one is injected into the cavity of the QD laser-under-test through beam splitter PBS2, and the other part is shifted by 100 MHz using an acousto-optic modulator (AOM) and then combined with laser-under-

test output signal carrying the all the wave-mixing components using a fiber coupler. The output from fiber coupler FC is detected by the photodetector (PD) whose signal is analyzed using the RF spectrum analyzer (SA). The probe frequency is tuned from a value 10 GHz below to a value 10 GHz above the QD laser wavelength.

The magnitude of the frequency component measured with the SA at 100 MHz corresponding to the beating of the 100 MHz shifted probe and the regenerated probe, while the component at  $2|f_{pump} - f_{probe}| \pm 100 \text{ MHz}$  corresponding to the beating of the 100 MHz shifted probe and wave mixing. These components are directly proportional to the square of the fields given by Eq. 3.15 and 3.16 respectively.

Figure 3.23 (a) and (b), displays both measurement when the PDFB1 QD laser is biased at  $3 \times I_{th}$ . Fitting the curves with Eq. 3.15 and 3.16 shown in blue solid lines, a weak value of  $\alpha_H$ -factor is extracted at 0.42.

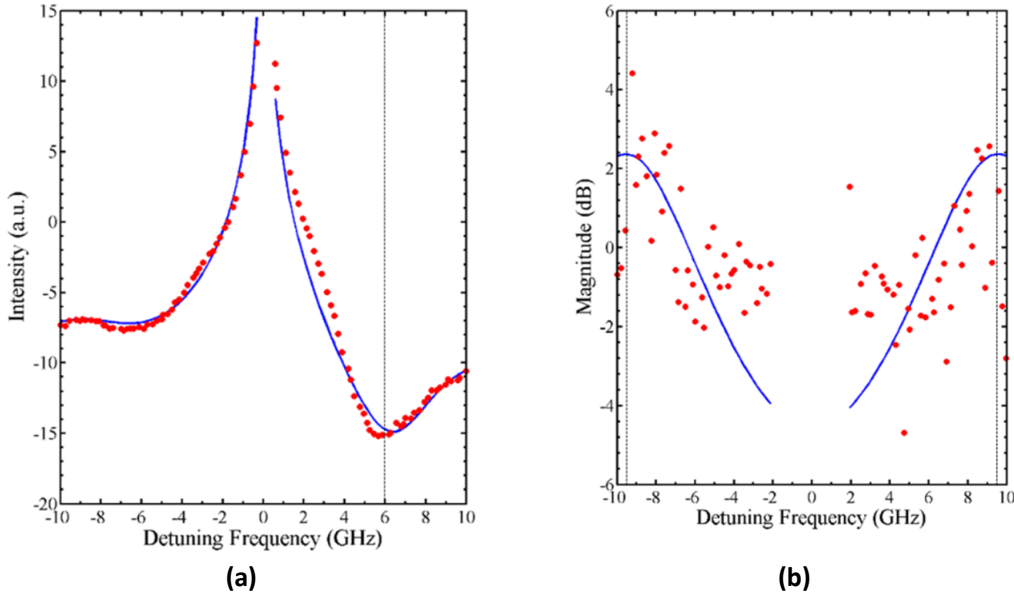


**Figure 3.23.** Measured (a) normalized regenerated signals intensity and (b) normalized beating intensity of the 100 MHz shifted probe and wave mixing QD laser PDFB1 under FWM at  $3 \times I_{th}$  (red dots). Blue solid curves represent the fitting calculated from the analytical model.

Figure 3.24 depicts the retrieved values of the  $\alpha_H$ -factor as a function of the bias current  $I$ . Overall the values are a bit smaller than those obtained on QD lasers PFP1 made with the same semiconductor material. Unlike the standard injection locking technique, which makes

the extraction of the  $\alpha_H$ -factor from the minimum of the Hopf local bifurcation or to determine the locking boundaries is very inaccurate [240], the proposed FWM method requires only a weak injection levels. In conclusion, the retrieved  $\alpha_H$ -factor values are in a good agreement with those obtained from the ASE technique. The decrease of the  $\alpha_H$ -factor with the bias current requires more investigation at this stage but taking into account the noise from the ESA and the current source, a fitting error of about 10% is estimated which can also contribute to the behavior observed in Figure 3.24.

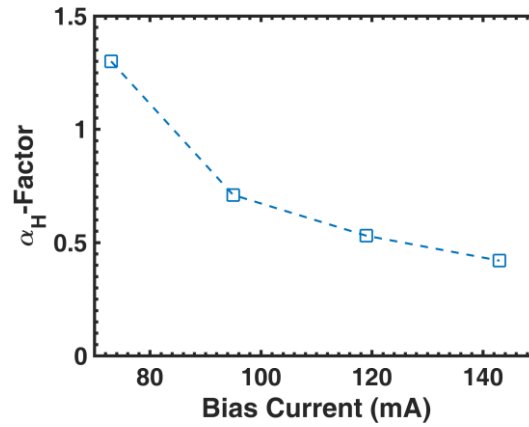


**Figure 3.24.** The retrieved  $\alpha_H$ -factor of QD laser PDFB1 as a function of the bias current.

## b) FM/AM method

Firstly demonstrated by Harder et al. in 1983 [228], the FM/AM method constitutes a well-established technique to measure the above-threshold  $\alpha_H$ -factor. The FM/AM technique consists of determining the ratio between the frequency modulation and amplitude modulation indices of the diode laser operating under modulation. Since the gain and refractive index are both related to the carrier density, the direct modulation of the bias current generates both amplitude modulation (AM) and frequency modulation (FM) at the output of the laser. The determination of the ratio of the FM over AM components gives a direct measurement of the effective  $\alpha_H$ -factor at the device level. The FM/AM measurements presented hereinafter were performed at Nokia Bell Labs, France under the supervision of Dr. Jean-Guy Provost. The experimental setup is shown in Figure 3.25 and the experimental procedure is similar to the one described in ref. [229].

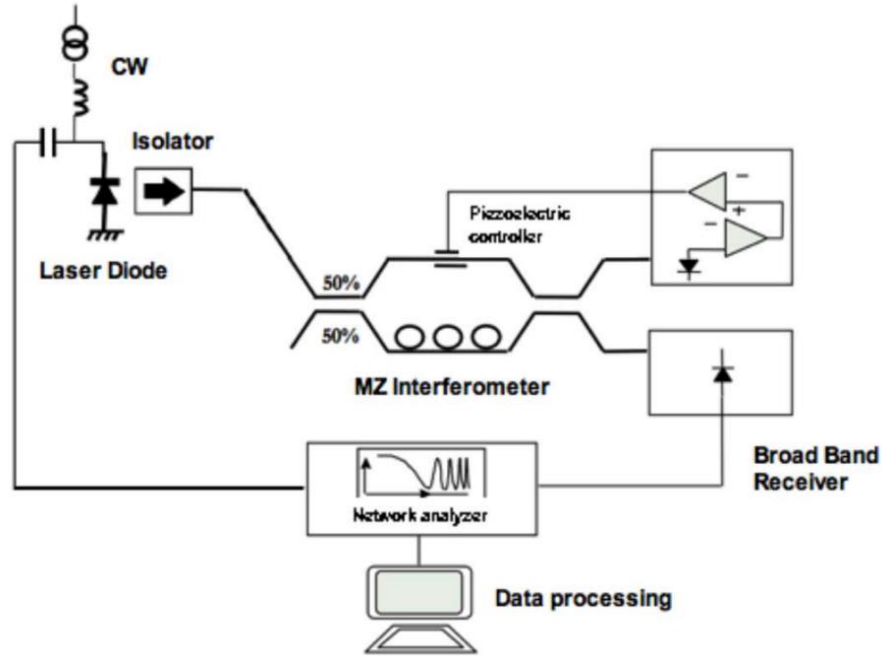


**Figure 3.25.** Schematic of the experimental setup used for FM/AM measurements, after [229].

The output power of the directly modulated laser diode is divided into two arms of the fibered Mach-Zehnder (MZ) interferometer with two different propagation time  $T_1$  and  $T_2$ . The free-spectral range (FSR) of the interferometer is the inverse of the  $|T_1 - T_2|$ . A polarization controller is used in one of the arms to ensure that the two divided signals have parallel states. Figure 3.26 represents the power at the output of the interferometer as a function of the optical frequency. To accurately control the optical path difference, a cylindrical piezoelectric transducer is used. The transducer located onto one of the MZ's arms is fiber interdependent and directly controlled by an external locking circuit. The system allows adjustment of the interferometer on all points of the characteristics. For instance, points A and B being in opposition, they correspond to two signals interfering in quadrature with each other, as shown in Figure 3.26. Around these two locations, where the following measurements were performed, the interferometer's characteristics remaining linear, thus the photocurrent from the photodetector (PD) is proportional to the phase (or frequency) variations of the optical signal [229].

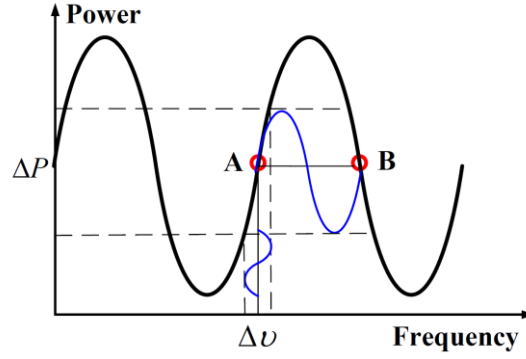


**Figure 3.26.** Transfer function of the MZ interferometer [37].

While applying a sinusoidal modulation, the electric field of the laser  $e(t)$  is such as [228]:

$$e(t) = \sqrt{P_0}(1 + m \cos(2\pi f_m t))^{1/2} \exp[j(2\pi f_0 + \beta \sin(2\pi f_m t + \phi))] \quad (3.19)$$

where  $P_0$  is the average power,  $m$  and  $\beta$  the AM and FM indexes,  $f_m$  the modulation frequency,  $f_0$  the lasing frequency, and  $\phi$  the phase difference between the FM and AM frequencies. In what follows, the FM/AM method is valid under small-signal modulation i.e. for  $m \ll 1$ . Nevertheless, it is possible to extend the method to large signal modulation as in reference [241].

The output signal of the interferometer can be written as:

$$s(t) = \frac{1}{2} [e(t - T_1) + e(t - T_2)] \quad (3.20)$$

Since the measurements around points A and B correspond to a quadrature interference condition, thus the photocurrent of the PD is proportional to  $s(t)s^*(t)$ . Therefore, as the network analyzer is only sensitive to the frequency components, and that higher order terms are neglected, the normalized measured signals  $M_-$  and  $M_+$  can be expressed as:

$$M_{\pm} = P_0 m \cos\left(\frac{\pi f_m}{FSR}\right) \exp(-j2\pi f_m \tau) \pm P_0 \beta \sin\left(\frac{\pi f_m}{FSR}\right) \exp j(-2\pi f_m \tau + \phi) \quad (3.21)$$

where  $\tau = (T_1 + T_2)/2$  the transit time within the interferometer. In Eq. 3.21, the first term depends only on the AM, while the second is only FM dependent. Thus, the following expressions can be deduced:



$$\frac{2\beta}{m} = \frac{1}{\tan\left(\frac{\pi f_m}{FSR}\right)} \left| \frac{M_+ - M_-}{M_+ + M_-} \right| \quad (3.22)$$

$$\phi = \arg\left(\frac{M_+ - M_-}{M_+ + M_-}\right) \quad (3.23)$$

The ratio  $2\beta/m$  is given by [242]:

$$\frac{2\beta}{m} = \alpha_H \sqrt{1 + \left(\frac{f_c}{f_m}\right)^2} \quad (3.24)$$

where  $f_c$  is defined as the corner frequency [243]:

$$f_c = \frac{1}{2\pi} v_g \frac{\partial g}{\partial P} P \quad (3.25)$$

with

$$\frac{\partial g}{\partial P} = \frac{\epsilon_P g}{1 + \epsilon_P P} \quad (3.26)$$

which describes the impact of the nonlinear gain compression effect as a function of output power with  $\epsilon_P$  the gain compression factor related to the output power [243]. Eq. 3.24 shows that the ratio  $2\beta/m$  is modulation frequency dependent  $f_m$ , hence when  $f_m$  increases, the ratio decreases and reaches an asymptote for  $f_m \gg f_c$  from which the  $\alpha_H$ -factor can be retrieved such as [244]:

$$\alpha_H = \frac{2\beta}{m} \quad (3.27)$$

Let us stress that a versatile version of the interferometer exploiting the birefringence of a polarization-maintaining fiber (PMF) has also been recently published [245]. In what follows, the FM/AM method is applied on QD laser PFP1 which has an HF-compatible technology. The extraction of the photocurrents at points A and B (Figure 3.26) does require to properly adjust the bias of the MZ modulator so that it matches the lasing mode under study. As such the applicability of the FM/AM method is more straightforward for single-mode emitters. In case of multimode FP lasers, an optical filter is required to isolate the desired lasing mode and to prevent the laser from destructive interferences among the other FP modes. In our case, since the FSR of QD laser PFP1 ( $\sim 40$  GHz) matches the MZ interferometer one, meaning that each FP mode coincide with one fringe, the insertion of an optical filter is not mandatory.

Figure 3.27 (a) represents the  $2\beta/m$  ratio of QD laser PFP1 measured at 298K at  $2 \times I_{th}$ .

From the asymptote, the  $\alpha_H$ -factor is found at 6 with an error on the order of 4% [229].

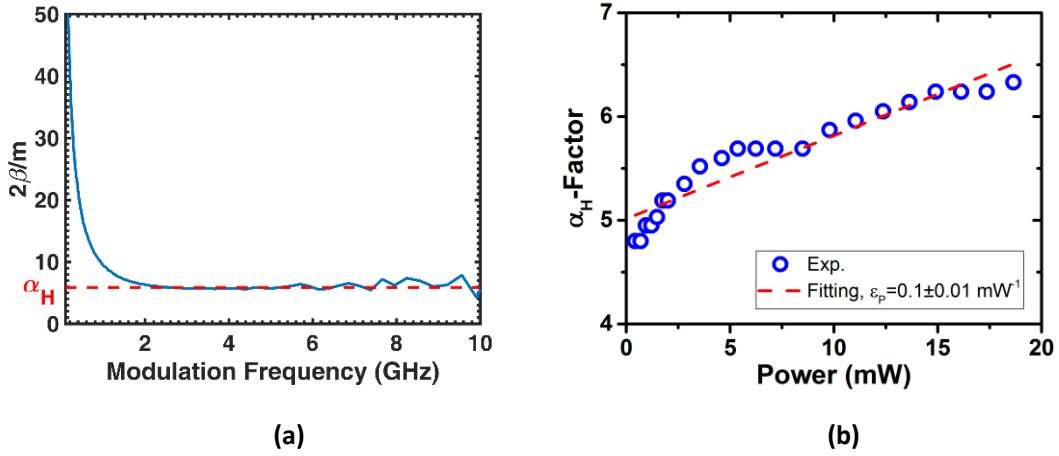


**Figure 3.27.** (a) The measured  $2\beta/m$  ratio of QD laser PFP1 at 298K under  $2 \times I_{th}$  bias, the red solid line gives the  $\alpha_H$ -factor value  $\sim 6$ ; (b) the measured  $\alpha_H$ -factor as a function of the bias current.

The measurements have been repeated for different bias currents  $1.1 \times$  to  $3 \times I_{th}$ , as shown in Figure 3.27 (b). Let us note that, because all the FP modes are injected into the MZ interferometer, an average value of the  $\alpha_H$ -factor of the GS transition is obtained. Overall, the  $\alpha_H$ -factor shows a relative increase due to the power dependence through the gain compression, which is predicted from Eq. 2.34. Curve-fitting the  $\alpha_H$ -factor values with Eq. 2.34 leads to a gain compression factor of about  $0.1 \pm 0.01 \text{ mW}^{-1}$  which is in agreement with prior values published [246]. However, if we compare the values measured right below the threshold from the ASE (1.4) with those taken right above from the FM/AM ( $\sim 4.8$ ), a discrepancy is unveiled. Such a difference is more important than in QW lasers because of the competition between the resonant GS population (clamped) and the off-resonant ones (unclamped). According to recent numerical simulations, carrier populations are indeed strongly sensitive to the modulation frequency [35]. In Figure 3.28, it is shown that the current modulation does affect both resonant and off-resonant energy levels hence increasing the  $\alpha_H$ -factor of the GS transition.

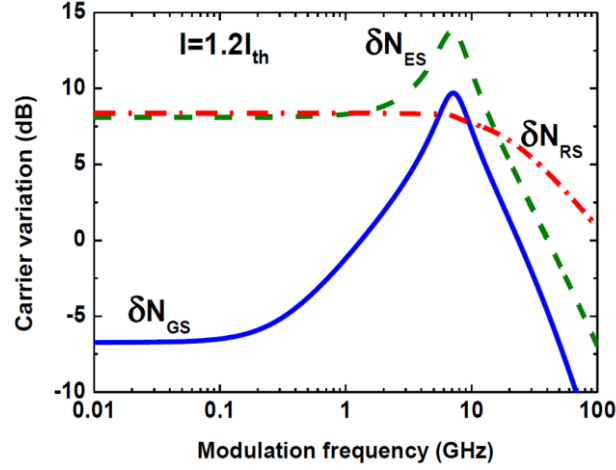


**Figure 3.28.** Numerical simulation of carrier variations at  $I = 1.2 \times I_{th}$ . The carrier variations are normalized to the value  $\delta N_{GS}$  of 0.01 GHz at lasing threshold  $I_{th}$ , after [37].

To this end, it turns out that the FM/AM method reflects most likely a current modulation driven  $\alpha_H$ -factor, since the carrier fluctuations are perturbed by the current modulation while other methods show that QD lasers perturbed by the optical noise exhibits a smaller  $\alpha_H$ -factor. These conclusions are essentially valid for QD lasers in which the  $\alpha_H$ -factor is strongly dependent on the energy separation between the resonant GS and off-resonant states [247]. There is no such issue in QW lasers since the GS-ES energy separation is much larger (e.g. > 100 meV for a 6 nm GaAs based QW [42]) than in any QD lasers. As a conclusion, the applicability of the FM/AM method is limited when characterization of the laser phase noise is required such as in coherent communication systems. However, from a transmission system point of view, this conclusion is no longer supported since the figure of merit is merely the  $2\beta/m$  ratio rather than the  $\alpha_H$ -factor.

The same measurements have been performed on QD laser PDFB2. The extracted  $\alpha_H$ -factor is represented in Figure 3.29. Although the material structure is similar to QD laser PFP1, the  $\alpha_H$ -factor is found much larger at 6~8 because of a stronger spatial hole burning due to the HR-coating. Indeed, curve-fitting the data depicted in Figure 3.30 with Eq. 2.34, reveals a higher gain compression factor  $\epsilon_P$  of  $0.36 \pm 0.09 \text{ mW}^{-1}$  and confirms this assumption.

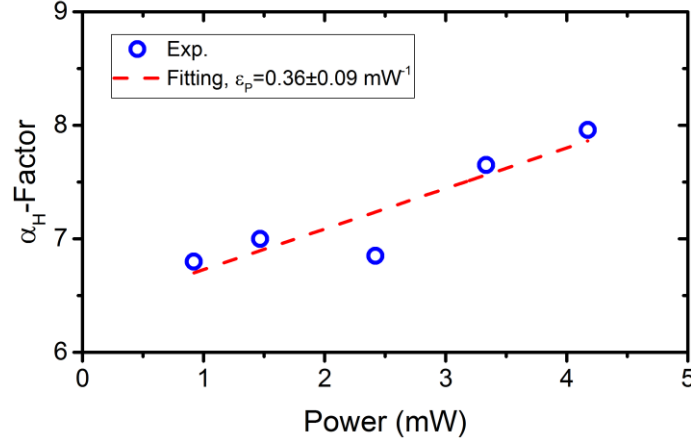


**Figure 3.29.** The measured  $\alpha_H$ -factor of QD laser PDFB2. The red line is the fitting from Eq. 2.34.

### III. Optical spectral linewidth

Quantum fluctuations associated with the lasing process affect both the intensity and the phase of the optical field. While all lasers experience phase fluctuations caused by spontaneous emission, carrier fluctuations in semiconductor lasers provide a second mechanism of phase fluctuations due to the coupling between the carrier density, the optical gain, and the refractive index in the optical cavity. As previously mentioned, the linewidth broadening factor is a key feature distinguishing semiconductor lasers from any other type of lasers, and is responsible for a much broader spectral linewidth. In contrast to the fundamental quantum limit originally proposed by Schawlow and Townes taking into account the spontaneous emission, the spectral linewidth of a semiconductor laser is broadened by a factor of  $(1 + \alpha_H^2)$ . Commercial QW lasers usually exhibit optical linewidths of a few MHz [248], [249]. In this section, we analyze the spectral linewidth of InAs/InP QD DFB lasers and unveil the possibility to reach very narrow spectral linewidth with nanostructured materials.

#### 1. Self-heterodyne method

In order to characterize the optical linewidth, a self-heterodyne method is used [250]. The experimental setup represented in Figure 3.30 simply converts the optical spectrum into an RF spectrum centered at a frequency easily measurable by the ESA [193].

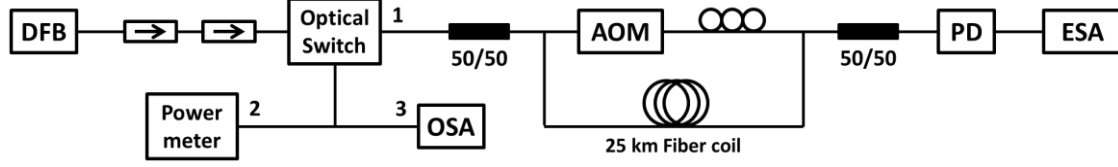


**Figure 3.30.** Self-heterodyne experimental setup used for the optical linewidth measurement.

In Figure 3.30, the laser is biased with a low noise current source. The output light is coupled into the interferometer by using an AR coated lens-end fiber. In order to avoid the external feedback into the DFB cavity, two cascaded isolators are applied for isolation better than 60 dB. An optical switch is inserted allowing monitoring the optical spectrum (OSA) and the optical power by powermeter. Once the laser emission is launched into the fiber interferometer, part of the signal is sent to a 100 MHz frequency-shifted acousto-optic modulator (AOM) while the other part propagates through a 25 km fiber coil. A relatively long fiber length provides a sufficient time delay larger than the laser's coherence time  $\tau_{coh}$  related to the laser linewidth  $\Delta\nu$  [193]:

$$\Delta\nu = 1/\pi\tau_{coh} \quad (3.28)$$

with  $\tau_{coh} = L_{coh}/v_g$  where  $L_{coh}$  is the laser's coherence length which is typically of a few hundred meters in semiconductor lasers [193]. The polarization controller is used to match the polarizations in the two arms. At the output of the interferometer, the optical signals from the two arms are superimposed and the resulting beat note centered at the AOM frequency is recorded with the PD and send to the ESA.

## 1. Experimental results

Measurements are performed on QD DFB lasers PDFB1 and PDFB2. Figure 3.31 represents the RF spectrum recorded at the output of the interferometer for QD laser PDFB2 at 95 mA (298K).

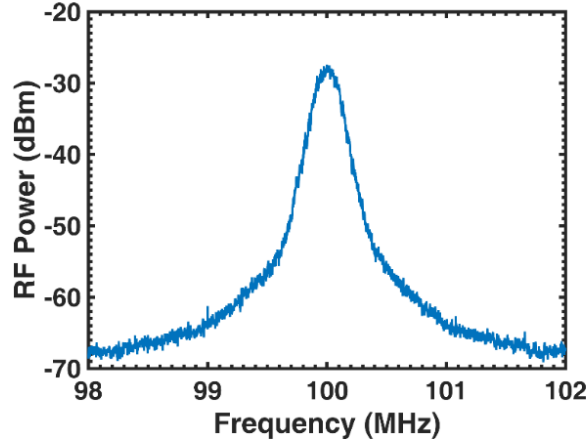


**Figure 3.31.** RF spectrum of QD DFB laser PDFB2 recorded at 95 mA (298K).

The fitting of the RF spectrum depicted in Figure 3.31 leads to the laser spectral linewidth at the full-width at half maximum (FWHM). In theory, the spectral linewidth has a Lorentzian shape, however, due to the Gaussian shape filter in the ESA and the residual electrical noise from the power supply, the signal taken is rather in the shape of a Voigt function  $V$ , which is defined as the convolution of a Gaussian function  $G$  and a Lorentzian function  $L$ :

$$V = G \otimes L \quad (3.29)$$

As previously pointed out in [28], the retrieval procedure can be further simplified by using a normalized pseudo-Voigt function  $f_V$  defined such as:

$$f_V(x) = (1 - \eta)f_G(x, \gamma_G) + \eta f_L(x, \gamma_L) \quad (3.30)$$

where  $f_G(x, \gamma_G)$  and  $f_L(x, \gamma_L)$  are the normalized Gaussian and Lorentzian functions:

$$f_G(x, \gamma_G) = (1/\pi^{1/2}\gamma_G) \exp(-x^2/\gamma_G^2) \quad (3.31)$$

$$f_L(x, \gamma_L) = (1/\pi\gamma_L)(1 + x^2/\gamma_L^2)^{-1} \quad (3.32)$$

where  $\gamma_G$  and  $\gamma_L$  are related to the FWHM  $\Gamma_G$  and  $\Gamma_L$  of the Gaussian and Lorentzian functions respectively, and  $\eta$  is the mixing parameter.

In the experiments, the captured RF spectrum is the spectral aliasing of the negative side and the positive side of the full spectral range, thus the output of the ESA represents the

convolution of two parts, which must be taken into account to retrieve the original spectral linewidth.

Hence, the FWHM from the Gaussian and Lorentzian parts is expressed as:

$$\Gamma_G = 2\sqrt{\ln 2} \gamma_G \quad (3.33)$$

$$\Gamma_L = 2\gamma_L \quad (3.34)$$

and the FWHM  $\Gamma_V$  of the Voigt profile is defined as [251]:

$$\Gamma_V = \left( \Gamma_G^5 + 2.69269\Gamma_G^4\Gamma_L + 2.42843\Gamma_G^3\Gamma_L^2 + 4.47163\Gamma_G^2\Gamma_L^3 + 0.07842\Gamma_G\Gamma_L^5 + \Gamma_L^5 \right)^{\frac{1}{5}} \quad (3.35)$$

Figure 3.32 represents the fitting of the RF spectrum depicted in Figure 3.31. A normalized linear scale has been used. The blue dots correspond to the experimental data, and the red solid line is the Voigt fitting. The FWHM spectral linewidth,  $\Delta\nu$ , extracted from this figure is of 160 kHz.

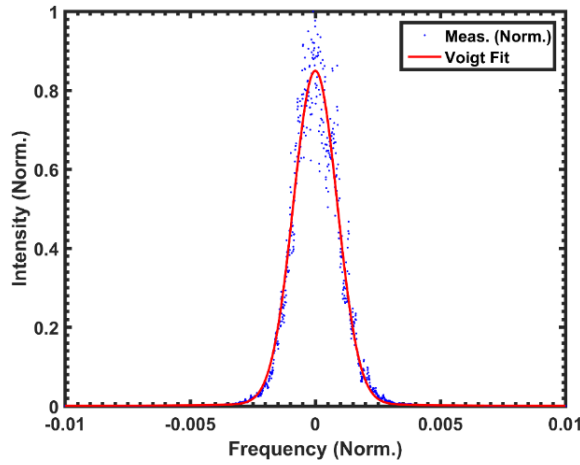


**Figure 3.32.** Normalized RF spectrum from Figure 3.31 (blue dots) and the corresponding Voigt fitted spectrum (red solid line).

By varying the bias current of the laser, the overall dependence of the spectral linewidth,  $\Delta\nu$ , with the total output power is represented in Figure 3.33. In this data set, the blue and orange colors refer to measurements obtained by increasing and decreasing bias current respectively. The two curves almost overlap each other, except at low bias (low output power), where the down sweep measurements give a higher spectral linewidth. This difference is

attributed to the residual thermal effects while the bias current is decreased. Overall, the precision of the measurement is really satisfactory leading to a minimal spectral linewidth of around 160 kHz at 2.2 mW output power which is much lower than in any standard QW DFB lasers made without artificial solutions (see chapter II).

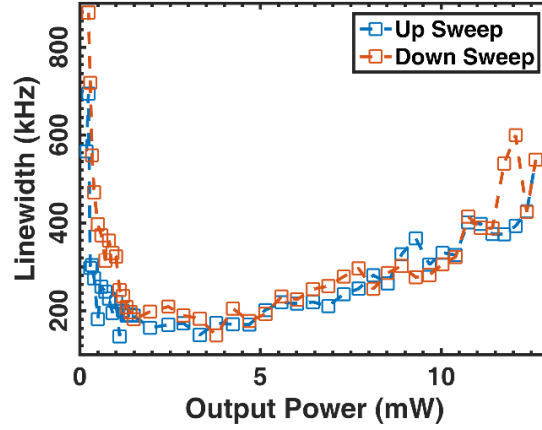


**Figure 3.33.** The measured optical spectral linewidth as a function of the total output power of QD laser PDFB2.

By applying Eq. 2.35, the figure of merit  $n_{sp}(1 + \alpha_H^2)$  is then extracted following the procedure in Table. 3.4 [54].

Mirror loss of FP laser PFP1	$\alpha_m^{DFB} = \frac{1}{2L} \ln \left( \frac{1}{R_1 R_2} \right) = 11.4 \text{ cm}^{-1}$
Mirror loss of DFB laser PDFB2	$\alpha_m^{DFB} = \frac{1}{2L} \ln \left( \frac{1}{R_1 R_2} \right) = 4.8 \text{ cm}^{-1}$
Material internal loss	$\alpha_i = 8 \text{ cm}^{-1}$
$\eta_{ext}$ of FP laser PFP1	$26\% \propto \frac{\alpha_m^{FP}}{\alpha_m^{FP} + \alpha_i}$
$\eta_{ext}$ of DFB laser PDFB2	$11\% \propto \frac{\alpha_m^{DFB}}{\alpha_m^{DFB} + \alpha_i + \alpha_{grating}}$
PDFB2 grating loss	$\alpha_{grating} = \frac{\eta_{ext}^{FP}}{\eta_{ext}^{DFB}} \frac{\alpha_m^{DFB}(\alpha_m^{FP} + \alpha_i)}{\alpha_m^{FP}} - \alpha_m^{DFB} - \alpha_i = 6.4 \text{ cm}^{-1}$
PDFB2 threshold gain	$\Gamma g_{th} = 19.2 \text{ cm}^{-1}$
Output coupling factor	$F = 1$
Linewidth-power product	$\Delta\nu \cdot P = \frac{\Gamma g_{th} v_g^2 \alpha_m h\nu}{4\pi} n_{sp}(1 + \alpha_H^2) = 0.22 \text{ MHz} \cdot \text{mW at } 1 \text{ mW}$
$n_{sp}(1 + \alpha_H^2) = 3.1$	

**Table 3.4.** Extraction procedure of  $n_{sp}(1 + \alpha_H^2)$  for QD DFB laser PDFB2.



In our case,  $n_{sp}(1 + \alpha_H^2)$  is found at 3.1 which is smaller compared to [54] where a value of 23 was reported in an InAs/GaAs QD DFB laser with a spectral linewidth of 800 kHz at 1 mW output power. More generally, the factor  $n_{sp}(1 + \alpha_H^2)$  is by far reduced in QD lasers as opposed to their QW counterparts (see Figure 2.12) because the population inversion factor is much smaller owing to the abrupt DOS [217], [252]. In our case, taking  $n_{sp} = 1$  would lead to an  $\alpha_H$ -factor of about 1.5 which is in agreement with the measured values performed with the ASE on a QD FP laser sharing the same material structure (Figure 3.20). However, we observe that such a value is not in agreement with those extracted from the FM/AM method (6~8, Figure 3.33) which is expected since the modulation method reflects a current modulation driven  $\alpha_H$ -factor.

From Figure 3.33, it has to be noted that further increase in the output power leads to a spectral rebroadening with a maximum value of about 4 times the minimum linewidth. As mentioned in the previous chapter, the linewidth rebroadening occurs in any semiconductor lasers due to thermal effects, mode instability [94], side modes [95], spatial hole burning [13], and gain compression [97], [98]. As compared to QW lasers, the rebroadening can be more pronounced in QD lasers because of increased scattering rates and larger gain nonlinearities [253], [254]. In particular, the latter can be reduced by using a design engineering with AR/AR coating on both facets [253].

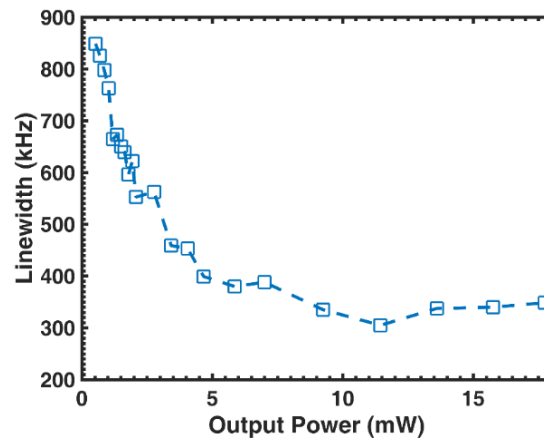


**Figure 3.34.** The measured optical spectral linewidth as a function of the total output power for QD laser PDFB1.

Figure 3.34 represents the optical spectral linewidth measured as a function of the output power on the AR/AR coated QD laser PDFB1. Although the minimum linewidth is found a bit

broader (around 300 kHz), its power dependence does not show any sign of rebroadening as in the case AR/HR PDFB2. This improvement does not only result from the reduced spatial nonlinearities (AR coatings) but also from the high side-mode suppression ratio (SMSR) making the side-modes contribution to the rebroadening effect negligible.

As a conclusion, these results indicate that QD nanostructures are excellent candidates for low phase noise operation as opposed to other complex, bulky and costly solutions already described in Chapter I. A low  $n_{sp}(1 + \alpha_H^2)$  is a knob that can be used as a manufacturing guideline for reducing the spectral linewidth. Very recently, Reithmaier et al. has also demonstrated a narrow linewidth down to 110 kHz in a QD DFB [26]. To this end, we believe that the spectral linewidth of 160 kHz reported in this chapter is among the best values published so far since a realistic curve-fitting based on a Voigt profile has been considered. In order to give a better comparison, the spectral linewidth of a packaged QW DFB laser from Nokia is shown in Figure 3.35. If we compare results from Figure 3.35 with those in Figure 3.32, it is clear that the spectral linewidth of the QW DFB laser is much broader with a minimum value as large as 7 MHz against 160 kHz for the QD laser. Applications of narrow linewidth lasers are of paramount importance for coherent communications in which the phase of the optical field is used to transmit information. Finally, narrow linewidth lasers can also be of first importance to probe atomic frequency standards to reduce drift, leading to applications in chip-scale atomic clocks [255], [256].

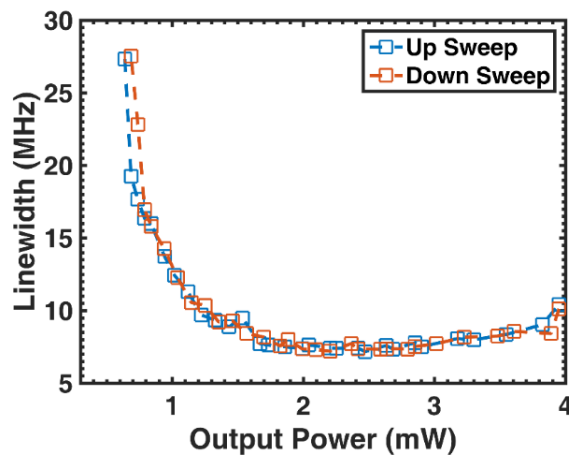


**Figure 3.35.** The measured optical spectral linewidth as a function of the total output power for a packaged QW DFB laser from Nokia.

## 2. Spectral linewidth reduction under external control

Using an external control based on optical feedback can further narrow the spectral linewidth. The procedure to precisely stabilize the laser emission within the proper regime of feedback is explained in Chapter V. The experimental setup is similar to that in Figure 3.30, except that the feedback arm is inserted between the laser and two isolators. The schematic of the feedback arm is shown in Figure 3.36.

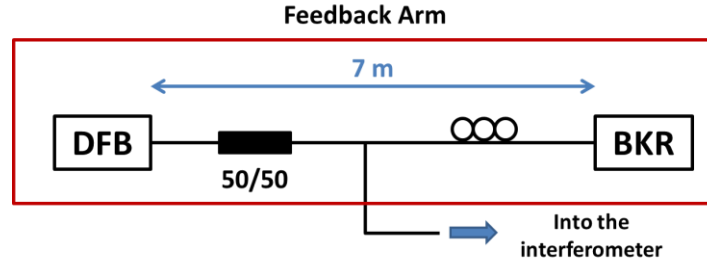


**Figure 3.36.** Feedback arm inserted at the upstream of the linewidth measurement setup shown in Figure 3.30.

The feedback arm consists of a 7 m long fibered external cavity. The laser signal is 3dB-coupled to a back-reflector (BKR) which can reflect the incoming light with a controllable attenuation. The polarization of the reflected field is made identical to that of the emitting one in order to maximize the feedback effects. By carefully tuning the feedback conditions in terms of reflected power, the optical linewidth of QD laser PDFB1 was narrowed down to 100 kHz, which is three times smaller than the free-running value (black dotted line). The measurements have been repeated five times in sequence with a time step around 1 minute, as shown in Figure 3.37 (blue triangles). Such result shows the possibility to further stabilize the laser emission and so to reduce the optical linewidth by using a proper external control configuration. This technique has been widely used for the development of tunable and monolithically integrated external cavity semiconductor lasers [22], [24], [25]. Overall, the tunability is an important feature for DWDM systems, in which the tuning can be exploited in switching scenarios and for improving network resilience to downtime and typically requires tuning across the communication band. Additionally, recent results have also unveiled that spectral linewidth can be as low as 50 kHz by using a proper modal engineering of III-V materials on silicon [24]

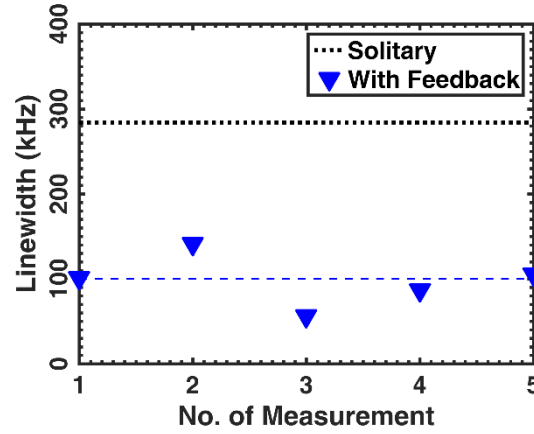


**Figure 3.37.** Measured spectral optical linewidth of QD laser PDFB1 under external optical feedback. The blue triangles correspond to five different measurements done in sequence; the black dotted line represents the spectral linewidth of the free-running laser.

## IV. Summary

This chapter classifies the fundamental properties of both QD FP and DFB lasers investigated in this PhD work. In particular, the  $\alpha_H$ -factor and the optical spectral linewidth have been deeply characterized. The main results can be summarized as:

- (1) The  $\alpha_H$ -factor has been measured using different methods. The ASE method is the most straightforward with a good precision providing that the thermal effects are properly removed. The ASE method retrieves the material characteristics of the  $\alpha_H$ -factor without being affected from the nonlinear gain and higher electronic states. Above the threshold, the FWM method generated from optical injection allows to retrieve the  $\alpha_H$ -factor with a good precision and in agreement with the ASE method. As for the FM/AM method its applicability to complex structures with multiple electronic states is limited in particular when the phase noise needs to be properly characterized like in coherent systems. Indeed, the method overestimates the  $\alpha_H$ -factor of QD lasers, which should be considered as a current modulation driven  $\alpha_H$ -factor as opposed to an optical noise driven one. However, in a transmission system with amplitude shift keying (ASK) or OOK modulation, phase noise is not relevant because information is only transmitted from the amplitude of the signal and can be detected without measuring the phase.
- (2) Narrow spectral linewidths have been unveiled in InAs/InP QD DFB lasers. Owing to the

high-quality of the epitaxial structure and the low value of the  $n_{sp} (1 + \alpha_H^2)$ , spectral linewidth as low as 160 kHz has been reported. It has been shown that further reduction down to 100 kHz is possible owing to a proper controlled optical feedback. Applications of such lasers are of paramount importance not only for coherent communications but also for atomic frequency standards to reduce the frequency drift, leading to applications in chip-scale atomic clocks [255], [256].



# Chapter IV Nonlinear conversion in optically-injected QD lasers

## I. Introduction

Four-wave mixing (FWM) describes the phenomenon that occurs when two co-polarized fields  $E_1$  and  $E_2$  at frequencies  $\omega_1$  and  $\omega_2$  co-propagate within in a nonlinear gain media having a third-order nonlinear susceptibility. The beating between them leads to the generation of two new fields  $E_3$  and  $E_4$ , at frequencies  $\omega_3 = \omega_1 - (\omega_2 - \omega_1)$  and  $\omega_4 = \omega_2 + (\omega_2 - \omega_1)$ .

In the above-described configuration,  $\omega_1$  and  $\omega_2$  are assumed different from each other, as well as  $\omega_3$  and  $\omega_4$ . Such case is referred as the non-degenerate FWM (NDFWM), as illustrated in Figure 4.1. Other FWM configurations exist with regards the spectroscopic characteristics, i.e. degenerate FWM and nearly degenerated FWM where two of the four fields coincide or nearly coincide at the same frequency [257]. In this thesis, we will focus on the NDFWM, the degenerate and nearly degenerate FWM will not be presented.

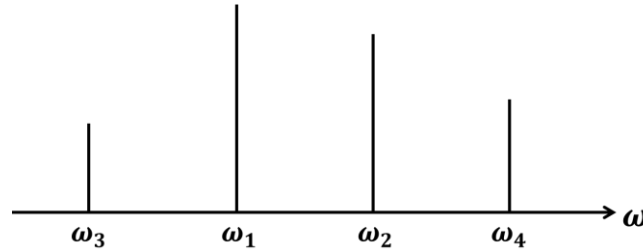


**Figure 4.1.** Illustration of the NDFWM process, the interaction of fields  $E_1$  and  $E_2$  at the frequencies of  $\omega_1$  and  $\omega_2$  leads to the generation of fields  $E_3$  and  $E_4$  at  $\omega_3$  and  $\omega_4$ .

While FWM occurs, the interactions between the four fields are sensitive to the intensity, the phase and the polarization of the incident  $E_1$  and  $E_2$ , such property can be used to preserve the information and transform into the newly generated fields. Thus, FWM can be applied to transfer a signal modulated on an optical carrier from one wavelength channel onto another within the optical domain, regardless the modulation format. However, there are other ways to pass information between different wavelengths like cross-gain modulation

(XGM) and cross-phase modulations (XPM) that are based on nonlinear gain and refractive index responses [258], [259]. Nevertheless, in contrast to FWM, XGM and XPM are limited in modulation format transparency [115]. Therefore, FWM can be envisioned to develop optical wavelength converters for the current wavelength-division multiplexing (WDM) based communication systems that are emerging with coherent communication technologies. These novel types will be compatible with advanced modulation formats such as phase-shift keying (PSK), quadrature amplitude modulation (QAM) [101], [105], which are already introduced in the coherent communication systems nowadays. Furthermore, FWM-based converters can be employed in future PICs for all-optical signal processing [106], [107].

Compare to the other devices such as holey silica fibers and photonic crystal fibers [109], [260] or silicon based micro-rings [110]–[112] that are previously suggested by several works, the use of III-V semiconductor devices such as SOAs and laser cavities [113], [114], [261] is advantageous:

- 1) in contrast to the fibers, these devices are usually very short (from less than 1 mm to several cm), the wavelength dispersion effects are negligible, thus the phase-matching can be easily assured, and their compactness is suitable for monolithic integration;
- 2) in contrast to micro-rings which require high quality vertically coupling to low-loss bus waveguides, the fabrication of SOAs and laser cavities is simpler with a lower cost.

In the literature, most published FWM studies based on III-V semiconductor devices are concentrated on SOAs, as they provide higher linear gain and longer interaction lengths, however, little is known on the potential of resonant oscillators based on either Fabry-Perot (FP) or distributed feedback (DFB) configurations. Taking advantage of cavity resonances and reduced amplified spontaneous emission (ASE) noise, resonant oscillators can constitute an alternative that can also produce efficient NDFWM. For instance, in DFB lasers where the Bragg mode is directly used as the pump, prior works have reported efficient frequency conversions for both QW and QD active materials [262]–[264]. However, one of the major drawbacks in using DFBs is that the complex DFB features are difficult to control from device to device without careful design and processing optimizations, such as facet phase effects or grating coupling coefficient which can deteriorate strongly the conversion efficiency [265]. In contrast,



FP laser cavities are a simpler choice as the fabrication processes is less complicated.

In this chapter, experimental studies of NDFWM in FP laser cavities are presented. In order to further compress the ASE and overcome bandwidth limitations stemming from the lasers relaxation oscillation frequency (ROF), the devices under study are optically injection-locked as described in [125]. Under proper injection conditions, the beating between the injected light frequency and the cavity resonant frequency dominates the dynamic behavior and enhances the carrier modulation resonance at frequencies higher than the ROF.

## II. Four-Wave Mixing

### 1. Phase conjugation generation

The nonlinear response of an optical material is usually expanded by considering the induced polarization  $P$  as a power series in the electric field strength [266]:

$$P = \epsilon_0 (\chi^{(1)} \bar{E} + \chi^{(2)} \bar{E} \bar{E} + \chi^{(3)} \bar{E} \bar{E} \bar{E} + \dots) \quad (4.1)$$

where  $\chi^{(1)}$  is the linear optical susceptibility and  $\chi^{(2)}$ ,  $\chi^{(3)}$  are respectively the second- and third-order nonlinear susceptibilities.

The input field in Eq. 4.1 incorporates both pump and probe contributions such as:

$$\bar{E} = \frac{1}{2} [E_1 \exp i(\omega_1 t + \phi_1) + c. c. + E_2 \exp i(\omega_2 t + \phi_2) + c. c.] \quad (4.2)$$

In Eq. 4.2, it is assumed that  $E_1$  and  $E_2$  co-propagate along the cavity and the term c.c. corresponds to the complex conjugate of the electric fields. Hence, the third order term can be expressed as:

$$\bar{E} \bar{E} \bar{E} = \frac{1}{8} \left( \begin{aligned} &E_1^3 [\exp(j3\Phi_1) + c. c.] + E_2^3 [\exp(j3\Phi_2) + c. c.] \\ &+ E_1 (3E_1^2 + 6E_2^2) [\exp(j3\Phi_2) + c. c.] + E_2 (6E_1^2 + 3E_2^2) [\exp(j3\Phi_2) + c. c.] \\ &+ 3E_1^2 E_2 \{ \exp j(2\Phi_1 + \Phi_2) + c. c. + \exp j(2\Phi_1 - \Phi_2) + c. c. \} \\ &+ 3E_1 E_2^2 \{ \exp j(2\Phi_2 + \Phi_1) + c. c. + \exp j(2\Phi_2 - \Phi_1) + c. c. \} \end{aligned} \right) \quad (4.3)$$

with:

$$\Omega_1 = \omega_1 t + \phi_1, \Omega_2 = \omega_2 t + \phi_2$$

By injecting Eq. 4.3 into 4.1, the macroscopic polarization in the gain medium can be expressed as follows (assuming negligible all terms with an order higher than 3):

$$P \cong \frac{3\epsilon_0\chi^{(3)}}{4} \begin{pmatrix} E_1(E_1^2 + 2E_2^2) \cos(\Omega_1) \\ +E_2(2E_1^2 + E_2^2) \cos(\Omega_2) \\ +E_1^2 E_2 \cos(2\Omega_1 - \Omega_2) \\ +E_1 E_2^2 \cos(2\Omega_2 - \Omega_1) \end{pmatrix} \quad (4.4)$$

from which the two new fields  $E_3$  and  $E_4$  generated at the frequencies  $\omega_3$  and  $\omega_4$ :

$$\begin{aligned} \bar{E}_3 &= E_3 \exp(i\Omega_3) \\ \bar{E}_4 &= E_4 \exp(i\Omega_4) \end{aligned} \quad \text{with} \quad \begin{aligned} E_3 &= E_1^2 E_2 \\ E_4 &= E_1 E_2^2 \end{aligned} \quad \text{and} \quad \begin{aligned} \Omega_3 &= 2\Omega_1 - \Omega_2 = \omega_1 t + \phi_1 - (\omega_2 t + \phi_2 - \omega_1 t - \phi_1) \\ \Omega_4 &= 2\Omega_2 - \Omega_1 = \omega_2 t + \phi_2 + (\omega_2 t + \phi_2 - \omega_1 t - \phi_1) \end{aligned}$$

Eq. 4.4 indicates that for every two photons removed from  $E_1$ , one photon is added in  $E_2$  and the other one in  $E_3$ , and two photons are added in  $E_1$  and  $E_2$  from  $E_2$ . Therefore, the energy conservation is verified:

$$\begin{aligned} \overbrace{2\hbar\omega_1 + 2\hbar\omega_2}^{\text{input}} &= \overbrace{\hbar\omega_1 + \hbar\omega_2 + \hbar\omega_3 + \hbar\omega_4}^{\text{output}} \\ \text{with } \begin{cases} \omega_3 = 2\omega_1 - \omega_2 \\ \omega_4 = 2\omega_2 - \omega_1 \end{cases} \end{aligned}$$

By convention, among the input fields, the stronger one is referred as the pump, and the other the probe. The angular frequency difference  $\Delta\omega = \omega_1 - \omega_2$  is referred as the pump-probe frequency detuning. In the following, we will denote  $\Delta f = f_{\text{probe}} - f_{\text{pump}}$  as the frequency detuning, and:

1. up-conversion for negative detuning ( $\Delta f < 0$ ), when the frequency of the converted signal is higher than that of the pump;
2. down-conversion for positive detuning ( $\Delta f > 0$ ), when the frequency of the converted signal is lower than that of the pump.

In practice, there are several criteria to evaluate the quality of the nonlinear conversion performance such as the bandwidth, and most importantly the normalized conversion efficiency (NCE), which is defined as [19]:

$$\eta_{NCE} = \frac{P_{conv}}{P_{probe}P_{pump}^2} \quad (4.5)$$

where all powers are the output powers taken after the propagation within the gain media. Let us stress out that NCE calculated from Eq. 4.5 is in  $\text{mW}^{-2}$ . Experimentally, these powers are usually approximated by using the peak powers in the measured optical spectra. When expressed in logarithmic scale, the values are given in dB and correspond to  $10 \times \log_{10}(\text{NCE}/1\text{mW}^{-2})$ .

Eq. 4.5 indicates that the NCE is directly linked to the third order nonlinear susceptibility hence it gives an insight of the nonlinear conversion at the material level. Another definition of the conversion efficiency can also be found in the literature, such as:

$$\eta_{CE} = \frac{P_{conv}}{P_{probe}^{input}} \quad (4.6)$$

where the  $P_{probe}^{input}$  is the input power of the probe. As opposed to the NCE, the CE gives a description of the nonlinear conversion at the device level, which is more explicit as far as the input-output conversion is concerned particularly for system applications.

## 2. NDFWM in semiconductor gain medium

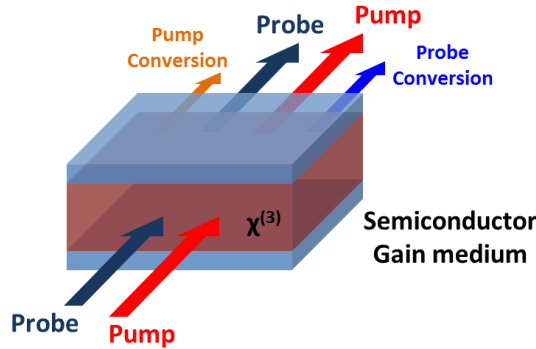


**Figure 4.2.** Schematic illustration of the NDFWM in a semiconductor gain medium.

Figure 4.2 schematically represents the NDFWM process arising in a III-V semiconductor gain medium such as a SOA [267] or a semiconductor laser [268]. In a SOA the architecture for FWM is a travelling wave configuration where all waves are launched at one end of the device

and the light is collected at the other end. In a semiconductor laser, the FWM mixing process takes place within the cavity between the waves. The pump can be either the free-running laser mode itself or an externally injected beam. In the latter case, the injected pump may lock the laser. This is the most stable configuration that will be studied in part 4 of this chapter. The probe is seeded into the cavity and both waves oscillate together and generate converted signals. The probe launching and amplification is enhanced if its wavelength corresponds to a resonance of the laser cavity.

In the semiconductor material, NDFWM is obtained from the beating between the incident pump and probe beams. From a microscopic viewpoint, the wave mixing is piloted by the third-order nonlinear susceptibility  $\chi^{(3)}$  through CDP, SHB and CH [117], [119], [269], [270]:

$$\chi^{(3)} = \chi_{CDP}^{(3)} + \chi_{SHB}^{(3)} + \chi_{CH}^{(3)} \quad (4.7)$$

For small detuning, CDP is the main contributor to  $\chi^{(3)}$ . It is induced by the pump-probe beating. However, due to the relatively slow response of this inter-band phenomenon, inherently limited by the carrier recombination lifetime ( $\sim 100$  ps timescale) [205] this effect rolls-off when the detuning increases. For higher detuning, both CH and SHB that occur within picosecond timescales become predominant. The latter two effects push the dynamic frequency conversion over much larger conversion bandwidths.

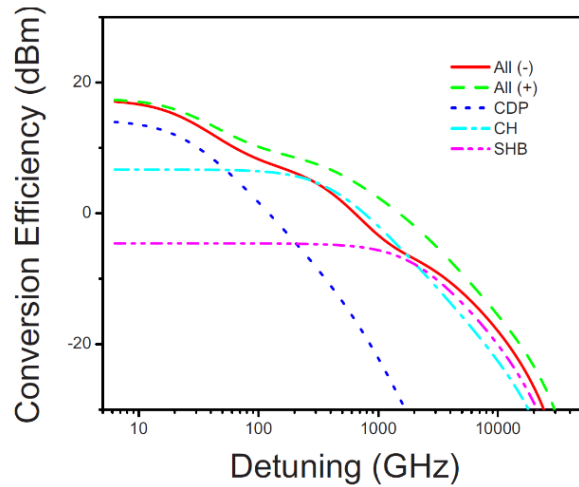


**Figure 4.3.** The contributions of the CDP, CH and SHB mechanisms to the nonlinear conversion efficiency in a QD SOA device, after [119].

While injecting a modulated probe into the active region, both SHB and CH are the main contributions driving the fast gain recovery, as shown in Figure 2.12, however, in the QW devices, such recovery is relatively long. As opposed to that, QDs constitute a class of nanostructures exhibiting large optical nonlinearities and higher response speeds owing to the fast carrier-carrier and carrier-phonon scatterings [117], [119], [120]. For instance, previous works (shown in Figure 4.3) have revealed that fast NDFWM can be obtained in QD SOAs through deeper spectral holes originating from the fast carrier scattering [119].

As mentioned in chapter II section IV.3, SHB and CH do not contribute to the conversion identically due to different timescales. Unlike in QW materials where the large carrier density increases the CH via free-carrier absorption, the latter is not necessarily the dominant process in QDs in particular for nanostructures with a large conduction-band offset [119]. However, SHB occurs through the depletion of carriers at their corresponding energies. These spectral holes induce a carrier redistribution via carrier-carrier scattering process in order to recover the depleted regions. In QWs, this effect is mostly driven either by inter-level or intra-level processes and is usually very fast ( $\sim 10\text{--}45$  fs). While the carrier localization and discrete DOS in QDs mean that the relaxation take place through intra-dot processes. However, the relatively large energy difference in the DOS between the dots and the RS means that the intra-dot process is slowed down with capture and relaxation times within a few to tens of picoseconds. This slower carrier dynamic allows for deeper spectral holes and lead to wider bandwidth conversions as opposed to QW materials.

Assuming that the gain coefficients for the probe and the converted signal are independent from the pump-probe detuning  $\Delta f$ , the CE is then proportional to square of  $\chi^{(3)}$ . Thus the dependence of CE on  $\Delta f$  can be described through that of  $\chi^{(3)}$  [117]:

$$\chi^{(3)} = \sum_m \chi_m^{(3)} = \sum_m \chi_{m,\Delta f=0}^{(3)} (1 - i2\pi\Delta f\tau_m) \quad (4.8)$$

where the index  $m$  specifies the contributions from the CDP, SHB and CH,  $\chi_{m,\Delta f=0}^{(3)}$  are the corresponding amplitude at  $\Delta f = 0$  and the characteristic time constant which is inversely proportional to the cut-off frequency  $f_{c,m} = 1/\tau_m$ .

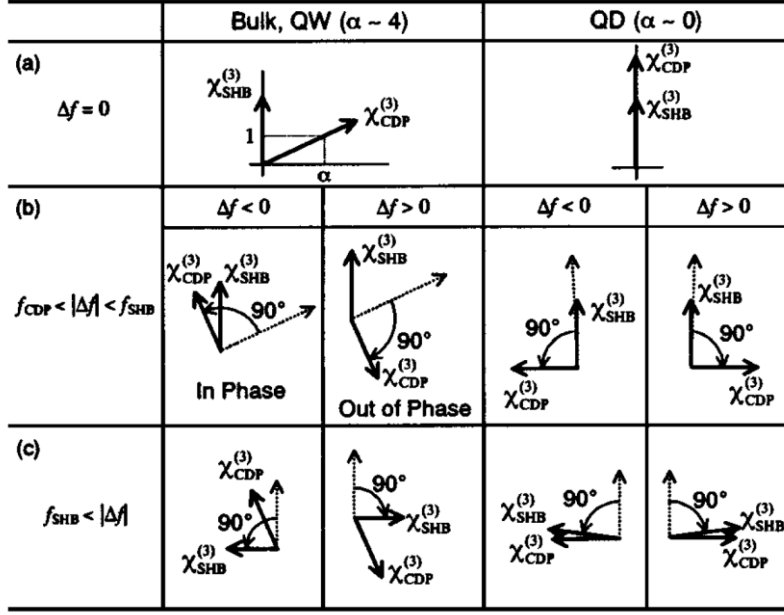


**Figure 4.4.** Directions of  $\chi^{(3)}$  of CDP and SHB for bulk, QW and QD, after [117].

Figure 4.4 illustrates the complex plane representation of SHB and CDP. The consequence of the non-zero CDP  $\alpha_H$ -factor for bulk and QW materials can be observed for  $\Delta f = 0$ . It can be compared to the SHB which  $\alpha_H$ -factor is close to 0. The QD case is illustrated on the second column. Since the  $\alpha_H$ -factor is null, the two representative vectors for CDP and SHB are parallel. When  $|\Delta f|$  increases above the cut-off frequency  $f_c$  of one of the non-linear effects, the argument of the corresponding  $\chi_m^{(3)}$  changes by  $\pm 90^\circ$  for up and down-conversion respectively. Then, for the detuning band ranging from  $f_{c,CDP}$  and  $f_{c,SHB}$ , one can clearly see that both effects add up differently, leading in the case of bulk and QW material to different amplitude of the resulting non-linear susceptibility for up or down conversion mechanisms. In the case of QD, the low  $\alpha_H$ -factor associated to the CDP strongly reduces this asymmetry of FWM conversion. The experimental results of Figure 4.5 issued from [29] confirms this difference.

In SOA devices, by setting the pump, the probe can be set to an arbitrary position on the gain profile and its wavelength can be tuned continuously. When the FWM is obtained in a laser cavity, the probe must coincide with one cavity mode in order to minimize the cavity loss, thus the probe wavelength variation is discrete, however, the conversion will be enhanced by the cavity resonance. Let us point out that, the optical signal-to-noise ratio (OSNR) is defined differently for SOAs than for lasers. Filtering out the converted signal, in SOAs, the noise level

is the local flat ASE level when probe is turned off, and the OSNR is defined as the ratio between the peak power of the conversion and the local ASE noise level; while for the laser cavity case, the noise is the resonant cavity mode, taking into account that this cavity mode is at almost the same intensity than the modes next to it, thus the OSNR in this scenario can be approximated by the ratio between the peak power of the converted signal and the that of the closest cavity mode.

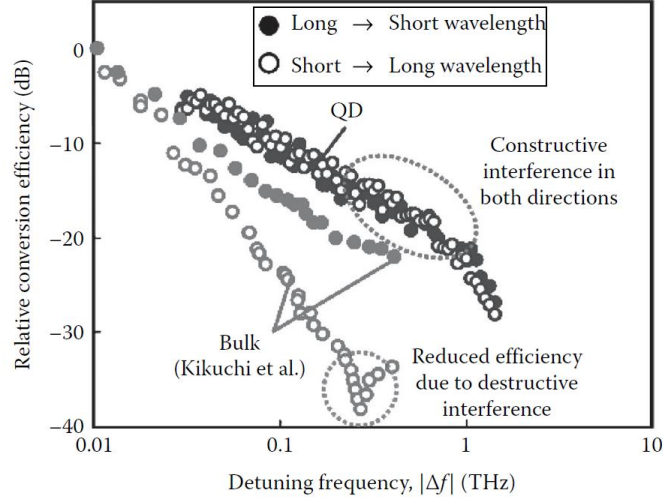


**Figure 4.5.** Comparison of the measured CE between a bulk and a QD SOA, after [103].

Table 4.1 summarizes the main results obtained for QD lasers and SOAs in terms of CE, and maximum bandwidth both for up- or down-conversion. A comparison with QW lasers is also provided. From a general viewpoint, all QD lasers studied in this work show much better nonlinear conversion properties than QD SOAs and QW lasers. The first two studies are based on DFB and FP lasers, where Murata et al. have demonstrated that an optical injection-locked FP laser could achieve similar conversion performance than a DFB laser, and offer THz range dynamical conversion of the modulated signal. Indeed, optical injection can be applied on DFB cavities to improve their spectral properties, although the issue from the complex cavity design remains. Let us direct our attention on the last two results coming from the same InAs/GaAs QD material system. For the SOA, a very high CE of -2 dB is obtained but at the price of a very large pumping current of 600 mA. At lower bias condition of 200 mA, the maximum CE drops down to -15 dB with a bandwidth of 2.7 THz. With the FP laser used in this work, the bias current is much lower (< 100 mA), while both the OSNR and the bandwidth are improved. Thus,

the results depicted hereinafter unveil that QD lasers can provide good CE, large bandwidth, and high OSNR with lower energy consumption and more compact dimensions.

Reference	Material	Device	Max Conv. bandwidth (THz)	Max. CE (dB)	Max. OSNR (dB)
S. Murata et al. (1991) [271]	InGaAsP QW	DFB Laser	1.1	-10	25
S. Murata et al. (1991) [124]	InGaAsP QW	FP Laser	1	-14	-
T. Akiyama et al. (2000) [117]	InAs/GaAs QD	SOA	1.5	0	20
H. Su et al. (2005) [264]	InAs/GaAs QD	DFB Laser	1.4	-14	-
Z.G. Lu et al. (2006) [122]	InAs/InP QD	SOA	< 1	-11.8	-
This work :H. Huang et al. (2015) [272]	InAs/InP QD	FP laser	3.5	-4	39
C. Meuer et al. (2011) [114]	InAs/GaAs QD	SOA	4.7	-2	34
This work: Huang et al. (2016) [273]	InAs/GaAs QD	FP Laser	3.5	-16	36

**Table 4.1.** Summary of the state-of-the-art of the NDFWM achievements in QD SOAs and lasers. QW laser results are included for comparison.

### 3. Extraction of the third-order nonlinear susceptibility

A traveling-wave model can be used to extract the third-order nonlinear susceptibility  $\chi^{(3)}$  of the semiconductor active region. The model describes the interaction between the pump, the probe and the converted signal [274]. The electric field related to the converted signal can be described as follow [264]:

$$\frac{dE_{conv}}{dz} = \frac{\Gamma g}{2} E_{conv} + i \frac{3\Gamma\mu_0\epsilon_0\omega^2}{8k_0n} \chi^{(3)} E_{pump}^2 E_{probe} \quad (4.9)$$

where the  $E_{pump}$ ,  $E_{probe}$  and  $E_{conv}$  corresponds to the field amplitudes of the pump, probe and the converted signal respectively, while  $k_0$  is the wavevector of the conjugate light in vacuum,  $n$  the refractive index,  $\Gamma g$  the modal gain in the active region and  $\mu_0$ ,  $\epsilon_0$  are the vacuum permeability and permittivity respectively. The model holds under the following



assumptions:

- 1) the interaction between the counter-propagating pump and co-propagating converted signal, and between the counter-propagating probe and co-propagating converted signal are neglected. This assumption is of course more disputable for a laser cavity than for SOA in which both the pump and the probe have a single-pass through the amplifier;
- 2) the nonlinear interactions take place only in the active region;
- 3) the same confinement factor  $\Gamma$  is considered for the pump, the probe and the converted signal;
- 4) the changes in the gain and the pump depletion resulting from the probe are neglected;
- 5) the nonlinear interactions between the pump-converted signal and probe-converted signal are neglected.

In Eq. 4.7, the second term on the right hand can be considered as a constant, therefore rearranging the equation yields:

$$\frac{d\left(E_{conv} + i\frac{3\Gamma\mu_0\epsilon_0\omega^2}{4gk_0n}\chi^{(3)}E_{pump}^2E_{probe}\right)}{dz} = \frac{\Gamma g}{2}\left(E_{conv} + i\frac{3\Gamma\mu_0\epsilon_0\omega^2}{4gk_0n}\chi^{(3)}E_{pump}^2E_{probe}\right) \quad (4.10)$$

hence, the solution of  $E_{conv}$  is in the form of:

$$E_{conv} + i\frac{3\Gamma\mu_0\epsilon_0\omega^2}{4gk_0n}\chi^{(3)}E_{pump}^2E_{probe} = a\exp(bz) \quad (4.11)$$

To simplify the calculation, wave boundary condition  $E_{conv}(z = 0) = 0$  was used. Although such approximation is perfectly valid for a SOA, experimental results presented hereinafter will confirm that this assumption is reasonable for the QD lasers investigated in this work.

Then,  $E_{conv}$  can be then expressed as:

$$E_{conv} = i\frac{3\Gamma\mu_0\epsilon_0\omega^2}{4gk_0n}\chi^{(3)}E_{pump}^2E_{probe}\left(\exp\left(\frac{\Gamma g}{2}z\right) - 1\right) \quad (4.12)$$

thus the integration of Eq. 4.10 from  $z = 0$  to  $L$  ( $L$ : interaction length) is found as:

$$\eta_{CE} = \left| \frac{E_{conv.}}{E_{probe}} \right|^2 = \left| \frac{3k_0}{4n} \Gamma \chi^{(3)} E_{pump}^2 \frac{\exp(\Gamma g L) - 1}{\Gamma g} \right|^2 \quad (4.13)$$

leading to

$$\eta_{NCE} = \left| \frac{E_{conv.}}{E_{pump}^2 E_{probe}} \right|^2 = \left| \frac{3k_0}{4n} \Gamma \chi^{(3)} \frac{\exp(\Gamma g L) - 1}{\Gamma g} \right|^2 \quad (4.14)$$

Since the laser is operating above threshold, the net gain  $\Gamma g_0$  is clamped and equals to the mirror loss of the laser cavity  $\alpha_m$ :

$$\Gamma g_0 = \alpha_m = \frac{1}{L} \ln \left( \frac{1}{\sqrt{R_1 R_2}} \right) \quad (4.15)$$

where  $R_1$  and  $R_2$  are the reflectivity of the two laser cavity facets.

In Eq. 4.14, the intensity of the electrical field can be calculated from the optical spectra, for instance, the pump peak power can be expressed as follows:

$$P_{pump} = I_{pump} A_{eff} \quad (4.16)$$

where  $A_{eff}$  represents the effective mode area in the waveguide cross-section, and  $I_{pump}$  the intensity of the pump with:

$$I_{pump} = \frac{1}{2} c \epsilon_0 n E_{pump}^2 \quad (4.17)$$

where  $c$  is the light vacuum velocity. Thus, the conversion between the spectral power and the field amplitude of the pump is:

$$E_{pump} = \sqrt{\frac{2P_{pump}}{c \epsilon_0 n A_{eff}}} \quad (4.18)$$

By rewriting Eq. 4.14, the normalized third-order nonlinear susceptibility to the material gain can be expressed as:

$$\frac{\chi^{(3)}}{g_0} = \frac{4n}{3k_0} \frac{1}{\exp(\Gamma g L) - 1} \sqrt{\eta_{NCE}} \quad (4.19)$$

## 4. Optical injection-locking

The main difference between frequency conversion in amplifiers and lasers is the cavity

resonance, as stimulated emission enhances the conjugate generation and amplification and reduces the carrier lifetime. Overall, two methods have been proposed to generate frequency conversion in semiconductor laser devices. The first approach is simply to inject the signal to be converted into the laser cavity that is biased above the threshold. However, such method has been proved to degrade the coherence properties of the conjugate beam [265]. The second method relies on the use of optical injection-locking, which involves a master laser – slave laser coupling, as represented in Figure 4.6. The master is a single-mode laser with a narrow spectral linewidth that is injected into the slave laser under study. Under proper injection conditions, the slave laser can be locked by the master and emits on the locked lasing mode. This injection-locked mode will act as the pump of the FWM mechanism. The probe is launched separately and conversion occurs within the cavity.

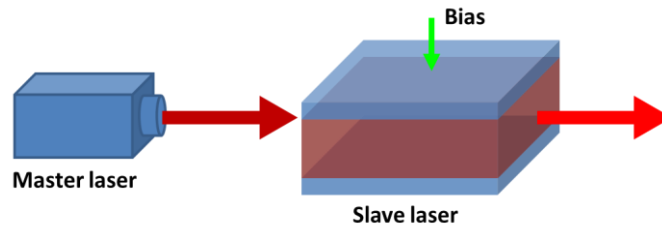


**Figure 4.6.** Scheme illustrating the optical injection-locking.

Figure 4.7 illustrates the optical spectra of an injection-locked slave FP laser as compared to the free-running case (without optical injection), for which the laser exhibits a multimode behavior. While locked, the slave laser becomes single mode with a high peak power and a large side mode suppression ratio.

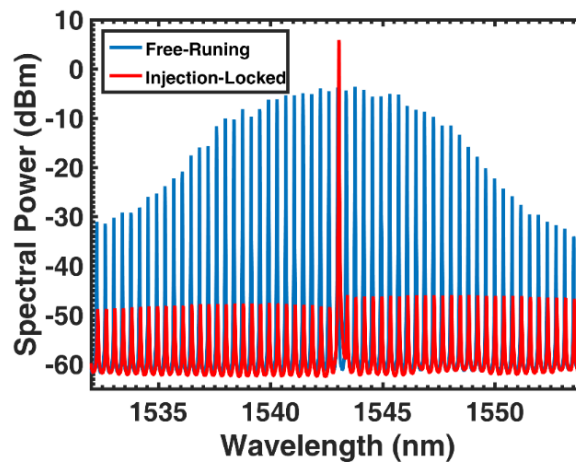


**Figure 4.7.** Optical spectra of the free-running FP laser (blue) and of the injection-locked laser (red).

The key parameters for controlling the injection locking mechanism are:

- the injection detuning  $\Delta\Omega_{inj}$ , corresponding to the difference between the angular frequencies of the master laser  $\Omega_{inj}$  and the injected cavity mode  $\Omega$  of the injected laser;
- the injection strength, defined as the ratio between the master laser power and the slave laser power. Usually, the latter is fixed for the optical injection study, thus the injection strength is proportional to the master laser power.

The complex electrical field  $\tilde{E}(t) = A(t) \exp i(\Omega t + \Phi(t))$  of an optically-injected laser can be derived from the differential equation [275]:

$$\frac{d\tilde{E}(t)}{dt} = \left\{ \frac{1}{2} (1 + i\alpha_H) \left[ \Gamma G_N (N(t) - N_{tr}) - \frac{1}{\tau_p} \right] + i\Omega \right\} \tilde{E}(t) + k_c \tilde{E}_{inj}(t) \quad (4.20)$$

where  $\tilde{E}_{inj}(t) = A_{inj}(t) \exp i(\Omega_{inj}t + \Phi_{inj}(t))$  is the injected field from the master laser,  $\Gamma$  the confinement factor,  $G_N = v_g \frac{\partial g}{\partial N}$  is the linear gain with  $v_g$ ,  $g$  and  $N$  the group velocity, the gain and the carrier intensity,  $N_{tr}$  is the transparent carrier density,  $\tau_p$  the photon life time and  $k_c$  the coupling coefficient. From Eq. 4.8, the rate equations for the amplitude and the phase of the slave laser can be deduced:

$$\frac{dA(t)}{dt} = \frac{1}{2} \left[ \Gamma G_N (N(t) - N_{tr}) - \frac{1}{\tau_p} \right] A(t) + k_c A_{inj}(t) \cos(\phi(t)) \quad (4.21)$$

$$\frac{d\phi(t)}{dt} = \frac{\alpha_H}{2} \left[ \Gamma G_N (N(t) - N_{tr}) - \frac{1}{\tau_p} \right] - \Delta\Omega_{inj} - k_c \sin(\phi(t)) \frac{A_{inj}(t)}{A(t)} \quad (4.22)$$

where  $\phi(t) = \Delta\Omega_{inj} + \Phi_{inj}(t) - \Phi(t)$  is the phase difference between the master laser and the free-running laser. In addition, the equation of carrier density is given as:

$$\frac{dN(t)}{dt} = \frac{\eta_i I}{qV} - \frac{N(t)}{\tau_c} - G_N (N(t) - N_{tr}) A^2(t) \quad (4.23)$$

where the  $\tau_c$  is the carrier lifetime,  $\eta_i$  the fraction of terminal current that generates carriers into the active region,  $I$  the bias current,  $q$  the electron charge and  $V$  the volume of the active

region.

The steady-state solutions  $A_s$ , and  $\phi_s$  can be deduced from Eqs. 4.21 and 4.23:

$$A_s^2 = \left[ \frac{\eta_{il}}{qV} - \frac{N_s}{\tau_c} \right] / G_N(N(t) - N_{tr}) \quad (4.24)$$

$$N_s = N_{tr} + \frac{1}{\Gamma_{GN}\tau_p} - \frac{2}{\Gamma_{GN}} \frac{A_{inj}}{A_s} k_c \cos \phi_s \quad (4.25)$$

By injecting Eq. 4.25 into Eq. 4.22, we obtain:

$$\Delta\Omega_{inj} = -\frac{A_{inj}}{A_s} k_c \cos(\phi_s) \alpha_H - \frac{A_{inj}}{A_s} k_c \sin(\phi_s) \quad (4.26)$$

Applying the trigonometric relation  $a \sin \theta + b \cos \theta = \sin \left( \theta + \arctan \frac{b}{a} \right)$ , Eq. 4.25 can be rewritten as:

$$\Delta\Omega_{inj} = -\frac{A_{inj}}{A_s} k_c \sqrt{1 + \alpha_H^2} \sin(\phi_s + \arctan \alpha_H) \quad (4.27)$$

Eq. 4.27 can be used to determine the possible locking boundaries for injecting detuning  $\Delta\Omega_{inj}$  [276] as the term  $\sin(\phi_s + \arctan \alpha_H)$  is between -1 and 1:

$$-\frac{A_{inj}}{A_s} k_c \sqrt{1 + \alpha_H^2} \leq \Delta\Omega_{inj} \leq \frac{A_{inj}}{A_s} k_c \sqrt{1 + \alpha_H^2} \quad (4.28)$$

Eq. 4.28 indicates the possible injection-locking boundaries of  $\Delta\Omega_{inj}$ ; the locking range shall extend further with high  $k_c$  or with a large  $\alpha_H$ . However, the stability analysis has demonstrated that the stable master-laser locking range is limited by the Hopf bifurcation through the whole possible locking range deduced from Eq. 4.28. As illustrated in Figure 4.8 [277], the locking range can be either stable (SL, stable locking) or may involve some more complex nonlinear dynamical behaviors (NL) such as periodicities and chaos. In addition, with increasing the  $\alpha_H$ -factor, the Hopf bifurcation is shifted towards negative frequencies, narrowing the SL range, and the NL range will become dominant [240], [278].

Within the stable-locking area, the laser exhibits an enhanced ROF, a larger modulation bandwidth [277], [279], and a reduced frequency chirp [125], [280]–[282], as well as lower phase noise and intensity noise that will enhance the dynamic conversion efficiency [124], [283].

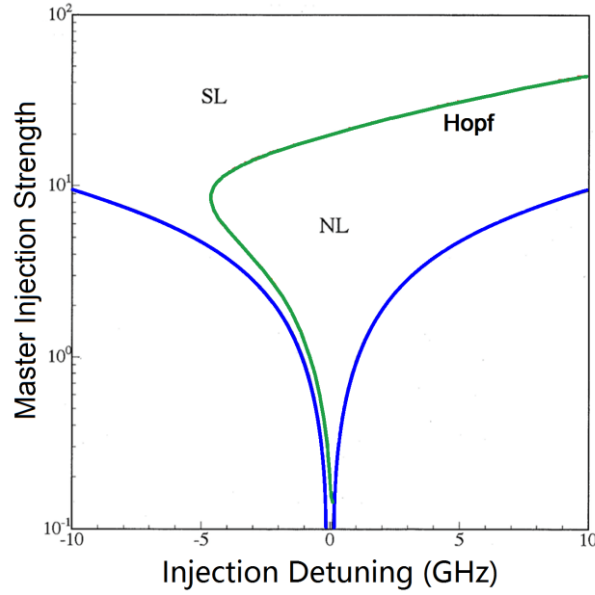


**Figure 4.8.** Illustration of the injection-locking boundaries in terms of injection detuning and injection strength, after [277]. SL: stable locking; NL: nonlinear dynamics area.

### III. Experimental investigation of four-wave mixing in injection-locked QD lasers

In the following part, we present experimental studies of NDFWM in injection-locked QD FP lasers.

#### 1. Experimental setup

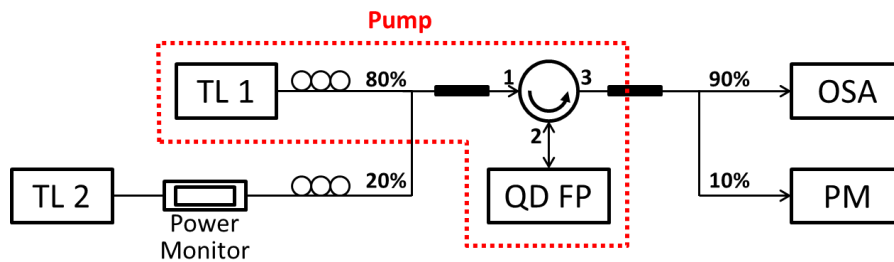


**Figure 4.9.** Experimental setup for NDFWM investigation, the pump signal originates from tunable laser TL1, whose beam is seeded into the QD laser and injection-locked it.

Figure 4.9 shows the experimental setup used for NDFWM investigation. The elements figuring in the red frame allow injection-locking the QD FP laser. The second tunable laser TL2 generates the probe signal; a power monitor, which includes an integrated attenuator, controls

its power. Polarization controllers are added at the output of both TL1 and TL2. The polarization controllers allow matching the polarizations of both tunable lasers to that of the light emitted by the slave laser. Generally, to ensure stable locking, the power from TL1 is higher than TL2, therefore we used uneven coupling, 20% for the TL2 and 80% for the TL1. The injection into the QD laser cavity is achieved through a lens-ended fiber, the latter being also used to collect the light emitted by the laser. The collected light travels back toward the circulator and exits through port 3. An OSA is used to acquire the optical spectrum, and a powermeter (PM) is used to monitor the output power to ensure stability of the coupling. According to Eq. 4.5 and Eq. 4.6, the extracted CE and NCE depend on the power of the pump, the probe and the converted signal, thus, in order to not underestimate these powers, the losses in the fibers, the optical circulator and the coupler are carefully considered, i.e. the losses between the FP laser facet and the OSA are taken into account. In the following part, the list of equipment and the operating experimental conditions will be specified for each QD laser device studied. The QD FP lasers have been designed and processed either in NRC Canada or in TU Berlin. The former are InAs/InP QD lasers (5 QD layers) emitting in the C-band while the latter are InAs/GaAs QD ones (10 QD layers) emitting in the O-band.

## **2. Static conversion in InAs/InP FP QD lasers**

The laser studied in this section is the QD FP laser PFP1 described in chapter III. Table 4.2 summarizes the experimental conditions. The laser device is biased at  $2.4 \times I_{th}$  and is temperature controlled at 293K. TL1 is an external cavity laser (Anritsu Tunics Plus) with a linewidth around 150 kHz; the injection ratio is set to be 3 dB below the emission power of the free-running slave QD FP, and its wavelength is tuned to be 80 pm (-10 GHz) above that of the targeted FP mode. The injected power from TL2 is set around to 400  $\mu$ W. Its wavelength is tuned in order to adjust the FWM frequency detuning. Let us stress that the real injection ratio is calculated as the ratio between the power from master laser injected into the active region of slave laser and the output power from the slave laser. However, it is difficult to know the actual power coupled into the slave laser active region, thus in our case, the injection ratio is estimated as the ratio between the tunable laser power reaching the injecting facet and the power emitted from the injecting facet of the FP laser.

Experimental Condition	Preset Level
Temperature	293 K
QD FP Bias Current	$2.4 \times I_{th}$ (98 mA)
QD FP Output Power $P_{out}$	8.4 mW
Injection Angle	Collinear ( $0^\circ$ )
TL1	Anritsu Tunics Plus
TL2	Yenista T100 (1550 nm)
Master Injection Ratio	-3 dB (4.2 mW)
Master-Slave Detuning	-10 GHz
Probe Injection Ratio	-13 dB (0.4 mW)

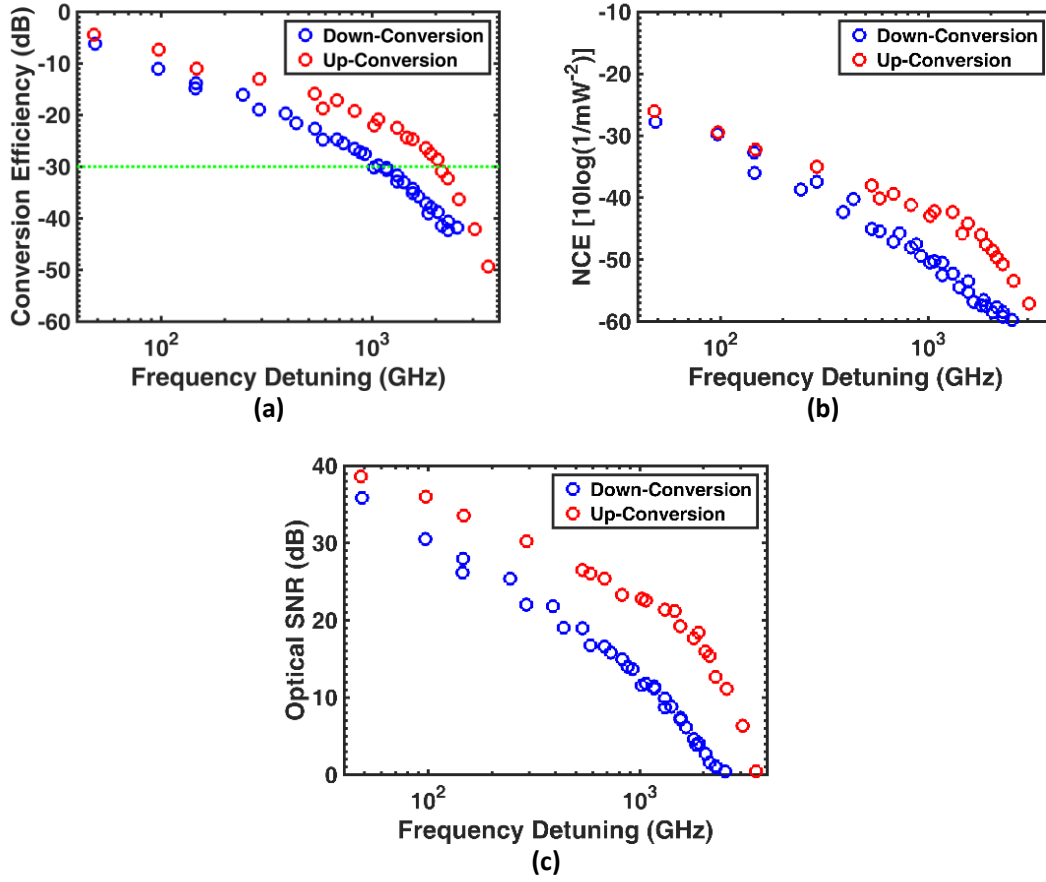
**Table 4.2.** Experimental conditions used for testing PFP1.

Figure 4.10 (a) presents the evolution of the CE as a function of the pump-probe frequency detuning  $\Delta f$  when the FP mode located at the gain peak is locked as pump wave. The CE for up- and down-conversion being shown in red and blue circles respectively on a single graph for comparison. Each point on the CE profile is obtained by tuning the frequency of the probe so as to coincide with one of the cavity modes of the QD laser, where maximal conversion is obtained. The corresponding wavelength detunings are thus multiples of the free spectral range of the injection-locked laser, and correspond to local maxima in the curve of the CE as a function of the pump-probe detuning. As expected, the static conversion is found to be more efficient when the CDP mechanism dominates, namely for detunings of a few GHz, with a maximum CE of about -4 dB. Most importantly, a CE above -30 dB (horizontal dot line in Figure 4.10 (a)) is achieved between -1 THz and +2 THz. At larger frequency detunings, SHB and CH fully dominate allowing a weaker conversion but with CE above -50 dB for detunings between -2.5 THz and +3.5 THz. These results are better than those found with InP-based QD SOAs [117].

- The measured efficiency is of the order of -3 dB at low detuning which compares well with that of the SOA in [21];
- The conversion bandwidth is much larger 6 THz in total versus 2 THz.
- The laser cavity is only 1 mm long and the pumping level is less than 120 mA, which is by far less than [21] where the bias current was 7 A for a 25 mm long SOA.



- The asymmetry of CE between up- and down-conversion is around 9 dB, which is higher than that in the SOA ( $\sim 5$  dB).



**Figure 4.10.** Measured CE (a), NCE (b) and OSNR (c) of FWM in the QD laser PFP1 as a function of the pump-probe frequency detuning.

As presented in chapter III, the dot-size of this laser is relatively large ( $\sim 50$  nm), with an inhomogeneous broadening around 40 meV. Thus, from the principle exposed in chapter II, we can expect that the in-dot carrier population is increased, and the contribution from CH is improved. In addition, larger dot-size implies less quantum confinement, hence the ES will be closer to the above RS, meaning that the capture processes will be accelerated, therefore, the contributions from CDP will be enhanced. Besides, the two-photon absorption (TPA) effect, which corresponds to the carrier excitation into the bulk region by the simultaneous absorption of two photons, may contribute to the gain recovery and hence improve the CE.

Figure 4.10 (b) presents the evolution of the corresponding NCE. As the FP laser is stably locked by an external laser with a relatively stable output, the measured NCE follows the same tendency as the CE profile. As in the NCE, the power of the converted signal is divided by the

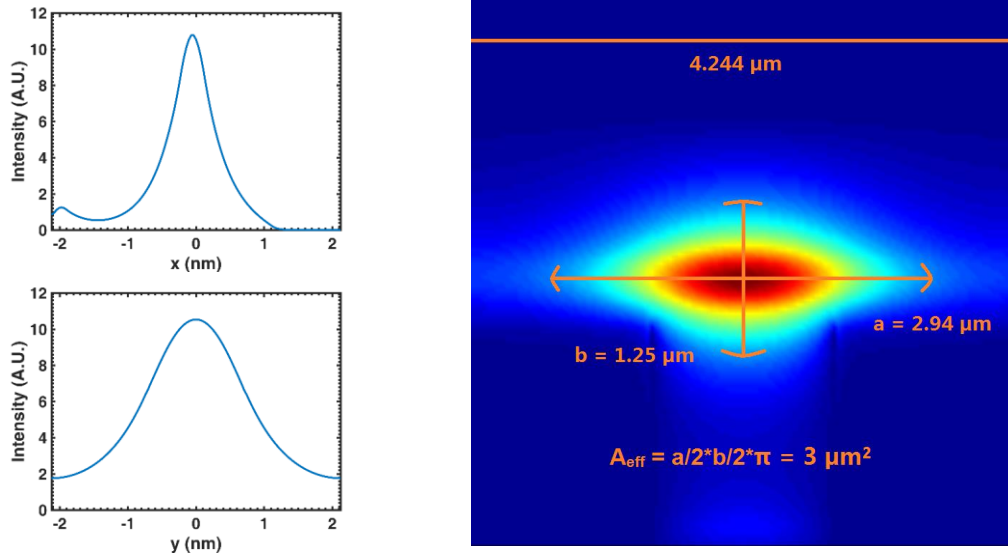
squared pump power and the probe power after propagation, which are both already been amplified by the active region, thus the corresponding amplitude is low.

Figure 4.10 (c) shows the OSNR. While OSNRs above 20 dB are achieved between -500 GHz and +1.5 THz (up-conversion), the converted signal quickly drops down to the noise level for absolute detuning above 2 THz. In addition, the experiments show a larger OSNR associated to a clear extension of the NDFWM frequency detuning range further in the THz window, without the need of very long interaction lengths [122], as compared to other results in Table 4.1.

Figure 4.10 reveals that the asymmetry between up- and down-conversion profiles is not completely eliminated because the  $\alpha_H$ -factor measured on PFP1 is about 1.4, hence the phase condition arising between the nonlinear processes (CDP, SHB and CH) still produces destructive interference, as indicated in Figure 4.4.

## 2.1. Extraction of the third-order nonlinear susceptibility

By applying Eq. 4.19, the profile of  $\chi^{(3)}$  can be extracted. The effective mode area  $A_{eff}$  of the laser must be first calculated.



**Figure 4.11.** Intensity mode profile in the x and y directions (left) and corresponding distribution in the waveguide cross-section (right).

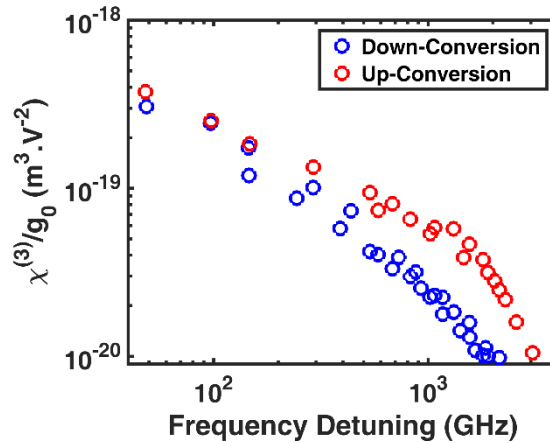
The effective mode area is calculated by modeling the intensity distribution in the waveguide cross-section of the transverse component. Using the software PhotonDesign,

Figure 4.11 shows the calculated intensity mode profile in the x and y directions (left) and the corresponding distribution of the transverse mode in the waveguide cross-section (right) assuming a section of  $4.244 \times 4.244 \mu\text{m}$ . As shown in Figure 4.11, the mode profile has a Gaussian shape; therefore the effective area is retrieved by considering 90% of the total power in both directions leading to  $A_{eff}$  of about  $3 \mu\text{m}^2$ .

Parameters	Values
Reflective index n	3.5
Wave vector $k_0$	$6.1 \times 10^4 \text{ m}^{-1}$
Net modal gain $\Gamma g_0$	$11.4 \text{ cm}^{-1}$
Laser cavity length L	0.1 cm
Effective mode area $A_{eff}$	$3 \mu\text{m}^2$

**Table 4.3.** Parameters used in Eq. 4.19.

Therefore, by injecting the values from Table 4.3 into Eq. 4.19, we extract  $\chi^{(3)}/g_0$  and plot it as a function of  $\Delta f$ . In the short detuning range,  $\chi^{(3)}/g_0$  is enhanced due to the stronger CDP induced by the beating between the pump and probe while at larger detuning,  $\chi^{(3)}/g_0$  is reduced following the same trend as predicted in Figure 4.3. The maximum value is around  $2.8 \times 10^{-19} \text{ m}^3/\text{V}^2$ , which is at the same order with prior values reported for InAs/GaAs QD DFB lasers [264], and therefore validate the wave boundary approximation for Eq. 4.10.



**Figure 4.12.** The normalized third-order nonlinear susceptibility  $\chi^{(3)}/g_0$  as a function of the pump-probe frequency detuning.

With the setup shown in Figure 4.9, while adjusting the master laser TL1 to lock the slave laser PFP1, the output power of locked PFP1 should increase; however, experiments has

shown the opposite. Using a multi-population rate equation model, numerical simulations of the output power from a slave laser have been performed in collaboration with Politecnico di Torino. Figure 4.13 shows that the output power of an injection-locked QD laser is not identical for both facets while the master laser is injected through the left facet [284]. The laser power exiting from the side of the injection (Green) is found to decrease in the locking range. However, due to the reduction of the carrier density, the output power of an injection-locked laser should increase as depicted in the simulations under the transmission configuration (pink). Thus, simulations unveil that injecting and detecting from the same facet may underestimate the output power since destructive interferences between the reflected pump and the lasing field arise in the cavity. This uneven behavior in the output power bring question to the values of  $\chi^{(3)}/g_0$  previously extracted.

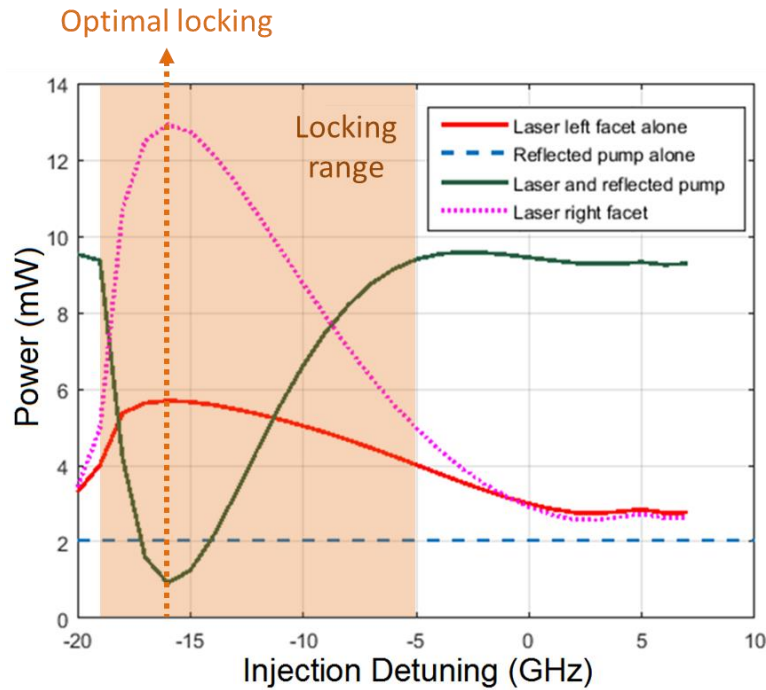


**Figure 4.13.** Numerical simulations showing the output power as a function of the injection detuning for an injection-locked QD FP laser. Green:  $P_{out}$  from the same facet (left); Red:  $P_{out}$  of the slave laser only from the left facet; Pink:  $P_{out}$  from the right facet of the laser; Dashed line: reflected pump alone.

In order to check these theoretical predictions, Figure 4.14 shows the measured output power as a function of the injection detuning. Detection is done either at the left facet or at the right one and three values of the injection ratio are considered. It is clear that the stronger

the injection is, the larger is the locking area, which is in perfect agreement with the theory [277]. Besides, the experiments unveil similar behaviors than those predicted from the numerical simulations.

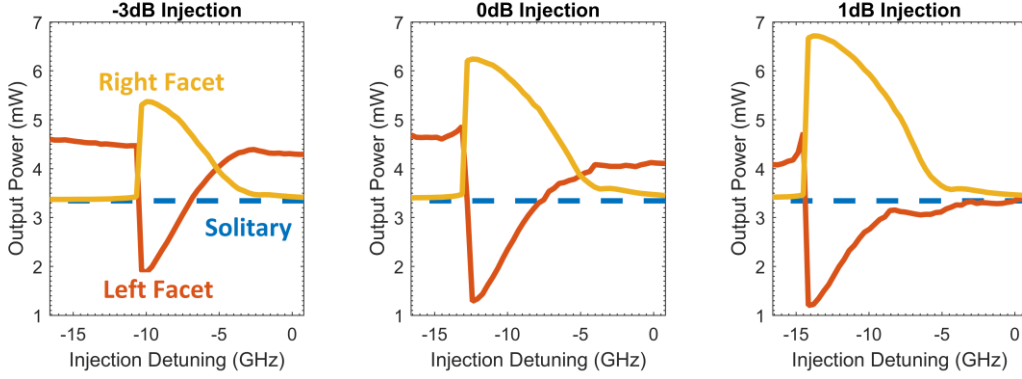


**Figure 4.14.** Experimental results illustrating the impact the injection ratio on the output power measured at the two facets of a QD FP laser. The pump is injected from the left facet.

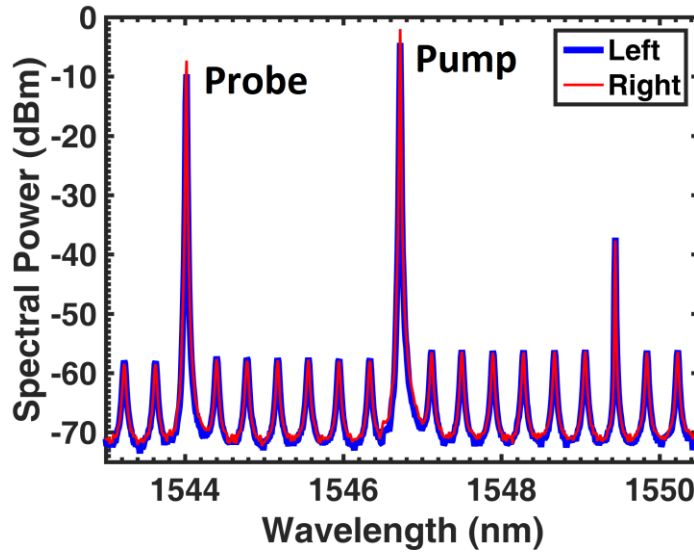


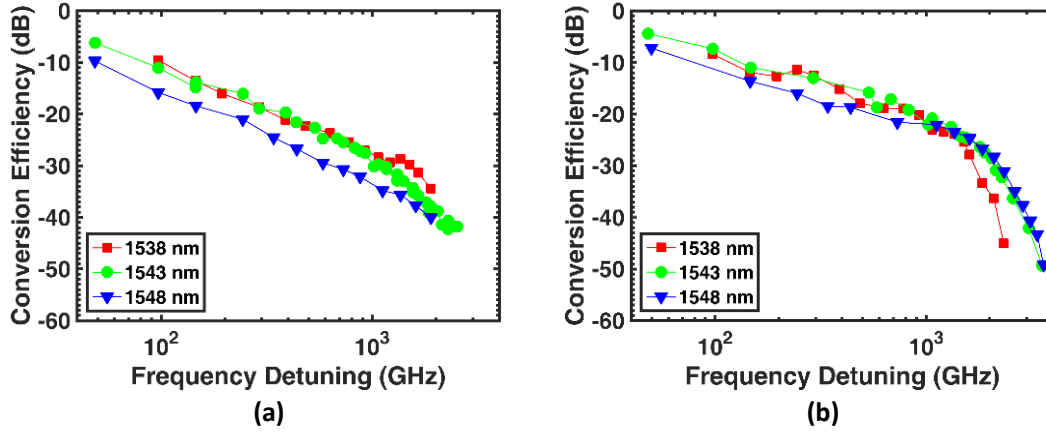
**Figure 4.15** NDFWM spectra of the QD FP laser measured in reflection and transmission configurations for a pump-probe frequency detuning of 340 GHz (down-conversion).

Due to this uneven behavior in output power, we performed the NDFWM measurements from both facets of the QD laser PFP1 (with the optical injection at the left facet), the optical spectra are depicted in Figure 4.15 for a pump-probe frequency detuning of 340 GHz. As one can observe, there is a small discrepancy between both the pump and the probe peak power issued from each facets. The extracted  $\chi^{(3)}/g_0$  are  $9 \times 10^{-20}$  (left) and  $7.9 \times 10^{-20} \text{ m}^2/\text{V}^2$  (right) while, values of  $1.6 \times 10^{-19}$  (left) and  $1.4 \times 10^{-19} \text{ m}^2/\text{V}^2$  (right) are extracted with  $\Delta f =$

–340 GHz, the difference between the two configurations remains around 10%. As such, the extracted values of  $\chi^{(3)}/g_0$  reported in Figure 4.12 give the correct magnitude order with slight overestimations.

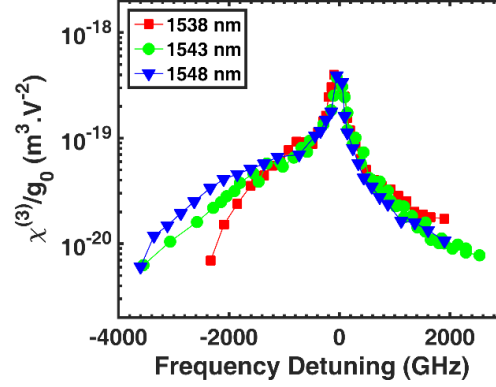
## 2.2. Influence of the pump wavelength

In this subsection, the influence of the pump wavelength, or its position in the gain spectrum is assessed. The underlying objective is to demonstrate the impact of the  $\alpha_H$ -factor on the CE symmetry, taking advantage of the wavelength-related  $\alpha_H$ -factor spectrum shown in Figure 3.20.



**Figure 4.16.** Measured CE versus frequency detuning for different pump wavelengths for (a) down-conversion and (b) up-conversion. The red, blue and green curves represent the results obtained for 1538, 1543 and 1548 nm respectively.

Figure 4.16 shows the measured CE for (a) down- and (b) up-conversion as a function of the pump-probe frequency detuning and for three pump wavelengths namely 1538, 1543 and 1548 nm. For a 1 THz detuning, the difference in the CE for up- and down-conversion is 5 dB for a pump at 1538 nm, 9 dB at 1543 nm and 13 dB at 1548 nm. The wavelength dependent  $\alpha_H$ -factor extracted from Figure 3.20 gives 1.25 at 1538 nm, 1.4 at 1543 nm and 1.53 at 1548 nm respectively. As aforementioned, a lower value of the CDP related  $\alpha_H$ -factor reduces the asymmetry between up- and down-conversion [103]. However, the shape of the gain spectrum shown (Figure 3.18) must also be taken into account: with a pump at 1548 nm, the up-converted signal has a wavelength close to the gain peak. On the contrary, with a pump at 1538 nm, it experiences a lower gain.



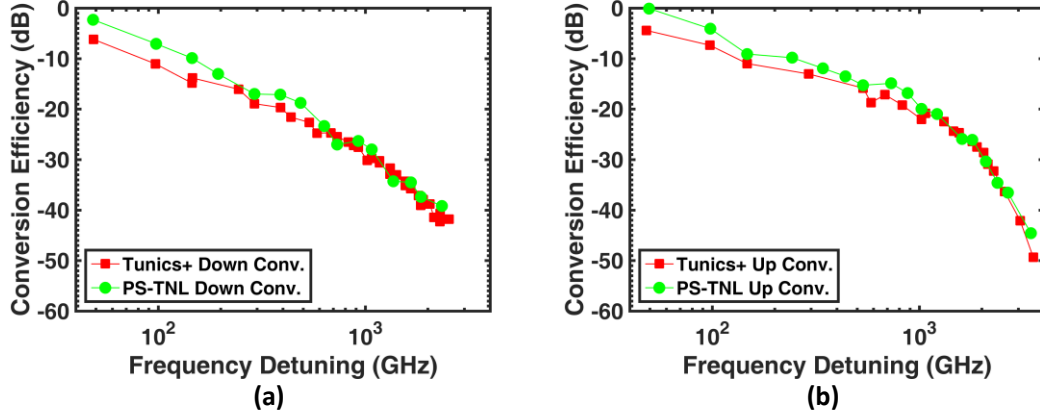
**Figure 4.17.** The normalized  $\chi^{(3)}/g_0$  as a function of the pump-probe frequency detuning and for different injected pump wavelengths. The red, green and blue colors represent the results obtained when the pump mode is at 1538, 1543 and 1548 nm, respectively.

Figure 4.17 represents the normalized parameter  $\chi^{(3)}/g_0$  issued from the various measurements versus pump-probe frequency detuning for different pump wavelengths. For weak frequency detuning, the curves for  $\chi^{(3)}/g_0$  are almost superposed for all wavelengths. For larger detuning the up- versus down-converted symmetry is lost while the three curves starts diverging one from the other. The asymmetry is larger for shorter wavelength, due to the lower  $\alpha_H$ -factor as previously discussed.

### 2.3. Influence of the pump linewidth

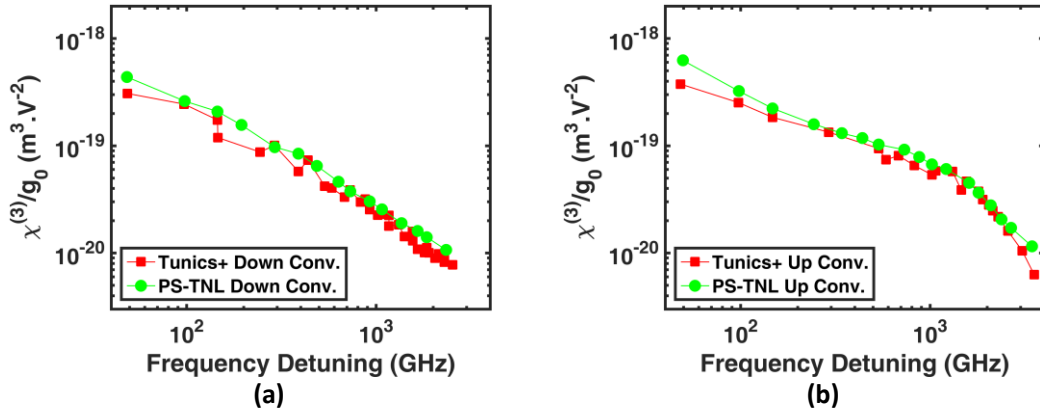
In order to assess the influence of the pump linewidth on the conversion efficiency, we compare experiments done with two pump lasers; the former is a 150 KHz Tunics Plus external cavity laser and the second a 1-kHz Teraxion PS-TNL ultra-narrow linewidth tunable laser. All other experimental conditions are unchanged.

Figure 4.18 (a) and (b) compare the down- and up-conversion obtained with the both pump lasers. For low frequency detuning, the interaction between the pump and the probe is larger using the Teraxion, hence the extracted values of the CE are more sensitive to the phase and intensity noises. Measurements exhibit a 4 dB stronger conversion for the narrow linewidth laser at low detuning. Conversely, in the THz range, the pump-probe interaction becomes weaker and the low noise level of the pump is less beneficial, hence the CE curves are almost superposed.



**Figure 4.18.** The measured CE as a function of the pump-probe frequency detuning for down-conversion (a) and up-conversion (b) for the two TL1 under study.

Figure 4.19 compares the extracted  $\chi^{(3)}/g_0$  by using both pump lasers, the profile is similar than that of CE. This can be attributed to the fact that for the same amount of injecting power from TL1, due to the narrower linewidth, the peak power of Teraxion is higher than the Tunics Plus, therefore the amplitude of excited  $\chi^{(3)}/g_0$  is higher, as well as the CE.



**Figure 4.19.**  $\chi^{(3)}/g_0$  as a function of the pump-probe frequency detuning for the two TL1 under study.

With a larger pump linewidth, the linewidth of the converted signal will be broadened, even if the probe stays constant [283]. To this end, a narrower pump is crucial for the dynamical conversion of modulated signal, more particularly for advanced modulation such as PSK or QAM, in order to avoid the introduction of additional noises.



## 2.4. Influence of the nanostructure aspect

In this section, we move to studying the influence of the nanostructure shape in the slave FP laser active region. The investigation considers two InAs/InP FP lasers, consisting respectively of a QD structure (PFP2) and a QDash structure (PFP3) both provided by TUB. Both devices are grown by metal-organic vapor phase epitaxy (MOVPE) on n-type InP(001) substrate, different from the QD laser PFP1 presented previously. The active region consists of 7 stacked nanostructure layers in an  $\text{In}_{0.78}\text{Ga}_{0.22}\text{As}_{0.47}\text{P}_{0.53}$  matrix. The dot size is 20 nm for the former, and the dash size of the latter is  $20 \text{ nm} \times 60 \text{ nm}$ , smaller than the dots in PFP1. The structure is enclosed in an  $\text{In}_{0.82}\text{Ga}_{0.18}\text{As}_{0.40}\text{P}_{0.60}$  heterostructure forming an optical slab waveguide. Finally, lateral optical confinement is obtained by deep etching through the active region and regrowth of p/n-blocking. Contact layers are added [285]. The PFP2 and PFP3 cavity lengths are 1.26 mm and 1.49 mm respectively; both ridges are  $1 \mu\text{m}$  wide; the lasing threshold at 293 K is 20 mA for PFD2 and 24mA for PFD3; the center wavelength 1520 nm and 1560 nm. The LIV characteristics and the optical spectrum measured at  $2.5 \times I_{th}$  are presented in Figure 4.20.

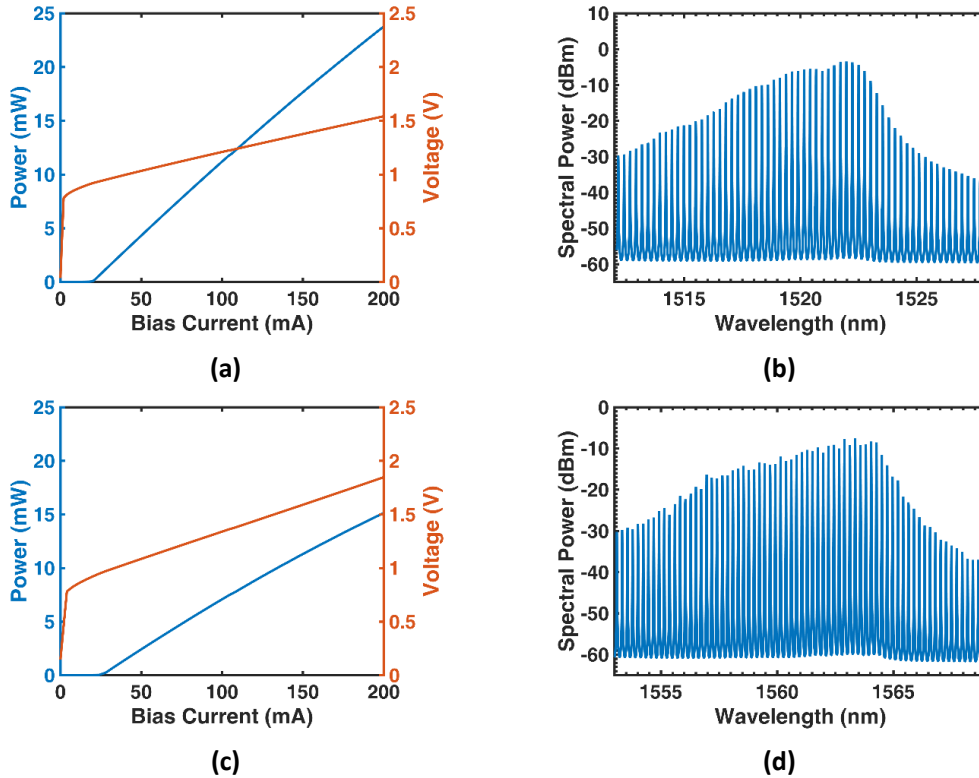


**Figure 4.20** The LIV characteristics of the (a) QD FP laser PFP2 and (c) QDash FP laser PFP3; the optical spectrum of (b) PFP2 and (d) PFP3 is measured at  $2.5 \times I_{th}$ .

As illustrated in Figure 4.21 (a), the net modal gain spectra for both devices experiences

a blue shift with increasing current below the threshold. The asymmetry in the net gain profile can be attributed to the decreasing population of higher energy levels (shorter wavelength) due to carrier thermalization. Spectral widening at shorter wavelength is more pronounced for QDash material as a result of a higher number of active states located at the tails of QDash DOS function [286]. From ASE measurements, it is clear that QDash gain saturates at lower currents as compared to QD laser; this can be attributed to a stronger carrier coupling between states within dash and the WL. The net gain is found higher in the QD laser as a result of a higher degree of population inversion due to lower number of active states, as well as the smaller inhomogeneous broadening (around 40 nm at 20 mA) than QDash laser PFP3 (around 23 nm at 20 mA). The wavelength dependant  $\alpha_H$ -factor for both lasers is plotted in Figure 4.21 (b). At the gain peak, the values of  $\alpha_H$ -factor for both lasers PFP2 and PFP3 are 4.4 and 5.2 respectively, thus a larger asymmetry in the conversion profile is expected.

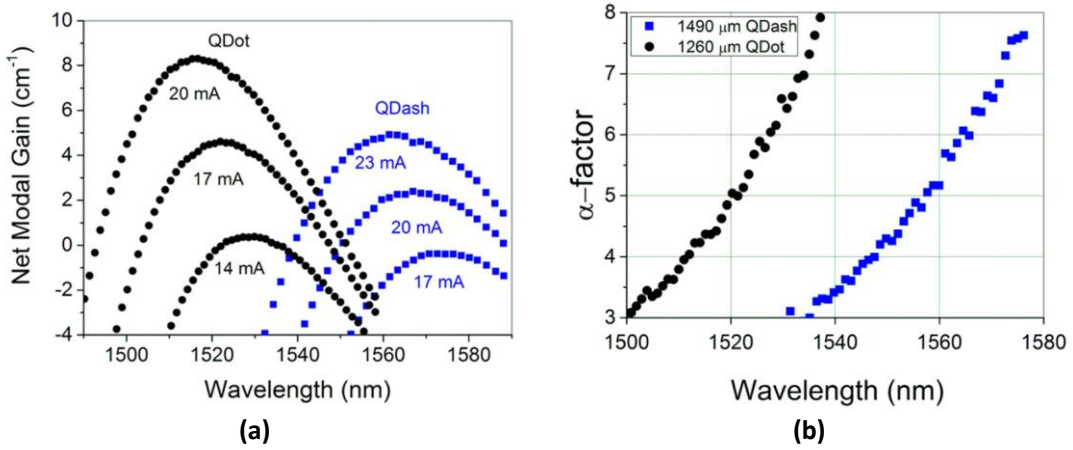


**Figure 4.21** (a) Net gain and (b)  $\alpha_H$ -factor spectral dependence for both QD FP laser PFP2 and QDash FP laser PFP3.

The NCE is measured using the setup represented in Figure 4.9, under the same conditions as for PFP1. The results are represented in Figure 4.22. For QD laser, the CE corresponding to the maximum NCE point is around -27 dB, while it is -10 dB for the QDash one.

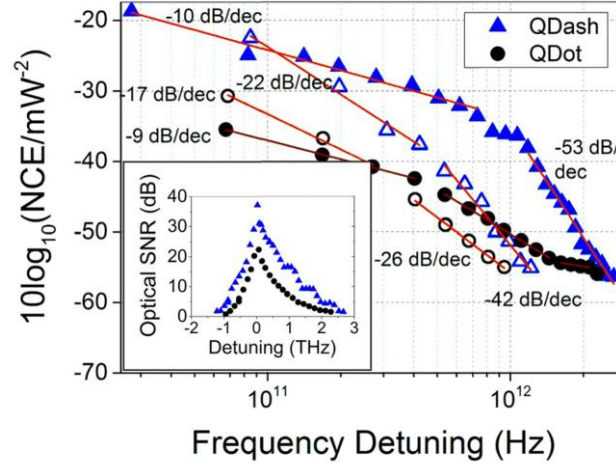


**Figure 4.22** NCE of QD PFP2 and QDash PFP3 measured using the same setup and experimental conditions as for PFP1. The inset represents the corresponding OSNR.

The maximum NCE of -18.6 dB, measured for the QDash laser PFP3 is 12 dB larger than that of the QD laser PFP2 (and 7 dB larger than QD laser PFP1). The QDash device also demonstrates efficient FWM conversion for a broader frequency detuning ranging from -1.2 to 2.7 THz. On the other hand, a similar asymmetry comparable to that observed in PFP1 arises in both devices, [287]. For detunings larger than 400 GHz the largest discrepancy between up- and down-conversion observed for PFP3 is 10 dB and 5 dB for PFP2. Comparing the NCE of PFP2 and PFP3, we note that both amplitude and bandwidth are larger in PFP3, which may be explained by the difference the shape of the nanostructures [147]. The dashes have more resemblance to QWire structures, hence the contributions from CDP and CH are higher, as well as that of TPA, owing from the smaller quantum confinement.

Qualitatively, the NCE illustrated in Figure 4.22 can be separated into two regions with two different decay rates below and above 1 THz detuning. This is very close to what has been measured on QDash SOA [288] showing three regions. The first region with picoseconds characteristic time-scale [289] is driven the CDP process with additional contribution from the TPA mechanism. The rapid decrease of the curve above 1 THz correspond to the frequency roll-off of the CDP effect which first becomes comparable and then lower than the CH and the SHB [290]. The general behavior of the QD laser PFP2 is similar but the NCE is found smaller because of a lower CDP and TPA contributions due to a lower number of active states and a reduced  $\alpha_H$ -factor. This difference between QDash and QD lasers may be attributed to the

following features.

- 1) The QDash higher energy levels that are submerged into the continuum level of the surrounding bulk material may be an significant impact. Conversely, QD DOS function is known to restrain the coupling of carriers between spatially isolated QDs and the surrounding material with large energy spacing.
- 2) The gain clamping level is lower in QDash lasers as shown in Figure 4.21 (a), carriers are captured from the WL into the numerous states of dashes DOS function. They may contribute to different parts of the gain spectrum through inter-dash/intra-dash scattering process or non-radiative recombinations, leading to the WL carrier population change in both scenarios.
- 3) TPA may be also a major contribution: in [291] TPA was found to stimulate ultra-fast gain recovery in QDash SOA below and above pump energy. While in QD case, the contribution from TPA is slowed down by the phonon bottleneck discussed in chapter II. The flattening of on the NCE profile around 1 THz detuning in QDash devices may witness this phenomenon. Therefore, the wire-like nature of QDash DOS can provide additional gain that leads to higher NCE.
- 4) The sensitivity to the optical polarization of the nanostructures is another potential feature. Depending on the structure orientation and the epitaxy processing, the isotropy of the dashes and the dots can be modified, hence affecting the gain and the NCE amplitude [292], [293].

Overall, the conversion efficiency for QD devices is very low and nearly equal for large positive detunings  $\Delta f > 2$  THz ( $\sim 15$  nm) and negative detunings  $\Delta f > -1$  THz ( $\sim 8$  nm). This indicates that pump-probe wave detuning reaches the edge board of the gain profile (see in Figure 4.21 (a)), and the gain is reduced in this region compare to the gain peak, thus NCE demonstrates rapid decay rate of 21 dB/decade, whereas NCE in the QD laser rolls off at 53 dB/decade.

The nomalized  $\chi^{(3)}/g_0$  parameter is calculated from Eq. 4.19 and found to decrease from  $1.0 \times 10^{-18} \text{ m}^3/\text{V}^3$  down to  $1.2 \times 10^{-22} \text{ m}^3/\text{V}^3$  in the 27 GHz to 2.66 THz detuning range for QDash lasers and from  $2.2 \times 10^{-19} \text{ m}^3/\text{V}^3$  to  $1.2 \times 10^{-20} \text{ m}^3/\text{V}^3$  in the detuning range from 86 GHz to 2.27

THz for QD lasers. The  $\chi^{(3)}/g_0$  value of the QDash laser is larger than the one measured for DFB lasers from ref. [264] and references therein.

### 3. Nonlinear conversion with InAs/GaAs QD lasers

In this section, the NDFWM is performed using different InAs/GaAs QD FP lasers presented in Chapter III. Since the InAs/GaAs QD are compatible with silicon wafer [24], these results can be useful for optical signal processing in silicon PICs.

#### 3.1. Impact of the ridge waveguide width on CE

Experimental Condition	Preset Level of GaFP3	Preset Level of GaFP4
Experiment Temperature	20 °C	20 °C
QD FP Bias Current	$2.4 \times I_{th}$ (70 mA)	$2.4 \times I_{th}$ (87 mA)
QD FP Output Power Pout	3.4 mW	6.2 mW
Injection Angle	Collinear (0°)	Collinear (0°)
TL1	Yenista T100S-HP	Yenista T100S-HP
TL2	Yenista T100 (1310 nm)	Yenista T100 (1310 nm)
Master Injection Ratio	1 dB (4.2 mW)	1 dB (7.9 mW)
Master-Slave Detuning	-6 GHz	-6 GHz
Probe Injection Ratio	-6.3 dB (0.8 mW)	-6.3 dB (1.5 mW)

**Table 4.4.** Experimental conditions used in InAs/GaAs QD FP laser GaFP3 and GaFP4.

Two GaAs-based QD FP lasers, GaFP3 and GaFP4, with different ridge waveguide (RWG) widths are investigated. Both lasers have the same cavity length of 1.5 mm, though the ridge width of GaFP4 is larger (4  $\mu\text{m}$ ) than GaFP3 (2  $\mu\text{m}$ ). The LIV characteristics and the optical spectra for both devices can be found in chapter III. Table 4.4 summarizes the experimental conditions of the experiments performed. They use the same setup from Figure 4.9. The injected power from TL1 (Yenista T100S-HP) is fixed 1 dB above the free-running power of the FP lasers. The injected power from TL2 (Yenista T100) is then chosen 6.3 dB below the free-running FP laser power.

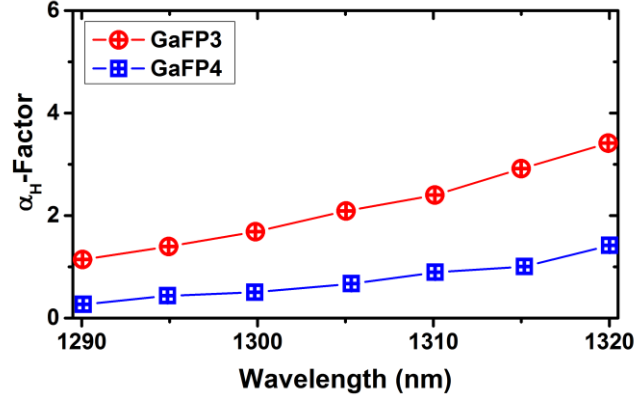


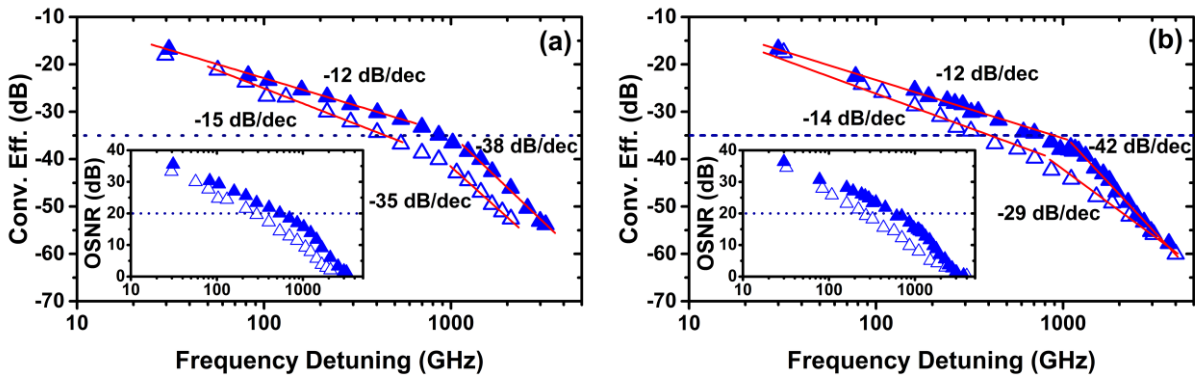
**Figure 4.23.** The  $\alpha_H$ -factor spectral dependence for QD lasers GaFP3 and GaFP4 measured by the ASE method. The gain peaks are around 1309 nm for both lasers.

The  $\alpha_H$ -factor measured by the ASE method is represented in Figure 4.23. At the gain peak, the  $\alpha_H$ -factor is about 2.5 for GaFP3, higher than GaFP4 ( $\sim 0.9$ ). On the basis of the previous analysis, a symmetric CE profile can be expected for GaFP4.

Figure 4.24 (a) depicts the measured CE and OSNR for QD laser GaFP3 as a function of the absolute value of the detuning  $\Delta f$ . Two regions can be distinguished for both up- and down-conversions. For detuning below 1 THz, CE decreases with respect to detuning with a rate of -15 dB/decade for down-conversion and -12 dB/decade for up-conversion, where CDP pulsation is the dominant effect. The second region exhibits a decreasing rate of -35 dB/decade for down-conversion and -38 dB/decade for up-conversion, where SHB is the dominant process with sub-picosecond timescales. A rather good symmetry between the up- and down-conversion characteristics can be observed. This can be interpreted by the low asymmetry in the gain profile as well as the small  $\alpha_H$ -factor meaning that the dominant processes, i.e. the CDP and SHB, are almost in phase and interfere constructively. It also tends to prove that the photon energy from the lasing frequency is relatively close to the resonant dot population GS energy within the inhomogeneous broadening, given that little carrier-induced change in refractive index is expected near the resonance.

Conversion efficiency of -16 dB is observed for  $\Delta f < 100$  GHz. The CE is then always maintained above -35 dB for down-conversion within frequency detunings up to 400 GHz, and up to 900 GHz for up-conversion. For  $\Delta f > 1$  THz the SHB dominates, and while the interaction is weaker the conversion greatly expands over a large bandwidth of up to 2.1 THz

for down-conversion and 3.2 THz for up-conversion. In addition, the OSNR measurements shown in the inset of Figure 4.24 (a) proves that spontaneous emission, which is further compressed under OIL, maintains the signal-to-noise ratios above 20 dB over a wide bandwidth. As a minimum of pump power is required to have a stable locking of the laser, the best results for both the amplitude and the conversion bandwidth are obtained with a 1-dB injection strength. Further increase of the pump power induces a slight decrease of the CE of about 4 dB at 30 GHz and 2 dB at 1 THz that can be attributed to reduction of the gain with optical injection [294].



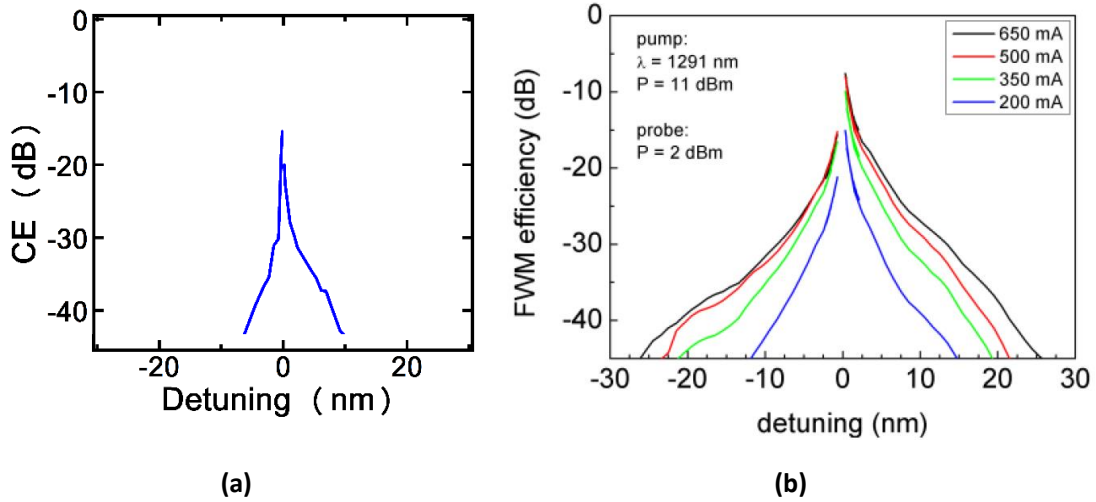
**Figure 4.24** The measured CE as a function of the pump-probe frequency detuning for QD lasers (a) GaFP3 and (b) GaFP4 under  $2.4 \times I_{th}$  and 1 dB pump injection strength. Filled (resp. empty) triangles represent up (resp. down) conversion. The figures in inset show the corresponding OSNR of QD lasers GaFP3 and GaFP4.

Figure 4.24 (b) presents the CE and the OSNR measured with QD laser GaFP4. The behavior below 1 THz is very similar to that of GaFP3, with a maximum CE of -16 dB and similar slopes for both up- and down-conversion. Above 1 THz, the slopes of up- and down-conversion differ from those measured for GaFP3, and wavelength conversion above 4 THz is now observed for both up- and down-conversion, larger than the laser GaFP3.

Finally, the inset of Figure 4.24 (b) depicts an OSNR ranging from 40 dB to 0 dB, similar to the one obtained with GaFP3. The enhanced conversion bandwidth may be attributed to the wider ridge, which further enhances optical nonlinearities owing to a better overlap of the QD plane with the optical mode. Figure 4.24 (b) shows that the up- and down-conversion are more symmetrical than in the case of GaFP3. Such symmetrical response is consistent with the very low  $\alpha_H$ -factor measured on GaFP4. Let us note that, owing to the large number of QD

stacks and the high concentration of nanostructures in the active region of GaFP3 and GaFP4, a large bandwidth is unveiled with a rather large efficiency.

Comparing the results from GaFP3 with a SOA having a similar active regions, we found that the OIL configuration allows reaching similar conversion bandwidths but with much lower bias currents and shorter interaction lengths [114]. As illustrated in Figure 4.25, the maximum for the amplitude conversion reaches for both devices about -16 dB. However, for such achievement, the SOA was pumped at 200 mA with a pump power of 11 dBm while the slave laser only operates at  $2.4 \times I_{th}$  and the master laser power is kept below 6.2 dBm. With further increase of the pump, the SOA is able to reach higher and wider CE profile (up to -8 dB and 4.4 THz at 650 mA), but at the price of a much larger energy consumption.



**Figure 4.25** (a) CE as a function of the pump-probe wavelength detuning; (b) CE within an SOA made with the same material, after [114].

### 3.2. Impact of the cavity length

The influence of the cavity length is also studied, and for such purpose, we used the laser GaFP5 with a 2 mm long cavity to compare with GaFP3, which is 1.5 mm long. The ridge width  $W_{RWG}$  is 2  $\mu\text{m}$  for both structures.

Figure 4.26 represents the extracted CE and OSNR profiles. Qualitatively, the improvements from the longer cavity are not that significant ( $< 1$  dB), either in the CE or in the OSNR. Although in practice, a longer interaction length is always better to enhance the conversion, these results point out that it is not necessarily the case for an optically-injected



QD laser where the compression of the ASE from the injected field plays a dominant role.

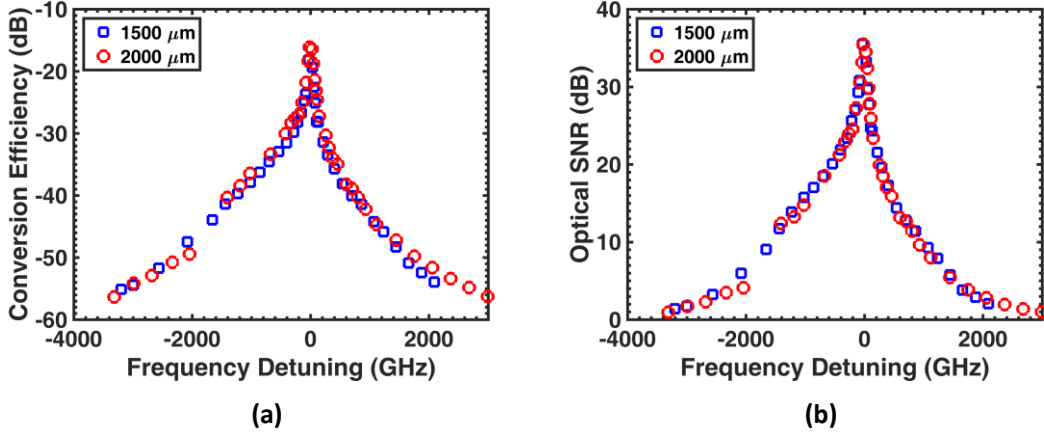


**Figure 4.26.** (a) CE and (b) OSNR in QD laser GaFP5 (2 mm) and QD laser GaFP3 (1.5 mm).

### 3.3. Influence of the laser bias conditions

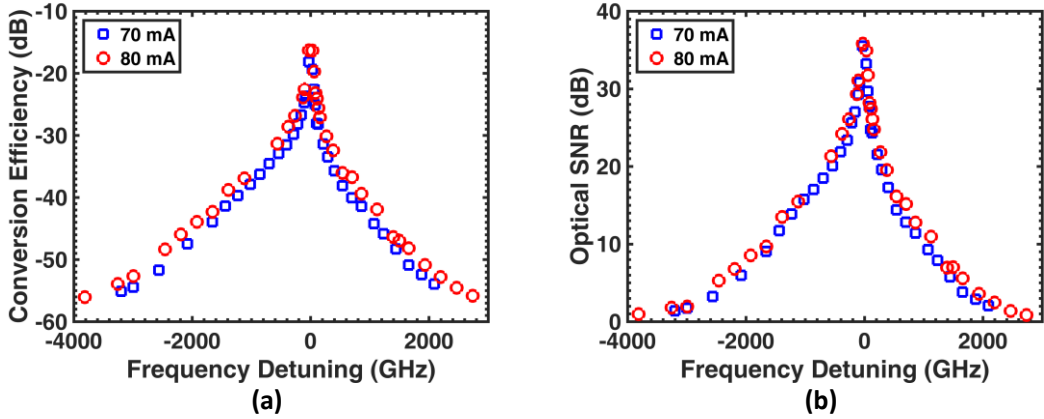


**Figure 4.27.** (a) CE and (b) OSNR in the 1.5 mm  $\times$  2  $\mu\text{m}$  QD GaFP3 laser at two different bias currents.

According to Eq. 4.19, the amplitude of  $\chi^{(3)}$  is related to the gain, thus at higher bias, a larger  $\chi^{(3)}$  can be expected, leading to higher conversion performance. Therefore, in this subsection, an increase of the bias current, from  $2.4 \times I_{\text{th}}$  to  $2.7 \times I_{\text{th}}$  (from 70 mA to 80 mA) is performed in QD laser GaFP3. The corresponding CE and OSNR profiles are represented in Figure 4.27 (a) and (b). As observed, the slight increase of the bias level enhances both the magnitude and the conversion bandwidth of the CE by about 2 dB and up to 4 THz respectively. These improvements are related to the carrier injection increase, which accelerates the capture and relaxation into the dots. In addition, results also show that the OSNR is slightly

enhanced hence demonstrating that higher bias currents lead to better conversion performance owing to a faster carrier-carrier scattering.

### 3.4. Influence of the injection-locking conditions

From Eq. 4.12, the CE is directly related to the pump power meaning that, the master-slave injection conditions should be considered for the optimization of the conversion performance. Results obtained on QD laser GaFP3 are depicted in Figure 4.31. Both the injection strength and frequency detuning are locally tuned within the stable-locking range (blue arrows). Let us stress out that such variations differ from those studied in section III. 2.2, where the pump wavelength only was tuned regarding the gain peak, however, as schematically illustrated in Figure 4.29, the operating condition within the locking map was kept unchanged (red dot).

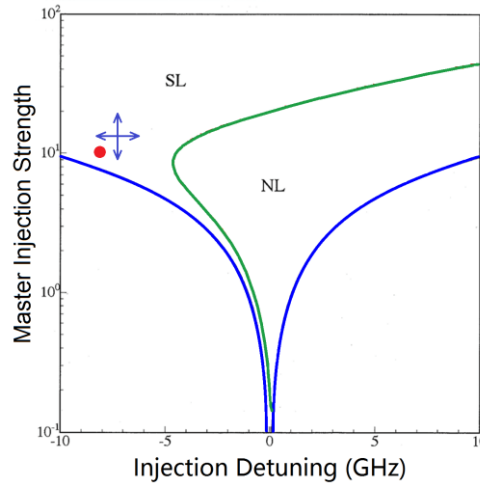


**Figure 4.28.** Schematic of injection-locking map, red dot marks the same injection conditions for the three pump wavelengths used in section III.2.2, and the blue arrows indicate the local tuning of the injection conditions with respect to the stable-locking (SL) area.

According to Eq. 4.12, the CE is related to the pump field intensity, higher pump power will normally offer higher conversion. However, this is not always the case when external optical injection is activated. As shown in Figure 4.29 (a), the increase of the pump injection power reduces the entire CE profile for down- and up-conversion down by 3 dB. This can be attributed to reduction of the gain with the optical injection level (see Eq. 4.25). Indeed, a minimum amount of pump power is required to obtain a stable locking of the slave laser while

the probe is injected into the active region. As a consequence, there is a tradeoff on the pump power: once the laser is locked at an optimal master injection ratio, further increase of the injected power does improve neither the amplitude of the conversion nor the OSNR as shown in Figure 4.29 (a) and (b).

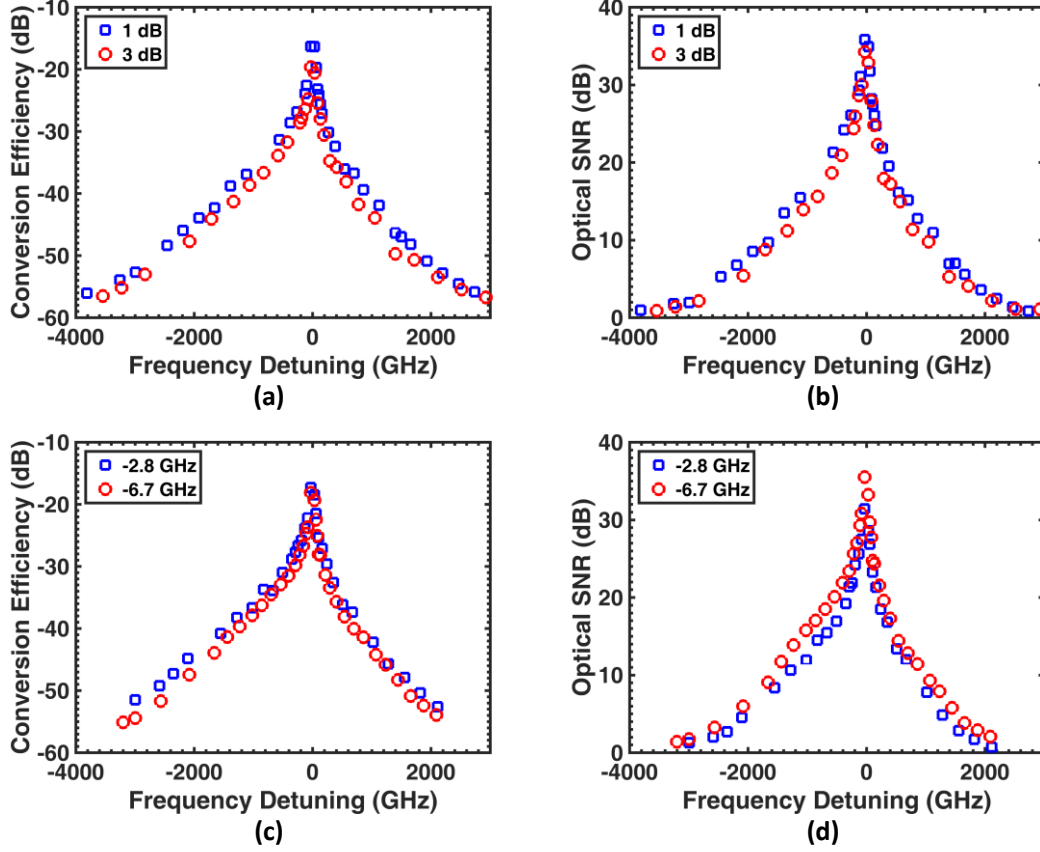


**Figure 4.29.** (a) CE and (b) OSNR in QD laser GaFP3 at two different pump injection ratios; (c) CE and (d) OSNR in GaFP3 at two different pump master-slave injection detunings.

Figure 4.29 (c) displays the effect of the frequency detuning. A -6.7 GHz frequency detuning between the master and the slave reduces the CE by about 1 dB with respect to a smaller detuning of -2.8 GHz. Figure 4.30 gives the injection locking spectra of the laser for these two conditions. Clearly, at lower injection frequency detuning, the peak power of the locked-pump is higher, while the side-modes get higher hence leading to a 5 dB reduction in OSNR (Figure 4.29 (d)). Such a difference can be explained from the gain reduction induced by the frequency detuning that leads to a change in the carrier density (see Eq. 4.25). Therefore, the decrease of the master laser injection detuning shifts the lasing mode towards the cavity resonance, hence reducing the gain through modification of the phase of the laser field. These

results indicate that an optimum condition exists regarding the injection frequency detuning, where improvements in both the CE and the OSNR can be obtained simultaneously.

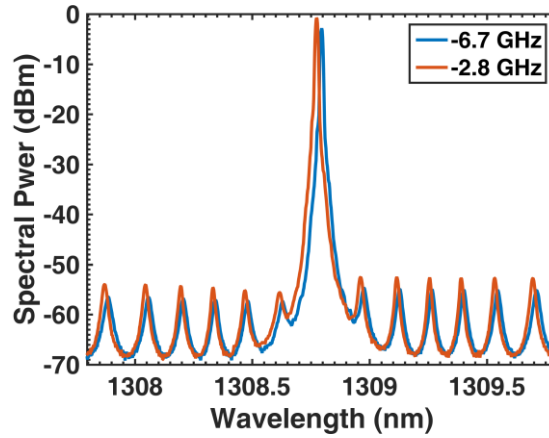


**Figure 4.30.** Pump optical spectra at different injection frequency detunings.

## 4. Summary

From the above results, it is possible to list the key-parameters that can be used for rising manufacturing guidelines regarding future photonics wavelength converters. All results summarized below include the main parameters and quickly recall how they influence the magnitude or the bandwidth of the static conversion.

### (1) Material parameters

#### a. Nanostructures

Efficient conversion efficiency does require a sufficient number of QD/QDash layers ( $> 5$ ) in the active area with a high density ( $> 5 \times 10^{10} \text{ cm}^{-2}$ ). The shape of the nanostructures also influences the gain dynamics. Smaller nanostructures can increase the SHB contribution while larger ones provide higher carrier population, which lead to additional CH and TPA contributions. QDash nanostructures demonstrate better FWM performances than QDs mostly because the corresponding DOS function has no energy tail in the latter, so homogeneous broadening occurs only between GSs leading to smaller carrier coupling probability. Table 4.5 summarizes the maximum CE and bandwidth for the different InP-based nanostructures. Let us note that the 50 nm dots were not grown from the same technology than the other two, hence the results from laser (PFP1) is used as a qualitative reference. On

the other hand, the 20 nm dots and 20 nm × 60 nm dashes were all grown by MBE, i.e. the clear difference between them demonstrates the importance of the nanostructure shape in the optimization of conversion performance.

	Parameters	Max. CE (dB)	Bandwidth (THz)
<b>Nanostructure</b>	~50 nm dots	-5	6.2
	~20 nm dots	-27	3.5
	20 nm × 60 nm dashes	-10	4

**Table 4.5.** Impact of the type of nanostructures on the conversion performance (results from InP-based nanostructures).

#### b. Linewidth broadening factor ( $\alpha_H$ -factor)

The asymmetry in the nonlinear conversion with respect to the pump wavelength arises from the difference in the arguments of the complex susceptibility associated with the CDP and the SHB. To this end, a low linewidth broadening factor ( $<2$ ) is better. As indicated in Table 4.6, the asymmetry between up- and down-conversion decreases with the value of  $\alpha_H$ -factor. Finally, a narrow inhomogeneous gain broadening ( $<50$  meV) i.e. a smaller QD size dispersion, favors to reduce the  $\alpha_H$ -factor, hence improving the contribution of the resonant dot populations.

	Parameters	Max. CE (dB)	Bandwidth (THz)	Max. asymmetry
<b><math>\alpha_H</math>-factor</b>	1.25	-6	4.5	5 dB
	1.4	-5	6.2	9 dB
	1.53	-7	5.5	13 dB

**Table 4.6.** Impact of the  $\alpha_H$ -factor on the conversion performance (results from InP-based QD).

#### c. Cavity dimension

The slave laser geometry influences the conversion efficiency, meaning that a trade-off should be considered between the interaction length (ranging from 1 to 2 mm) and the ridge width  $W_{RWG}$  (ranging from 2 to 4  $\mu\text{m}$ ) with the device compactness. The overlap of the QD plane with the optical mode and the QD surface occupancy make the absorption coefficient of the QD plane strongly dependent on  $W_{RWG}$ . For instance, by comparing the results from the GaAs-based QD lasers, Table 4.7 points out that a wider  $W_{RWG}$  can improve the conversion bandwidth whereas the length has

a little effect.

Parameters		Max. CE (dB)	Bandwidth (THz)
Cavity dimension	1.5 mm $\times$ 2 $\mu$ m	-16	5.6
	1.5 mm $\times$ 4 $\mu$ m	-16	8
	2 mm $\times$ 2 $\mu$ m	-15	6.5

**Table 4.7.** Impact of the cavity dimensions on the conversion performance (results from GaAs-based nanostructures).

## (2) External conditions

### a. Bias current

Higher bias current hence larger carrier density available in the barrier is preferred since it accelerates the carrier-carrier scattering into the nanostructures. Consequently, both the magnitude and the bandwidth are improved, as shown in Table 4.8.

Parameters		Max. CE (dB)	Bandwidth (THz)
Bias current	$2.5 \times I_{th}$	-16	5.6
	$2.9 \times I_{th}$	-14	7

**Table 4.8.** Impact of the bias current on the conversion performance (results from GaAs-based nanostructures).

### b. Injection-locking conditions

The slave laser must be locked within the stable-locking area. Thus the injection strength and the injection detuning must be carefully considered. A tradeoff between the injected pump power and the injection frequency detuning exists as these two parameters alter the amplitude of the conversion through gain reduction, as indicated by Table 4.9 and 4.11.

Parameters		Max. CE (dB)	Bandwidth (THz)
Master laser injection strength	1 dB	-16	5.6
	3 dB	-20	5.6

**Table 4.9.** Impact of the injection strength on the conversion performance (results from GaAs-based nanostructures).

Parameters		Max. CE (dB)	Bandwidth (THz)
Master laser injection	-2.8 GHz	-15	5.6

<b>detuning</b>	-6.7 GHz	-16	5.6
-----------------	----------	-----	-----

**Table 4.10.** Impact of the injection frequency detuning on the conversion performance (results from GaAs-based nanostructures).

A master with a narrow linewidth (<500 kHz) is better to further reduce the phase noise.

Table 4.11 shows that a narrow linewidth enhances the magnitude of the conversion.

Parameters		Max. CE (dB)	Bandwidth (THz)
<b>Master laser linewidth</b>	150 kHz	-5	6.2
	1 kHz	0	6.2

**Table 4.11.** Impact of the pump linewidth on the conversion performance (results from InP-based nanostructures).

## IV. Dynamic conversion

This section aims to experimentally demonstrate the conversion of a modulated signal through a laser cavity by NDFWM. Because the available high frequency modulators and receivers are in the C-Band (1535 – 1560 nm), we chose the InP-based QD laser PFP1 as the converter, which also offers the largest CE as previously presented.

### 1. Experimental setup

Figure 4.31 depicts the experimental setup for the investigation of the dynamical conversion. Compare to Figure 4.9, a Mach-Zehnder modulator with a 20 GHz modulation bandwidth is inserted at the output of TL2 to modulate the probe signal. The input modulation is 2.5 Gbps pseudo-random bit sequence (PRBS) with a length of  $2^7-1$ , generated by the pulse-pattern generator (PPG). The pump-probe injection detuning is fixed at 100 GHz in up-conversion. At the output 3 of the circulator, the converted signal is filtered out by a narrow band-pass filter (TBPF) and transmitted through a 25-km single mode fiber (SMF) coil. Afterwards, the signal is sent to the oscilloscope (Osc.) for eye diagram analysis or to the error detector for bit error rate (BER) detector. The trigger for both PPG and oscilloscope/BER detector is provided by a frequency synthesizer. Other experimental conditions are remained as the same than in Table 4.2.

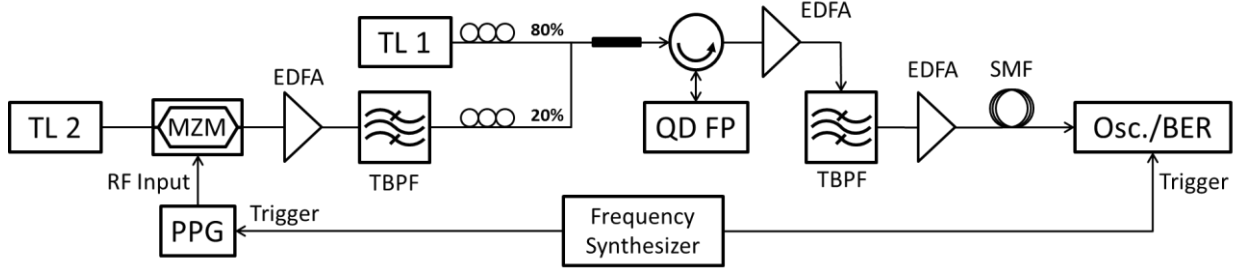


**Figure 4.31.** Schematic of the experimental setup dedicated for dynamical conversion. MZM: Mach-Zehnder modulator; PPG: pulse pattern generator; TBPF: thin band-pass filter; SMF: single mode fiber; EDFA: Erbium-doped fiber amplifier; Osc.: oscilloscope; BERT: bit error rate test.

## 2. Conversion optimization

In the first place, we considered the narrow linewidth tunable laser Teraxion as the master laser TL1 to reduce the linewidth of the converted signal. However, because the wavelength of this laser was not stable enough the conversion of the modulated signal is degraded, thus this laser is not considered in this section, although such instability does not affect the static conversion.

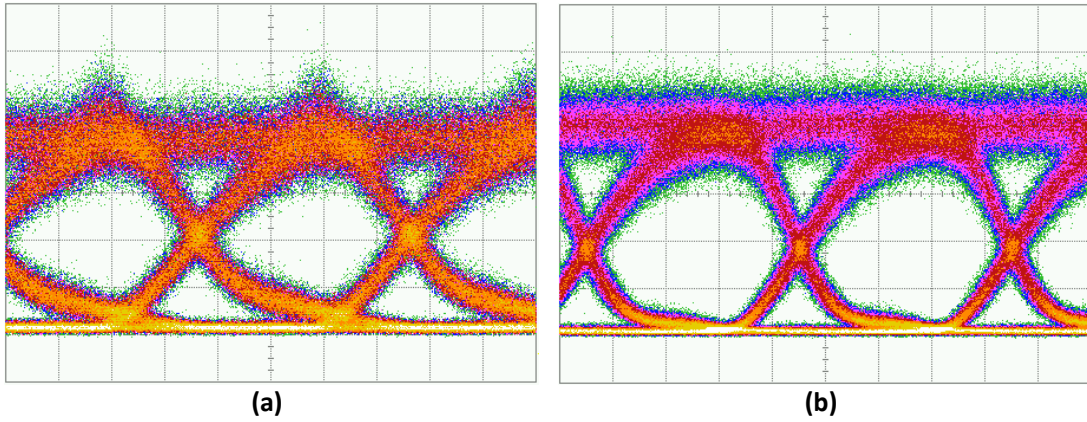


**Figure 4.32.** Back-to-back eye diagram of the converted signal with a modulation of 2.5 Gbps PRBS sequence of length of  $2^7-1$  by using (a) Yenista T100 (1550 nm) and (b) Tunics as the TL2.

Secondly, we considered using a narrow linewidth tunable laser TL2 to reduce the phase noise from the source, the chosen model is Nano-Tunics (different from the previously used tunable laser Anritsu Tunics Plus), this laser provides a remarkable wavelength stability and a narrow linewidth below 100 kHz. Figure 4.32 represents the eye diagram of the converted signal measured under back-to-back configuration (without fiber transmission) by using the



TL2 lasers Yenista T100 1550 nm (as in the setup in Figure 4.9) and the Nano-Tunics, with the same input power to the oscilloscope. It is very clear that, by using the new TL2, the eye is more symmetric and opened wider. In addition, in Figure 4.32, the probe conversion experienced the overshooting problem, i.e. the eye rises from the level of 1. Such issue is eliminated by using Nano-Tunics.

### 3. Conversion performance characterization

In this section, the measurement of BER is performed for the probe (before injecting into the FP laser), the converted signal in back-to-back and after 25 km fiber transmission. The BER curves of these three signals are plotted in Figure 4.33. The horizontal dotted black line corresponds the BER level of  $10^{-9}$ , which is conventionally referred as the error-free boundary. Comparing the curve of converted signal after its transmission to its back-to-back curve, the power penalty is only 0.5 dB, without arising error floor. These results indicate that the signal is not degraded by the fiber dispersion after the transmission. However, due to the limited sensitivity of the BER detector, the curves are cut off around  $10^{-11}$ .

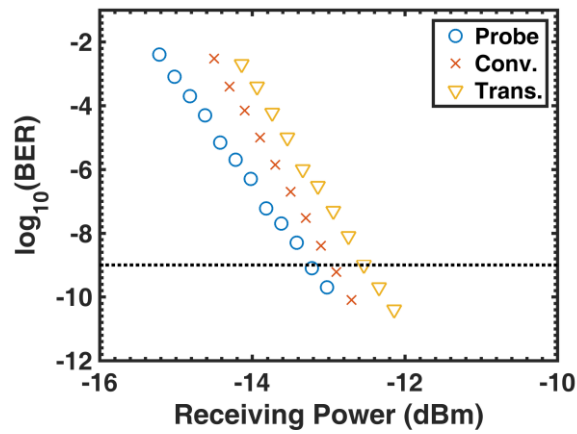


**Figure 4.33.** BER curves as a function of the receiving power by the detector for the probe before injection, the converted signal on back-to-back (Conv.) and after the transmission within 25 km SMF coil. The horizontal dotted black line corresponds to the conventional error-free boundary ( $\text{BER} = 10^{-9}$ ).

Let us stress out that, due to the limitation of the equipment such as the relatively high noise level of the frequency synthesizer, the non-packaged lens-end fiber coupling stage which is sensitive to the environmental vibration, we could not perform dynamic conversion with

higher modulation rates nor higher pump-probe detunings, however, the experiments have still demonstrated the potential of using injection-locked QD FP lasers to perform wavelength conversion of modulated signals.

## V. Conclusions

In this chapter, a systematical study of NDFWM is performed with injection-locked QD FP lasers. Experimental results have shown comparable CE level than that in similar SOA devices, with much lower pump/probe power and bias current [114], [117]. A list of important parameters related to the optimization of conversion amplitude and bandwidth is extracted. For instance, the amplitude of CE is enhanced with larger nanostructures and relatively wider active region, as well as higher bias current; a small  $\alpha_H$ -factor is crucial to decrease the asymmetry between the up- and down-conversion, taking advantages from reduced destructive interferences between the different arguments of the complex nonlinear susceptibility. In addition, the master injection conditions are also important on this stage, e.g. properly set master injection power at the optimum level can enhance the conversion efficiency, however, if the power is further increased, the conversion is decreased due to the reduced gain.

A demonstration of modulated signal conversion is also performed. At a pump-probe detuning at -100 GHz, the converted signal modulated at 2.5 Gbps has achieved an error-free transmission with a power penalty as low as 0.5 dB. Although these results may not be comparable with previous studies in the literature, this work has still unveiled the potential of using injection-locked FP lasers as optical wavelength converters.

## Chapter V. Delay dynamics in quantum dot Lasers

It is known that the dynamics of a semiconductor laser is modified by external optical feedback. Even under a feedback level in the percent range, the laser can become unstable hence exhibiting complex nonlinear dynamics like periodic or chaotic oscillations. While in the important case of high-speed transmissions, optical isolators are mandatory to prevent from any unstable operation, complex dynamics can also be used for chaotic secure communications or improved RF transmission links [202], [295], [296]. This chapter focuses on the first experimental investigations showing the impact of external optical feedback in QD lasers emitting on different lasing states.

### I. Introduction

#### 1. Principle of optical feedback

Conventional Optical Feedback (COF) is introduced into a laser diode by sending part of its emitted beam back to the laser cavity. As shown in Figure 5.1, optical feedback is performed by aligning a mirror on the beam's path. The distance of the laser to the mirror  $L_{ext}$  is related to the external round-trip time  $\tau_{ext}$  in the external cavity that is defined as:

$$\tau_{ext} = \frac{2n_{ext}L_{ext}}{c} \quad (5.1)$$

with  $n_{ext}$  the refractive index of the external cavity and  $c$  the celerity of light. In practical, the reflectivity of the reinjecting facet  $R'$  may not be zero, hence the returning light can be bounced onto multiple round-trips within the external cavity. Such a configuration can become an important issue in the case of short external cavities, as the beam's path is equivalently multiplied.

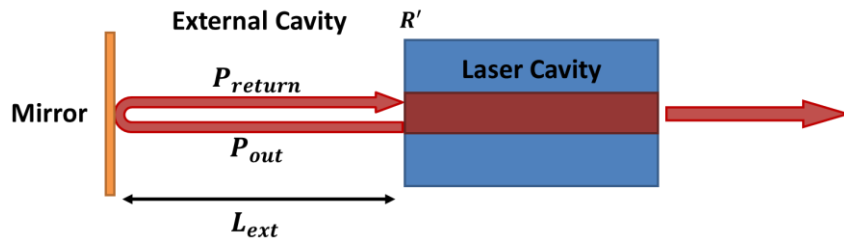


**Figure 5.1.** Schematic representing a semiconductor laser subjected to conventional optical feedback (COF).

The feedback strength is defined as the ratio between the output power ( $P_{out}$ ) from the laser facet subjected to the optical feedback to the returned power ( $P_{return}$ ) such as:

$$r_{ext} = \frac{P_{return}}{P_{out}} \quad (5.2)$$

In what follows, we will see that the feedback strength, the mirror reflectivity and the distance to the reflection point have a strong impact on the laser dynamics. While this work concentrates on COF, other architectures such as optoelectronics feedback [297], filtered optical feedback [298], phase-conjugated optical feedback [4] have been proposed over the last decades with the view to overcome the damped relaxation oscillations and therefore to generate more complex nonlinear dynamics. However, such configurations are out of the scope of the present thesis hence the reader is invited to consult Ref. [299] for further information.

## 2. Fundamentals of optical feedback

The optical feedback has been widely studied in semiconductor lasers since 70s [300]–[303]. The formalism of a diode laser operating under external optical feedback was originally proposed in 1980 by Lang and Kobayashi (LK) [304]. Later on, multiple research works have been published [305]–[313], most of them focused on the improvement of the LK model [265], [305], [307], [308], [310], [314]–[320]. Over time, various experiments were also conducted to further investigate the impact this phenomenon has on the semiconductor laser and the communication system [306], [307], [311], [321]. For instance, it was shown that, the spectral linewidth can be either narrowed or broadened depending on the feedback conditions [305], [307], [319]. Other investigations have revealed that strong mode-hopping effects can take place in presence of optical feedback [306], [310]. It was also proved that when the laser output exhibits a chaotic dynamic, the bit error rate is substantially affected [322].

As previously mentioned, the dominant parameters driving the laser's dynamics under optical feedback are the external delay time  $\tau_{ext}$  and the feedback strength  $r_{ext}$ . In 1986, Tkach *et al.* classified the different feedback regimes in a semiconductor distributed feedback (DFB) laser. As shown in Figure 5.2, five different regimes can be identified, the optical spectra

on the sides illustrate the laser dynamics of the lasing mode within the different regimes [309], [323].

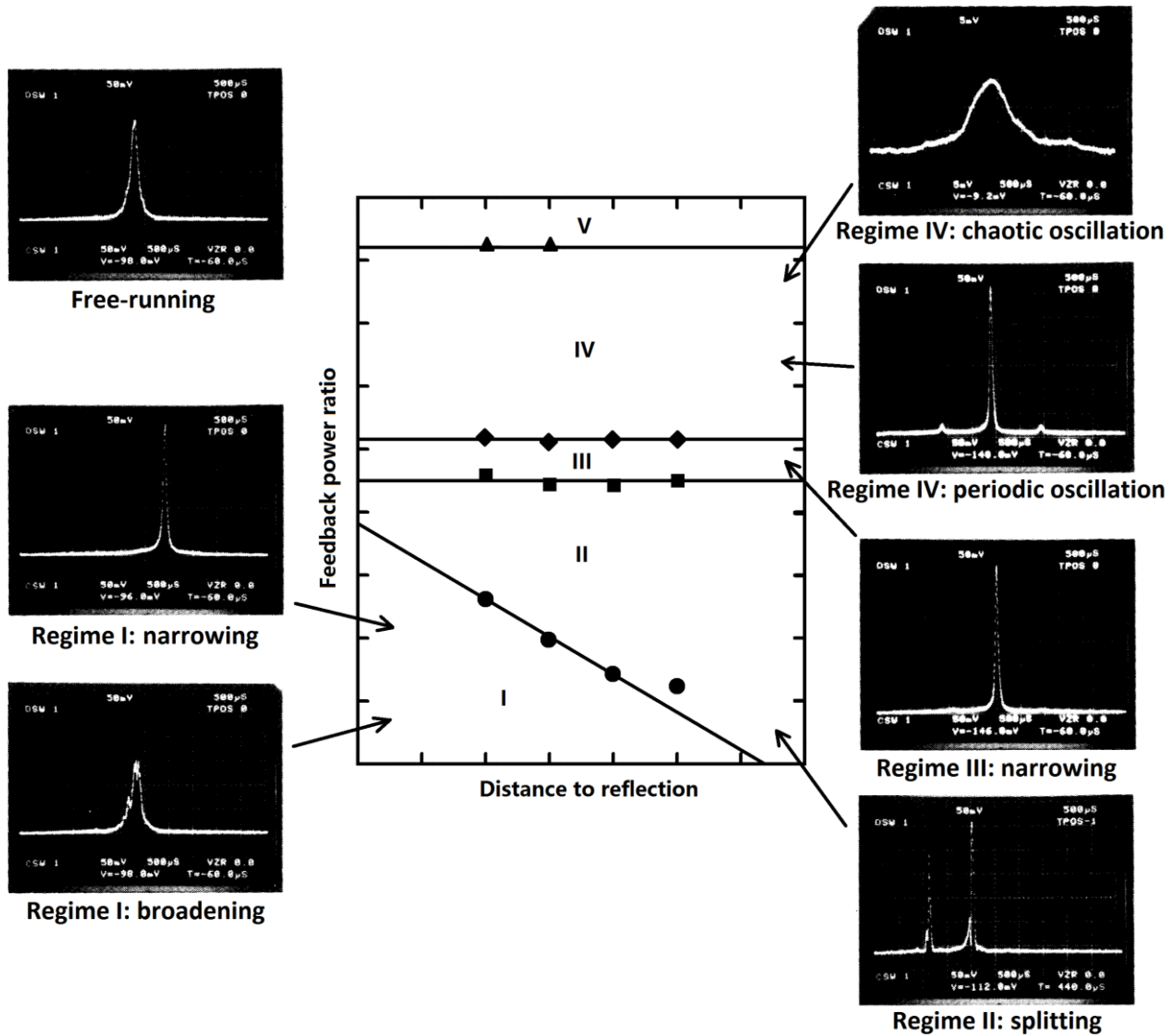


**Figure 5.2.** Feedback regimes in a semiconductor DFB laser (center), after Ref. [309]. The optical spectra on both sides illustrate the laser dynamics under optical feedback, after [323].

In regime I, which corresponds to the lowest level of feedback, depending on the feedback phase, the spectral linewidth can be either narrowed or broadened; in regime II, mode hopping arises between external cavity modes (ECM) induced by the feedback phase. ECM correspond to modes formed between the laser output facet and the external mirror with frequencies multiples of  $c/2n_{ext}L_{ext}$ ; in regime III, the laser experiences a restabilization and operates on the mode with the minimal linewidth. In this regime, the distance to the reflection point has no consequence on the laser dynamics. Figure 5.2 shows that when the laser

operation is tuned into regime III, the mode with the minimum linewidth can be solicited. This is exactly the condition encountered in chapter III when the spectral linewidth of an InAs/InP QD DFB laser was narrowed down to 100 kHz. In regime IV, the lasing linewidth is broadened with growing side-modes separated from the main modes by the ROF  $f_{RO}$ . The undamping of the relaxation oscillations, corresponding to periodic oscillations at  $f_{RO}$  (P1) is a precursor of the quasi-periodicity route to chaotic oscillations through the so-called coherence collapse regime [307]. This route to chaos is commonly observed in semiconductor lasers with optical feedback where two frequencies with incommensurable ratio namely the ROF and the external cavity frequencies interact with each other and result in the quasi-periodicity route to chaos as the feedback strength increases.

Although regime IV can strongly alter the performance of a high-speed communication system hence requiring the insertion of an optical isolator, it is also possible to take advantage of the deterministic chaos for developing secured communications, random bit generators and light detection and ranging (LIDAR) systems with improved resolutions [296], [324]. The onset of the regime IV also referred as the critical level  $r_{crit}$  can be estimated from [127]:

$$r_{crit} = \gamma^2 \frac{\tau_{int}^2}{16C_l^2} \frac{1+\alpha_H^2}{\alpha_H^4} \quad (5.3)$$

where  $\gamma$  is the damping factor,  $\tau_{int} = 2n_{int}L_c/c$  the internal round-trip time with  $n_{int}$  and  $L_c$  being the refractive index and the cavity length of the laser,  $C_l$  the coupling coefficient from the facet to the external cavity and  $\alpha_H$  the linewidth broadening factor (see chapter III). Eq. 5.3 indicates that the birth of instabilities is only linked to internal laser parameters. Compare to QW lasers, the relaxation oscillations of QD lasers are heavily damped, hence the critical feedback level is usually higher, making such transmitters more resistant to external perturbations. As an example, a value of  $r_{crit}$  of -8 dB was reported in a 1.5 mm long InAs/GaAs QD FP laser which is by far well beyond the typical level observed in QW lasers [127], [325], [326]. Owing to a  $\alpha_H$ -factor as low as 0.1, a high feedback resistance with a  $r_{crit}$  of -14 dB was also reported in an InAs/GaAs QD DFB laser. However, because the carrier variations in the off-resonant energy levels are strongly sensitive to the modulation (see chapter III) enhancing the  $\alpha_H$ -factor of the GS transition, experiments have also unveiled a dramatic

reduction of  $r_{crit}$  down to -30 dB under direct modulation [327].

Finally, the last regime is the extended cavity regime in which the laser is highly stable operating on a single narrow-linewidth longitudinal mode defined by the distance to the mirror. The system is similar to a short active medium within a very long cavity bounded by the laser back facet and the conventional mirror. This regime is very difficult to reach and requires an antireflection coating on the facet subjected to the feedback [328]–[330].

Last but not the least, although the cartography depicted in Figure 5.2 remains valid for all single-mode semiconductor lasers, it has been complemented, especially to describe some sub-regimes of the coherence collapse [331] or to address the short-cavity regime [318].

In the following, investigation of the optical feedback dynamics is performed with QD lasers emitting on different lasing states (GS and ES). In the view of a potential inclusion of such lasers into a fiber-pigtailed telecom module, single-mode DFB lasers are usually required. However, in what follows, to avoid any additional effect arising from the DFB grating, the response of the different lasing states to optical feedback is only analyzed on QD FP lasers. In particular, we will show that the ES QD laser which has displayed a near-zero  $\alpha_H$ -factor [137] exhibits richer optical feedback dynamics including a self-pulsating regime.

## II. Theoretical analysis of external optical feedback

### 1. Lang & Kobayashi equations

The dynamics of a semiconductor laser with optical feedback is investigated with the LK model [304]. Assuming a single round-trip in the external cavity, the complex electric field  $\tilde{E}(t)$  of a semiconductor laser in presence of optical feedback is described as [304]:

$$\frac{d\tilde{E}(t)}{dt} = \left\{ \frac{1}{2} (1 + i\alpha_H) \left[ \Gamma G_N(N(t) - N_{tr}) - \frac{1}{\tau_p} \right] + i\omega_0 \right\} \tilde{E}(t) + \kappa \tilde{E}(t - \tau_{ext}) \quad (5.4)$$

where  $\kappa$  is the feedback coefficient given by [332]:

$$\kappa = \frac{1}{\tau_{in}} 2C_l \sqrt{r_{ext}} \quad (5.5)$$

where the expression of  $C_l$  for a FP laser is given by [320]:

$$C_l = \frac{1-R_2}{2\sqrt{R_2}} \quad (5.6)$$

In case of a DFB laser, the expression of  $C_l$  is more complex such as [265]:

$$C_l = \frac{2(1-|\rho_l|^2) \exp(-i\varphi_l)(q_0^2 + \kappa_0^2)L^2}{i\kappa_0 L(1+\rho_l^2) - 2\rho_l q_0 L_c} \frac{1}{2qL - \sum_{k=l,r} (1-\rho_k^2)\kappa_0 L / [2iq_0 L \rho_k + \kappa_0 L(1+\rho_k^2)]} \quad (5.7)$$

In Eq. 5.7, the terms  $\rho_k = |\rho_k| \exp(i\varphi_k)$  with  $k = l, r$  are the complex reflectivities at the left and right facets respectively (with the right facet towards the external cavity),  $L_c$  is the laser cavity length,  $\kappa_0$  the coupling coefficient of the grating and  $q_0 = \alpha_{tot} + i\delta_0$  with  $\alpha_{tot}$  the total internal losses and  $\delta_0$  the deviation between the lasing and the Bragg wavenumbers.

The dynamics of the electric-field amplitude is much slower than the angular frequency  $\omega_0$  of the fast optical carrier. Assuming  $\tilde{E}(t) = \tilde{A}(t) \exp(i\omega_0 t)$ , where the term  $\exp(i\omega_0 t)$  corresponds to the fast lasing oscillations, and  $\tilde{A}(t)$  is the slow envelop of the complex electric field, Eq. 5.4 can be rewritten as:

$$\frac{d\tilde{A}(t)}{dt} = \frac{1}{2}(1 + i\alpha_H) \left[ \Gamma G_N(N(t) - N_{tr}) - \frac{1}{\tau_p} \right] \tilde{A}(t) + \kappa \tilde{A}(t - \tau_{ext}) \exp(-i\omega_0 \tau_{ext}) \quad (5.8)$$

Eq. 5.8 corresponds to the LK equation for a slow complex electric field after the elimination of the fast optical carrier component. Considering  $\tilde{A}(t) = A(t) \exp(i\Phi(t))$ , with  $A(t)$  and  $\Phi(t)$  being the amplitude and the phase of the field, the real and imaginary parts of Eq. 5.8 can be separated:

$$\begin{aligned} \frac{dA(t)}{dt} + i \frac{d\Phi(t)}{dt} A(t) &= \frac{1}{2} \Gamma G_N \left[ (N(t) - N_{tr}) - \frac{1}{\tau_p} \right] A(t) + \kappa A(t - \tau) \cos(\theta(t)) \\ &+ i \left\{ \frac{\alpha_H}{2} \Gamma G_N \left[ (N(t) - N_{tr}) - \frac{1}{\tau_p} \right] A(t) - \kappa \frac{A(t-\tau)}{A(t)} \sin(\theta(t)) \right\} \end{aligned} \quad (5.9)$$

with:

$$\frac{dA(t)}{dt} = \frac{1}{2} \Gamma G_N \left[ (N(t) - N_{tr}) - \frac{1}{\tau_p} \right] A(t) + \kappa A(t - \tau_{ext}) \cos \theta(t) \quad (5.10)$$

$$\frac{d\Phi(t)}{dt} = \frac{1}{2} \alpha_H \Gamma G_N \left[ (N(t) - N_{tr}) - \frac{1}{\tau_p} \right] - \kappa \frac{A(t-\tau_{ext})}{A(t)} \sin \theta(t) \quad (5.11)$$

and,

$$\theta(t) = \omega_0 \tau_{ext} + \Phi(t) - \Phi(t - \tau_{ext}) \quad (5.12)$$



As for the carrier density, the rate equation is given by [295]:

$$\frac{dN(t)}{dt} = \frac{\eta_i I}{qV} - \frac{N(t)}{\tau_c} - G_N(N(t) - N_{tr})A^2(t) \quad (5.13)$$

Under steady-state conditions (i.e.  $d/dt = 0$ ), the output power is constant hence  $A(t) = A(t - \tau_{ext}) = A_s$ ,  $N(t) = N_s$ , while the steady-state phase  $\Phi_s$  can be written as  $\Phi_s = (\omega_s - \omega_0)t$  with  $\omega_s$  the steady-state angular frequency [295], [333].

Therefore, from Eqs. 5.10, 5.11 and 5.13 the steady-state solutions can be expressed as:

$$A_s^2 = \frac{\eta_i I / qV - N_s / \tau_c}{G_N(N_s - N_{tr})} \quad (5.14)$$

$$\omega_s - \omega_0 = \Delta\omega_s = -\kappa[\alpha_H \cos(\omega_s \tau_{ext}) + \sin(\omega_s \tau_{ext})] \quad (5.15)$$

$$N_s - N_{th} = \Delta N_s = -\frac{2\kappa}{\Gamma G_N} \cos(\omega_s \tau_{ext}) \quad (5.16)$$

## 2. Light-current characteristics with optical feedback

Eq. 5.16 implies that, under external feedback, the carrier density is reduced, and so the lasing threshold. Osmundsen and Gade [334] have derived the expression of the threshold current with optical feedback by considering multiple round-trips in the external cavity. In the limit case of small feedback ratios ( $r_{ext} \ll 1$ ), the threshold current  $I_{th}$  can be expressed as:

$$I_{th} = I_0(1 - 2\kappa \cos(\omega_s \tau_{ext})) \quad (5.17)$$

As an example, Figure 5.3 (a) represents the LI curves of a QD FP laser operating in the free-running operation and under three different amounts of optical feedback ( $r_{ext}=1.7\%$ ,  $3.4\%$  and  $6.7\%$ ). The threshold current  $I_{th}$  is reduced by about 7 mA under  $6.7\%$  feedback which is agreement with Eq. 5.17. The corresponding tendency is represented in Figure 5.3 (b), where the red triangle represents the free-running value ( $r_{ext} = 0$ ). In addition, due to the interaction between the ECMs and the laser cavity modes, residual undulations are observed in the output power. As depicted in Figure 5.4, at a given bias, while most of the laser cavity modes coincide with those of the external cavity, the constructive interferences enhance the output power while for the opposite the output power is reduced through destructive interferences. By

varying the bias current, the refractive index of the laser cavity changes due to carrier density variation and thermal effects, therefore the laser cavity modes are shifted, leading to such undulations in the light-current characteristics.

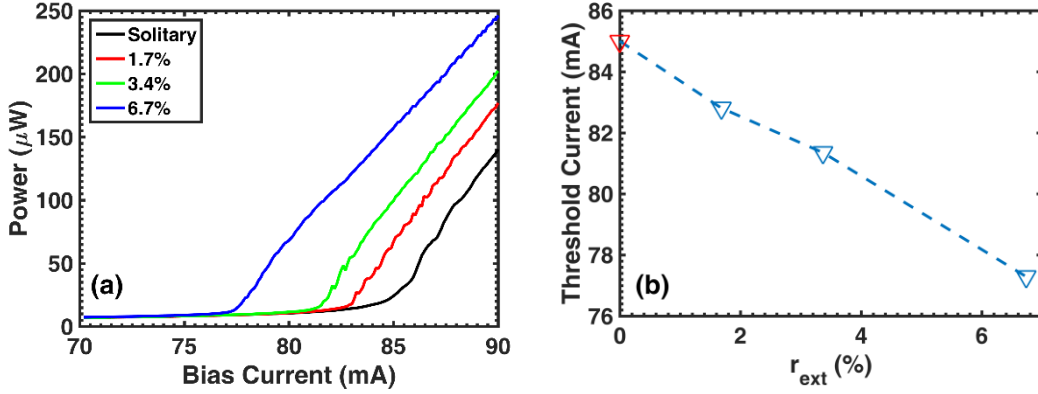


**Figure 5.3.** (a) LI curves of a QD FP laser under free-running operation (black) and for three different amounts of feedback ( $r_{\text{ext}} = 1.7\%$ ,  $3.4\%$  and  $6.7\%$ ); (b) Extracted threshold current  $I_{th}$  from (a) as a function of  $r_{\text{ext}}$ , the red triangle is the free-running value ( $r_{\text{ext}} = 0$ ).

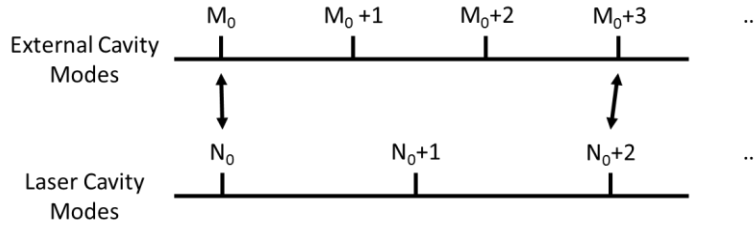


**Figure 5.4.** Interaction between the ECM  $M_i$  and the laser cavity modes  $N_i$ , after [304].

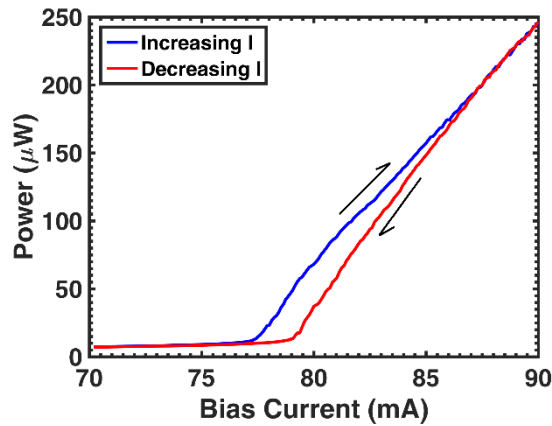


**Figure 5.5.** Hysteresis effect in the LI a QD FP laser operating under optical feedback ( $r_{\text{ext}} = 6.7\%$ ) while increasing and decreasing the bias current.

Figure 5.5 also illustrates the typical hysteresis effect arising in the LI considering a feedback strength of  $r_{ext} = 6.7\%$ . The output power does not follow the same path as the bias is increased or decreased. This hysteresis is attributed to the variation of the refractive index associated to the thermal effects [304].

### 3. Phase conditions

From Eq. 5.15, the following phase conditions can be derived

$$\Delta\omega_s\tau_{ext} = -C \sin \varphi_0 \quad (5.18)$$

with

$$C = \kappa\tau_{ext}\sqrt{1 + \alpha_H^2} = \frac{\tau_{ext}}{\tau_{in}} 2C_l\sqrt{1 + \alpha_H^2}\sqrt{r_{ext}} \quad (5.19)$$

$$\varphi_0 = \omega_s\tau_{ext} + \arctan(\alpha_H) \quad (5.20)$$

where  $\Delta\omega_s\tau_{ext}$  is the phase difference between the laser cavity field and the delayed field, and  $C$  the feedback parameter, which is, according to Eq. 5.19, dependent on the  $\alpha_H$ -factor, the feedback delay  $\tau_{ext}$  and the feedback strength  $r_{ext}$ . According to numerical simulations, when  $C \leq 1$ , Eq. 5.18 has only one solution, while if  $C > 1$ , the number of existing solutions increases but is always an odd number as represented in the  $(C, \varphi_0)$  space in Figure 5.6 [295].

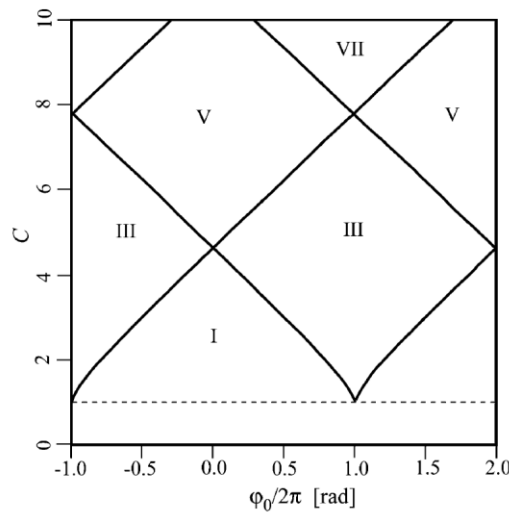


**Figure 5.6.** Solutions of Eq. 5.18 in the  $(C, \varphi_0)$  space. The roman numbers represent the number of solutions, after [295].

Another way to solve Eq. 5.17 is to calculate the interception between  $y = \omega_s \tau_{ext}$  and  $y = \omega_s \tau_{ext} + C \sin[\omega_s \tau_{ext} + \arctan(\alpha_H)]$ . Figure 5.7 represents the graphical solutions obtained for  $C = 0.76$  and  $C = 9.5$ . In the former case ( $C < 1$ ), there is only one stable solution, while for the latter ( $C > 1$ ), various stable or unstable solutions are possible [295].

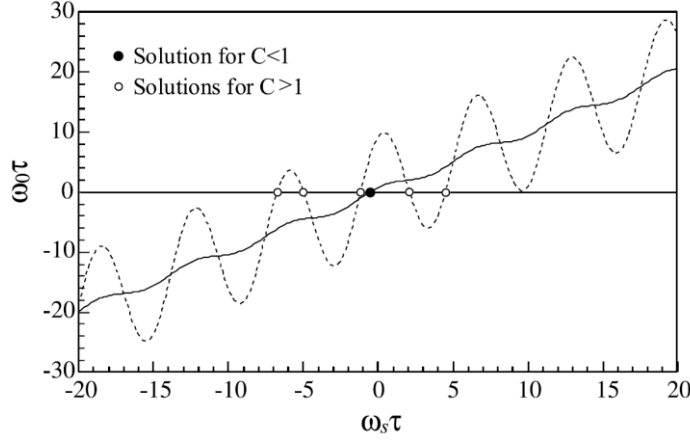


**Figure 5.7.** Steady-state solutions with respect to parameter  $C$ . Solid and dashed lines are obtained for  $C = 0.76$  and  $C = 9.50$ , respectively. The black circle corresponds to the single solution for  $C < 1$  and white circles represent the various solutions for  $C > 1$ , after [295].

Another way to graphically represents the possible oscillations has been introduced by Henry and Kazarinov [308]. In Figure 5.8 the carrier density variation  $\Delta N$  (Eq. 5.16) is represented as a function of the phase difference  $\Delta \omega_s \tau_{ext}$  (Eq. 5.15). Their interceptions give the possible solutions of Eq. 5.18, which are located on an elliptical orbit whose expression can be retrieved from Eq. 5.16 and 5.17 as follows [295]:

$$\left( \Delta \omega_s \tau_{ext} - \frac{\alpha_H \tau_{ext}}{2} \Gamma G_N \Delta N_s \right)^2 + \left( \frac{\tau_{ext}}{2} \Gamma G_N \Delta N_s \right)^2 = (\kappa \tau_{ext})^2 \quad (5.21)$$

The stable solutions are the ECMs located on the lower half of the ellipse (black dots), whereas the unstable ones (antimodes) are located on the upper half (black circles), and the free-running mode in red is located at the center. In Eq. 5.21, it has to be stressed that both the  $\alpha_H$ -factor and  $\kappa$  play important roles in the ellipse eccentricity, hence any increase of these parameters will expand the dimension of the orbit and more steady-states solutions will be involved making the laser less stable. Although the maximum gain mode located on the left hand-side of the ellipse was attributed to be the most stable [335], many studies have proved

that the laser tends to stabilize on the mode with the minimum linewidth, which is located much closer to the free-running one [335].

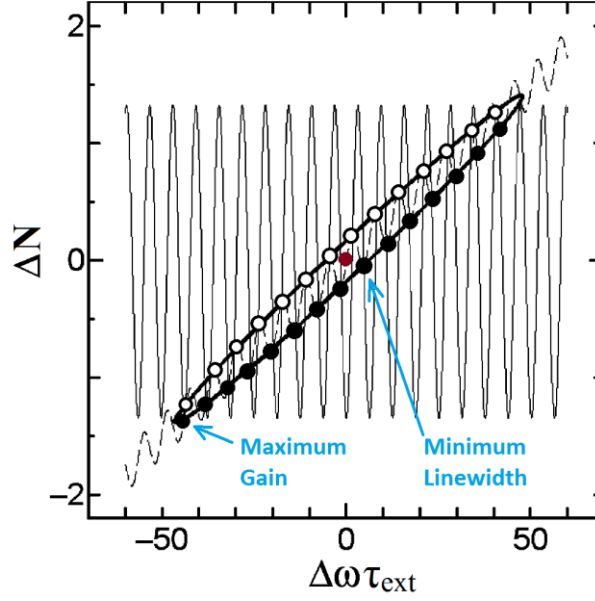


**Figure 5.8.** Carrier density  $\Delta N$  variation versus the phase difference  $\Delta\omega\tau_{ext}$ . Crossing points between solid and dashed sine waves give the locations of the modes. The red dot is the free-running mode, while black dots/circles correspond to ECM and antimodes respectively [295].

Regarding the spectral properties, it has been shown that the optical spectral linewidth  $\Delta\nu$  of a semiconductor laser operating under COF can be expressed as follows [193]:

$$\Delta\nu = \Delta\nu_0 / (1 + C \cos \varphi_0)^2 \quad (5.22)$$

where  $\Delta\nu_0$  is the free-running optical spectral linewidth (Eq. 2.28). Thus, for different feedback regimes namely different values of  $C$ , the spectral linewidth behaves as illustrated in Figure 5.9 [311], [331]. In regime I ( $C < 1$ ), only one solution exists, hence the linewidth may be either narrowed or broadened depending on the feedback phase. When  $C$  increases slightly above unity, only very few ECMs are excited meaning that the linewidth remains strongly dependent on the feedback phase (regime II). However, for  $C > 5$ , multiple ECMs are involved, hence the system is no longer dependent on the feedback phase, and progressively the laser restabilize on the mode with the minimum linewidth (regime III). If the feedback ratio is further increased, the laser reaches the critical level  $r_{crit}$ , above which the spectral linewidth will be dramatically broadened (regime IV).

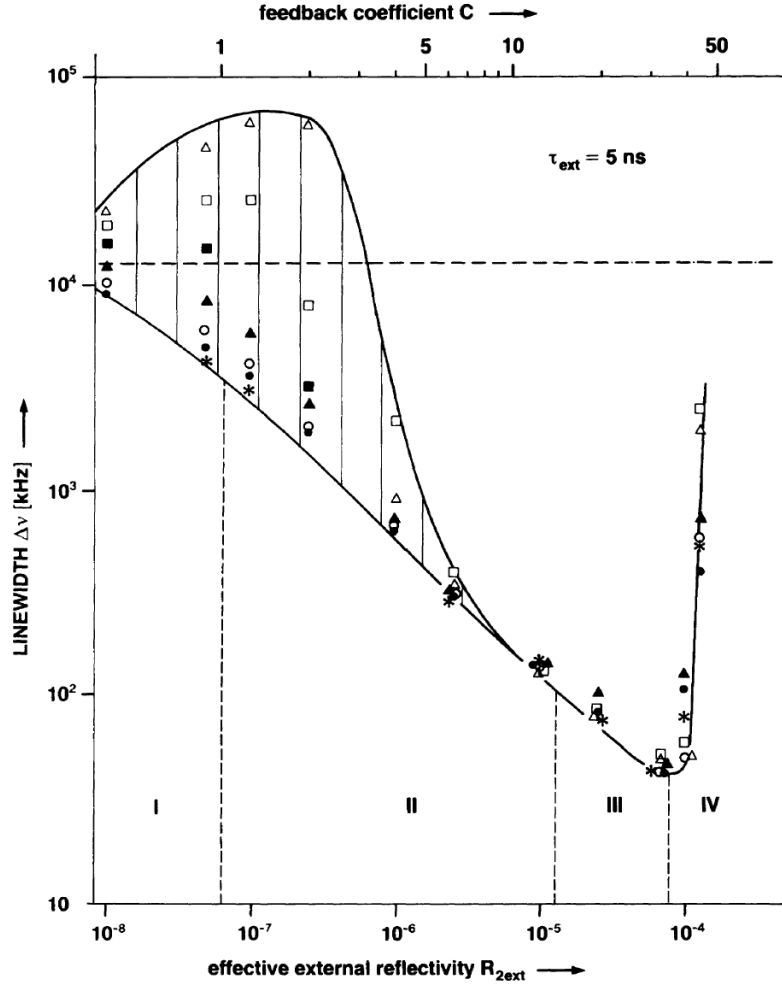


**Figure 5.9.** Optical spectral linewidth as a function of the feedback strength. The markers represent different feedback phase conditions, after [331].

#### 4. Critical level boundary

The critical feedback level has been widely studied in the literature and its dependence with the external cavity parameters has been unveiled in Ref [311]. In Figure 5.10, the solid line gives the onset of the regime IV as a function of the feedback strength and the external round trip time. The dashed line corresponds to the situation for which  $C = 1$ , and the vertical line is  $f_{RO} \times \tau_{ext} = 1$  with  $f_{RO}$  the relaxation oscillation frequency. The right and left sides are commonly referred as the long- and short-delay regimes. In the former ( $f_{RO} \times \tau_{ext} > 1$ ), the critical feedback level does not depend on the external round trip time but only on intrinsic laser parameters [320] as shown by Eq. 5.3. However, in the latter case ( $f_{RO} \times \tau_{ext} < 1$ ), the critical feedback level is up-shifted when decreasing the external round-trip time.

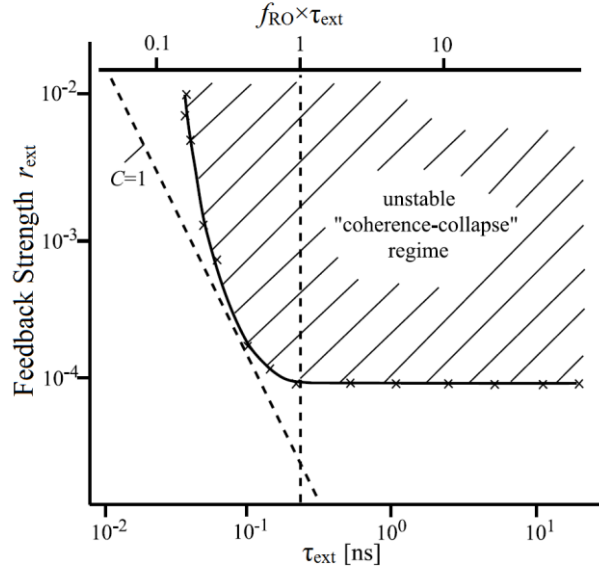


**Figure 5.10.** The critical feedback level  $r_{crit}$  as a function of the external round-trip time  $\tau_{ext}$  (solid line). The dashed line marks  $C = 1$ , and the vertical line indicates is  $f_{RO} \times \tau_{ext} = 1$ , after [311].

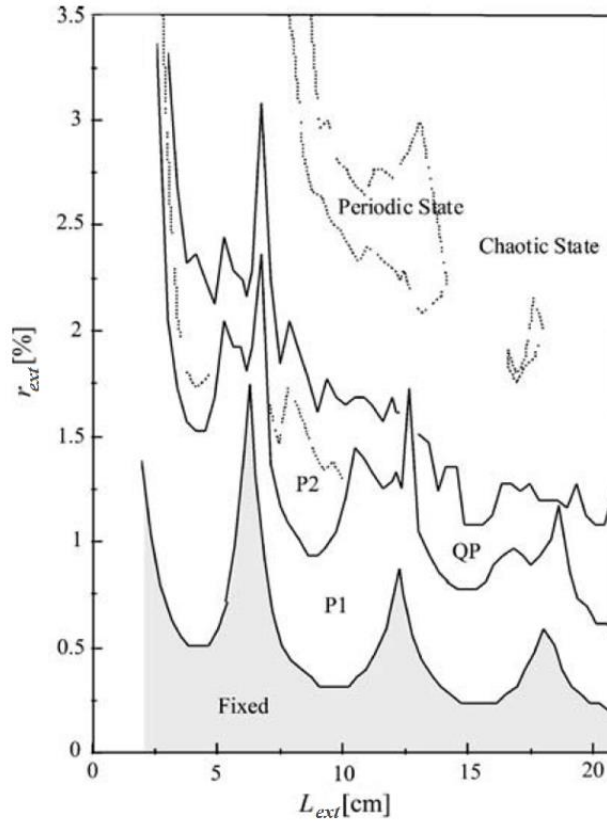


**Figure 5.11.** Sub-boundaries of regime IV as a function of the external cavity length  $L_{ext}$  and feedback strength  $r_{ext}$ . Fixed: stable state, P1, P2: periodic oscillations, QP: quasi-periodic oscillations, after [295].

Besides, it has been shown that in the short cavity regime, the boundary of regime IV

does not necessarily follow a linear trend as in Figure 5.10. Indeed, due to the interferences between the laser cavity modes and the ECMs, undulations arise as shown in Figure 5.11 [336]. In other words, when  $L_{ext}$  is a multiple of the laser cavity length, constructive interferences require a higher feedback strength to destabilize the laser which falls into the chaos rather abruptly. In case of destructive interference, a smaller amount of optical feedback is enough to disturb the laser hence the route to chaos is more regular and progressive through periodic states like P1 and P2 (where P2 is the dynamics for which the period of the oscillation is doubled) as well as quasi-periodic (QP) oscillations [337].

At weak feedback strength, the returning field can be considered as a small perturbation to the steady-state laser cavity field with the additional terms  $\delta x(t) \ll x_s$  with  $x = A, \Phi$  and  $N$ :

$$A(t) = A_s + \delta A(t) \quad (5.23)$$

$$\Phi(t) = \Phi_s + \delta \Phi(t) \quad (5.24)$$

$$N(t) = N_s + \delta N(t) \quad (5.25)$$

By injecting Eqs. 5.23 – 5.25 into Eqs. 5.10, 5.11 and 5.12, it comes:

$$\begin{aligned} \frac{dA(t)}{dt} = \frac{d\delta A(t)}{dt} = \frac{1}{2} \Gamma G_N A_s \delta N(t) - \kappa \cos(\omega_s \tau_{ext}) [\delta A(t) - \delta A(t - \tau_{ext})] \\ - \kappa A_s \sin(\omega_s \tau_{ext}) [\delta \Phi(t) - \delta \Phi(t - \tau_{ext})] \end{aligned} \quad (5.26)$$

$$\begin{aligned} \frac{d\Phi(t)}{dt} = \Delta\omega_s + \frac{d\delta\Phi(t)}{dt} = \frac{1}{2} \alpha_H \Gamma G_N \delta N(t) + \Delta\omega_s + \kappa \frac{1}{A_s} \sin(\omega_s \tau_{ext}) [\delta A(t) - \delta A(t - \tau_{ext})] \\ - \kappa \cos(\omega_s \tau_{ext}) [\delta \Phi(t) - \delta \Phi(t - \tau_{ext})] \end{aligned} \quad (5.27)$$

$$\frac{dN(t)}{dt} = \frac{d\delta N(t)}{dt} = -2G_N(N_s - N_{tr})A_s\delta A(t) - \left(G_N A_s^2 + \frac{1}{\tau_c}\right)\delta N(t) \quad (5.28)$$

The eigenvalues  $\lambda$  of the Jacobian matrix of the equation system Eq. 5.26 to 5.28 cannot be analytically extracted due to the presence of the delay terms. However, it is possible to apply a linearization by considering the perturbations in the form of  $\delta x(t) = x_p \exp(\lambda t)$  with  $x = A, \Phi$  and  $N$  [202].

In doing so the derivation terms on the left branches are such as:



$$\frac{d\delta A(t)}{dt} = \frac{d\delta A \exp(\xi t)}{dt} = \xi \delta A(t) \quad (5.29)$$

$$\frac{d\delta \Phi(t)}{dt} = \frac{d\delta \Phi \exp(\xi t)}{dt} = \xi \delta \Phi(t) \quad (5.30)$$

$$\frac{d\delta N(t)}{dt} = \frac{d\delta N \exp(\xi t)}{dt} = \xi \delta N(t) \quad (5.31)$$

And the delay terms can be expressed as:

$$\delta A(t) - \delta A(t - \tau_{ext}) = (1 - \exp(-\lambda \tau_{ext})) \delta A(t) = D \delta A(t) \quad (5.32)$$

$$\delta \Phi(t) - \Phi(t - \tau_{ext}) = (1 - \exp(-\lambda \tau_{ext})) \delta \Phi(t) = D \delta \Phi(t) \quad (5.33)$$

Thus Eqs. 5.26 – 5.28 can be rewritten in the form:

$$\frac{d}{dt} \begin{bmatrix} \delta A(t) \\ \delta \phi(t) \\ \delta N(t) \end{bmatrix} = \begin{bmatrix} -\kappa D \cos(\omega_s \tau_{ext}) & -\kappa D A_s \sin(\omega_s \tau_{ext}) & \frac{1}{2} \Gamma G_N A_s \\ \kappa \frac{D}{A_s} \sin(\omega_s \tau_{ext}) & -\kappa D \cos(\omega_s \tau_{ext}) & \frac{1}{2} \alpha_H \Gamma G_N \\ -2G_N(N_s - N_{tr})A_s & 0 & -\left(G_N A_s^2 + \frac{1}{\tau_c}\right) \end{bmatrix} \begin{bmatrix} \delta A(t) \\ \delta \phi(t) \\ \delta N(t) \end{bmatrix} = M_J \begin{bmatrix} \delta A(t) \\ \delta \phi(t) \\ \delta N(t) \end{bmatrix} \quad (5.34)$$

with  $M_J$  the Jacobian matrix.

In order to analyze the stability of the steady-state solutions, the eigenvalues of  $M_J$  are determined such as:

$$\begin{aligned} \text{Det}(M_J - \lambda I) &= \lambda^3 + 2[\gamma + \kappa D \cos(\omega_s \tau_{ext})]\lambda^2 + [\kappa^2 D^2 + 4\kappa D \cos(\omega_s \tau_{ext})\gamma + \omega_{RO}^2]\lambda \\ &\quad + \{\kappa^2 D^2 \gamma + \omega_{RO}^2 \kappa D [\cos(\omega_s \tau_{ext}) - \alpha_H \sin(\omega_s \tau_{ext})]\} = 0 \end{aligned} \quad (5.30)$$

where  $\omega_{RO}$  and  $\gamma$  are the relaxation oscillation angular frequency and the damping factor of the free-running laser as previously defined in Eqs. 2.30 and 2.31.

When the feedback strength is weak, we can assume that  $\omega_{RO}^2 \gg \kappa^2$  and  $\omega_{RO}^2 \gg -\kappa\gamma$  [338], thus Eq. 5.30 is reduced to:

$$\text{Det}(M) \approx \lambda^3 + 2[\gamma + \kappa D \cos(\omega_s \tau_{ext})]\lambda^2 + \omega_{RO}^2 \lambda + \omega_{RO}^2 \kappa D [\cos(\omega_s \tau_{ext}) - \alpha_H \sin(\omega_s \tau_{ext})] = 0 \quad (5.33)$$

By approximating  $1 - \exp(-\lambda t) \approx \lambda t$ , and taking  $\lambda = i\omega$  in the Eq. 5.33, it comes after identifications of real and imaginary parts:

$$\left\{1 - 2 \left( \frac{\omega^2}{\omega_{RO}^2} \right)\right\} \cos(\omega_s \tau_{ext}) - \alpha_H \sin(\omega_s \tau_{ext}) = - \frac{\gamma \left( \frac{\omega}{\omega_{RO}} \right)^2}{\kappa \sin^2 \left( \frac{\omega \tau_{ext}}{2} \right)} \quad (5.34)$$

$$\omega^2 - \omega_{RO}^2 = 2\gamma\omega \cot \left( \frac{\omega \tau_{ext}}{2} \right) \quad (5.35)$$

Eq. 5.35 unveils the existence of excited periodic oscillations with a frequency strongly dependent on the external cavity round-trip time and varying periodically around the free-running angular ROF  $\omega_{RO} = 2\pi f_{RO}$ . Figure 5.12 shows that the oscillations frequencies corresponding to the periodic region (P1) in Figure 5.11 can be tuned with respect to the external cavity length.

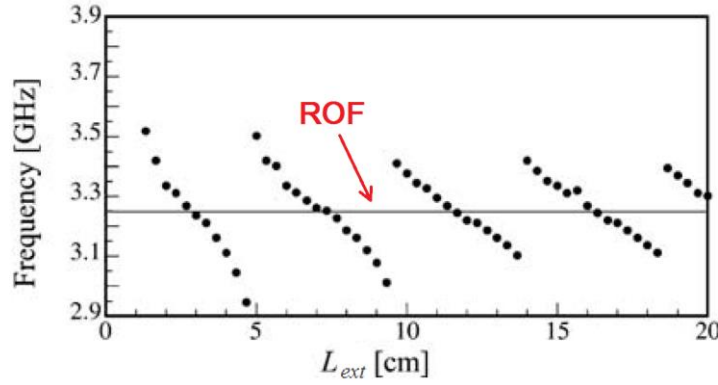


**Figure 5.12.** Excited periodic oscillation frequencies as a function of  $L_{ext}$  (black dots), the horizontal line is the free-running ROF ( $r_{ext} = 0$ ), after [336].

## 5. Low-frequency fluctuations

In a semiconductor laser, deterministic chaos usually takes place through coherence collapse, however, chaotic temporal dynamics can also occur via the occurrence of aperiodic pulsations called low-frequency fluctuations (LFF). The LFF regime is characterized from irregular dropouts in the output power [339]. The LFF regime usually requires to operate the laser near the threshold in the long delay configuration such as  $f_{ext} \ll f_{RO}$  meaning that a large number of modes is involved in the dynamics. Figure 5.13 represents the mapping of the LFF dynamic as a function of the injection current and optical feedback strength. In particular,

it is shown that the LFF can coexist either with the coherence collapse regime and stable operation.

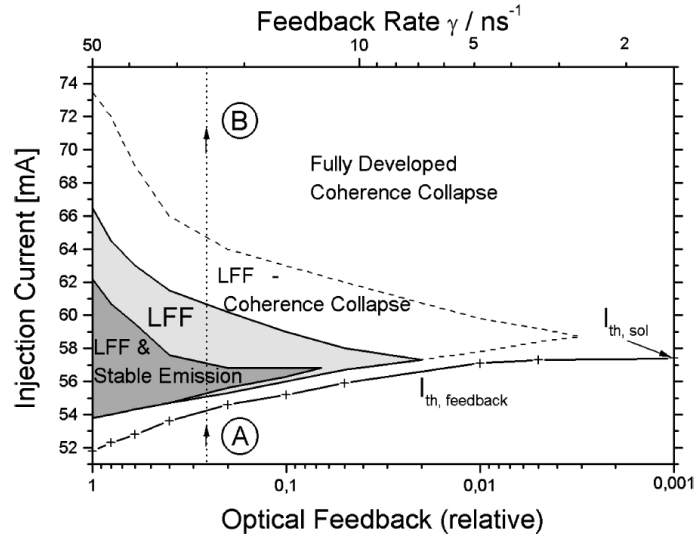


**Figure 5.13.** Mapping of the LFF dynamic as a function of the injection current and optical feedback strength. The LFF regime is depicted in light gray. In the dark-gray region stable emission and LFF dynamic coexist. In the undashed region LFF and fully developed coherence collapse coexist, after [340].

Figure 5.14 represents the antimodes and the ECMs located around the free-running mode (red) similar to Figure 5.8. Fundamentally, when the LFF takes place, the free-running mode is attracted by an ECM (C) and travels down to the maximum gain mode located in the left hand side of the ellipse (D), then jumps back (A) to the free-running state (B) and then the process starts again [295]. However the LFF is not periodic but irregular hence, the laser may not always be able to reach the maximum gain mode, and the process can be interrupted by another antinode, meaning that the power dropout can occur even before reaching the maximum gain mode (E) [341]. In the time series, the jumps A and E through B induce a carrier density variation increase, which is responsible for the several power dropouts. The jumping back process is related to a so-called crisis which corresponds to a collision between an ECM that temporarily loses its stability due to the occurrence of chaos and the associated antinode [340]. As shown in Figure 5.14, another case is the reversion of the power recovery whereby the state goes up against the direction of the maximum gain mode (F).

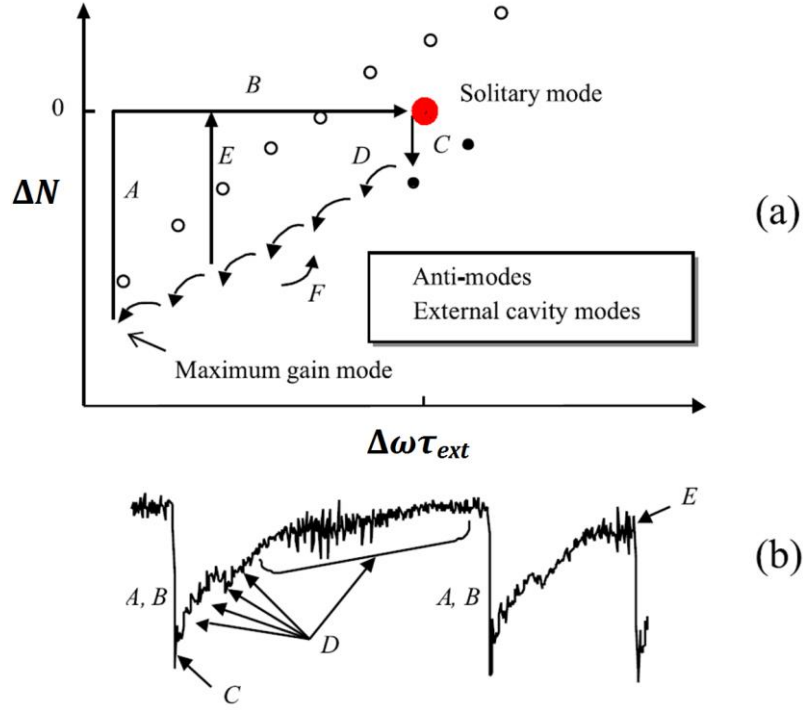


**Figure 5.14.** (a) Trajectory of the modes in the  $(\Delta N, \Delta\omega\tau_{ext})$  plane; (b) Corresponding LFF waveform, after [337].

## 6. Regular pulse package

The regular pulse package (RPP) regime is another type of complex dynamics arising under optical feedback, which manifests as regular pulsations in the output power. It occurs in the ultra-short cavity regime such as  $f_{ext} \gg f_{RO}$  meaning that a very small number of modes is involved [341], [342].

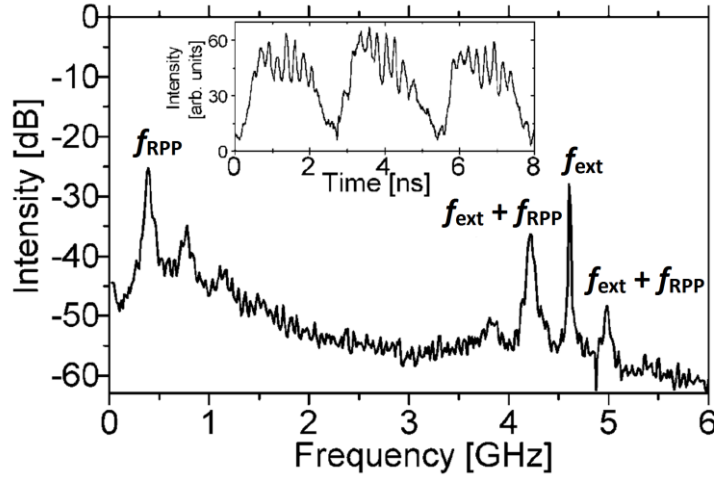


**Figure 5.15.** The RF spectrum and the corresponding temporal waveform of a semiconductor laser operating under the RPP regime, after [341].

Figure 5.15 illustrates a typical RF spectrum of a semiconductor laser operating within the RPP regime where the two most intensive peaks are the external cavity frequency  $f_{ext}$  and the pulsation frequency  $f_{RPP}$ . The related RPP waveform shown in the inset indicates that a fast regular pulse oscillation takes place at the frequency  $f_{ext}$  while the amplitude is modulated at the slower frequency of  $f_{RPP}$ .

At this stage, it is interesting to compare the main differences between the LFF and RPP dynamics. Table 5.1 hereinafter probes such differences [341]:

	<i>Short-cavity regime RPP</i>	<i>Long-cavity regime LFF</i>
<i>System internal frequency</i>	$f_{ext} \gg f_{RO}$	$f_{ext} \ll f_{RO}$
<i>No. of modes</i>	Small number $\sim 10$	Large number $\sim 100$
<i>Influence of feedback phase</i>	Qualitative changes	No qualitative changes
<i>Dynamics on short time scale</i>	Regular fast pulses $\sim f_{ext}$	Irregular fast pulses $\sim f_{RO}$
<i>Dynamics on long time scale</i>	Regular global trajectory along several modes	Mostly irregular global trajectory along several modes

**Table 5.1.** Main differences between the RPP and LFF dynamics.

- 1) The LFF can be seen as a chaotic dynamic with strong aperiodic self-pulsations that usually take place near the optical threshold and under long-delay feedback, while the RPP shows periodic self-pulsations under ultra-short-delay feedback;

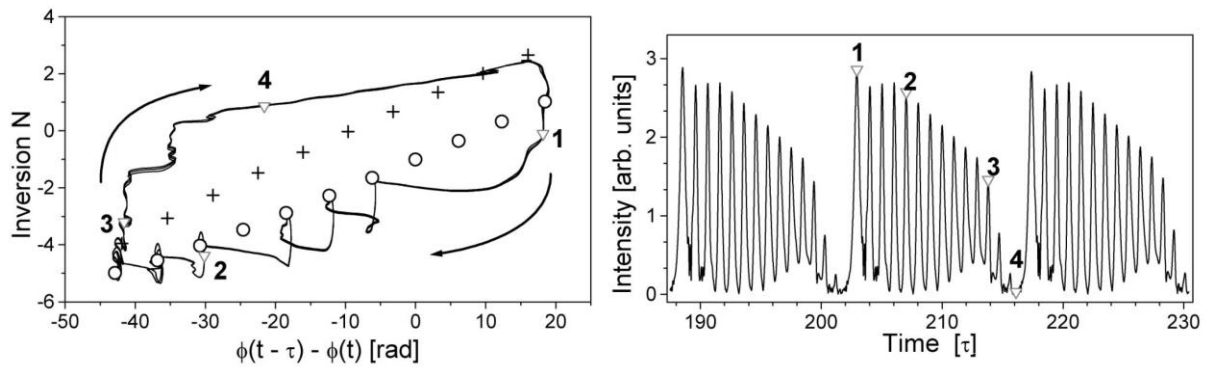


**Figure 5.16.** Trajectory of the modes in the phase domain illustrating the RPP dynamic and the corresponding temporal waveform.

- 2) The trajectory of the RPP and the corresponding temporal waveform are illustrated in Figure 5.16. In the phase space, ECMs are indicated by circles and antimodes by crosses.

Unlike the LFF, the path is one direction, which means that the crisis is not present, and the trajectory always visits the same ECMS leading to the birth of fast and regular oscillations at the frequency of  $f_{ext}$ . The temporal evolution occurs clockwise and the numbers in Figure 5.16 provide the correspondence between the temporal waveform and the phase-space portrait.

- 3) The RPP regime is sensitive to the feedback phase, while the LFF does not [342], [343];
- 4) The RPP temporal waveform consists only in a periodic sequence of a few pulsations ( $\sim 10$ ) within a slower envelope [341], while for the LFF, a secondary much slower envelope can eventually appear with a relaxation-oscillation-like behavior [344], [345];
- 5) The RPP dynamics is more regular and can take place over a larger window of operation [346] as opposed to the LFF [344], [345].

In what follows, the long-delay feedback will be first presented. The feedback regimes illustrated in Figure 5.1 will be experimentally retrieved, and the delay dynamics of both ES and GS QD lasers will be investigated and compared. Secondly, we will extend the ES-GS comparison to the short-cavity regime. In particular, the transition between short- and long-delay feedback dynamics will be studied and a self-pulsating regime will be unveiled.

### III. Experimental analysis of the long-delay feedback dynamics of QD lasers

#### 1. Experimental setup

Figure 5.17 represents the experimental setup used for the long delay feedback dynamics. The QD lasers are inserted into a fiberized external optical feedback loop. The laser emission is coupled by a lens-ended fiber, which is AR coated, in order to prevent any additional reflections from the fiber tip. Then, 90% of the power is sent to the feedback loop while the remaining 10% goes to the detection path. In the feedback loop, the light is reflected back to the QD using a back-reflector (BKR), consisting in a variable attenuator and a mirror. A polarization controller was used to make the feedback beam's polarization identical to that of the emitted wave in order to maximize the feedback effects. The length of the external cavity

is fixed at 7 m, which corresponds to an external round-trip time  $\tau_{ext} = 47$  ns. In the detection path, electrical and optical spectrum analyzers (ESA and OSA) are used to study the feedback dynamic. The free-running relaxation oscillation frequency of the lasers under study are a few GHz, therefore the long delay condition, i.e.  $f_{RO} \times \tau_{ext} \gg 1$  is fulfilled. However, because of the different output divergence from laser to laser, the range of attainable feedback strength  $r_{ext}$  is not exactly the same.

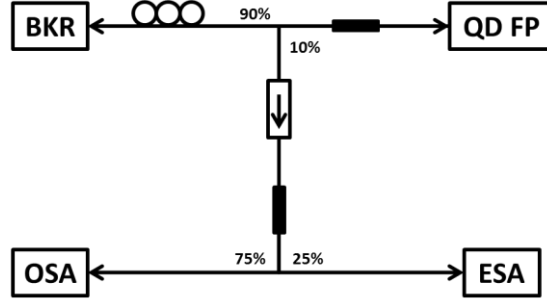


**Figure 5.17.** Experimental setup used for the long-delay feedback dynamics.

## 2. Identification of the feedback regimes

First, the feedback regimes discussed in the first section are retrieved assuming a single mode DFB laser (PDFB1). The laser is biased at  $2.5 \times I_{th}$ . Figure 5.18 (a) and (b) depict the route to chaos measured at 298 K within the optical and electrical domains as a function of  $r_{ext}$ . From these cartographies, four regimes out of five are well retrieved in agreement with those depicted in Figure 5.2. Due to the limited maximum feedback strength, the last regime was not observed.

### Regime I:

In this regime, the laser remains stable and single mode ( $C < 1$ ). The optical and RF spectra are represented in Figure 5.18 (c) and (d). The DFB mode is slightly red-shifted which agrees with Eq. 5.14.

### Regime II:

As  $r_{ext}$  increases,  $C$  becomes slightly above 1, more solutions can be identified (see Eq. 5.17). Depending on the phase condition, the laser output can exhibit either a stable and single frequency emission with a narrow linewidth or strong mode-hopping phenomenon. In the latter, two solutions may co-exist with the same amount of phase noise hence the laser

frequency switches between these two modes [309]. Figure 5.18 (e) represents the experimental observation of the mode-hopping which leads to a low-frequency peak in the electrical response, as depicted in Figure 5.18 (f).

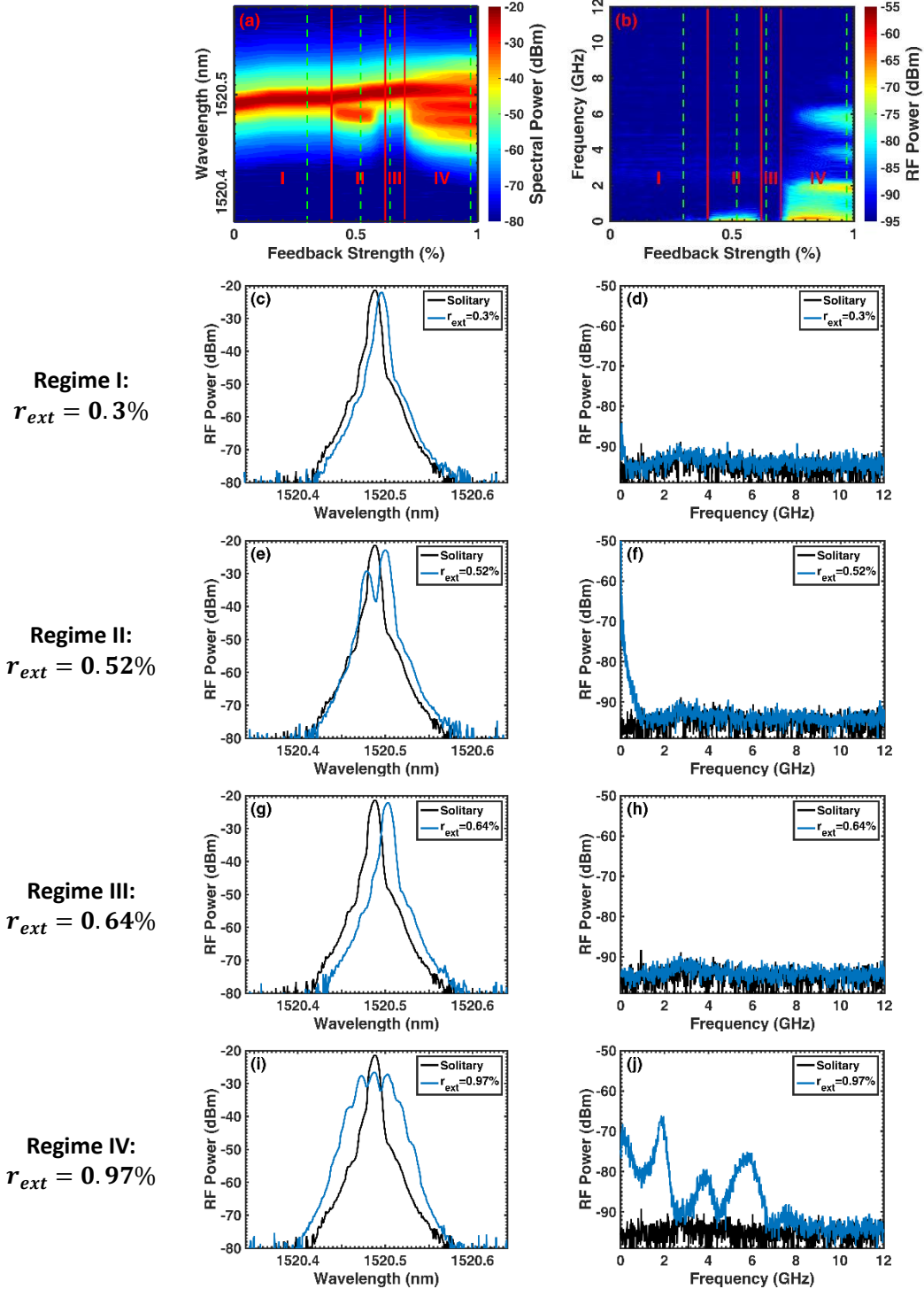


**Figure 5.18.** The optical (a) and RF (b) spectra of QD DFB laser PDFB1 under external feedback with  $r_{ext}$  ranging from 0 to 1%. The vertical lines in red allow to distinguish the different feedback regimes. Green dashed lines correspond to the measured operation points of optical ((c), (e), (g), (i)) and RF spectra ((d), (f), (h), (j)).



**Regime III:**

With the increase of  $r_{ext}$ , the rate of mode-hopping decreases until the transition to regime III, where the laser restabilizes and operates on the mode with the minimum linewidth (Figure 5.18 (g) and (h), see also Figure 5.8). This regime is insensitive to the phase of the delayed field, as already pointed out in Figure 5.2. However, this regime occurs in a very small window of operation (Figure 5.18 (a) and (b)), which makes it extremely difficult to observe, especially at low output powers [309]. Figure 5.19 illustrates the difficulties to locate such a regime. In these cartographies showing both the optical and RF spectra of the DFB laser under feedback, the regime III does not open up neither at  $1.5 \times$  ((a), (b)) and  $2 \times I_{th}$  ((c), (d)), nor at higher bias of  $3 \times I_{th}$  ((e), (f)). The opening of regime III at  $2.5 \times I_{th}$  has been used in chapter III to stabilize the laser emission and narrow the spectral linewidth of this DFB laser down to 100 kHz.

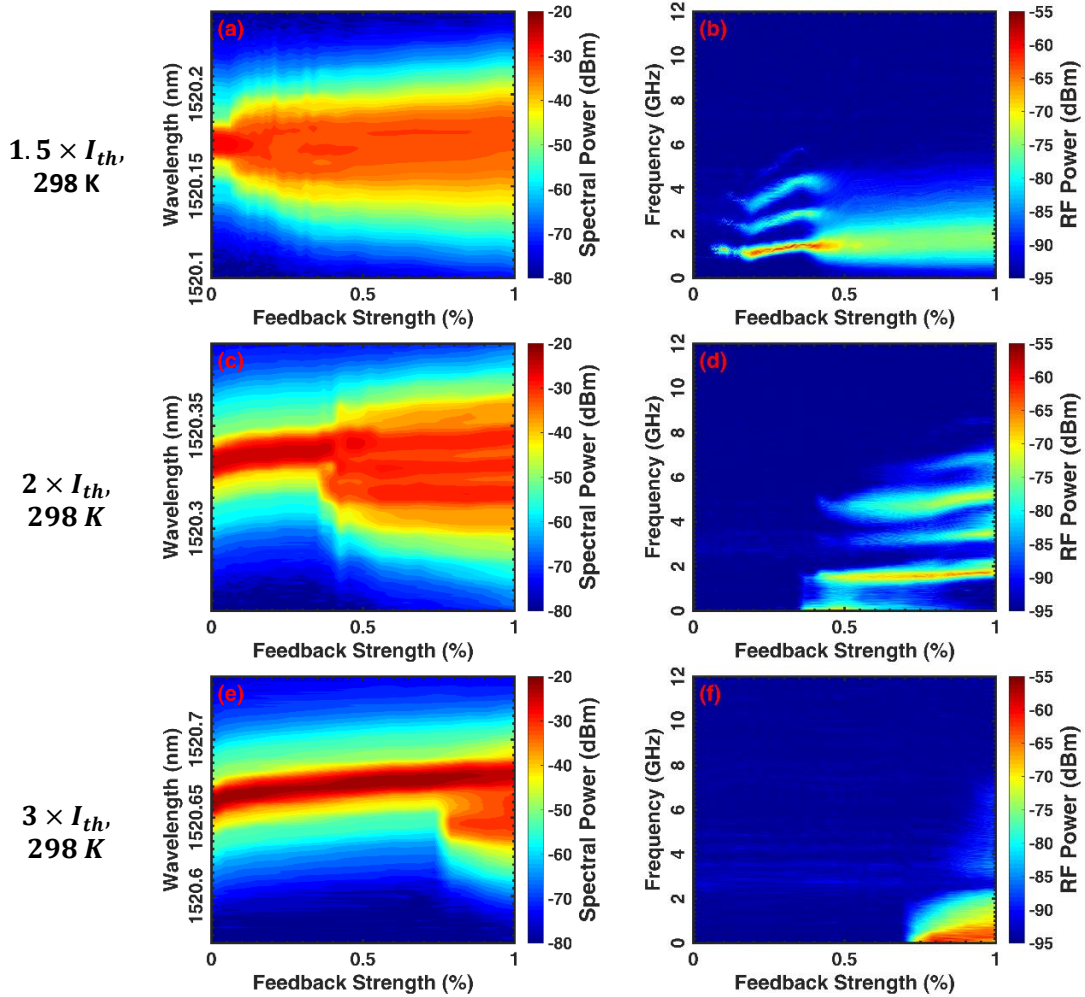


**Figure 5.19.** Optical and spectral mappings of QD DFB laser PDFB1 under external optical feedback at different bias conditions of  $1.5 \times$  ((a), (b)),  $2 \times$  ((c), (d)) and  $3 \times I_{th}$  ((e), (f)).

**Regime IV:**

Figure 5.18 (i) and (j) represent the optical and electrical mappings of the laser at the onset of regime IV ( $r_{ext} = 0.97\%$ ). As illustrated, at a larger feedback strength ( $C \gg 1$ ), quasi-periodic oscillations are induced by the undamped relaxation oscillations. When the regime IV is fully developed, the coherence length of the laser is dramatically reduced meaning that this regime is also referred as the coherence collapse [307]. Under the long-delay conditions, the regime IV does not depend on the external cavity length. Combining Figure 5.18 (a) and (b) with Figure 5.19 leads to the critical feedback level  $r_{crit}$  and its dependence with the normalized bias current. As shown in Figure 5.20,  $r_{crit}$  increases with the bias current which is in agreement with prior works [347]. This dependence is attributed to the larger intra-cavity photon density and the increased damping rate at higher bias currents.

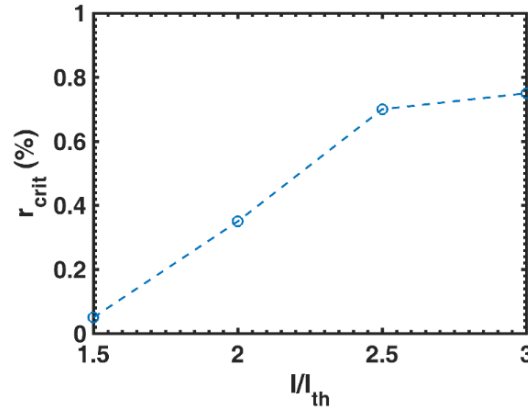


**Figure 5.20.** The critical feedback level  $r_{crit}$  as a function of the normalized bias level  $I/I_{th}$ .

These five regimes of operations are valid for a single-mode laser. In what follows, we will see that in case of FP lasers, the dynamics is more complex since ECMs interact with various longitudinal cavity modes.

### 3. InAs/GaAs QD FP lasers

This study is conducted on QD FP lasers GaFP1 (GS) and GaFP2 (ES) with identical cavity but emitting on different lasing states. All the CW characterizations can be found in chapter III. Measurements hereinafter are done at 293 K.

### 3.1. Multimode feedback dynamics

Due to the different output divergence of both devices, the maximal attainable feedback strength  $r_{ext}$  ranges up to  $\sim 5.9\%$  for QD laser GaFP1, while it only goes up to  $\sim 4.6\%$  for QD laser GaFP2. The multimode feedback dynamics is still investigated with electrical and optical spectrum analyzers. Since the external cavity length is several meter long, the impact of the feedback phase is neglected.

The optical feedback dynamics of the GS QD laser GaFP1 is first investigated. While bias conditions of  $1.5\times$ ,  $2.5\times$  and  $3\times I_{th}$  (25, 33 and 50 mA resp.) were considered, the GS laser remains stable for the whole range of currents and feedback strengths studied, only a small red-shift of the FP modes was observed with no sign of spectral broadening. Figure 5.21 represents optical and RF spectra recorded at  $3\times I_{th}$ , without feedback ( $r_{ext} = 0$ ) and for the maximal feedback strength ( $r_{ext} = 5.9\%$ ). This increased feedback resistance of the GS lasing has already been reported several times and is attributed to the large damping rate of the relaxation oscillations [54], [127], [128].

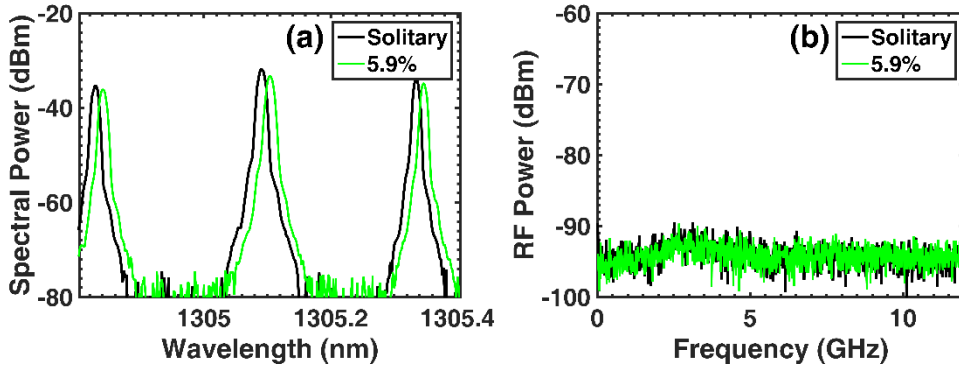


**Figure 5.21.** (a) Optical and (b) RF spectra of the GS QD laser GaFP1 measured at  $3 \times I_{th}$  without feedback ( $r_{ext} = 0$ ) and for the maximal feedback strength.

As for ES QD laser GaFP2, the bias conditions are fixed to  $1.5\times$  and  $2\times I_{th}$  (133 and 177 mA resp.). Due to the strong rollover observed in the output power above 180 mA (see in Figure 3.5), higher bias currents are not considered. Figure 5.22 represents the optical and RF spectral mappings for GaFP2 as a function of  $r_{ext}$  and under different bias currents. At  $1.5\times I_{th}$ , the laser is found to be rather insensitive to optical feedback up to 0.4%, beyond which the modes start broadening (Figure 5.22 (a) and (b)).

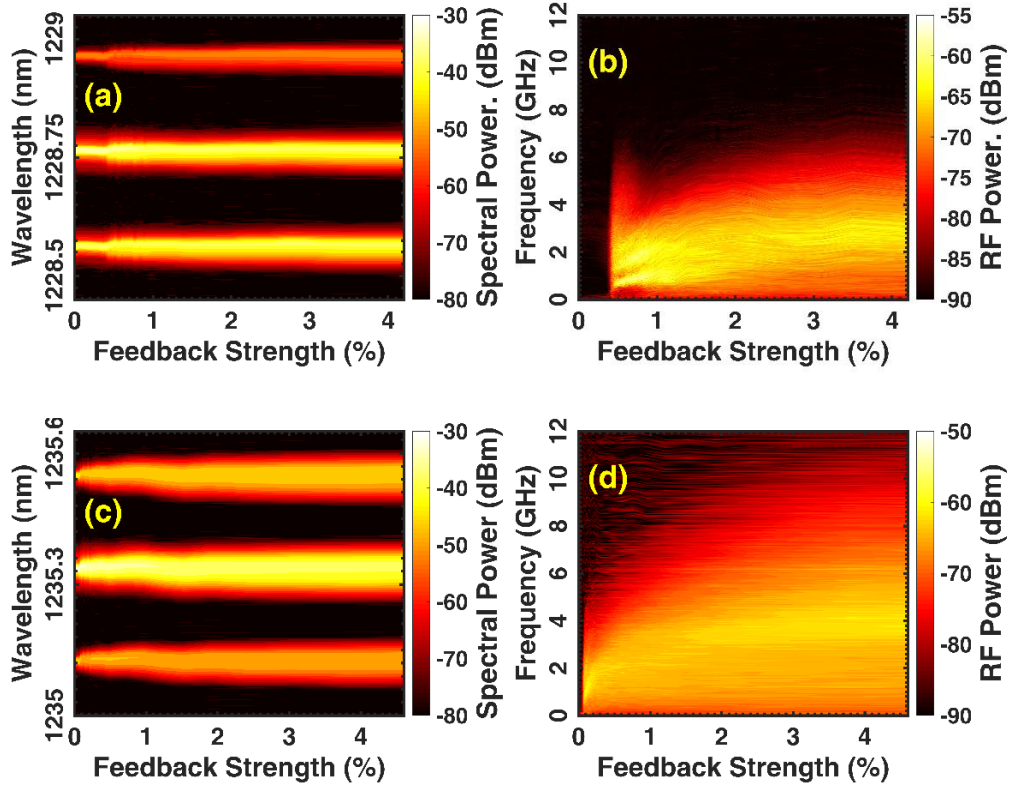


**Figure 5.22.** Optical (left) and RF (right) spectral mappings for ES QD laser GaFP2 at (a-b)  $1.5 \times I_{th}$ , and (c-d)  $2 \times I_{th}$ .

Figure 5.23 presents optical and RF spectra recorded at both bias levels for the ES laser without feedback as well as under low and maximal optical feedback. Figure 5.23 (a) and (c) illustrate the mode broadening in the optical spectrum for both pumping levels, while Figure 5.23 (b) and (d) depict the destabilization in the RF spectrum. In particular, Figure 5.23 (b) shows that around 0.6% of optical feedback, quasi-periodic oscillations with a high pedestal take place. At maximum feedback strength, broadband spectrum is observed that is a characteristic of chaotic behaviors. At higher bias currents and similar feedback strengths, no quasi-periodic dynamics is observed in Figure 5.23 (d). In addition, the comparison between Figure 5.23 (b) and (d) unveils that chaos is intensified at higher bias exhibiting a larger bandwidth. In contrast to DFB lasers, for which a better stability against optical feedback is observed at larger bias currents [299], [348], we found here that the destabilization of FP lasers is more complex due to the stronger modal competition. Finally, at higher bias levels, the ES laser appears even more sensitive to optical feedback since the critical feedback level beyond which the route to chaos occurs drops down to 0.05% as opposed to 0.4% at lower bias. Once

the quasi-periodic oscillations window disappears, the laser directly oscillates chaotically.

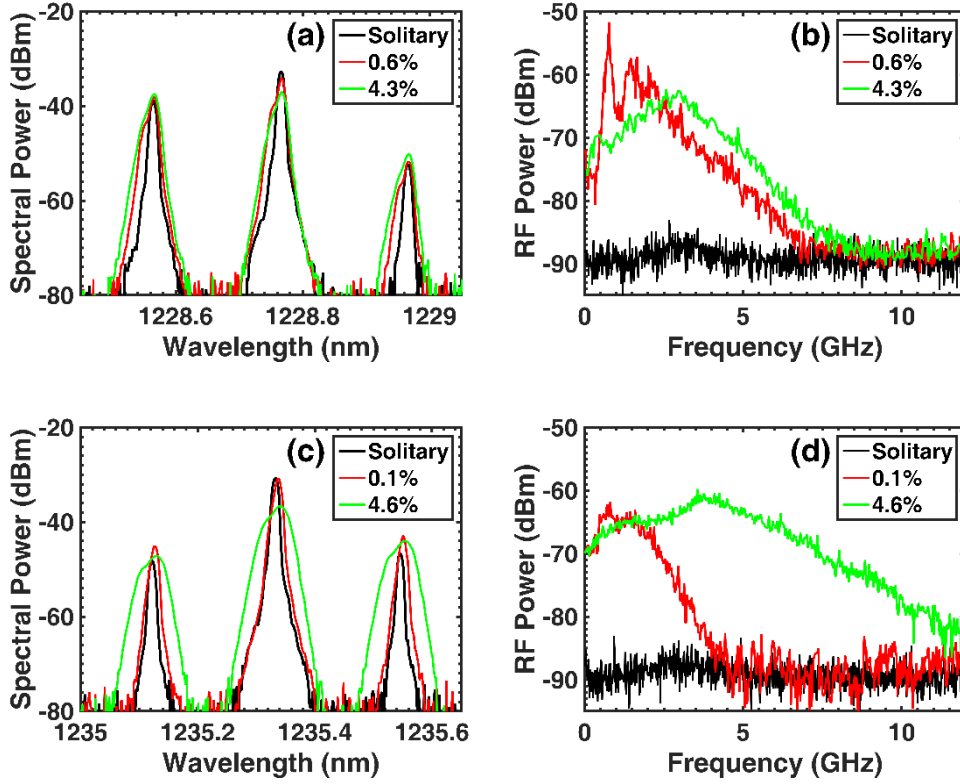


**Figure 5.23.** ES QD laser GaFP2 at  $1.5 \times I_{th}$  bias level: (a) optical and (b) RF spectra of the free-running laser, at 0.6% and 4.3% optical feedback; GaFP2 at  $2 \times I_{th}$  bias level: (c) optical and (d) RF spectra of the free-running laser, at 0.1% and 4.6% optical feedback.

With the  $\alpha_H$ -factor measured by the ASE method (chapter III), it is possible to retrieve the damping factor  $\gamma$  from Eq. 5.3. For the GS QD laser GaFP1 ( $\alpha_H=1$ ) as no coherence collapse was observed, the lower bound of the critical feedback level  $r_{crit,GS}$  is taken at 5.9%. Then, taking  $R = 0.32$ ,  $C_l = 0.6$ ,  $\tau_{int} = 21$  ps,  $\gamma_{ES}$  is estimated to be of 1.6 GHz and 0.6 GHz at  $1.5 \times$  and  $2 \times I_{th}$  for GaFP2 with  $\alpha_H=0.5$  against  $\gamma_{GS} > 18$  GHz for GaFP1. Such a difference between the GS and ES damping factors contributes to explain the observed changes in the optical feedback dynamics. Let us stress that although larger  $\alpha_H$ -factor values could have been measured under these bias conditions, the result would not have affected the order of magnitude of such large damping. In addition, the shapes of the optical spectra can also affect the dynamics [131] (see in Figure 3.4 and 3.5). Indeed, GaFP2 appears to be more sensitive to optical feedback because of a stronger modal competition as compared to GaFP1, which has a rather flat optical spectrum around the central lasing wavelength. Lastly, the different optical

feedback dynamics can also be attributed to the ES degeneracy where the existence of two closely spaced p-levels can lead to more radiative transitions [349].

#### 4. GS chaotic dynamics

Since no chaos was observed in GaFP1 because of the limited range of attainable feedback, identical measurements were performed on another QD laser GaFP3 emitting on the GS transition but having a longer cavity length of 1.5 mm. To this end, because the free-spectral range is smaller than that of GaFP1, stronger modal interaction is expected with GaFP3. Besides as GaFP3 has a smaller beam divergence, it was possible to extend the maximal value of  $r_{ext}$  up to 17%. Figure 5.24 represents the optical and RF spectral mappings of QD laser GaFP3 operating under optical feedback at  $2.5 \times I_{th}$ .

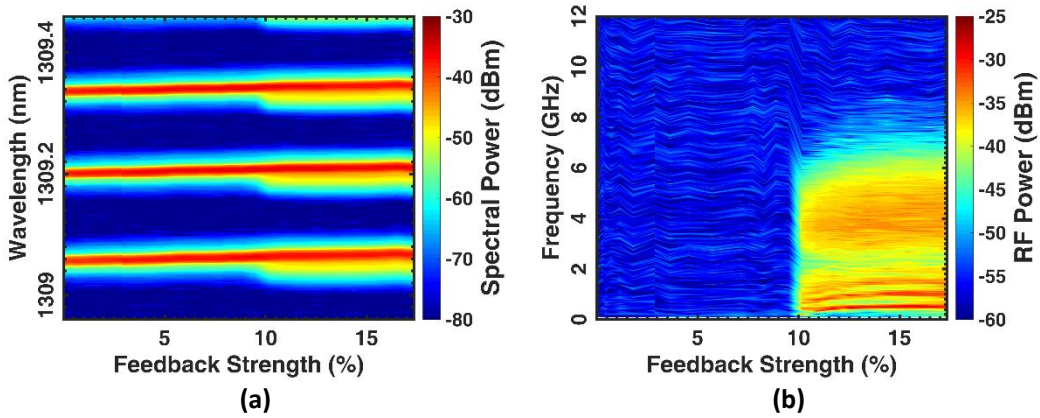


**Figure 5.24.** (a) Optical and (b) RF spectral mapping of GS QD laser GaFP3 at  $2.5 \times I_{th}$  with optical feedback.

As observed, the laser remains perfectly stable up to  $r_{ext} = 10\%$ , then sharply starts entering into the chaotic regime. From Eq. 5.3, and taking  $r_{ext} = 10\%$ ,  $R = 0.32$ ,  $C_l = 0.6$ ,  $\alpha_H = 1$ ,  $\tau_{int} = 35$  ps, the damping factor  $\gamma$  of this laser is estimated to be at 45 GHz, which is much larger than for GaFP1. Although the larger damping moves the destabilization point to  $r_{ext} = 10\%$  against 5.9% for GaFP1, it was nevertheless possible to observe the chaotic state in this laser owing to the stronger optical feedback strength.

## IV. Experimental analysis of the short-delay dynamics of QD lasers

In PIC applications, semiconductor lasers are integrated with other on-chip photonics components, thus potential feedback could originate from close-by reflecting waveguiding discontinuities. Indeed, interfaces such as active and passive transitions, waveguide crossings, regrowth interfaces, or process imperfections are source of unwanted reflections that can travel back into the laser cavity resulting in a variety of nonlinear dynamics arising under the five distinct regimes, depending on feedback strength and cavity length. In this work, we present a careful investigation of the GS and ES optical feedback dynamics in the short cavity regime. In particular, we unveil the existence of a quasi-RPP regime resulting in self-pulsating behavior with pulse emission close to the external cavity frequency.

### 1. Experimental Setup

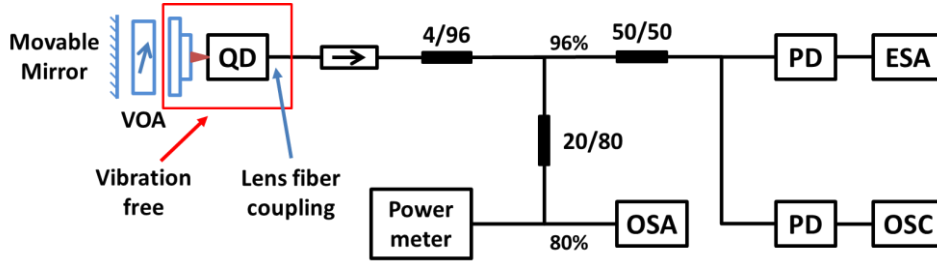


**Figure 5.25.** Experimental setup used for the short-delay feedback investigation.

Figure 5.25 represents the free-space experimental platform for studying the short-delay feedback dynamics with Prof. Fan-Yi Lin's group at the National Tsing Hua University (NTHU), Taiwan. QD devices under study are similar to those used in the previous section. As the FP lasers are left as-cleaved, the dynamics can be analyzed either out of the same facet than the one used for the feedback operation, or from the other side of the laser cavity. In the figure above, the free-space external cavity is on the left side of the laser, the light that comes out from the laser cavity is coupled through an AR coated lens which is also used to redirect the light from the mirror back to the laser cavity. The feedback strength  $r_{ext}$  is controlled by a free-space variable attenuator (VOA). In the experiments, the lens coupling ratio is similar for both



GaFP1 and GaFP2, allowing a maximal feedback ratio up to 60%. By moving the position mirror, the external cavity length was varied from 2 to 50 cm. Since the ROF for both lasers is of the order of few GHz (see Table 5.2), such a tuning range allows locating the transition from short- to long-delay regime with  $f_{RO} \times \tau_{ext}$  varying from 0.2 to 10.

	GaFP1 (GS)	GaFP2 (ES)
$1.5 \times I_{th}$	2 GHz	1.2 GHz
$1.7 \times I_{th}$	2.4 GHz	1.6 GHz

**Table 5.2.** ROFs measured at both bias levels for GS laser GaFP1 and ES laser GaFP2.

On the right side of the laser, the emission is coupled by an AR coated lens-end fiber and passes through an optical isolator for analysis. On the detection path, an OSA, an ESA and a sampling oscilloscope (OSC) are connected simultaneously to visualize the signals characteristics. The sampling scope used in this experiment has a 6 GHz bandwidth and a 20 Gb/s sampling rate. In the short-cavity regime, the measurements do require a reduced environmental noise and enhanced mechanical stability. In order to obtain such conditions both the laser and the coupling stages are fixed on a vibration-isolating table.

## 2. GS vs. ES feedback dynamics

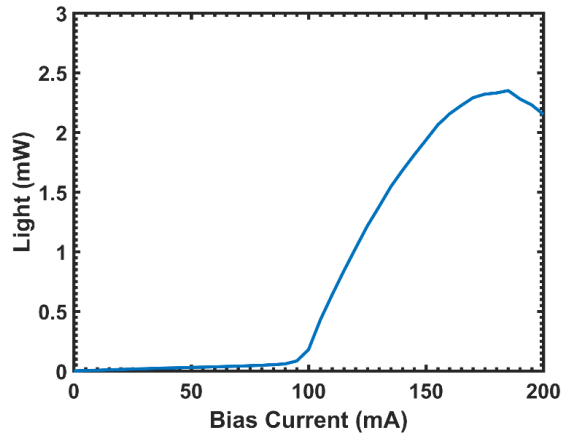


**Figure 5.26.** LI characteristics of the QD ES laser GaFP2 measured at 293 K.

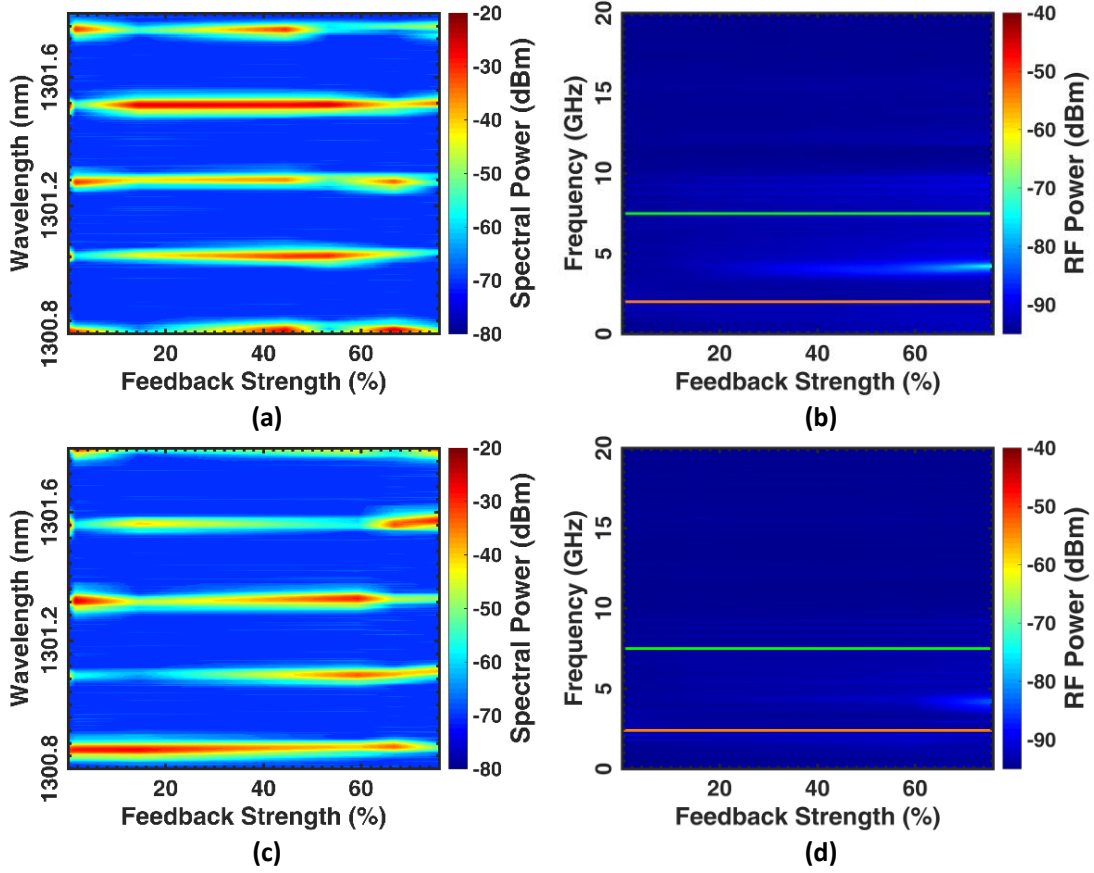
Figure 5.26 shows the LI of ES QD laser GaFP2 measured at NTHU. Due to different heat sink performance, the threshold current is slightly up-shifted to 94 mA as compared to that in Figure 3.5. Regarding GS QD laser GaFP1, as the bias level is much lower, the LI remains



unchanged. The experimental studies are performed at 298 K at  $1.5 \times I_{th}$ , where both lasers operate in the linear part of the LI. Then, higher bias levels are considered, however, limited to  $1.7 \times I_{th}$  (160 mA) in order to avoid the thermal roll-over.

## 2.1. GS optical feedback dynamics

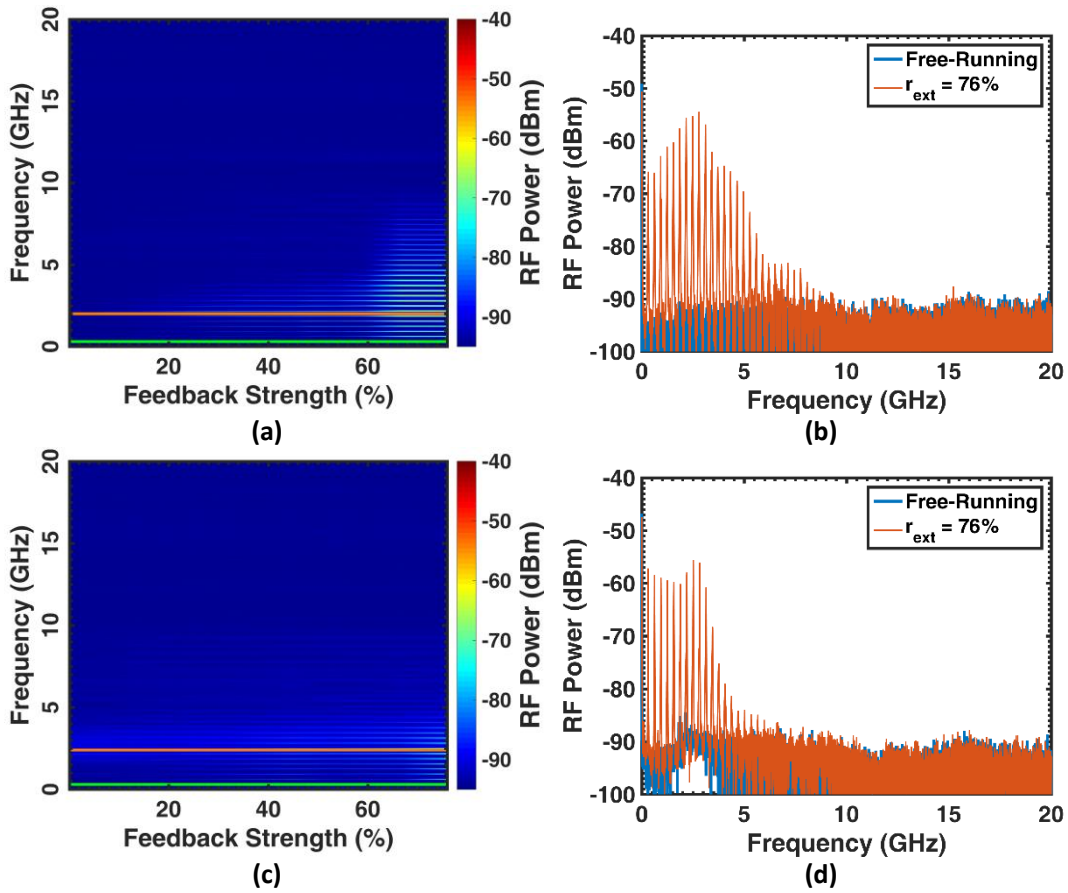
Figure 5.27 shows the optical and RF spectral mappings measured for GaFP1 with a 2 cm long external cavity ( $f_{RO} \times \tau_{ext} \sim 0.2$ ) and for two different bias levels.



**Figure 5.27.** Optical and RF spectral mappings of GS QD laser GaFP1. The external cavity length is 2 cm long. The bias currents are at  $1.5 \times$  ((a) and (b)) and  $1.7 \times I_{th}$  ((c) and (d)). The green and the orange horizontal solid lines mark the frequencies  $f_{ext}$  and  $f_{RO}$  respectively.

Figure 5.27 (a) and (c) show the evolution of FP modes around the gain peak as a function of  $r_{ext}$ . The maps reveal that the optical spectra are not stable regardless the value of the bias current, exhibiting some broadenings of the modes. Over the whole emission spectrum, two sets of modes are interacting inversely: while one set is strongly lasing, the other is rejected with a suppression ratio above 15 dB for the modes around the gain peak. This effect could be

attributed to an antiphase modal dynamics but further investigations are required at this stage to confirm this assumption [350]. While no evidence of such dynamics was observed in the RF spectral maps depicted in Figures 5.27 (b) and (d), it is however possible to identify in the electrical domain a trace of a weak peak ( $\sim -80$  dBm) observed around 4 GHz. Given that an external cavity length of 2 cm ( $f_{ext} = 7.5$  GHz), this peak corresponds to the double round-trip within the external cavity which is induced by the reflection of the delayed field from the cleaved facet (cf. Figure 5.1). As opposed to the long delay configuration, the laser is found here more sensitive to the reflection from the facet.



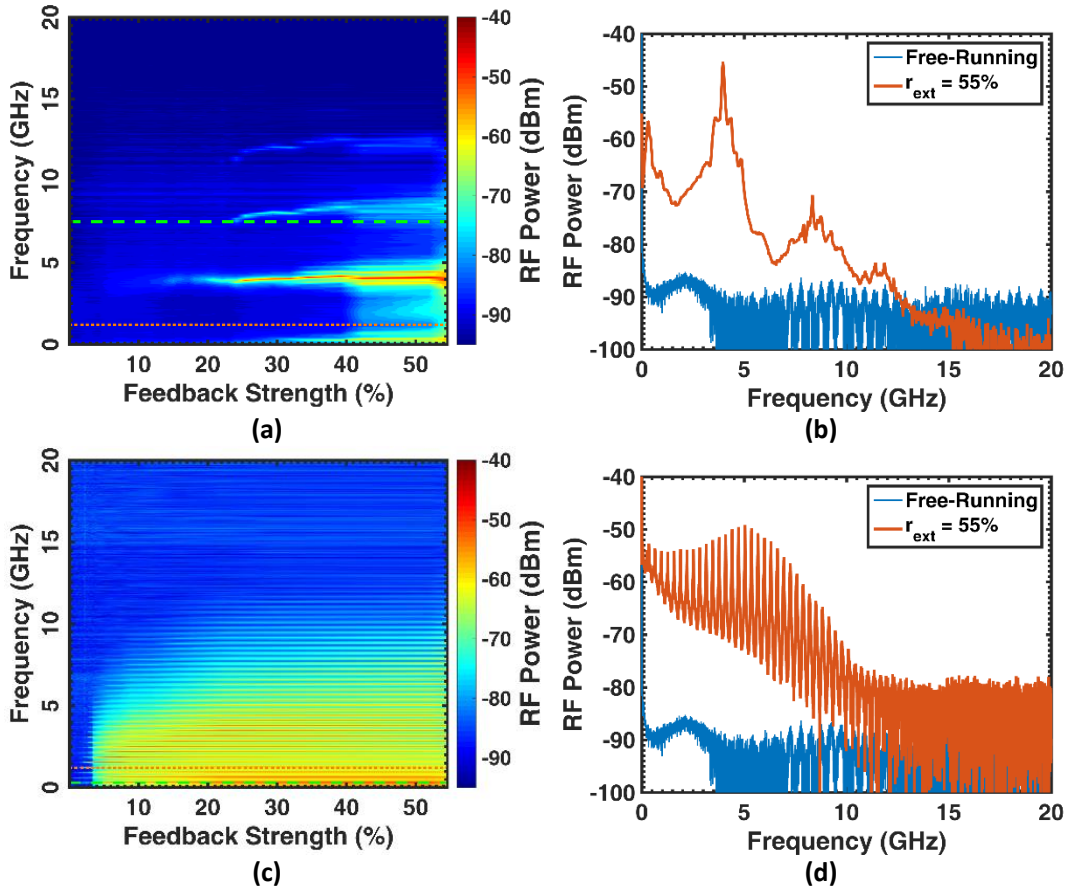
**Figure 5.28.** RF spectral mappings ((a), (c)) and RF spectra under free-running ( $r_{ext}=0$ ) and for the maximal optical feedback strength ( $r_{ext} = 76\%$ ) ((b), (d)) of GS QD laser GaFP1. The external cavity length is 50 cm long. Bias currents are at  $1.5\times$  ((a), (b)) and  $1.7 \times I_{th}$  ((c), (d)). The green and the orange horizontal solid lines mark the frequencies  $f_{ext}$  and  $f_{RO}$  respectively.

Figure 5.28 shows the RF spectral mappings and the corresponding RF spectra at  $1.5 \times$  and  $1.7 \times I_{th}$  under free-running ( $r_{ext} = 0$ ) and for the maximal optical feedback strength ( $r_{ext}$

= 76%) of QD laser GaFP1 within an external cavity length of 50 cm ( $f_{RO} \times \tau_{ext} \sim 10$ ). Here, the observed dynamics is similar to that obtained with the fiberized long delay configuration. First, the laser remains stable then follows a destabilization route driven by quasi-periodic behaviors but without reaching chaotic state as already pointed out in Figure 5.21.

## 2.2. ES optical feedback dynamics

Compare to GaFP1, the dynamics of ES QD laser GaFP2 is found richer. Figure 5.29 (a) and (c) show the RF spectral mapping of GaFP2 biased at  $1.5 \times I_{th}$  under free-running ( $r_{ext} = 0$ ) and for the maximal optical feedback strength ( $r_{ext} = 55\%$ ) considering 2 and 50 cm long external cavity. Figure 5.29 (b) and (d) depict the corresponding electrical spectra at maximal feedback ( $r_{ext} = 55\%$ ) that are compared to the free-running case ( $r_{ext} = 0$ ).



**Figure 5.29.** RF spectral mappings of ES QD laser GaFP2 biased at  $1.5 \times I_{th}$  under free-running ( $r_{ext} = 0$ ) and for the maximal optical feedback strength ( $r_{ext} = 55\%$ ) considering 2 and 50 cm long external cavity ((a) and (c)); RF spectra under free-running ( $r_{ext} = 0$ ) and for the maximal optical feedback strength ( $r_{ext} = 55\%$ ) ((b) and (d)).

In Figure 5.29 (a) and (b), the strong beating at 3.8 GHz still corresponds to the signature

of the double roundtrip within the external cavity, similar to what observed with GaFP1. However, in such case, the oscillation peak is enhanced beyond the noise level, and a high pedestal begins to develop at around 40% as opposed to the GS laser for which the oscillations were much weaker due to the stronger damping rate. By increasing the external cavity up to 50 cm, a typical destabilization scenario is retrieved hence the ES laser starts oscillating under low feedback and then falls quickly into chaos through quasi-periodic oscillations.

### 2.3. Analysis of the excited periodic oscillations

Similar to what is shown in Figure 5.12 this section investigates the birth of optical feedback induced excited periodic oscillations both for ES and GS lasers. In order to do so, the external cavity length is varied from 2 cm to 50 cm, which corresponds to a variation of  $f_{RO} \times \tau_{ext}$  from 0.2 to 10. Figure 5.30 depicts the evolution of the excited periodic oscillations with the external cavity length. The blue points show the extracted oscillation frequencies  $f_p$  for the two lasers (GaFP1 and GaFP2) from the RF spectra as a function of the external cavity length. In addition, the red solid, dashed, dashed-dotted curves represent the frequency of the  $n^{\text{th}}$  ECM ( $n=1, 2, 3$ ) which is given by:

$$f_{ECM,n} = n \times f_{ext} \quad (5.36)$$

The solid line in green represents the evolution of the double round-trip within the external cavity. The vertical solid line in orange marks the boundaries between short- and long-delay feedback regimes while the horizontal one in black gives the level of the ROF  $f_{RO}$  of the free-running laser.

As shown in Figure 5.30 and from Eq. 5.35, the excited periodic oscillation frequency changes with respect to the external cavity length with a value  $f_p$  varying around  $f_{RO}$  which is qualitatively in agreement with what is observed in Figure 5.12 before that the laser reaches the long-delay regime ( $f_{RO} \times \tau_{ext} > 1$ ). However, according to Eq. 5.5, these excited periodic oscillations should be observed for feedback above 1%, and for  $\kappa > 5.2$  GHz, hence the feedback conditions used in this work are a bit out of the range of the assumptions used to extract Eq. 5.35, i.e.  $\omega_{RO}^2 < \kappa^2$ . As a result, a perfect variation of the excited frequency  $f_p$  around the ROF like in Figure 5.12 is not reproduced. From Figures 5.30, it is important to stress out that under the short-delay configuration, the first points in each figure may correspond to

the frequency of the double roundtrip within the external cavity, indicating that the laser field still interacts with both single and double round-trip fields. For longer external cavities of 20 or 50 cm for which  $f_{RO} \times \tau_{ext} > 1$ ,  $f_P$  gets very close to the free-running ROF  $f_{RO}$  meaning that the laser is no longer sensitive to the phase of the back-reflected light. However, this situation is different for GaFP2 at higher bias (Figure 5.30 (d)) since the excited frequency is similar to that of ECM2. As aforementioned, this effect can be explained from the stronger modal competition arising in such laser, which enhances the laser instability against optical feedback in particular at higher bias. Indeed, from Figure 3.5, the optical spectrum of GaFP2 exhibits more partition noise due to various longitudinal modes with different amplitudes. In addition, the threshold of GaFP2 is increased due to the free-space platform, hence implying a lower performance in heat evacuation and a reduced relaxation frequency  $f_{RO}$  at  $1.7 \times I_{th}$ .

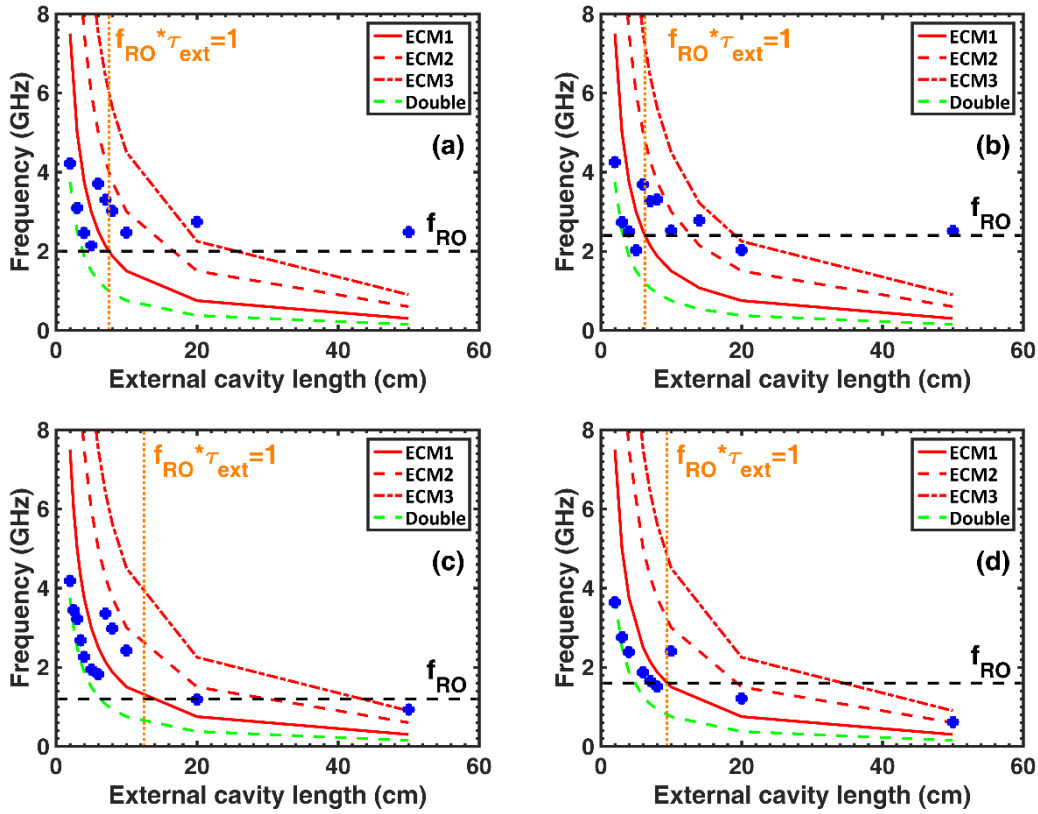


**Figure 5.30** Excited periodic oscillation frequency  $f_P$  as a function of external cavity length for QD lasers GaFP1 and GaFP2 at  $1.5 \times I_{th}$  ((a), (c)) and at  $2 \times I_{th}$  ((b), (d)). The vertical solid lines in orange mark the boundaries between the short- and long-delay feedback regime, and the horizontal one in black gives the ROF  $f_{RO}$  of the free-running laser.

In what follows, we extract the feedback level at which excited periodic and chaotic oscillations take place with respect to the external cavity length. In order to do so, the following

criteria are considered.

- 1) The threshold of excited periodic oscillation (P1) is defined when the excited peak is 5 dB above the free-running noise level;
- 2) The threshold of chaotic oscillations is defined when the noise level of the RF spectrum is more than 10 dB above the free-running noise level.

Using the above criteria, the boundaries between the different regimes are extracted and presented in Figure 5.31.

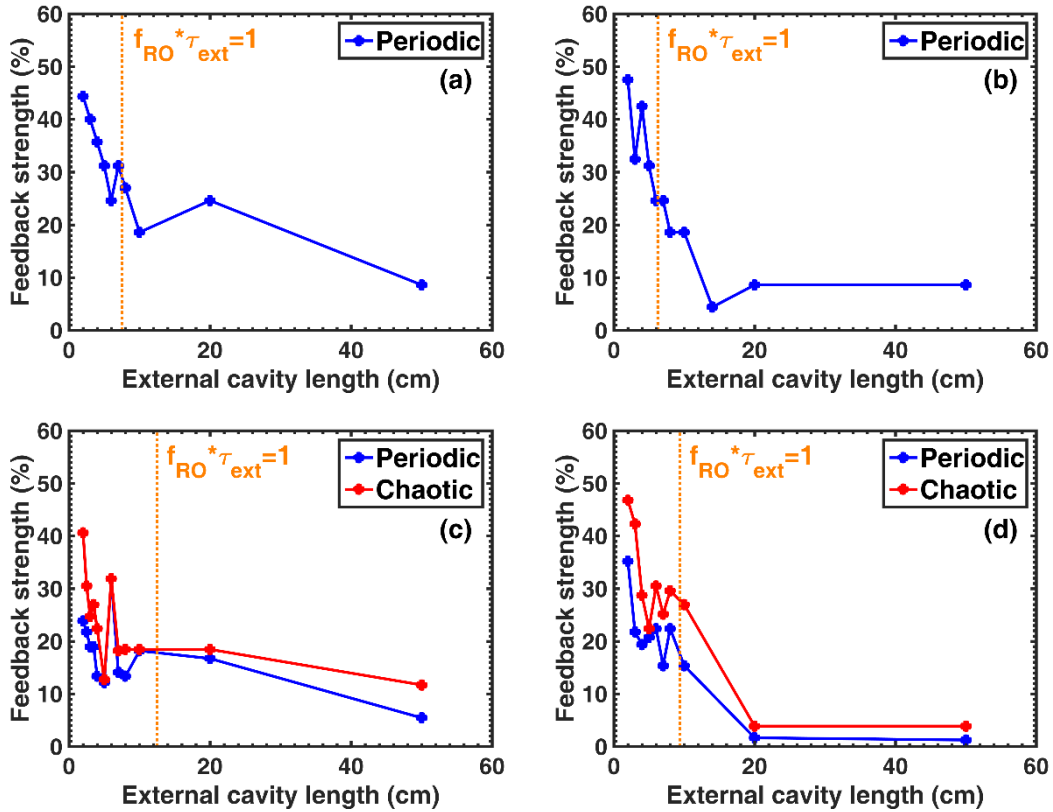


**Figure 5.31.** Boundaries of excited periodic and chaotic oscillations as a function of the external cavity length for QD GS laser GaFP1 and QD ES laser GaFP2 at  $1.5 \times I_{th}$  ((a), (c)) and  $1.7 \times I_{th}$  ((b), (d)). The vertical solid lines in orange mark the boundaries between short- and long-delay feedback regimes.

In Figure 5.31, the vertical solid lines in orange mark the separation between the short- and long-delay feedback regimes. In the case of GS laser GaFP1 (Figure 5.31 (a) and (b)), chaotic oscillations are not observed under any feedback conditions. As previously mentioned, owing to the large damping factor, no route to chaos was observed in this laser. Overall, Figure 5.31 shows that the lower limit of the excited periodic boundaries are always found at a higher feedback level for the GS laser than for the ES one (Figure 5.31 (c) and (d)), which agrees with

the results discussed in the previous section from the long external cavity regime.

Within the short-cavity regime, the boundaries are composed by some residual undulations, which are related to the inferences between the internal and external cavity resonances (see Figure 5.4), similar to what is shown in Figure 5.11. In the particular case of GaFP2, for a certain external cavity length, the increase of the feedback strength can move the fixed point to periodic and chaotic states after crossing the boundaries. Depending on the external cavity length, the laser either constructively or destructively interferes with the external cavity meaning that the extrema in the undulations correspond to situations where the laser is either stable or unstable. As opposed to that, when the lasers operate within the long-cavity regime, the feedback level for which excited periodic and chaotic oscillations take place continuously decreases and tends to become rather independent of the external cavity length. This smooth transition between the short- and long-cavity regimes differs from what occurs in single-frequency DFB lasers for which a clear and abrupt behavior is observed [342].

## 2.4. Self-pulsating dynamics

In this section, we unveil that the ES QD laser can exhibit self-pulsating behaviors both for long- and short delay feedback conditions. In what follows, the external cavity length has been varied from 2 cm to 50 cm. The occurrence of the self-pulsations has been observed from 5 to 50 cm which represent a variation of  $f_{RO} \times \tau_{ext}$  from 0.4 to 10.

Figure 5.32(a) represents the time series of QD laser GaFP2 laser biased at  $1.5 \times I_{th}$  under 8.5% optical feedback, within 20 cm external cavity ( $f_{RO} \times \tau_{ext} = 2$ ). As observed, the temporal waveform shows the occurrence of a dynamics with a fast and regular pulse oscillation whose amplitude is modulated at a slower frequency. The RF spectrum depicted in Figure 5.32 (b) confirms a periodicity of about 600 MHz, which is close to the frequency of the external cavity (750 MHz). Super-harmonics where the frequency components correspond to multiples of the pulsating frequency are also observed. Such observations have already been reported in semiconductor lasers but never on QD devices [351].

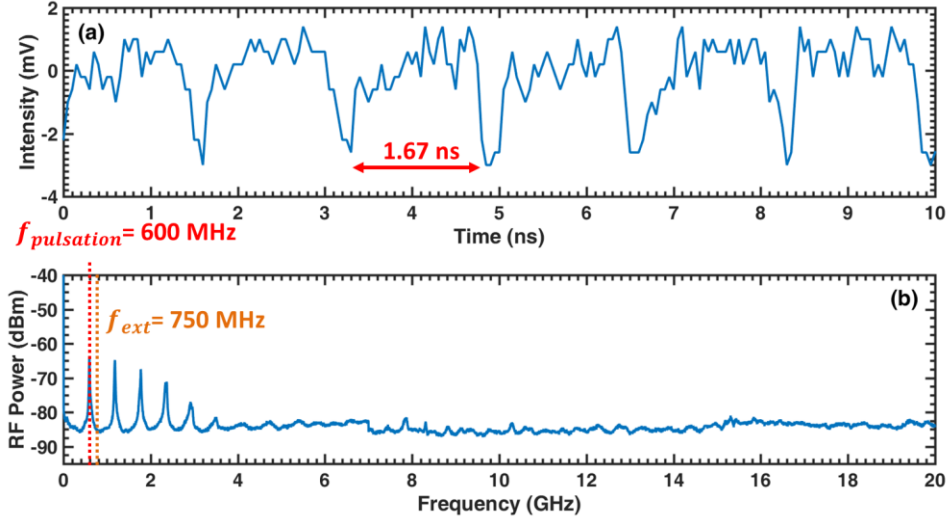


**Figure 5.32.** (a) Temporal waveform and (b) RF spectrum of QD laser GaFP2 cavity at  $1.5 \times I_{th}$  under 8.5% optical feedback in 20 cm long external cavity at  $1.5 \times I_{th}$ .

In Figure 5.32(a), each regular pulse package should include several fast oscillations, which are in our case, not resolved with sufficient precision because of the weak amplitude of the oscillations (Figure 5.32 (b)). Indeed, due to the low optical power emitted by GaFP2 (see Figure 5.26), the received power by the photodiode was limited to about 0.3 mW (Figure 5.25). Overall, the observed temporal waveform looks very similar to the RPP regime observed in Figure 5.15. However, although we observed the occurrence of self-pulsations for cavity lengths down to 5 cm namely for  $f_{RO} \times \tau_{ext} = 0.4$  and  $f_{ext} = 3 \text{ GHz}$ , the pure RPP regime normally takes places within the ultrashort cavity regime for which  $f_{ext} \gg f_{RO}$ . Besides, we do not see the low-frequency component ( $f_{RPP}$ ), which is the signature of the RPP regime whose dynamic results from a global attractor encompassing a large number of modes. Instead, in Figure 5.32 (a), the low-frequency component observed in the temporal waveform is found to be very close to  $f_{ext}$  meaning that the observed dynamics cannot be related to the pure RPP regime. To this end, the pulsing frequency is rather a direct consequence of the interplay between the frequencies of both the relaxation oscillations and the external cavity.

As aforementioned the self-pulsations have been also observed for shorter external cavity lengths. As an example, Figure 5.33 depicts the result obtained with a 6 cm long external cavity ( $f_{RO} \times \tau_{ext} = 0.5$ ). Although the quality of the temporal waveform is not as good as that in Figure 5.31, regular pulse oscillation can still be identified with a fundamental frequency of



about 2 GHz, which is very close to  $f_{ext} = 2.5$  GHz.

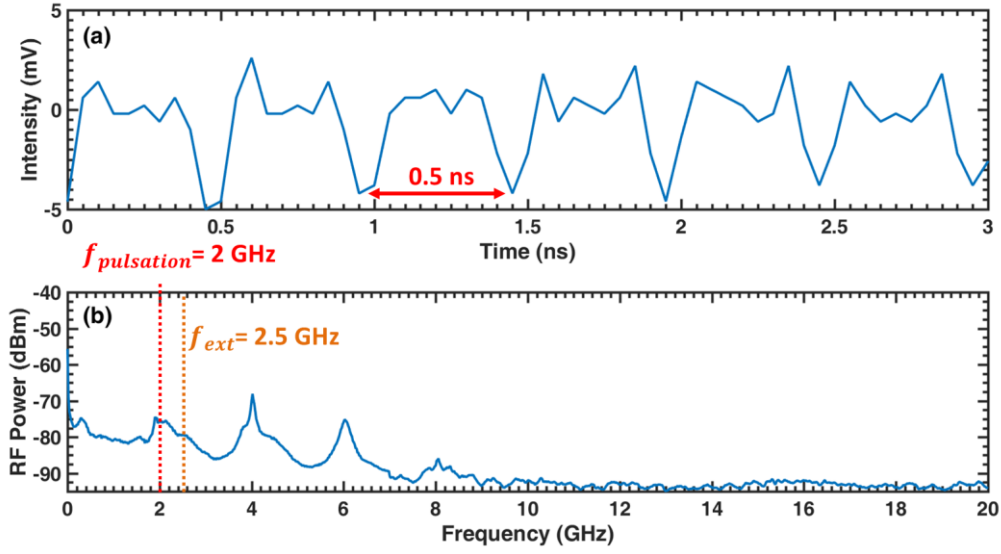


**Figure 5.33.** (a) Temporal waveform and (b) RF spectrum of QD laser GaFP2 under 29% optical feedback in 6 cm long external cavity at  $1.5 \times I_{th}$ .

Further increase of the external cavity length would definitely increase the beating between ECMs hence accelerating the transition from the quasi-RPP to the LFF dynamic for which the short time scale can become irregular and dominated by the relaxation oscillations. Surprisingly, the experiments have also unveiled that such quasi-RPP dynamics is not present for the GS laser while it does take place for the ES one, which is a direct consequence of the stronger damping factor induced by the slower carrier dynamics across the nanostructures.

Due to the coupling between the internal and external cavities, the evaluation of the sensitivity to the feedback phase is of prime importance. Therefore, the impact of the phase has been studied by adding a piezo-electric controller in the setup, allowing a mirror displacement within the micrometer scale. The step was set at  $\pi/3$  with an interval of  $4\pi$ . Figure 5.34, (a) and (b) corresponds to the initial position of the mirror with a phase  $\varphi_0$ , while (c) and (d) are obtained for  $\varphi_0 + 10\pi/3$ . As observed, both RF spectral properties and time series are modified. When changing the phase of the back-reflected light, the RF power is reduced, and the time series is also perturbed. Quantitatively, changing the phase can alter the window in which the quasi-RPP regime was originally observed. These results agree with prior works showing that the sensitivity to the phase is enhanced for shorter cavity lengths [337], [352].

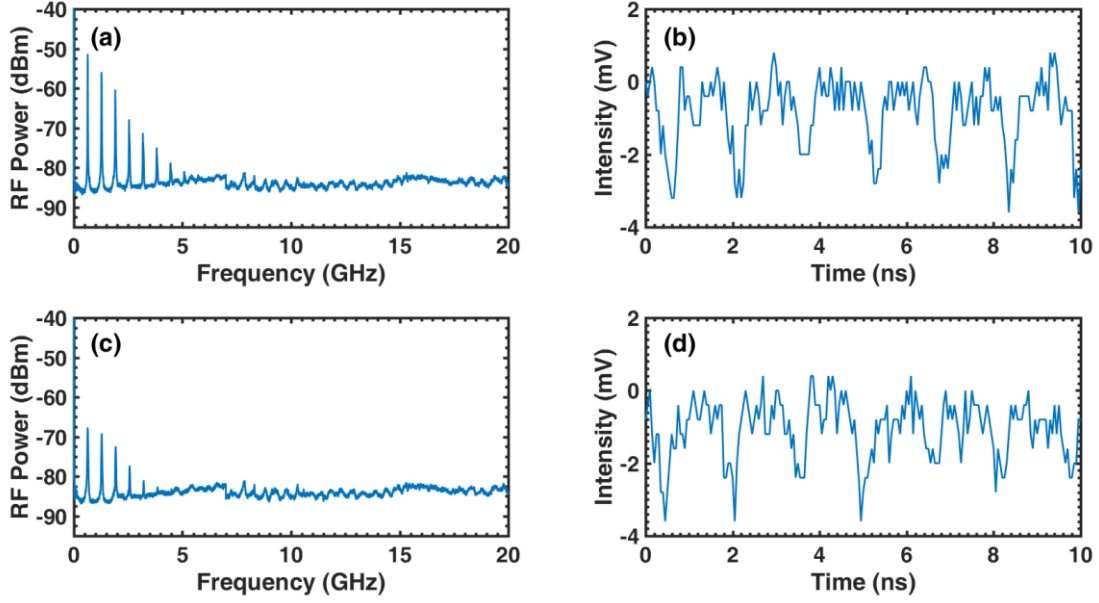


**Figure 5.34.** (a) RF spectrum and (b) temporal waveforms of QD laser GaFP2 for a phase  $\varphi_0$ ; (c) RF spectrum and (d) temporal waveform of GaFP2 for a phase of  $\varphi_0 + 10\pi/3$ .

The self-pulsating regime has been contoured as illustrated in Figure 5.35. P1 and chaotic boundaries are still extracted using the same criteria depicted in section 2.3. Thus, using a multimode semiconductor laser allows observing self-pulsations for external cavity lengths ranging from 5 cm to 50 cm. Besides, results unveil that a higher bias level is more beneficial for the generation of dominant self-pulsations without competing with other complex dynamics. Figure 5.36 shows the extracted self-pulsating frequency as a function of the external cavity length for two operating currents. From this viewgraph, the pulse frequency rather follows the external cavity frequency  $f_{ext}$  represented in blue and values up to 3 GHz are measured for a 5 cm long external cavity length. The driving frequency is rather  $f_{ext}$  instead of  $f_{RO}$ , as illustrated, the self-pulsation frequency is almost superposed with  $f_{ext}$ , the small discrepancy between the curves comes from the higher refractive index in the laser cavity than free-space and from the precision of the measured cavity length.

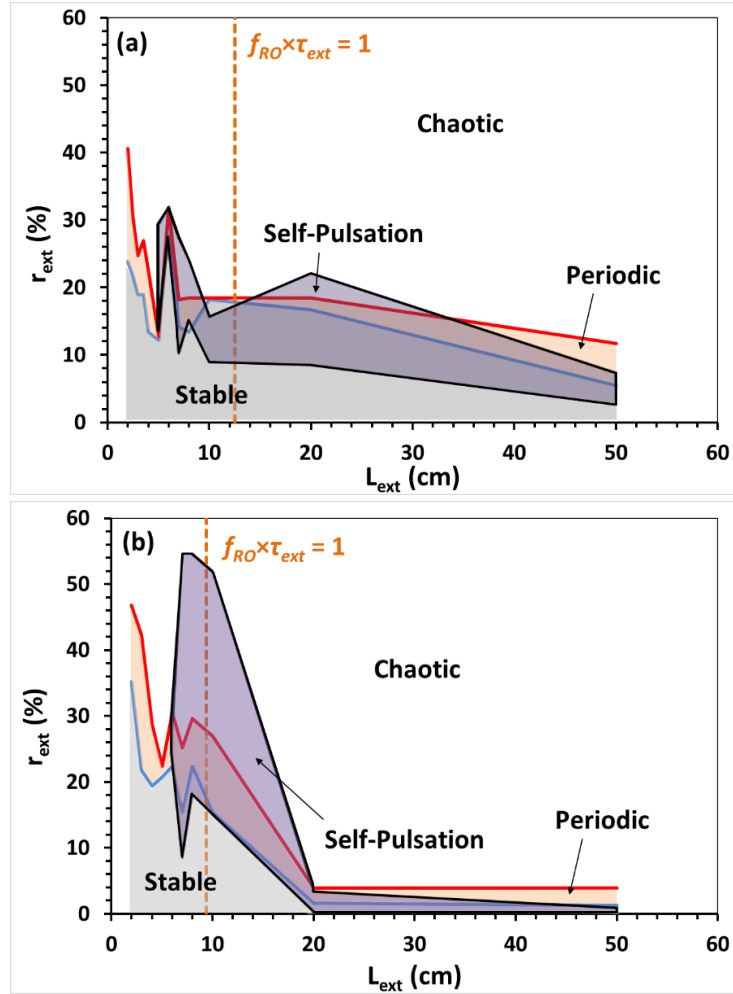


**Figure 5.35.** Mapping of the dynamical transitions with respect to the feedback strength  $r_{ext}$  and the external cavity length  $L_{ext}$  (a)  $1.5 \times$  and (b)  $1.7 \times I_{th}$ . In blue and red, the periodic and chaotic oscillation boundaries; the black contours show the windows of self-pulsations.

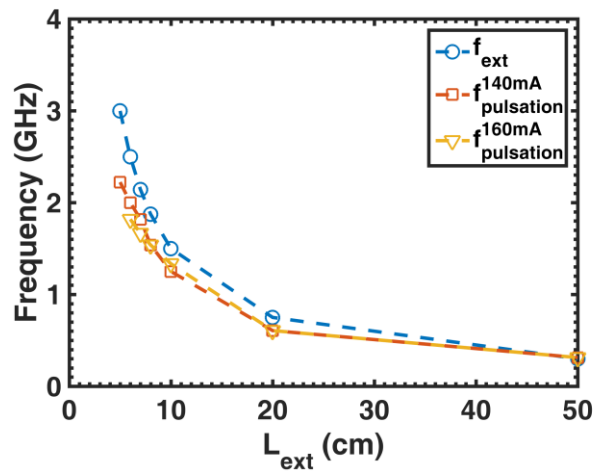


**Figure 5.36.** Measured self-pulsation frequency for ES QD laser GaFP2 as a function of the external cavity length at two bias currents.

## V. Summary

In this chapter, a comprehensive investigation of the multimode optical feedback dynamics was performed. Using two InAs/GaAs QD FP lasers sharing the same gain medium but emitting on two different lasing states, this study allows us accessing directly the material aspects of the ES and GS transitions. The experimental results have unveiled how the carrier dynamics in the QDs affect the sensitivity to external optical perturbations.

Under long-delay optical feedback, the ES laser can be easily destabilized while the GS one is found much more resistant with no clear route to chaos. Although the ES laser is potentially faster, its smaller damping rate combined to the strong partition noise contribute to increase the sensitivity to external optical feedback which is an important feature to be taken into account for the realization of future telecom modules.

Under short-delay feedback, a higher feedback sensitivity of the ES transition is found as well. Furthermore, we have unveiled the existence of a quasi-RPP regime resulting in self-pulsating behavior with pulse emission close to external cavity frequency. The standard way of generating self-pulsations usually relies on using optical nonlinearities through FWM and optical injection [103], [353].

Overall, this work is important not only for the understanding of QD laser dynamics but also for the generation of self-pulsating devices as well as for the realization of feedback resistant optical transmitters for short-reach communication links. In particular, the analysis of the pulsing states is driven by the growing interest in microwave photonic technology from which exciting perspectives can be envisioned such as the fabrication of an integrated device in a PIC capable of delivering microwave signals without the need of electrical modulation. Next experiments will be concentrated on DFB lasers emitting on different lasing states and further modeling is now required to better understand the multimode optical feedback dynamics.

## Chapter VI. Conclusions and perspectives

This thesis was devoted to study optical nonlinearities of InAs/GaAs and InAs/InP QD lasers operating under external control. Such nonlinearities were excited either from optical injection or external optical feedback in the view of developing all-optical wavelength-converters with improved performance as well as optical feedback-resistant transmitters. In addition, coherent systems and future chip-scale atomic clocks requires the implementation of optical sources with narrow spectral linewidth. This was another objective of the thesis where the benefits of the QD technology have allowed reaching optical linewidth as low as 160 kHz.

In the first place, the fundamental properties of both QD FP and DFB lasers investigated throughout this PhD work were presented with a focus on the linewidth broadening factor ( $\alpha_H$ -factor) and the optical spectral linewidth. Among the main conclusions, the ASE method was found to be the most straightforward technique to extract the  $\alpha_H$ -factor with a good precision providing that the thermal effects are properly removed. Above the laser threshold, it was shown that the optical injection method can also be used to properly retrieve the  $\alpha_H$ -factor namely by curve-fitting the FWM induced power spectrum. As opposed to other optical injection related methods, the extraction was found here much simpler since it does not require to track the minimum of the Hopf local bifurcation or to determine the locking boundaries. Although the values are in a rather good agreement with those obtained from the ASE method, further investigation is however required to improve the accuracy as well as to better understand the observed behavior with the bias current. As for the modulation, the FM/AM technique was found to overestimate the  $\alpha_H$ -factor of the GS lasing transition hence reflecting more a current modulation driven  $\alpha_H$ -factor rather than an optical noise driven one. In other words, the applicability of the FM/AM method to complex structures with multiple electronic states is limited in particular when the phase noise needs to be properly characterized like in coherent communication systems. However, in a standard transmission system, phase noise is not relevant because information is only transmitted from the amplitude of the signal and can be detected without measuring the phase. Owing to the very

low population inversion factor arising from the QD technology, a spectral linewidth as low as 160 kHz was reported in an InAs/InP QD DFB laser. Further reduction down to 100 kHz was also obtained by stabilizing the laser under optical feedback. Applications of narrow linewidth lasers are vital not only for coherent communications but also for other applications like chip-scale atomic clocks.

The following part of the thesis has investigated the potential of optical injection for wavelength conversion. Using optically-injected InAs/InP and InAs/GaAs QD lasers, large conversion efficiencies with high optical signal-to-noise ratios were unveiled. The static conversion bandwidth was extended far in the terahertz window with a quasi-symmetrical response between up- and down-converted signals. Although the conversion level was found similar to that of SOA devices, it does not require large pump/probe powers and bias currents. A comprehensive investigation of operating conditions (bias, pump wavelength, etc.) as well as external (injection strength and frequency detuning) and device parameters (length and ridge waveguide) were considered with the view to determine realistic guidelines for the realization of future wavelength converters. A good conversion efficiency requires a sufficient number of QD/QDash layers ( $> 5$ ) in the active area with a relatively high density ( $> 5 \times 10^{10} \text{ cm}^{-2}$ ). Smaller nanostructures can increase the SHB contribution while larger ones provide higher carrier population and shallow QDs can benefit from additional CH and TPA contributions. On the other hand, QDash nanostructures demonstrate better FWM performance compared to QDs because of the shape of the DOS function and the nanostructure polarization. A low  $\alpha_H$ -factor is also desired to symmetrize up- and down-conversions. To this end, a narrow inhomogeneous gain broadening is vital, hence keeping the oscillator strength close to the resonant dot populations. The laser geometry also influences the wavelength conversion, meaning there is a tradeoff between the interaction length (1 – 2 mm) and the ridge width (2 – 4  $\mu\text{m}$ ). Lastly, injection conditions such as the master power and the injection frequency detuning must be properly adjusted with respect to the locking conditions. The dynamic signal conversion has also been realized. At a pump-probe detuning at -100 GHz, the converted signal modulated at 2.5 Gbps has achieved an error-free transmission with less than 1 dB penalties, which is promising for future experiments at higher bit rates. This work has unveiled the potential of using optically-injected FP laser cavities as all-optical wavelength converters and

routing light in photonics integrated circuits.

The last part of the thesis has investigated the multimode delay dynamics of InAs/GaAs QD lasers emitting on different lasing states. Under long-delay optical feedback, the ES laser can easily be destabilized while the GS one was found to be much more resistant with no clear route to chaos. Although the ES laser is faster, its smaller damping rate combined to the stronger partition noise contribute to increase the sensitivity to external optical feedback which is an important feature to be taken into account for the realization of future telecom modules. Under short-delay feedback, a higher feedback sensitivity of the ES transition was found as well. Furthermore, experiments have unveiled the birth of self-pulsations with a pulse repetition rate tunable up to several GHz with the external cavity length. The regular behavior of the self-pulsation resembles to the RPP regime of the short-cavity regime however, the pulsations have been observed also with the long-delay feedback. Overall, this work will be very helpful for the development of feedback resistant transmitters compatible with short-reach communication links as well as for the generation of self-pulsating devices and microwave signals in PICs.

In future steps, various theoretical and experimental works can be envisioned

- First, regarding the narrow linewidth lasers, further work needs to be done to keep narrowing the optical linewidth, which is of paramount importance to probe atomic frequency standards to reduce drift, leading to applications in chip-scale atomic clocks. In addition, there has been a ramping interest for using coherent detection for silicon photonics applications meaning that the problematic of narrow linewidth lasers will be also a real challenge in a PIC [354]. As such, the development of novel hybrid sources on silicon with ultra-low phase noise is worth exploring. Future investigations will consider hybrid III-V QD DFB semiconductor lasers fabricated in collaboration with Nokia Bell Labs. Generating the light in the III-V material and storing the photons in the low-loss silicon material could be very promising to reach a few kHz optical linewidths, which would be compatible for future 64QAM modulation format [92].

- Secondly, further studies are needed to fully unveil the potential of FWM conversion

performance with optically-injected QD lasers. Future experiments may want to consider packaged laser devices with enhanced stability, and low-noise modulation signal sources including frequency synthesizer as well as tunable lasers to push further both the modulation rate and the pump-probe detuning. In particular, DFB laser devices with high-quality gratings and narrow linewidth need to be considered to complete this study. This would be more powerful for integrated optical converters since the DFB peak can directly be used as a pump. Furthermore, it has been demonstrated in the literature that FWM is able to convert advanced modulation formats [101], [105], hence experimental verification with a FP laser cavity will be part of our future work. With the recent advances in the silicon photonics technologies, the work performed in this thesis can also open the way to the realization of all-optical energy saving routers integrated on a silicon chip [22], [24], [25]. Last but not the least, FWM generation using the pure ES lasing emission is also to be an interesting perspective. Owing to the larger material gain and the reduced linewidth broadening factor from the ES, better wavelength conversion performance can be expected [355].

- Thirdly, the work initiated on the optical feedback dynamics with QD lasers emitting on different lasing states will keep ramping up. In order to better understand the complex dynamics occurring in QD FP lasers, numerical models including the multimode configuration will be considered. To this end, simulations will analyze the underlying physics of the complex route-to-chaos observed in such lasers with respect to the different lasing states. As a perspective, we would like also to conduct further experiments with single-frequency QD lasers emitting either on the GS or the ES. Such investigation will be absolutely necessary for analyzing the potential of using such DFB transmitters for high-speed applications [132]. Last but not the least, the self-pulsating regime identified in this work needs much more investigations both theoretically and experimentally. In particular, it would be meaningful to identify the knobs controlling the birth of the self-pulsations in order to optimize the performance and to identify the limitations of such regime. It would be important to further reduce the external cavity to fully probe the pure RPP regime from which the laser output can resemble to that of a mode-locked laser. In such way, phase-locking between ECMs would result in the emission of pulses at a frequency equal to the external cavity frequency. The



analysis of the pulsing states is strongly driven by the growing interest in microwave photonic technology from which exciting perspectives can be envisioned such as the fabrication of an integrated device in a PIC capable of delivering microwave signals without the need of electrical modulation [356].

- A long term perspective would also concern the development of mid-infrared (MIR) silicon photonic solutions [357]. The MIR silicon is currently very attractive as Si and Ge are transparent up to approximately 8 and 15  $\mu\text{m}$ , leading to a wide range of applications in biochemical and environmental sensing, medicine, astronomy and obviously in communications. The most popular silicon photonic platform that is the silicon-on-insulator (SOI) can be used up to develop optical solutions up to about 4  $\mu\text{m}$ . A number of SOI devices, such as low-loss waveguides, couplers, splitters, filters, interferometers and spectrometers already exist. Strong non-linear effects with FWM have also been demonstrated while multiple breakthroughs on modulators and detectors have been published. Active devices such as hybrid III–V sources integrated on SO have also been reported over the last years which means that the technology is today relatively mature. Above all, a recent work has unveiled the first MIR quantum cascade laser on silicon [358]. As a future work, the dynamics of semiconductor lasers integrated on silicon could be extended to the MIR silicon. The integration of novel active devices like quantum cascade lasers operating at longer wavelengths can reveal novel temporal dynamics. Indeed, as recently observed, although quantum cascade lasers have a sub-picosecond carrier dynamics and an ultra-large damping factor, bubble of chaotic dynamics have been identified [359]. To this end, nonlinear integrated photonics operating up to about 4  $\mu\text{m}$  and including quantum cascade emitters can also be envisioned for the development of secured communication channels integrated on a PIC.



# Appendix 1: Synthèse en français

## I. Introduction

L'évolution actuelle des systèmes de communications optiques est telle que la circulation d'information n'est plus exclusivement limitée par les liens longues-distances transocéaniques ou par les réseaux cœurs. De nombreuses applications courtes distances comme les réseaux d'accès où les débits des systèmes amenant la fibre chez l'abonné doivent être maximisés et les connexions internes et externes des centres de données transportent un trafic de données important produit en partie par les applications de type « Big Data ». Les critères imposés par ces nouvelles architectures notamment en termes de coût et consommation énergétique doivent être pris en compte en particulier par le déploiement de nouveaux composants d'extrémités. Grâce au très fort confinement des porteurs, les lasers à boîtes quantiques constituent une classe d'oscillateurs présentant des caractéristiques remarquables notamment en termes de courant de seuil et de stabilité thermique. En particulier, l'application d'une perturbation optique externe permet d'exploiter les non-linéarités optiques des boîtes quantiques pour la réalisation de convertisseurs en longueur d'onde performants ou de transmetteurs à haut-débit fonctionnant sans isolateur optique. Ce dernier point est particulièrement critique dans les réseaux courtes-distances où l'utilisation de sources modulées directement reste une solution technologique importante. Ce travail de thèse réalisé sur des structures lasers à base d'Arséniure de Gallium (GaAs) et de Phosphure d'Indium (InP) montre la possibilité d'améliorer l'efficacité de conversion nonlinéaire par injection optique et de générer de nombreuses dynamiques dans des oscillateurs rétroactionnés et émettant sur différents états quantiques. Par ailleurs, le déploiement massif des systèmes cohérents mais également la conception des futures horloges atomiques sur puces nécessite l'utilisation de sources optiques à faible largeur de raie et ce afin de limiter la sensibilité de la réception au bruit de phase du transmetteur et de l'oscillateur local et induire un taux d'erreur binaire important. La conception de laser à faible largeur spectrale constitue un autre objectif de ce travail thèse. Les avantages de la technologie boîtes quantiques ont été mis à profit pour d'atteindre une largeur spectrale de 160 kHz (100 kHz en présence de

rétroaction optique) ce qui est de première importance pour les applications susmentionnées.

## II. Conversion nonlinéaire en longueur d'onde dans les lasers QD

### 1. Principe du mélange à quatre-ondes

Le mélange à quatre ondes (FWM, four-wave mixing en terme anglais) décrit le phénomène qui se produit lorsque deux champs co-polarisés  $E_1$  et  $E_2$  aux fréquences  $f_1$  et  $\omega f_2$  co-propagent à l'intérieur dans un milieu de gain nonlinéaire ayant une susceptibilité nonlinéaire de troisième ordre ( $\chi^{(3)}$ ). Le battement entre eux conduit à la génération de deux nouveaux champs  $E_3$  et  $E_4$ , aux fréquences  $f_3 = f_1 - (f_2 - f_1)$  et  $f_4 = f_2 + (f_2 - f_1)$ . Dans cette configuration décrite,  $f_1$  et  $f_2$  sont supposés différents l'un de l'autre, ainsi que  $\omega f_3$  et  $f_4$ . Un tel cas est appelé le FWM non dégénéré (NDFWM), comme l'illustre la Figure A2.1. D'autres configurations de FWM existent en ce qui concerne les caractéristiques spectroscopiques, c'est-à-dire le FWM dégénéré et le FWM quasi-dégénéré où deux des quatre champs coïncident ou coïncident presque à la même fréquence [257]. Dans cette thèse, nous nous concentrerons sur le NDFWM, le FWM dégénéré et quasi-dégénéré ne sera pas présenté.

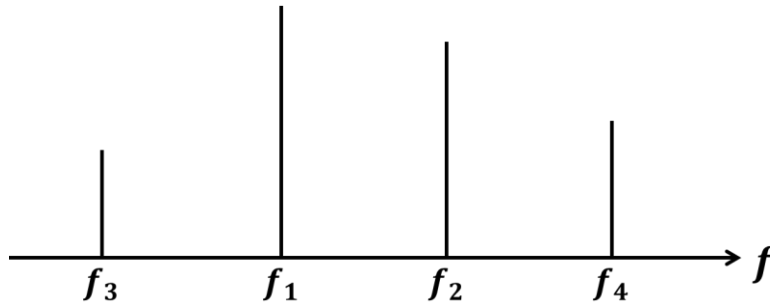


**Figure A2.1.** Illustration du processus NDFWM, l'interaction des champs  $E_1$  et  $E_2$  aux fréquences de  $\omega_1$  et  $\omega_2$  conduit à la génération des champs  $E_3$  et  $E_4$  à  $\omega_3$  et  $\omega_4$ .

Par convention, le champ le plus fort des  $E_1$  et  $E_2$  est appelé la pompe et l'autre sonde. La différence de fréquence  $\Delta f$  entre la pompe et la sonde est appelée le désaccord de fréquentiel. Dans ce qui suit, on désignera  $\Delta f = f_{sonde} - f_{pompe}$  en tant que désaccord de fréquence et:

- la conversion montant pour le désaccord négatif ( $\Delta f < 0$ ), lorsque la fréquence du signal converti est supérieure à celle de la pompe;
- la conversion descendante pour le désaccord positif ( $\Delta f > 0$ ), lorsque la fréquence du signal converti est inférieure à celle de la pompe.

La notion du rendement de conversion (CE, conversion efficiency en terme anglais) est utilisé pour caractériser la performance de la conversion, il est défini comme étant le rapport entre la puissance du signal converti à la sortie  $P_{conv}$  et la puissance d'entrée de la sonde  $P_{sonde,entrée}$ :

$$\eta_{CE} = \frac{P_{conv}}{P_{sonde,entrée}} \quad (A2.1)$$

Le terme CE normalisé (NCE) peut aussi être engagé pour décrire la conversion, il est défini comme étant le rapport entre la puissance du signal converti à la sortie  $P_{conv}$  et le produit de la puissance de sortie de la sonde  $P_{sonde,sortie}$  multipliée par la puissance de sortie de la pompe  $P_{pompe,sortie}$  au carré:

$$\eta_{NCE} = \frac{P_{conv}}{P_{sonde,entrée} P_{pompe,sortie}^2} \quad (A2.2)$$

## 2. Mélange à quatre-ondes dans les lasers QD

Le FWM est une technique décisive qui a été largement utilisée dans les systèmes de multiplexage par répartition en longueur d'onde, en particulier pour la conversion en longueur d'onde, le chirping de fréquence négative et la compensation de dispersion de la longueur de longueur de fibre [103], [104]. Avec l'émergence récente de systèmes commerciaux cohérents, FWM peut également être envisagé pour développer de nouveaux types de convertisseurs de longueur d'onde pour tous les formats de modulation avancés [101], [105], ainsi que pour le traitement du signal tout-optique [106] dans les circuits intégrés photoniques (PIC) à l'avenir [107].

La plupart des travaux publiés ont montré que FWM peut être généré dans différents milieux nonlinéaires tels que la silice nonlinéaire et les fibres de cristal photonique [108], [109], les micro-anneaux à base de silicium [110]-[112], et les amplificateurs optiques à semi-

conducteur (SOA) [113], [114]. Bien que l'utilisation de fibres optiques très non linéaires permette une conversion très efficace, elle nécessite habituellement une longueur d'interaction de plusieurs mètres et une grande puissance de pompe, qui ne conviennent pas à l'intégration monolithique. Un autre problème important avec les fibres optiques est que la longueur de fibre requise combinée à une opération loin de la longueur d'onde de dispersion nulle affecte fortement le mélange d'ondes et peut altérer l'efficacité de conversion. D'autre part, des travaux récents ont signalé un FWM efficace avec une consommation d'énergie relativement faible dans les résonateurs à micro-anneaux. Cependant, de tels résonateurs nécessitent habituellement 4 ports couplés verticalement aux guides d'ondes de bus à faible perte, et les coûts de fabrication peuvent donc être un problème par rapport à une SOA simple. Dans le dernier, FWM est obtenu à partir du battement entre la pompe incidente et les faisceaux de la sonde et la mise en phase est assurée en raison de l'isolement de la structure.

D'un point de vue microscopique, le mélange des ondes est piloté par la susceptibilité non linéaire de troisième ordre  $\chi^{(3)}$  par différents mécanismes [116]. Dans la région de basse fréquence, le battement entre la pompe et la sonde provoque une pulsation de densité de porteurs (CDP, carrier density pulsation en terme anglais) qui améliore  $\chi^{(3)}$ , donc la conversion statique, mais avec une vitesse de réponse lente intrinsèquement limitée par le temps de vie des porteurs des processus d'interbande (échelle de temps de nanoseconde). En revanche, le chauffage de porteurs (CH, carrier heating en terme anglais) et le brûlage des trous spectraux (SHB, spectral hole burning en terme anglais), se produisant dans les échelles de temps de la sub-picoseconde, permettent de pousser la conversion de fréquence dynamique sur des largeurs de bande beaucoup plus grandes, permettant des conversions de signaux avec des débits de modulation plus rapides. Bien que SHB et CH contribuent à augmenter la bande passante, ceux-ci réduisent également l'amplitude du  $\chi^{(3)}$ , ce qui entraîne un compromis entre l'efficacité et la bande passante de la conversion. Enfin, un autre effet néfaste qui doit être éliminé pour des applications pratiques est l'asymétrie de l'efficacité de conversion (c'est-à-dire entre les signaux converti vers le haut et vers le bas), qui découle des contributions hors phase à  $\chi^{(3)}$  du CDP, CH et SHB [103], [117]. Afin de surmonter ces limites, les points quantiques semi-conducteurs (QD) constituent une classe de nanostructures présentant de grandes non linéarités optiques et des vitesses de réponse élevées en raison des répartitions

rapides du porteur-transporteur et du transporteur-phonon [117], [119], [120]. Par exemple, les travaux antérieurs ont révélé que le FWM rapide peut être obtenu en milieu QD à travers des trous spectraux plus profonds provenant de la vitesse de diffusion rapide des porteurs dans les états appauvris [119]. Cependant, contrairement aux matériaux de puits quantiques (QW, quantum well en terme anglais), où la grande densité de support augmente le CH par absorption de porteurs libres, ce dernier est moins prédominant dans les QD en particulier pour les nanostructures avec un grand décalage de bande de conduction. Par conséquent, dans les matériaux QD, la symétrie de la conversion découlant de la différence de phase entre CDP, SHB et CH, est principalement pilotée par les deux premières contributions via le facteur  $\alpha_H$  [117]. Par conséquent, par opposition aux matériaux en bulk et en QW, une réponse quasi symétrique entre les signaux convertis vers le haut et vers le bas peut être obtenue avec des matériaux QD car le LEF réduit conduit à des contributions presque en phase de CDP et de SHB. Les études expérimentales ont principalement porté sur les SOA de QD en raison de leur large gain linéaire et de longues longueurs d'interaction [113], [114], [117], [122].

En revanche, on sait peu sur le potentiel de l'utilisation d'oscillateurs résonnants QD basés sur des cavités Fabry-Pérot (FP) ou à rétroaction distribuée (DFB, distributed feedback and terme anglais). En particulier, en profitant des résonances de la cavité et du bruit d'émission spontanée amplifié réduit (ASE, amplified spontaneous emission en terme anglais), les oscillateurs résonnants peuvent constituer une alternative capable de produire des FWM hautement non dégénérés avec une amplitude et une bande passante améliorées et des dimensions plus compactes. Par exemple, dans les lasers DFB où le mode Bragg est directement utilisé comme pompe, les articles précédents ont signalé des conversions de fréquence efficaces pour les matériaux actifs QW et QD [262]-[264]. Cependant, l'un des inconvénients majeurs dans l'utilisation de DFB est que l'efficacité intrinsèque non linéaire reste très sensible aux fonctionnalités DFB complexes telles que les effets de phase facette et le coefficient de couplage de grille, qui sont difficiles à contrôler d'un appareil à l'autre sans optimisation de conception et de traitement [265].

Dans cette partie, nous présentons une partie des études expérimentales sur le NDFWM qui se produit dans un laser QD FP InAs/InP. Afin de compresser l'ASE plus fort et de surmonter les limitations de bande passantes issues de la ROF, les lasers à l'étude sont également

optiquement verrouillés par injection [125]. Dans des conditions d'injection appropriées, le battement entre la fréquence de la lumière injectée et la fréquence de résonance de la cavité domine le comportement dynamique et améliore une résonance de la modulation du support à des fréquences supérieures à la ROF. Par conséquent, le verrouillage par injection peut permettre une modulation plus rapide des signaux convertis comme déjà signalé pour les lasers DFB QW InGaAs/InP [124] et a récemment été utilisé avec des lasers FP QD InAs/InP fabriqués avec différents types de nanomatériaux [269], [272].

### 3. Configurations expérimentales

Le laser étudié est un laser QD FP InAs/InP crû sur un substrat InP de type n orienté (001) [53]. Un cladding de type n a été déposé pour la première fois, suivie d'un cœur de guidage d'onde 1,15Q de 350 nm d'épaisseur contenant les couches de QD dans le centre. La densité des boîtes par couche est d'environ  $3,5 \times 10^{10} \text{ cm}^{-2}$ . Une couche de cladding InP de type p supérieure a ensuite été déposée (contenant une étape de gravure pour la fabrication de la crête), suivie d'une couche de contact InGaAs p-type fortement dopée. Un guide d'ondes de 3  $\mu\text{m}$  de large a ensuite été fabriqué, et la cavité clivée de 1 mm de long a été montée sur un substrat saphir. Les courbes PIV (puissance – courant – tension) à 20°C sont montrées dans la Figure A2.2 (a). Le courant du seuil  $I_{th}$  de ce laser est de 39 mA, avec un rendement externe de 26%. Figure A2.2 (b) représente un spectre optique du laser alimenté à  $2.5 \times I_{th}$  à 20°C. La longueur d'onde centrale du laser est autour de 1543 nm.

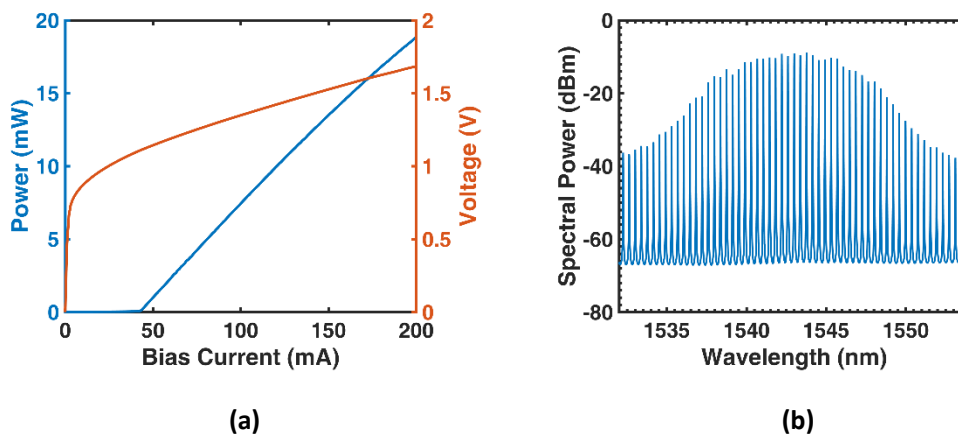


**Figure A2.2.** (a) courbes PIV et (b) spectre optique du laser QD FP InAs/InP.



L'appareil mesuré avait un courant de seuil de 39 mA correspondant à un courant de seuil Intensité de densité Dans la zone active de  $1,3 \text{ kA} / \text{cm}^2$ .

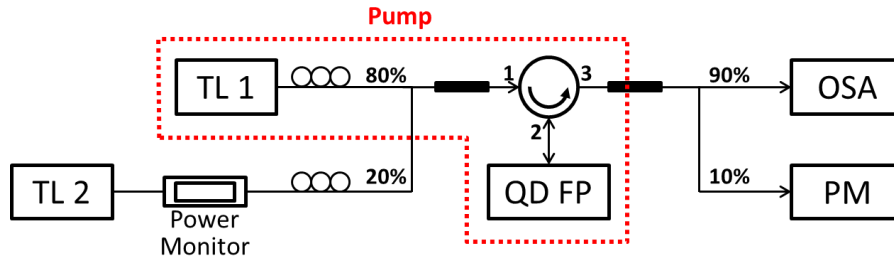


**Figure A2.3.** Configuration expérimentale pour l'étude NDFWM, le signal de pompe provient du laser accordable TL1, dont le faisceau est injecté dans le laser QD et le verrouille par injection.

La Figure A2.3 montre la configuration expérimentale utilisée pour l'enquête NDFWM. Les éléments figurant dans le cadre rouge permettent de verrouiller l'injection du laser QD FP. Le deuxième laser accordable TL2 génère le signal de sonde, un puissance-mètre, qui contient un atténuateur intégré, contrôle sa puissance. Les contrôleurs de polarisation sont ajoutés à la fois à la sortie des lasers TL1 et TL2. Les contrôleurs de polarisation permettent de faire correspondre les polarisations des deux lasers accordables à celle de la lumière émise par le laser esclave. Généralement, pour assurer un verrouillage stable, la puissance de TL1 est supérieure à TL2, nous avons donc utilisé un couplage inégal, 20% pour le TL2 et 80% pour le TL1. L'injection dans la cavité laser QD s'effectue par une fibre à extrémité de lentille, cette dernière étant également utilisée pour collecter la lumière émise par le laser. La lumière recueillie retourne vers le circulateur et sort par le port 3. Un OSA est utilisé pour acquérir le spectre optique et un powermeter (PM) est utilisé pour surveiller la puissance de sortie pour assurer la stabilité du couplage.

#### 4. Conversion statique

La Figure A2.4 (a) présente l'évolution de la CE en fonction du désaccord fréquentiel pompe-sonde  $\Delta f$  lorsque le mode FP situé au pic de gain est verrouillé comme pompe. Le CE pour la conversion vers le haut et vers le bas est représenté en cercles rouge et bleu respectivement sur un seul graphique pour comparaison.

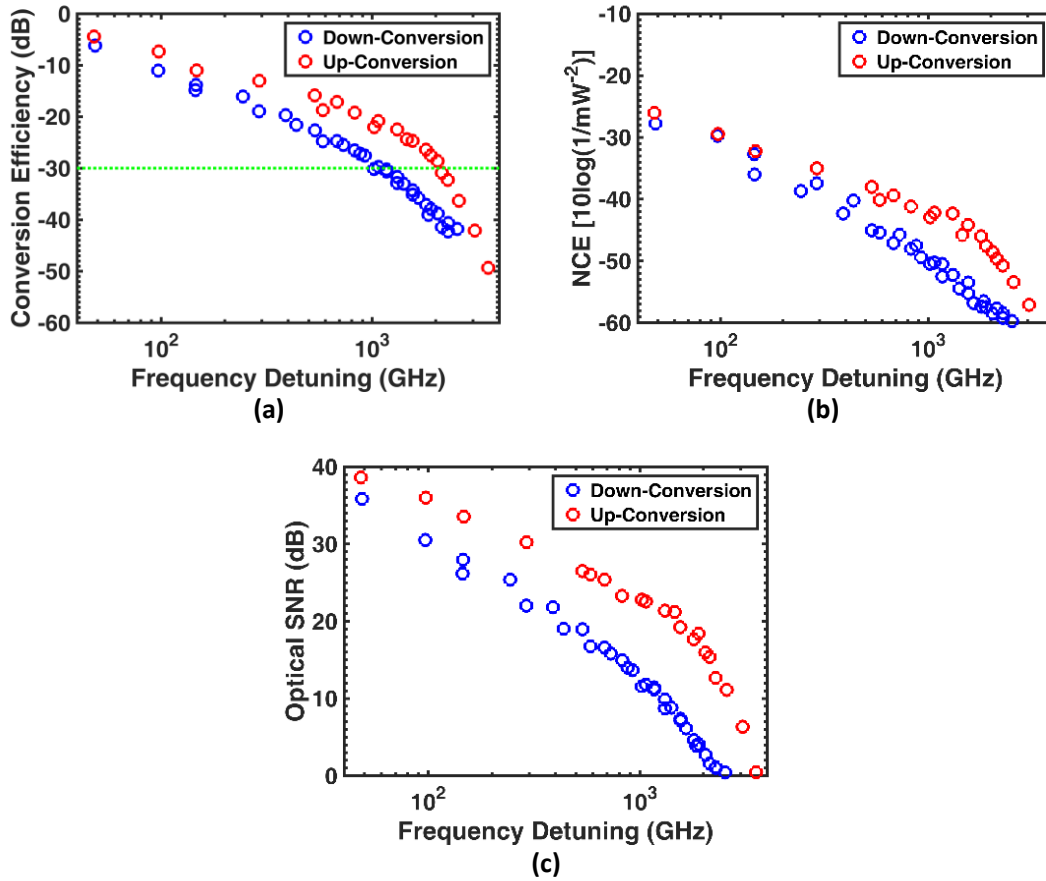


**Figure A2.4.** Mesuré CE (a), NCE (b) et OSNR (c) de FWM dans le laser QD en fonction du désaccord de fréquence de la pompe-sonde.

Dans la Figure A2.4, chaque point du profil CE est obtenu en accordant la fréquence de la sonde de manière à coïncider avec l'un des modes de cavité du laser QD, où la conversion maximale est obtenue. Les désaccords de longueur d'onde correspondent donc des multiples de la plage spectrale libre du laser à verrouillage par injection, et correspondent aux maxima locaux dans la courbe du CE en fonction du désaccord de la pompe-sonde. Comme prévu, la conversion statique se révèle plus efficace lorsque le mécanisme CDP domine, à savoir pour les désaccords de quelques GHz, avec un CE maximum d'environ -4 dB. Plus important encore, un CE au-dessus de -30 dB (ligne de points horizontale de la Figure A2.4 (a)) est atteint entre -1 THz et +2 THz. À des décongestionnements de fréquence plus importants, SHB et CH dominant complètement, ce qui permet une conversion plus faible mais avec CE supérieur à -50 dB pour les désaccords entre -2,5 THz et +3,5 THz. Ces résultats sont meilleurs que ceux trouvés avec les SOA basés sur InP [117].

- L'efficacité mesurée est de l'ordre de -3 dB à faible désaccord qui se compare bien à celle dans le SOA dans la référence [21];
- La bande passante de conversion est beaucoup plus grande de 6 THz au total contre 2 THz.
- La cavité laser mesure seulement 1 mm de long et le niveau de pompage est inférieur à 120 mA, ce qui est de loin inférieur à [21] où le courant de polarisation était de 7 A pour une SOA de 25 mm de long.
- L'asymétrie de CE entre la conversion vers le haut et vers le bas est d'environ 9 dB, ce qui est supérieur à celui de la SOA (~ 5 dB).

Comme susmentionné, la dimension des boîtes quantiques de ce laser est relativement grande (~ 50 nm), avec un élargissement inhomogène autour de 40 meV. Ainsi, nous pouvons nous attendre à ce que la population de porteurs en points augmente et que la contribution de CH soit améliorée [119]. En outre, une dimension des boîtes plus grande implique moins de confinement quantique, donc l'ES sera plus proche de la RS ci-dessus, ce qui signifie que les processus de capture seront accélérés, donc les contributions de CDP seront améliorées. En outre, l'effet d'absorption de deux photons (TPA, two-photon absorption en terme anglais), qui correspond à l'excitation du porteur dans la couche bulk par l'absorption simultanée de deux photons, peut contribuer à la récupération du gain et ainsi améliorer le CE.

La Figure A2.4 (b) présente l'évolution des RCE correspondants. Comme le laser FP est verrouillé de manière stable par un laser externe avec une sortie relativement stable, le NCE mesuré suit la même tendance que le profil CE. Comme dans le NCE, la puissance du signal converti est divisée par la puissance de la pompe carrée et la puissance de la sonde après la propagation, qui ont déjà été amplifiées par la zone active, de sorte que l'amplitude correspondante est faible.

La Figure A2.4 (c) montre l'OSNR. Alors que les OSNR supérieurs à 20 dB sont atteints entre -500 GHz et +1,5 THz (conversion ascendante), le signal converti diminue rapidement au niveau de bruit pour un désaccord absolu supérieur à 2 THz. En outre, les expériences montrent un OSNR plus grand associé à une extension claire de la gamme de désaccord de fréquence NDFWM plus loin dans la fenêtre THz, sans avoir des longueurs d'interaction très longues [122] par rapport aux autres résultats du tableau 4.1.

La Figure A2.3 révèle que l'asymétrie entre les profils de conversion ascendante et descendante n'est pas complètement éliminée car le facteur  $\alpha_H$  mesuré sur ce laser est d'environ 1,4, d'où la condition de phase apparaissant entre les processus non linéaires (CDP, SHB et CH) produit toujours des interférences destructrices, comme indiqué dans la figure 4.4.

## 5. Extraction de la susceptibilité nonlinéaire de troisième-order $\chi^{(3)}$

Le NCE est connecté à la susceptibilité  $\chi^{(3)}$ , de sorte qu'il donne une idée de la conversion nonlinéaire au niveau matériel, cette relation peut s'exprimer sous forme de [261]:

$$\eta_{NCE} = \left| \frac{E_{conv}}{E_{pump}^2 E_{probe}} \right|^2 = \left| \frac{3k_0}{4n} \Gamma \chi^{(3)} \frac{\exp\left(\frac{\Gamma g L}{2}\right) - 1}{\Gamma g} \right|^2 \quad (A2.3)$$

d'où  $k_0$  est le vecteur d'onde de la lumière conjuguée dans le vide,  $n$  l'indice de réfraction,  $\Gamma$  le facteur de confinement optique,  $g$  le gain de matériau net de la zone active et  $L$  la longueur de cavité du laser FP. Dans cette équations, les termes  $E_{pompe}$ ,  $E_{sonde}$  et  $E_{conv}$  correspondent aux amplitude des champs complexes de la pompe, de la sonde et du signal converti dans la cavité du laser, et ils dépendent de la puissance de chaque:

$$E_{pump,sonde,conv} = \sqrt{\frac{2P_{pump,sonde,conv}}{c\epsilon_0 n A_{eff}}} \quad (A2.4)$$

d'où  $c$  est la célérité de la lumière,  $\epsilon_0$  la permittivité du vide et  $A_{eff}$  l'aire modale effective de la zone active du laser.

En appliquant l'équation A2.3, le  $\chi^{(3)}$  peut être extrait par les mesures du NCE. Cependant, il faut connaître l' $A_{eff}$  du laser QD, laquelle est calculée en modélisant la distribution d'intensité dans la section transversale du guide d'ondes. À l'aide du logiciel PhotonDesign, la Figure A2.5 montre le profil du mode d'intensité calculé dans les directions  $x$  et  $y$  (gauche) et la répartition correspondante du mode transversal dans la section transversale du guide d'ondes (à droite) en supposant une section de  $4,244 \times 4,244 \mu\text{m}$ . Comme le montre la Figure A2.5, le profil modal a une forme gaussienne; par conséquent, l'aire effective est récupérée en considérant 90% de la puissance totale dans les deux sens, conduisant à  $A_{eff}$  d'environ  $3 \mu\text{m}^2$ .

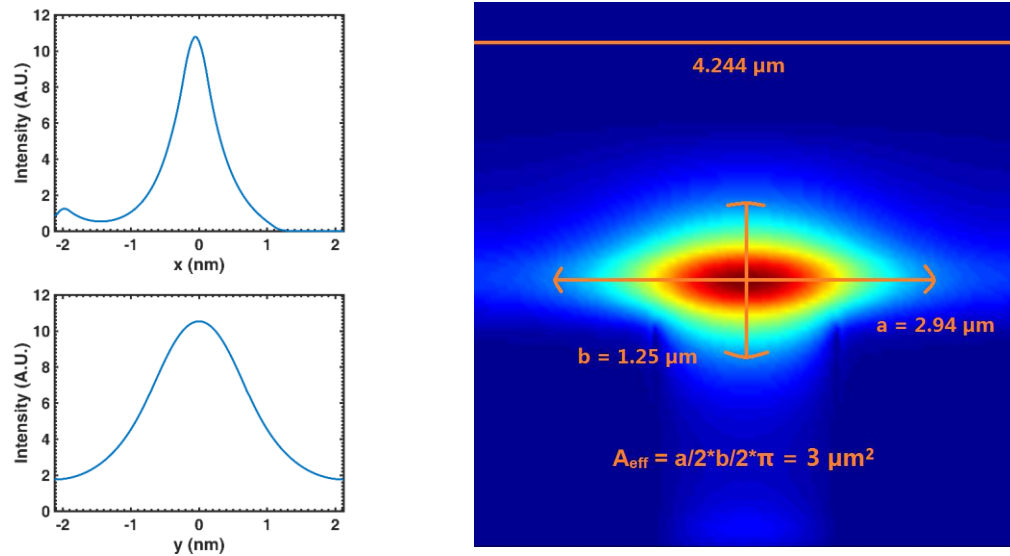


**Figure A2.5.** Profil d'intensité modal dans les directions x et y (gauche) et la distribution correspondante dans la section transversale du guide d'ondes (droite).

Paramètres	Valeurs
Indice de réfraction $n$	3.5
Vecteur d'ondes $k_0$	$6.1 \times 10^4 \text{ m}^{-1}$
Gain net modal $\Gamma_0$	$11.4 \text{ cm}^{-1}$
Longueur de cavité du laser $L$	0.1 cm
Aire effective modale $A_{\text{eff}}$	$3 \mu\text{m}^2$

**Tableau A2.1.** Valeurs de paramètres injectés dans l'équation A2.3.

Par conséquent, en injectant les valeurs du tableau A2.1 dans l'équation A2.3, nous extrayons  $\chi^{(3)}/g_0$  et le traçons en fonction de  $\Delta f$ . Dans la courte distance de désaccord,  $\chi^{(3)}/g_0$  est amélioré en raison du CDP plus fort induit par le battement entre la pompe et la sonde lors d'un désaccord plus grand,  $\chi^{(3)}/g_0$  est réduit suivant la même Comme prévu dans la figure 4.3. La valeur maximale est d'environ  $2,8 \times 10^{-19} \text{ m}^3/\text{V}^2$ , qui est au même ordre avec les valeurs antérieures signalées pour les lasers DFB QD InAs/GaAs [264].

## 6. Conversion dynamique dans les lasers QD

Cette section vise à démontrer expérimentalement la conversion d'un signal modulé dans le même laser QD par NDFWM.

## 6.1. Configuration expérimentale

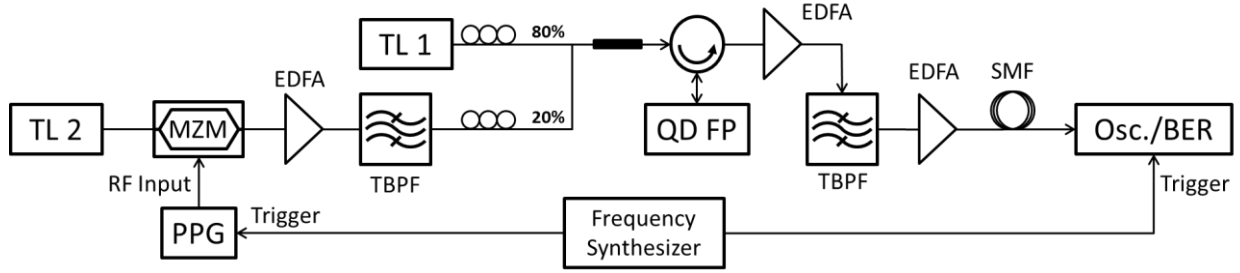


**Figure A2.6.** Schéma de la configuration expérimentale dédiée à la conversion dynamique.

MZM: modulateur Mach-Zehnder; PPG: générateur d'impulsion; TBPF: filtre passe-bande fin; SMF: bobine de fibre monomode; EDFA: amplificateur à fibre dopée à l'Erbium; Osc.: oscilloscope; BERT: testeur de taux d'erreur de bit.

La Figure A2.6 illustre la configuration expérimentale pour l'étude de la conversion dynamique. Comparez avec la Figure A2.3, un modulateur Mach-Zehnder avec une bande passante de modulation de 20 GHz est inséré à la sortie de TL2 pour moduler le signal de la sonde. La modulation d'entrée est une séquence de bits pseudo-aléatoire (PRBS) de 2,5 Gbps avec une longueur de  $2^7-1$ , générée par le générateur d'impulsions (PPG). Le désaccord pompe-sonde est fixé à 100 GHz en conversion montante. À la sortie 3 du circulateur, le signal converti est filtré par un filtre passe-bande fin (TBPF) et transmis par une bobine de fibre mono mode (SMF) de 25 km. Ensuite, le signal est envoyé à l'oscilloscope (Osc.) pour l'analyse du diagramme de l'œil ou au détecteur d'erreur pour mesurer le taux d'erreur de bit (BER). Le déclencheur pour le détecteur PPG et oscilloscope/BER est fourni par un synthétiseur de fréquence. D'autres conditions expérimentales demeurent identiques à celles du tableau A2.1.

## 6.2. Caractérisation de la performance de conversion dynamique

La mesure de BER est effectuée pour la sonde (avant injection dans le laser FP), le signal converti en retour et en arrière après 25 km de transmission de fibre. Les courbes BER de ces trois signaux sont tracées à la Figure A2.7. La droite noire pointillée horizontale correspond au niveau BER de  $10^{-9}$ , qui est classiquement désigné comme la limite sans erreur. En comparant la courbe du signal converti après sa transmission à sa courbe back-to-back, la pénalité de puissance est seulement de 0,5 dB, sans problème de plancher d'erreur. Ces résultats

indiquent que le signal n'est pas dégradé par la dispersion des fibres après la transmission. Cependant, en raison de la sensibilité limitée du détecteur BER, les courbes sont coupées autour de  $10^{-11}$ .

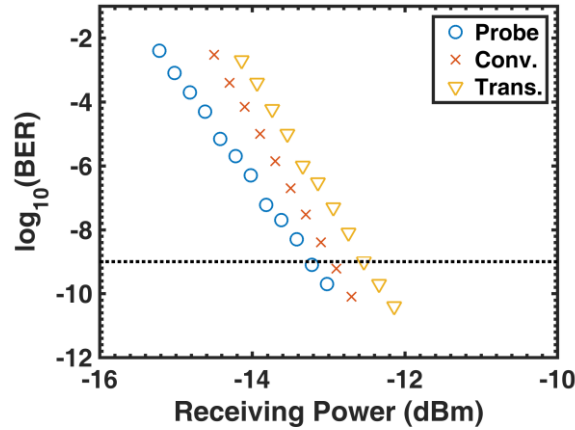


**Figure A2.7.** Les courbes BER en fonction de la puissance de réception par le détecteur pour la sonde avant l'injection, le signal converti avant et après la transmission dans une bobine SMF de 25 km. La ligne noire pointillée horizontale correspond à la limite conventionnelle sans erreur ( $\text{BER} = 10^{-9}$ ).

## 7. Résumé

Dans cette partie, une étude systématique de NDFWM est effectuée avec des lasers QD FP injectés. Les résultats expérimentaux ont montré un niveau CE comparable à celui des appareils SOA similaires, avec une puissance de la pompe/sonde beaucoup plus faible et un courant de polarisation [114], [117].

Une démonstration de conversion de signal modulé est également effectuée. Lors d'une défaillance de la pompe à 100 GHz, le signal converti modulé à 2,5 Gbps a permis une transmission sans erreur avec une pénalité de puissance aussi faible que 0,5 dB. Bien que ces résultats ne soient pas comparables à des études antérieures dans la littérature, ce travail a encore révélé le potentiel d'utilisation de lasers FP à verrouillage par injection en tant que convertisseurs de longueur d'onde optique.

### III. Dynamiques nonlinéaires des lasers QD sous retour optique externe

#### 1. Principe de la rétroaction optique

La rétroaction optique, ou le retour optique, est introduit dans une diode laser en envoyant une partie de son faisceau émis dans la cavité laser. Comme le montre la figure 5.1, la rétroaction optique est effectuée en alignant un miroir sur le chemin du faisceau. La distance du laser au miroir  $L_{ext}$  est liée au temps aller-retour externe  $\tau_{ext}$  dans la cavité externe qui est défini comme suit:

$$\tau_{ext} = \frac{2n_{ext}L_{ext}}{c} \quad (A3.1)$$

avec  $n_{ext}$  l'indice de réfraction de la cavité externe et  $c$  la célérité de la lumière.

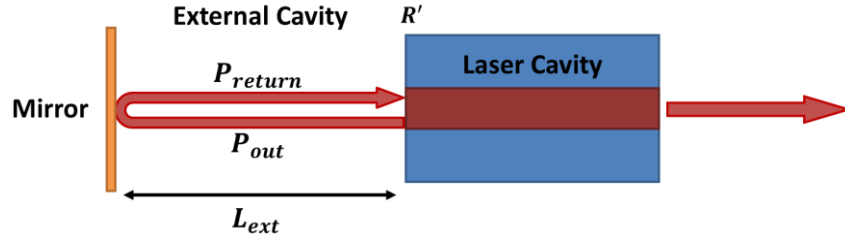


**Figure A3.1.** Schéma représentant un laser semiconducteur soumis à une rétroaction optique.

La force de rétroaction est définie comme le rapport entre la puissance de sortie ( $P_{out}$ ) de la facette laser soumise au retour optique à la puissance retournée ( $P_{return}$ ):

$$r_{ext} = \frac{P_{return}}{P_{out}} \quad (A3.2)$$

Les paramètres dominants conduisant la dynamique du laser sous la rétroaction optique sont le temps de retard externe  $\tau_{ext}$  et la force de rétroaction  $r_{ext}$ . En 1986, Tkach et al. ont classé les différents régimes de rétroaction dans un laser semi-conducteur DFB. Comme le montre la figure 5.2, cinq régimes différents peuvent être identifiés, les spectres optiques sur les côtés illustrent les dynamiques modales du laser dans les différents régimes [309], [323].



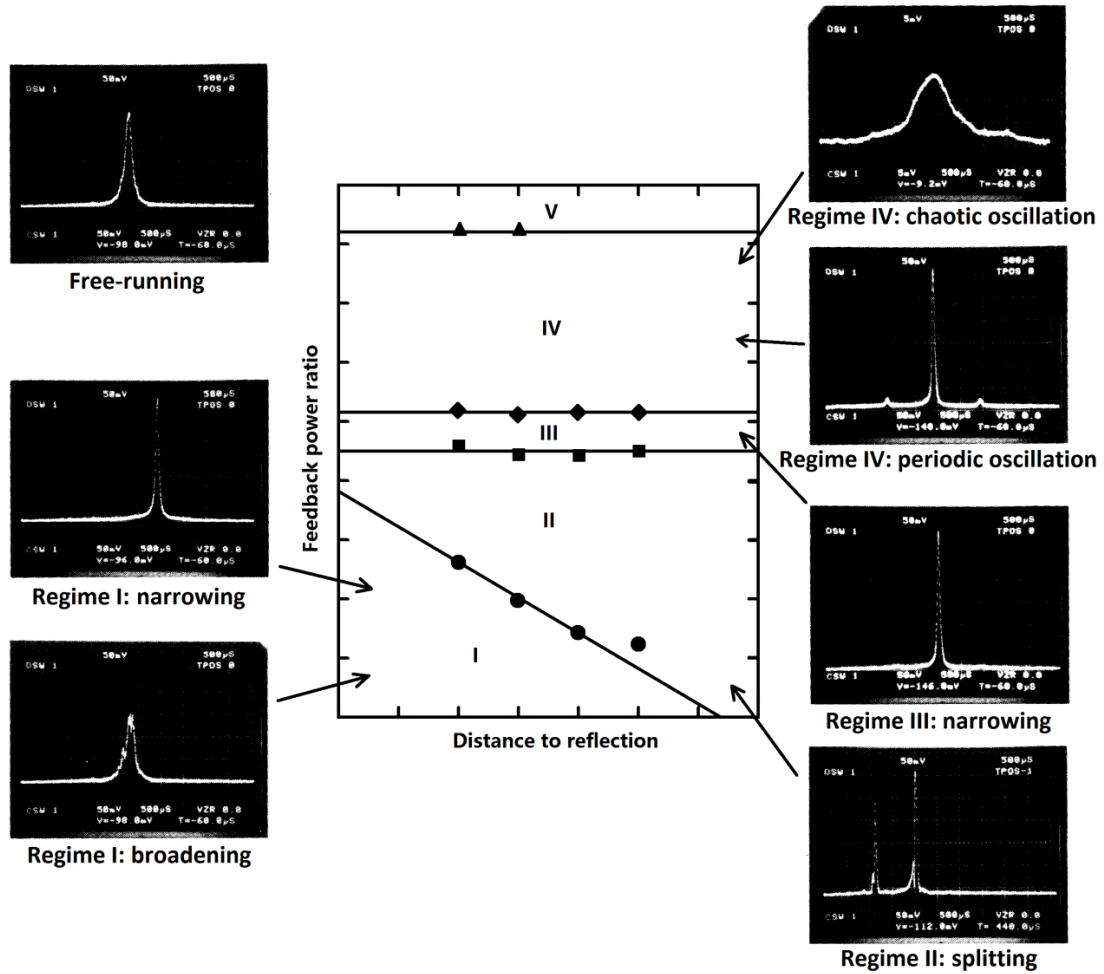


**Figure A3.2.** Régimes de rétroaction dans un laser semiconducteur DFB (centre), d'après la réf. [309]. Les spectres optiques des deux côtés illustrent les dynamiques modales du laser dans les différents régimes, d'après [323].

Dans le régime I, qui correspond au plus bas niveau de rétroaction, selon la phase de rétroaction, la largeur de ligne spectrale peut être soit réduite soit élargie; dans le régime II, le saut de mode se produit entre les modes cavité externe (ECM) induits par la phase de rétroaction. ECM correspond aux modes formés entre la facette de sortie laser et le miroir externe avec des fréquences multiples de  $c/2n_{ext}L_{ext}$ ; dans le régime III, le laser expérimente une restabilisation et fonctionne sur le mode avec la largeur de ligne minimale. Dans ce régime, la distance au point de réflexion n'a aucune conséquence sur la dynamique du laser. La Figure A3.2 montre que lorsque l'opération laser est réglée dans le régime III, le mode avec la largeur de ligne minimale peut être sollicité.

Dans le régime IV, la largeur de ligne des lances est élargie avec des modes latéraux croissants séparés des modes principaux par le ROF  $f_{RO}$ . L'amortissement des oscillations de relaxation, correspondant à des oscillations périodiques à  $f_{RO}$  (P1), est un précurseur de la voie de quasi-périodicité vers les oscillations chaotiques par le biais du régime d'effondrement de cohérence [307]. Cette voie vers le chaos est fréquemment observée dans les lasers semiconducteurs sous rétroaction optique où deux fréquences avec un rapport incommensurable, à savoir le ROF et les fréquences externes de la cavité, interagissent les unes avec les autres et aboutissent à la quasi-périodicité vers le chaos lorsque la force de rétroaction augmente.

Bien que le régime IV puisse modifier fortement la performance d'un système de communication à grande vitesse nécessitant ainsi l'insertion d'un isolateur optique, il est également possible de tirer parti du chaos déterministe pour le développement de communications sécurisées, des générateurs de bits aléatoires et la détection et la portée de la lumière (LIDAR) Avec des résolutions améliorées [296], [324].

Le seuil du régime IV aussi appelé le niveau critique  $r_{crit}$  peut être estimé à partir de [127]:

$$r_{ext,c} = \gamma^2 \frac{\tau_{int}^2}{16C_l^2} \frac{1+\alpha_H^2}{\alpha_H^4} \quad (A3.3)$$

où  $\gamma$  est le facteur d'amortissement,  $\tau_{int} = 2n_{int} L_c/c$  le temps de retour interne avec  $n_{int}$  et  $L_c$  étant l'indice de réfraction et la longueur de cavité du laser,  $C_l = (1 - R)/2\sqrt{R}$  le coefficient de couplage de la facette à la cavité externe, avec  $R$  la réflectivité de la facette.

Enfin, le dernier régime est le régime de cavité étendue dans lequel le laser est très stable fonctionnant sur un seul mode longitudinal de largeur de ligne étroite défini par la distance au miroir. Le système est similaire à un court milieu actif dans une cavité très longue délimitée par la facette arrière du laser et le miroir conventionnel. Ce régime est très difficile à atteindre et nécessite un revêtement antireflet sur la facette soumise à la rétroaction [328] - [330].

## 2. Rétroaction optique dans les lasers QD

Afin de répondre aux exigences de la croissance explosive du trafic de données, des transmetteurs rapides et peu coûteux à faible consommation d'énergie sont nécessaires en

particulier pour les liaisons de communication à portée limitée telles que les réseaux optiques d'accès, de métro et de centre de données [2], [5]. En raison de leur effet de taille quantique amélioré, les lasers QD InAs/GaAs fabriqués par des nanostructures auto-organisées sont l'un des meilleurs exemples pratiques de nanotechnologies émergentes, permettant ainsi des opérations de courant de seuil ultra-bas et de haute température [54], [168]. Très récemment, il a été prouvé que les QD ont un potentiel élevé pour surmonter les problèmes inhérents aux lasers à diode standard intégrés au silicium dans le contexte de l'intégration photonique à grande échelle et à faible coût [24], [25], [196]. Dans ce contexte, une plateforme d'interconnexion de centre de données à base de QD à 200 Gbps a été récemment lancée dans le but de réaliser 400 Gbps dans le futur [71].

Habituellement, on sait que les lasers QD opérant sur la transition état fondamental (GS) présentent une plus grande résistance au retour optique externe qui est d'une importance primordiale pour les applications sans isolateurs [127], [128]. Cependant, cette robustesse accrue aux perturbations optiques qui est principalement due à l'amortissement important des oscillations de relaxation définit également la limite des capacités de modulation du laser à quelques GHz à la température ambiante [128], [129]. Afin d'augmenter la vitesse et la portée, les arts antérieurs ont proposé de tirer parti des émissions stimulées issues des transitions des états excités (ES) [130]. En raison de la capture plus rapide du transporteur à partir du réservoir de transport environnant ainsi que d'un gain saturé plus élevé, les émetteurs d'ES QD ont été considérés comme une solution prometteuse pour les applications à grande vitesse [131]. La plus grande dégénérescence de l'ES se traduit par un gain différentiel plus important et une plus petite compression de gain non linéaire que par rapport à celles du GS. La première enquête réussie au niveau du lien a été réalisée avec des lasers QD de 1.3  $\mu\text{m}$  InAs/GaAs émettant sur la première transition ES, pour laquelle des capacités de modulation allant jusqu'à 25 Gbps (OOK) et 35 Gbps (PAM) ont été signalées [132], [133]. Les études antérieures ont également souligné que profiter de l'ES peut être utile pour la génération d'impulsions ultra-courtes [134], [135] et que la dynamique des lasers à verrouillage en mode ES QD en présence d'un retour optique est plus stable. En raison d'un facteur  $\alpha_H$  plus petit [136]. Très récemment, les travaux théoriques et expérimentaux ont prouvé que les lasers ES QD peuvent en effet présenter un LEF proche de zéro par rapport aux GS, ce qui est d'une

importance primordiale pour la réalisation d'émetteurs sans chirp ainsi que sur la cohérence laser et la Stabilité modale [130], [137]. Enfin, diverses études ont étudié la dynamique des aléas à deux états où les lances ES et GS peuvent avoir lieu simultanément avec ou sans feedback optique externe [136], [138]-[140]. En particulier, il a été récemment dévoilé que l'analyseur à deux états peut produire une grande amélioration de la modulation GS [141], [142].

Afin d'évaluer davantage l'impact potentiel de ces lasers dans l'optique de leur inclusion dans un module de télécommunications à porteurs de fibres, cette partie vise à caractériser la dynamique de retour optique retardée des lasers QD FP InAs/GaAs émettant Soit sur la GS unique ou exclusivement sur l'ES.

### **3. Configuration expérimentale**

Les deux lasers étudiés partagent exactement le même milieu de gain et la conception de la cavité. La cavité mesure 1 mm de long avec un guide d'onde de 2  $\mu\text{m}$  large, et la zone active est basée sur une structure de points dans un puits incluant 10 couches InAs QD développées par épitaxie par faisceau moléculaire (MBE, molecular beam epitaxy en terme anglais) intégrée dans le puits quantiques InGaAs [49]. Les spectres optiques des deux lasers sont représentés sur la Figure A3.3 (a) et (b), leurs courbes LI étant représentées dans les inserts. À la température ambiante (293 K), le laser GS a un courant de seuil  $I_{th}$  de 16.5 mA, une efficacité quantique externe différentielle de 21% et un pic de gain autour de 1300 nm. Le courant de seuil du laser ES est de 88,5 mA avec une efficacité quantique externe différentielle de 11%, et un pic de gain autour de 1220 nm. Pratiquement, les émissions sur l'état ES peuvent être réalisées de plusieurs manières, telles que l'augmentation du courant de la pompe pour atteindre le seuil de l'ES ou l'émission de l'émission stimulée GS en raccourcissant la longueur de la cavité, en revêtant les facettes ou par l'utilisation d'un miroir dichroïque [132]. Dans ce travail, les lignes d'émission GS/ES sont sélectionnées en exploitant la dispersion de la longueur d'onde naturelle du pic de photoluminescence à travers la plaquette, en veillant à ce que l'émission de GS soit naturellement inhibée pour le laser ES.

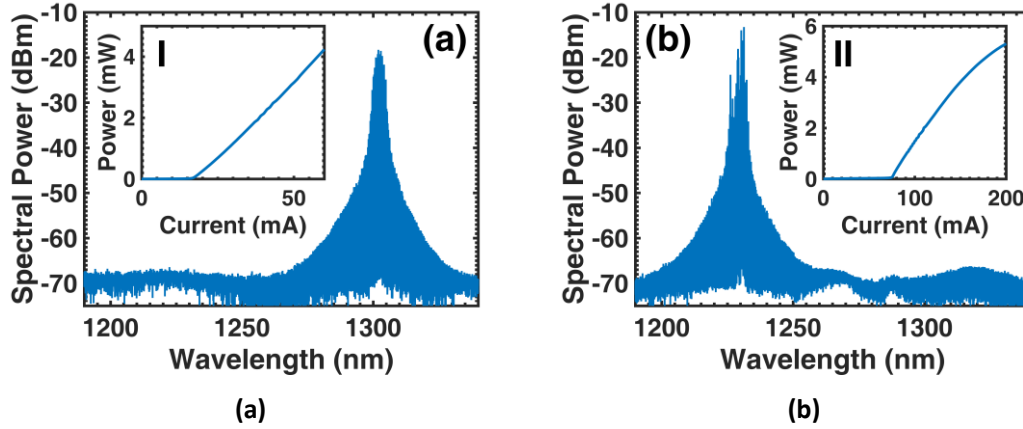


**Figure A3.3.** Les spectres optiques de (a) GS laser et (b) ES laser à  $2 \times I_{th}$ , les inserts représentent respectivement les courbes LI des gammes GS et ES.

Les lasers QD sont insérés dans une boucle de rétroaction optique externe fibrée. Comme le montre la Figure A3.4, l'émission laser est couplée à l'aide d'une fibre à extrémité de lentille et divisée par un coupleur 90/10 en chemins de réaction et de détection. Dans le chemin de rétroaction, la lumière est réfléchiée vers le QD à l'aide d'un contre-réflexeur (BKR, backreflector en terme anglais), composé d'un atténuateur variable et d'un miroir. Un contrôleur de polarisation dans le chemin de retour permet de faire correspondre les polarisations des lumières émises et réfléchiées afin d'équilibrer la perturbation de la biréfringence des fibres et de maximiser les effets du retour optique. La longueur de la cavité externe est estimée à 7 mètres, ce qui correspond à un temps aller-retour externe entre le laser et le réflecteur externe de  $\tau = 47 \text{ ns}$ . La fréquence d'oscillation de relaxation du laser à fonctionnement libre est d'environ 3 GHz pour le laser GS et 1 GHz pour le laser ES, donc la condition de cavité externe longue, c'est-à-dire  $f_{RO} \times \tau \gg 1$ , est remplie (le cas de la cavité courte correspond à  $f_{RO} \times \tau < 1$ ) [309]. Cependant, soulignons que, en raison de la divergence de sortie différente, la plage de variation de taux de retour externe ( $r_{ext}$ ) possible n'est pas exactement la même entre les périphériques GS et ES. À cette fin, pour le laser GS, le  $r_{ext}$  varie de 0% à 5,9%, alors qu'il est de 0% à 4,6%. Pour l'ES. Dans le parcours de détection, isolé du reste de l'installation, les analyseurs de spectre électriques et optiques (ESA et OSA) sont utilisés pour étudier la dynamique de rétroaction.

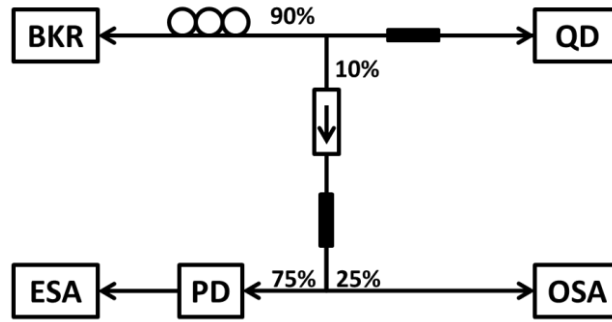


**Figure A3.4.** Schéma de la configuration expérimentale de retour optique externe.

#### 4. Dynamiques nonlinéaire des lasers QD rétroactionnés dans les cavités longues

La dynamique de rétroaction optique du laser GS est d'abord étudiée. Alors que les conditions d'alimentation de  $1,5 \times$ ,  $2,5 \times$  et  $3 \times I_{th}$  (25, 33 et 50 mA resp.) ont été considérées, le laser GS reste stable pour toute la gamme des courants et Les points forts de rétroaction étudiés, seul un petit décalage vers le rouge des modes FP a été observé sans signe d'élargissement spectral. Figure A3.5 représente les spectres optiques et électriques enregistrés à  $3 \times I_{th}$ , sans rétroaction (cas solitaire, par exemple  $r_{ext} = 0$ ) et pour la force de rétroaction maximale ( $r_{ext} = 5.9\%$ ).

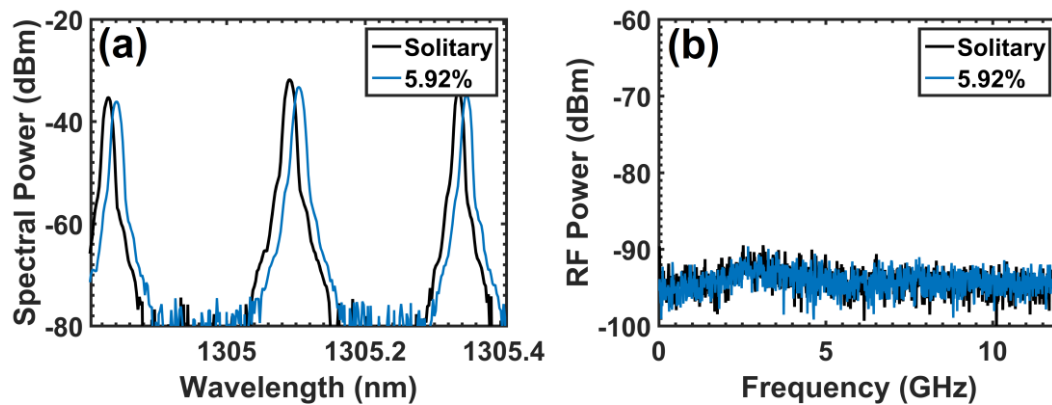


**Figure A3.5.** Spectres (a) optique et (b) électrique du laser GS mesurés à  $3 \times I_{th}$  sans rétroaction (solitaire) et pour la force de rétroaction maximale.

Cette augmentation de la résistance de rétroaction du laser de GS a déjà été rapportée à plusieurs reprises et attribuée au taux d'amortissement élevé des oscillations relaxation [54],

[127], [128]. En ce qui concerne le laser ES, les conditions de polarisation ont été fixées à  $1,5 \times$ , et  $2 \times I_{th}$  (133 et 177 mA resp.). En raison du renversement observé dans la puissance de sortie supérieure à 180 mA (voir l'encart de la Figure A3.4 (b)), les courants de pompe plus élevés n'ont pas été pris en considération. Figure A3.6 représente une cartographie des spectres optiques et électriques du laser ES mesuré en fonction de  $r_{ext}$  sous différents courants de polarisation. À  $2 \times I_{th}$ , le laser se révèle presque insensible au retour optique jusqu'à 0,4% de la réaction, au-delà de laquelle les modes s'élargissent (Figure A3.6 (a) et (b)).

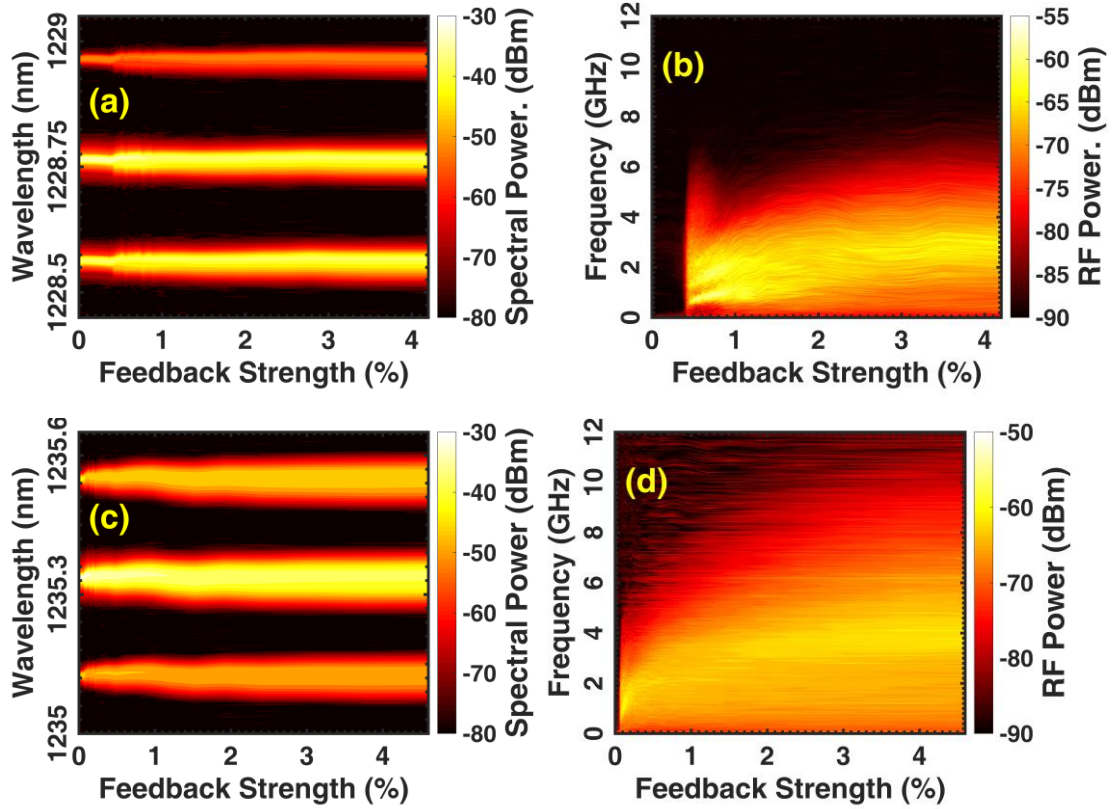


**Figure A3.6.** ES laser: cartographie spectrale optique (gauche) et électrique (droite) à (a-b)  $1,5 \times I_{th}$ , (c-d)  $2 \times I_{th}$ .

Figure A3.6 présente un ensemble de spectres optiques et électriques enregistrés aux deux niveaux de polarisation pour le laser ES en fonctionnement solitaire, ainsi que sous un retour optique faible et maximal. Figure A3.6 (a) et (c) illustrent l'élargissement du mode dans le spectre optique pour les deux niveaux de pompage, tandis que la Figure A3.6 (b) et (d) représentent la déstabilisation dans le spectre électrique. En particulier, la Figure A3.6 (b) montre qu'environ 0,6% de retour optique, des oscillations quasi périodiques avec un

piédestal élevé ont lieu. À la force de rétroaction maximale, on observe un spectre large bande sans pics clairs qui est une caractéristique des comportements chaotiques. En outre, à des courants de polarisation plus élevés et des forces de rétroaction similaires, aucune dynamique quasi-périodique n'est observée comme le montre la Figure A3.6 (d). En outre, la comparaison entre la Figure A3.6 (b) et (d) dévoile que le chaos est intensifié à une pompe plus élevée et présente une plus grande bande passante. Contrairement aux lasers distribués (DFB), pour lesquels une meilleure stabilité contre les retombées optiques est observée à des courants de polarisation plus importants [299], [348], nous avons constaté ici que la déstabilisation des lasers FP pourrait être plus complexe en raison de la concurrence modale. Enfin, à des niveaux de pompe plus élevés, le laser ES paraît encore plus sensible à la rétroaction optique car le niveau de retour critique au-delà duquel l'itinéraire vers le chaos se produit par des oscillations quasi périodiques baisse de 0,05% par rapport à 0,4% à un biais inférieur. Une fois que la fenêtre des oscillations quasi périodiques disparaît, le laser oscille automatiquement chaotiquement.

Une méthode simple pour analyser les différences dans la sensibilité de rétroaction est d'estimer le taux d'amortissement à partir de l'expression du niveau  $r_{crit}$  par l'équation A3.3. Comme le laser GS se trouve toujours stable, une limite inférieure pour le retour critique est supposée être le niveau de retour maximal, donc  $r_{crit} > 5.9\%$ . Le facteur  $\alpha_H$  est extrait par la méthode ASE. Figure A3.7 représente les spectres du facteur  $\alpha_H$  pour les deux lasers. La variation spectrale inférieure au seuil varie de 0,25 à 1,0 pour le laser GS (rouge) et de 0,5 à 1,5 pour l'ES (bleu). Au pic de gain, le facteur  $\alpha_H$  se trouve à 0,5 pour le laser ES et à environ 1 pour le laser GS.

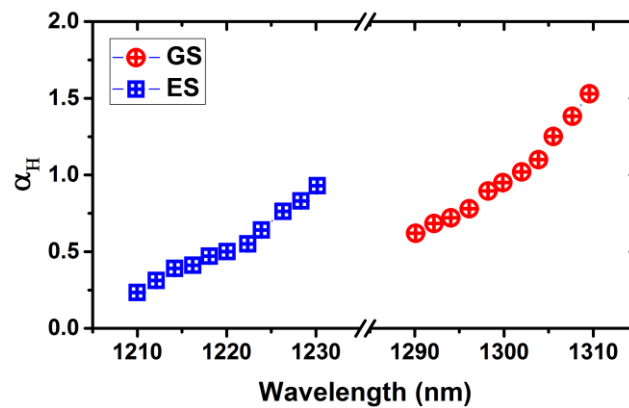


**Figure A3.7.** Les variations spectrales du facteur  $\alpha_H$  sous-seuil pour les lasers GS et ES.



De l'équation A3.3, et en injectant  $R = 0,32$ ,  $C_l = 0,6$ ,  $\tau_{int} = 21 \text{ ps}$ ,  $\gamma_{ES}$  est estimé à 1,6 GHz et 0,6 GHz à  $1,5 \times$  et  $2 \times I_{th}$  tandis que  $\gamma_{ES} > 18 \text{ GHz}$  pour le laser GS. La différence entre les émissions GS et ES peut s'expliquer qualitativement par la dynamique des opérateurs QD impliquant à la fois la capture et la relaxation pour le laser GS, contrairement à l'ES. Alors que nous montrons que l'ES seul présente une dynamique similaire aux lasers à puce quantique sous la rétroaction optique, les transports des porteurs supplémentaires requis pour l'émission sur le GS conduisent à un taux d'amortissement plus élevé qui empêche les oscillations sous un retour optique moyen. Cependant, il faut noter que les formes des spectres de gain des deux lasers peuvent également affecter la dynamique [131]. À cette fin, le laser ES à l'étude pourrait être plus sensible aux retombées optiques également en raison d'une concurrence modale plus forte par rapport au laser GS, qui a un spectre optique plutôt plat autour de la longueur d'onde centrale (ne figure pas ici). Les différentes dynamiques peuvent également être attribuées à la dégénérescence de l'ES où l'existence de deux niveaux p peut conduire à plus de transitions radiatives [349]. Enfin, bien que le  $\alpha_H$  ait pu être mesuré au-delà du seuil du laser, une valeur de  $\alpha_H$  supérieure au sous-seuil peut être mesurée dans les conditions de polarisation expérimentale, cela n'affectera pas l'ordre de grandeur des taux d'amortissement extrait puisque leurs rapport resteraient dominés par la racine carrée du rapport des niveaux de rétroaction critique.

## 5. Dynamiques nonlinéaire des lasers QD rétroactionnés dans les cavités courtes

En gardant les mêmes principes dans la section précédente, le montage dans la Figure A3.4 a été modifié, un miroir mobile est intégré en amount, permettant d'ajuster  $L_{est}$  allant de 2 à 50 cm, ce qui correspond à une transition de la cavité externe courte – longue ( $f_{RO} \times \tau_{ext}$  varie entre 0.2 et 10).

Par les mêmes procédures, la sensibilité à la rétroaction a été extrait pour les deux lasers QD.

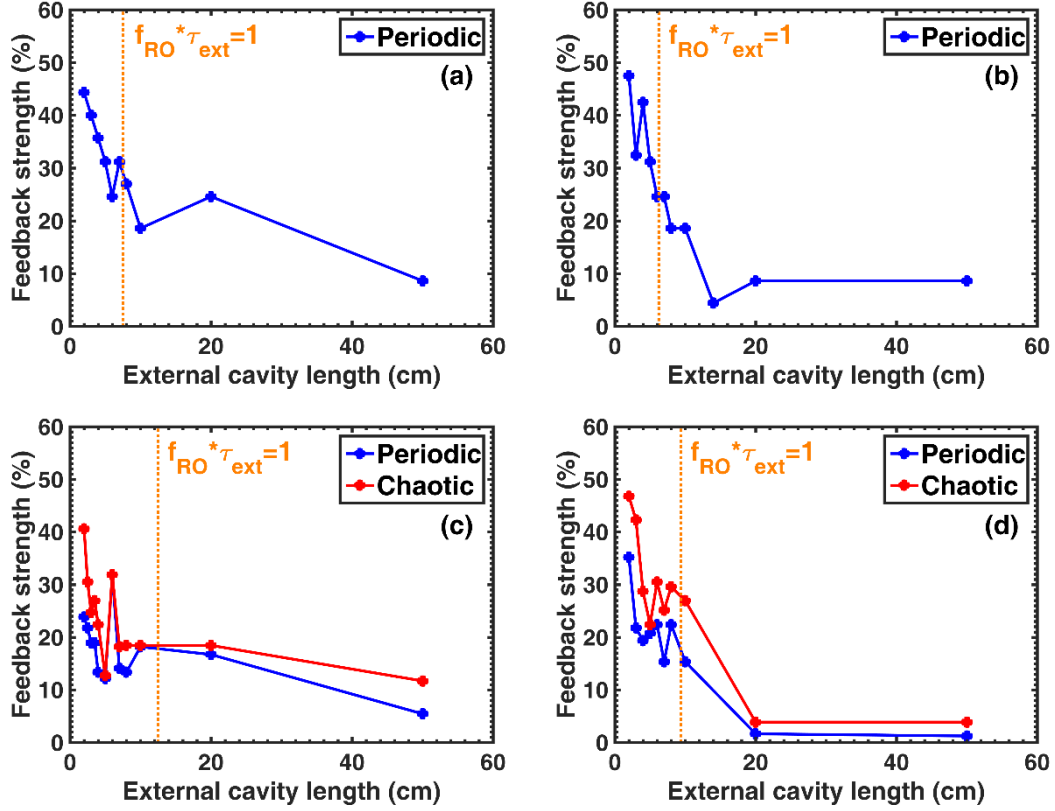


**Figure A3.8.** Limites d'oscillations périodiques et chaotiques excitées en fonction de la longueur de cavité externe pour les lasers GS et ES à  $1,5 \times I_{th}$  ((a), (c)) et  $1,7 \times I_{th}$  ((b), (d)). Les lignes solides verticales en orange marquent les limites entre les régimes de rétroaction à retard court et long.

Dans la Figure A3.8, les lignes solides verticales en orange marquent la séparation entre les régimes de rétroaction à retard court et long. Dans le cas du laser GS (Figure A3.8 (a) et (b)), les oscillations chaotiques ne sont pas observées dans les conditions de rétroaction. Comme mentionné précédemment, en raison du grand facteur d'amortissement, aucune trace de chaos n'a été observée dans ce laser. Dans l'ensemble, la Figure A3.8 montre que la limite inférieure des limites périodiques excitées se trouve toujours à un niveau de rétroaction plus élevé pour le laser GS que pour l'ES (Figure A3.8 (c) et (d)), ce qui correspond aux résultats discutés dans la section précédente du régime de cavité externe longue.

Dans le régime de la cavité courte, les limites sont composées de certaines ondulations résiduelles, qui sont liées aux inférences entre les résonances internes et externes de la cavité. Dans le cas particulier de GaFP2, pour une certaine longueur de cavité externe, l'augmentation de  $r_{ext}$  peut déplacer le point fixe vers des états périodiques et chaotiques après avoir franchi

les limites. Selon la longueur de la cavité externe, le laser interfère de façon constructive ou destructrice avec la cavité externe, ce qui signifie que les extrêmes dans les ondulations correspondent à des situations où le laser est stable ou instable. Contrairement à cela, lorsque les lasers fonctionnent dans le régime à cavité longue, le niveau de rétroaction pour lequel les oscillations périodiques et chaotiques excitées ont lieu en continu diminue et tend à devenir plutôt indépendant de la longueur de la cavité externe. Cette transition en douceur entre les régimes de cavité courte et longue diffère de ce qui se produit dans les lasers DFB à fréquence unique pour lesquels un comportement clair et brutal est observé [342].

## 6. Résumé

Dans cette partie, une étude approfondie de la dynamique de retour optique multimode a été effectuée. À l'aide de deux lasers QD FP InAs/GaAs partageant le même milieu de gain mais émettant sur deux états laser différents, cette étude nous permet d'accéder directement aux aspects matériels des transitions ES et GS. Les résultats expérimentaux ont révélé comment la dynamique des opérateurs dans les QD affecte la sensibilité aux perturbations optiques externes.

Le laser ES peut être facilement déstabilisé alors que le GS est beaucoup plus résistant, sans aucune voie claire vers le chaos. Bien que le laser ES soit potentiellement plus rapide, son plus petit taux d'amortissement combiné au fort bruit de partition contribue à accroître la sensibilité à la rétroaction optique externe qui est une caractéristique importante à prendre en compte pour la réalisation des futurs modules de télécommunications.

Dans l'ensemble, ce travail est important non seulement pour la compréhension de la dynamique du laser QD, mais aussi pour la réalisation d'émetteurs optiques résistant aux retours pour les liaisons de communication à portée réduite. En particulier, l'analyse des états est motivée par l'intérêt grandissant pour la technologie photonique hyperfréquences, à partir de laquelle des perspectives passionnantes peuvent être envisagées telles que la fabrication d'un dispositif intégré dans un PIC capable de délivrer des signaux hyperfréquences sans avoir besoin de modulation électrique. Les expériences suivantes seront concentrées sur les lasers DFB émettant sur différents états laser et une modélisation supplémentaire est maintenant nécessaire pour mieux comprendre la dynamique de retour optique multimode.

## **IV. Réduction de la Largeur de raie dans les lasers QD**

### **1. Largeur de optique des lasers QD**

L'augmentation de la capacité de transmission des réseaux fibrés et de la bande passante associée est aujourd'hui largement sous-tendue par le développement des communications optiques cohérentes. Dans ce cadre, l'information n'est plus uniquement portée par l'amplitude mais aussi par la phase ce qui signifie que ces systèmes requièrent des sources optiques à très faible largeur de raie, à la fois au niveau des transmetteurs et des oscillateurs locaux [213]. Plusieurs solutions éprouvées ont déjà été proposées dans le but de réduire substantiellement la largeur de raie d'un laser à semiconducteurs, soit en utilisant une cavité externe ou encore par le biais de procédés technologiques alliant technologies matériaux III-V et silicium [11]. Une alternative plus simple à mettre en œuvre repose sur l'utilisation d'un milieu de gain comportant un matériau nanostructuré. En effet, de par le caractère très localisé de la densité d'états et du très faible bruit d'émission spontanée [54], l'inclusion de boîtes quantiques dans la zone active procure au laser une largeur de raie naturelle relativement faible ( $< 1$  MHz) par comparaison aux sources à matériaux massifs ou à puits quantiques [26]. De plus, l'application de la rétroaction optique sur le laser et se plaçant dans le régime III peut permettre une compression plus importante du bruit d'émission spontanée et donc de la largeur de raie. Pour des taux de retour optique modérés, nous montrons ici qu'il est possible de verrouiller un laser InAs/InP à boîtes quantiques dans un régime de fonctionnement stable et pour lequel une la largeur de raie proche de 100 kHz est démontrée dans des conditions normales d'opération.

### **2. Configuration expérimentale**

Le laser étudié est un laser DFB à boîtes quantiques. Le milieu actif contient 5 plans de boîtes quantiques en arséniure d'indium (InAs) dont la croissance a été réalisée par épitaxie par jets moléculaire (MBE) sur phosphure d'indium InP [39]. La cavité longue de 1 mm possède des facettes traitées antireflets (AR). Le guide d'onde de largeur 3  $\mu\text{m}$  procure au laser un fonctionnement monomode transverse. Le coefficient de couplage du réseau de Bragg est d'environ  $20\text{ cm}^{-1}$ . A la température de la pièce (293K), le courant de seuil est de 47,5 mA et la

longueur d'émission est centrée à 1520 nm. Les courbes LIV et le spectre optique mesurés à 200 mA sont représentés sur les Figure A4.1 (a) et (b).

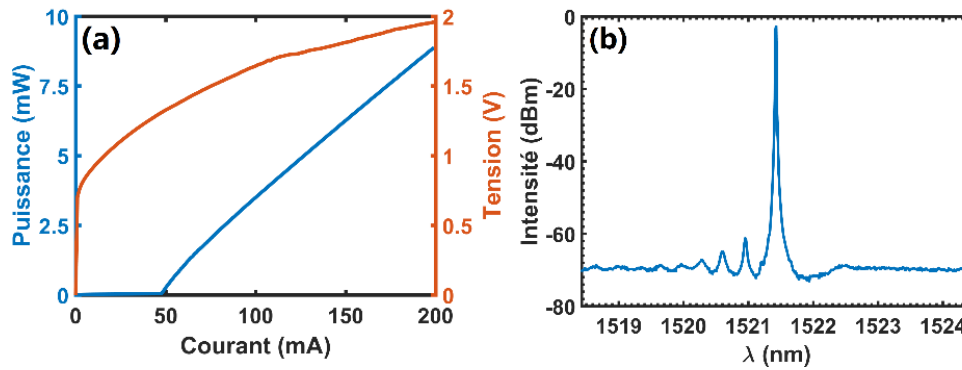


**Figure A4.1.** (a) courbes LIV du laser DFB ; (b) spectre optique du laser à 200 mA (mesures à 20 °C).

La Fig. 2 représente le montage expérimental utilisé pour les mesures de rétroaction optique et de largeur de raie. Le couplage du faisceau est réalisé à partir d'une fibre micro-lentillée traitée AR. La partie (a) du montage permet d'étudier la dynamique du laser sous rétroaction optique. La force de rappel est produite par un rétro-rélecteur (BKR) composé d'un miroir et d'un atténuateur optique variable. En tenant en compte des pertes dans le montage, le taux de réinjection  $r_{\text{ext}}$  est estimé entre 0 et 1%.

La mesure de la largeur de raie (partie b) repose quant à elle sur la technique éprouvée du battement auto-hétérodyne qui consiste à faire interférer un laser avec une version retardée de lui-même, déplacée en fréquence [54]. Afin de limiter les réflexions parasites, deux isolateurs optiques (isolation > 60 dB) sont insérés en amont. Le signal est envoyé dans un des bras de l'interféromètre puis décalé de 100 MHz par un modulateur acousto-optique (AOM), tandis que l'autre partie se propage dans le bras incorporant une bobine de fibre de 25 km. Si le retard appliqué est plus grand que le temps de cohérence du laser, alors il n'y a plus aucune relation entre les variations de fréquence du laser entre les deux bras de l'interféromètre. Ceci revient à dire que l'on fait interférer deux signaux totalement indépendants, autrement dit la mesure est équivalente à une mesure hétérodyne entre deux lasers exactement identiques. A la sortie, le battement entre les deux champs est détecté par une photodiode rapide puis mesuré sur un l'analyseur de spectre électrique (ESA). L'analyse

du spectre RF permet de remonter ensuite à la largeur de raie optique en utilisant un profil de Voigt [251]. Afin de suivre l'évolution de la puissance couplée et du spectre optique, un puissance-mètre et un analyseur de spectre optique (OSA) sont utilisés sur les sorties 2 et 3 de l'interrupteur optique.

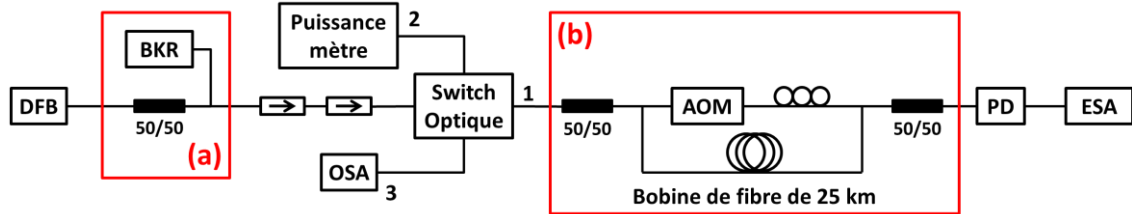


**Figure A4.2.** Montage incorporant la boucle de rétroaction optique (a) et celle pour l'auto-hétérodynage (b).

### 3. Réduction de la largeur de raie par rétroaction optique

Les Figure A4.3 (a) et (b) représentent les cartographies des spectres optiques et électriques du laser opérant sous rétroaction optique et pompé à  $2.5 \times I_{th}$ . L'analyse de la dynamique de rétroaction révèle ici une route vers le chaos typique jalonnée de plusieurs régimes de fonctionnement (distingués par des droites verticales rouges dans les Fig. 3 (a) et (b)) [6] : 1)  $r_{ext} < 0.4\%$ , le mode DFB se décale vers le rouge mais reste stable avec aucun battement ni oscillations observés sur les spectres électriques (régime I). Ce régime est particulièrement dépendant de la phase du champ retardé ce qui n'est pas étudié ici en raison de la longueur de la cavité externe (7 mètres) ; 2)  $0.4\% < r_{ext} < 0.62\%$  le laser entre dans le régime II où l'on observe de l'instabilité modal (sauts de mode) ; 3)  $0.62\% < r_{ext} < 0.7\%$ , le laser se re-stabilise et se verrouille sur le mode de cavité externe de plus faible largeur de raie (régime III). Ce régime est en générale difficile à localiser eu égard à l'étroitesse de la plage de rétroaction considérée [6] ; 4)  $r_{ext} > 0.7\%$ , le laser entre dans le régime d'effondrement de la cohérence où l'on observe l'occurrence d'une dynamique chaotique composée de nombreux modes de cavité externe (régimes IV).

La Figure A4.3 (c) représente les mesures de largeurs de raies effectuées dans le régime III pour  $r_{ext} = 0.65\%$ . La droite horizontale représente la valeur de la largeur de raie naturelle (sans rétroaction optique). Pour ce niveau de pompage, on peut constater que la valeur de

280 kHz est déjà beaucoup plus faible que celles rapportées dans des lasers DFB à puits quantiques. Les cercles rouges correspondent quant à eux à cinq mesures effectuées dans à des intervalles de temps successifs. Le résultat montre que dans régime III, le bruit de phase du laser est compressé à son maximum et la largeur de raie est réduite proche de 100 kHz.

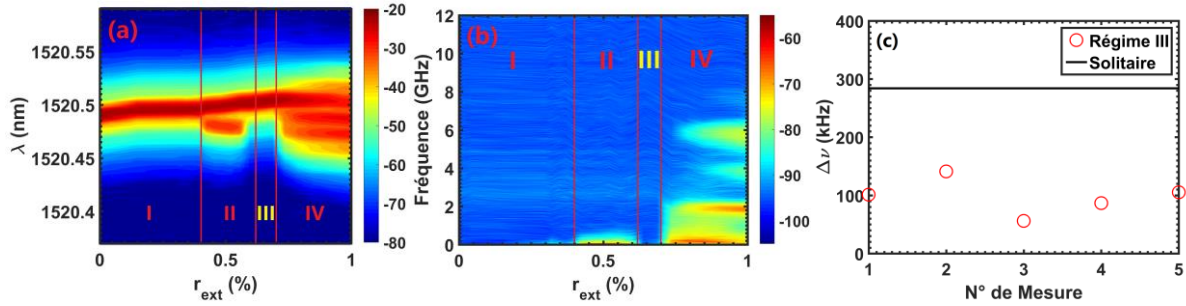


**Figure A4.3.** Cartographies des spectres (a) optique et (b) électrique du laser DFB en fonction de  $r_{ext}$  ; (c) largeur de raie en l'absence de rétroaction optique (droite horizontale) et sous rétroaction (cercles rouges).

#### 4. Résumé

Cette partie montre la stabilisation d'un laser QD DFB InAs/InP opérant dans le régime de plus faible largeur de raie. L'association d'un milieu de gain nanostructuré et d'une force de rappel optique judicieusement contrôlée permet de compresser substantiellement le bruit de phase et d'atteindre des largeurs de raies proches de 100 kHz.





## Appendix 2: List of Publications

### Journal Papers

1. **H. Huang**, K. Schires, P.J. Poole and F. Grillot, "Non-Degenerate Four-Wave Mixing in an Optically Injection-Locked InAs/InP Quantum Dot Fabry-Perot laser", Appl. Phys. Lett., Vol. 106, pp, 143501, 2015.
2. **H. Huang**, K. Schires, D. Arsenijević, T. Sadeev, D. Bimberg and F. Grillot, " Efficiency of four-wave mixing in injection-locked InAs/GaAs quantum-dot lasers", AIP Adv., Vol. 6, pp. 125105, 2016.
3. **H. Huang**, K. Schires, D. Arsenijević, T. Sadeev, D. Bimberg and F. Grillot, "Multimode dynamics of InAs/GaAs quantum-dot lasers with long-delay optical feedbacks", AIP Adv., 2016.
4. T. Sadeev, **H. Huang**, D. Arsenijević, K. Schires, F. Grillot and D. Bimberg, "Highly efficient non-degenerate four-wave mixing under dual-mode injection in InP/InAs quantum-dash and quantum-dot lasers at 1.55  $\mu\text{m}$ ", Applied Physics Letters, Vol. 107, pp. 191111, 2015.
5. C. Wang, M. E. Chaibi, **H. Huang**, D. Erasme, P. Poole, J. Even and F. Grillot, Frequency-dependent linewidth enhancement factor of optical injection-locked quantum dot/dash lasers, Optics Express, Vol. 23, pp. 21761, 2015.
6. C. Gosset, I. Aldaya, C. Wang, **H. Huang**, X. You, J. Even, G. Campuzano, and F. Grillot, "Self-referenced technique for monitoring and analysing the non-linear dynamics of semiconductor lasers," Opt. Express, vol. 22, no. 13, p. 16528, 2014.

### Conference Papers

1. C.Redlich, B.Lingnau, **H. Huang**, R. Raghunathan, K. Schires, F. Grillot, and K.Luedge, "Linewidth rebroadening in quantum dot semiconductor lasers", (Oral Presentation), European Semiconductor Laser Workshop, Sept. 23-24, Darmstadt, Germany, 2016.
2. **H. Huang**, K. Schires, P.J. Poole and F. Grillot, "Etude de la largeur de raie d'un laser à boîte quantique InAs/InP soumis à une force de rappel optique", (Poster), Journée Nationale de l'Optique Guidée (JNOG) conference, July 4th – 7th, Bordeaux, France, 2016.

3. **H. Huang**, K. Schires, L.C. Lin, C.Y. Chen, D. Arsenijević, T. Sadeev, D. Bimberg F-Y Lin and F. Grillot, "Dynamics of Excited-State InAs/GaAs Fabry-Perot Quantum-Dot Lasers under Optical Feedback", (Oral Presentation), Conference on Lasers and Electro-Optics (CLEO), June 5th to 10th, San Jose, CA, USA, 2016.
4. **H. Huang**, K. Schires, D. Arsenijević, T. Sadeev, D. Bimberg and F. Grillot, "InAs/GaAs excited state quantum-dot transmitters operating under long-delayed optical feedback", SPIE Photonics Europe conference, (Oral Presentation), April 3rd to 7th, Brussels, Belgium, 2016.
5. **H. Huang**, K. Schires, D. Arsenijević, T. Sadeev, D. Bimberg and F. Grillot, "Feedback Sensitivity of InAs/GaAs Fabry-Perot Quantum-Dot Lasers Operating on the Excited State Transition", Semiconductor and Integrated Opto-Electronics (SIOE) Conference, (Oral Presentation), April 5th to 7th, Cardiff, UK, 2016.
6. **H. Huang**, K. Schires, D. Arsenijević, T. Sadeev, D. Bimberg and F. Grillot, "Excited-State and Ground-State Optical Feedback Sensitivity in InAs/GaAs Quantum-Dot Lasers", International Symposium on Physics and Applications of Laser Dynamics (IS-PALD), (Oral Presentation), November 4th to 6th, Metz, France, 2015.
7. R. Raghunathan, K. Schires, **H. Huang**, A. Hurtado, L. F. Lester, and F. Grillot, "Dual mode interaction dynamics in a 1310 nm quantum dot DFB laser under distant side mode injection", (Oral Presentation), International Symposium on Physics and Applications of Laser Dynamics (ISPALD), November 4-6, Metz, France, 2015.
8. **H. Huang**, K. Schires, R. Raghunathan, D. Erasme, D. Arsenijević, T. Sadeev, D. Bimberg and F. Grillot, "Highly Efficient Wavelength Conversion in InAs/GaAs Quantum Dot Lasers", IEEE Photonics Conference, (Oral Presentation), October 4th to 8th, Reston, VA, USA, 2015.
9. T. Sadeev, **H. Huang**, K. Shires, D. Arsenijević, F. Grillot, and D. Bimberg, "Non-linear and dynamic properties of MOVPE-grown InAs/InP quantum-dot and quantum-dash Fabry-Perot lasers", (Oral Presentation), The 28th Photonics Society Meeting, October 4-8, Reston, USA, 2015.
10. T. Sadeev, **H. Huang**, K. Shires, D. Arsenijević, F. Grillot, and D. Bimberg, "InP/InAs quantum-dot and quantum-dash lasers: mode-locking, non-linear and dynamic properties", (Oral Presentation), 23rd International Symposium on Nanostructures:

Physics and Technology, June 22-26, Saint Petersburg, Russia, 2015.

11. **H. Huang**, K. Schires, M. Chaibi, P. Poole, D. Erasme and F. Grillot, "Nonlinear Conversion Efficiency of InAs/InP Nanostructured Fabry-Perot Lasers", (Oral Presentation), SPIE Photonics West conference, Feb 7th – 12th, San Francisco, USA, 2015.
12. **H. Huang**, K. Schires, P.J. Poole, D. Erasme, R. Gabet, B. Lingnau, K. Lüdge and F. Grillot, "Etude du Rendement de Conversion Nonlinéaire dans un Oscillateur InAs/InP à Nanostructures Quantiques Emettant à 1550 nm", (Oral Presentation), Journée Nationale de l'Optique Guidée (JNOG) conference, Oct 29th – 31th, Nice, France, 2014.
13. **H. Huang**, C. Wang, K. Schires, P.J. Poole, J. Even and F. Grillot, "Wave Mixing Effects in a 1525 nm InAs/InP Optically-Injected Quantum Dot Distributed Feedback Laser", Semiconductor and Integrated Opto-Electronics (SIOE) Conference, (Oral Presentation), April 29th to May 1st, Cardiff, UK, 2014



## References

- [1] E. Murphy, "The semiconductor laser: Enabling optical communication," *Nat. Photonics*, vol. 4, no. 5, pp. 287–287, 2010.
- [2] Cisco, "Cisco Visual Networking Index: Forecast and Methodology, 2015–2020," 2016.
- [3] Cisco, "The Hierarchical Network Design Model," 2016. [Online]. Available: [www.cisco.com/web/learning/netacad/demos/CCNP1v30/ch1/1\\_1\\_1/index.html](http://www.cisco.com/web/learning/netacad/demos/CCNP1v30/ch1/1_1_1/index.html).
- [4] K. Hinton, J. Baliga, M. Feng, R. Ayre, and R. Tucker, "Power consumption and energy efficiency in the internet," *IEEE Netw.*, vol. 25, no. 2, pp. 6–12, 2011.
- [5] C. F. Lam, H. Liu, and R. Urata, "What Devices do Data Centers Need ?," *Conf. Opt. Fiber Commun. Tech. Dig. Ser.*, pp. 5–7, 2014.
- [6] K. Kikuchi, "Fundamentals of Coherent Optical Fiber Communications," *J. Light. Technol.*, vol. 34, no. 1, pp. 157–179, 2016.
- [7] K. Kikuchi, "Coherent Optical Communications: Historical Perspectives and Future Directions," in *High Spectral Density Optical Communication Technologies*, Berlin, Heidelberg: Springer Berlin Heidelberg, pp. 11–49, 2010.
- [8] M. Okai, M. Suzuki, and T. Taniwatari, "Strained multiquantum-well corrugation-pitch-modulated distributed feedback laser with ultranarrow (3.6 kHz) spectral linewidth," *Electron. Lett.*, vol. 29, no. 19, p. 1696, 1993.
- [9] B. Kelly, R. Phelan, D. Jones, C. Herbert, J. O'Carroll, M. Rensing, J. Wendelboe, C. B. Watts, A. Kaszubowska-Anandarajah, P. Perry, C. Guignard, L. P. Barry, and J. O'Gorman, "Discrete mode laser diodes with very narrow linewidth emission," *Electron. Lett.*, vol. 43, no. 23, p. 1282, 2007.
- [10] V. Weldon, P. Pineda-Vadillo, M. Lynch, R. Phelan, and J. F. Donegan, "A novel discrete mode narrow linewidth laser diode for spectroscopic based gas sensing in the 1.5  $\mu\text{m}$  region," *Appl. Phys. B Lasers Opt.*, vol. 109, no. 3, pp. 433–440, 2012.
- [11] C. T. Santis, S. T. Steger, Y. Vilenchik, A. Vasilyev, and A. Yariv, "High-coherence semiconductor lasers based on integral high-Q resonators in hybrid Si/III-V platforms," *Proc. Natl. Acad. Sci.*, vol. 111, no. 8, pp. 2879–2884, 2014.
- [12] M. R. Matthews, K. H. Cameron, R. Wyatt, and W. J. Devlin, "Packaged frequency-stable tunable 20 kHz linewidth 1.5  $\mu\text{m}$  InGaAsP external cavity laser," *Electron. Lett.*, vol. 21, no. 3, p. 113, 1985.
- [13] M. Okai, "Spectral characteristics of distributed feedback semiconductor lasers and their improvements by corrugation-pitch-modulated structure," *J. Appl. Phys.*, vol. 75, no. 1, pp. 1–29, 1994.
- [14] W. A. Ling, Y. Matsui, H. M. Daghighian, and I. Lyubomirsky, "112 Gb/s transmission with a directly-modulated laser using FFT-based synthesis of orthogonal PAM and DMT signals," *Opt. Express*, vol. 23, no. 15, p. 19202, 2015.
- [15] D. Erasme, T. Anfray, M. E. Chaibi, K. Kechaou, J. Petit, G. Aubin, K. Merghem, C. Kazmierski, J.-G. Provost, P. Chanclou, and C. Aupetit-Berthelemot, "The Dual-Electroabsorption Modulated Laser, a Flexible Solution for Amplified and Dispersion Uncompensated Networks Over Standard Fiber," *J. Light. Technol.*, vol. 32, no. 21, pp. 4068–4078, 2014.
- [16] Y. Matsui, T. Pham, W. Ling, R. Schatz, G. Carey, H. Daghighian, T. Sudo, and C. Roxlo, "55-GHz Bandwidth Short-Cavity Distributed Reflector Laser and its Application to 112-Gb/s PAM-4," in

- Optical Fiber Communication Conference Postdeadline Papers*, p. Th5B.4, 2016.
- [17] Y. Matsui, R. Schatz, G. Carey, T. Sudo, C. Roxlo, F. Corp, and C. Street, "Direct modulation laser technology toward 50-GHz bandwidth," International Semiconductor Laser Conference (ISLC), 2016.
  - [18] K. Sato, S. Kuwahara, Y. Miyamoto, and N. Shimizu, "40 Gbit/s direct modulation of distributed feedback laser for very-short-reach optical links," *Electron. Lett.*, vol. 38, no. 15, p. 816, 2002.
  - [19] K. Nakahara, T. Tsuchiya, T. Kitatani, K. Shinoda, T. Taniguchi, T. Kikawa, M. Aoki, and M. Mukaikubo, "40-Gb/s direct modulation with high extinction ratio operation of 1.3- $\mu$ m InGaAlAs multiquantum well ridge waveguide distributed feedback lasers," *IEEE Photonics Technol. Lett.*, vol. 19, no. 19, pp. 1436–1438, 2007.
  - [20] T. Tadokoro, T. Yamanaka, F. Kano, H. Oohashi, Y. Kondo, and K. Kishi, "Operation of a 25-Gb/s Direct Modulation Ridge Waveguide MQW-DFB Laser up to 85 °C," *IEEE Photonics Technol. Lett.*, vol. 21, no. 16, pp. 1154–1156, 2009.
  - [21] D. Gready, G. Eisenstein, C. Gilfert, V. Ivanov, and J. P. Reithmaier, "High-Speed Low-Noise InAs/InAlGaAs/InP 1.55- $\mu$ m Quantum-Dot Lasers," *IEEE Photonics Technol. Lett.*, vol. 24, no. 10, pp. 809–811, 2012.
  - [22] Z. Mi, J. Yang, P. Bhattacharya, G. Qin, and Z. Ma, "High-Performance Quantum Dot Lasers and Integrated Optoelectronics on Si," *Proc. IEEE*, vol. 97, no. 7, pp. 1239–1249, 2009.
  - [23] A. Y. Liu, C. Zhang, J. Norman, A. Snyder, D. Lubyshev, J. M. Fastenau, A. W. K. Liu, A. C. Gossard, and J. E. Bowers, "High performance continuous wave 1.3  $\mu$ m quantum dot lasers on silicon," *Appl. Phys. Lett.*, vol. 104, no. 4, p. 41104, 2014.
  - [24] A. Y. Liu, S. Srinivasan, J. Norman, A. C. Gossard, and J. E. Bowers, "Quantum dot lasers for silicon photonics [Invited]," *Photonics Res.*, vol. 3, no. 5, p. B1, Oct. 2015.
  - [25] S. Chen, W. Li, J. Wu, Q. Jiang, M. Tang, S. Shutts, S. N. Elliott, A. Sobiesierski, A. J. Seeds, I. Ross, P. M. Smowton, and H. Liu, "Electrically pumped continuous-wave III–V quantum dot lasers on silicon," *Nat. Photonics*, vol. 10, no. 5, pp. 307–311, Mar. 2016.
  - [26] A. Becker, V. Sichkovskyi, M. Bjelica, O. Eyal, P. Baum, A. Rippien, F. Schnabel, B. Witzigmann, G. Eisenstein, and J. P. Reithmaier, "Narrow-linewidth 1.5 $\mu$ m quantum dot distributed feedback lasers," in *Proc. of SPIE*, vol. 9767, no. 1, p. 97670Q, 2016.
  - [27] H. Kroemer, "Theory of a Wide-Gap Emitter for Transistors," *Proc. IRE*, vol. 45, no. 11, pp. 1535–1537, 1957.
  - [28] Z. I. Alferov and R. F. Kazarinov, "Semiconductor laser with electric pumping," Inventor's Certificate 181737 in Russian, Appli. 950840, priority as of March 30, 1963.
  - [29] R. Dingle and C. H. Henry, "Quantum Effects in Heterostructure Lasers," *US Pat. No 3982207*, vol. 20, 1976.
  - [30] A. Kaloyeros and S. Oktyabrsky, "Self-Assembled Quantum Dots," in *Dekker Encyclopedia of Nanoscience and Nanotechnology, Second Edition - Six Volume Set (Print Version)*, CRC Press, pp. 3775–3788, 2008.
  - [31] J. P. van der Ziel, R. Dingle, R. C. Miller, W. Wiegmann, and W. A. Nordland, "Laser oscillation from quantum states in very thin GaAs-Al<sub>0.2</sub>Ga<sub>0.8</sub>As multilayer structures," *Appl. Phys. Lett.*, vol. 26, no. 8, p. 463, 1975.
  - [32] A. Y. Cho, "Film Deposition by Molecular-Beam Techniques," *J. Vac. Sci. Technol.*, vol. 8, no. 5, pp. S31–S38, 1971.
  - [33] Y. Arakawa and H. Sakaki, "Multidimensional quantum well laser and temperature dependence

- of its threshold current," *Appl. Phys. Lett.*, vol. 40, no. 11, pp. 939–941, 1982.
- [34] Y. Arakawa, K. Vahala, and A. Yariv, "Quantum noise and dynamics in quantum well and quantum wire lasers," *Appl. Phys. Lett.*, vol. 45, no. 9, p. 950, 1984.
- [35] M. Asada, Y. Miyamoto, and Y. Suematsu, "Gain and the threshold of three-dimensional quantum-box lasers," *IEEE J. Quantum Electron.*, vol. 22, no. 9, pp. 1915–1921, 1986.
- [36] T. Takahashi and Y. Arakawa, "Nonlinear gain effects in quantum well, quantum well wire, and quantum well box lasers," *IEEE J. Quantum Electron.*, vol. 27, no. 6, pp. 1824–1829, Jun. 1991.
- [37] C. Wang, "Modulation Dynamics of InP-Based Nanostructure Laser and Quantum Cascade Laser," Institut National des Sciences Appliquées de Rennes, 2015.
- [38] N. N. Ledentsov, "Quantum dot laser," *Semicond. Sci. Technol.*, vol. 26, no. 1, p. 14001, Jan. 2011.
- [39] P. Poole, "InP-Based Quantum Dot Lasers," in *Advances in Semiconductor Lasers*, E. R. Weber and C. Jagadish, Eds., pp. 419–453, 2012.
- [40] Y. Miyamoto, M. Cao, Y. Shingai, K. Furuya, Y. Suematsu, K. G. Ravikumar, and S. Arai, "Light emission from quantum-box structure by current injection," *Jpn. J. Appl. Phys.*, vol. 26, no. 4 A, pp. L225–L227, 1987.
- [41] H. Hirayama, K. Matsunaga, M. Asada, and Y. Suematsu, "Lasing action of  $\text{Ga}_{0.67}\text{In}_{0.33}\text{As}/\text{GaInAsP}/\text{InP}$  tensile-strained quantum-box laser," *Electron. Lett.*, vol. 30, no. 2, p. 142, 1994.
- [42] Y. Nagamune, S. Tsukamoto, M. Nishioka, and Y. Arakawa, "Growth process and mechanism of nanometer-scale GaAs dot-structures using MOCVD selective growth," *J. Cryst. Growth*, vol. 126, no. 4, pp. 707–717, 1993.
- [43] D. Bimberg, M. Grundmann, and N. N. Ledentsov, *Quantum Dot Heterostructures*. Wiley, 1999.
- [44] I. N. Stranski and L. Krastanow, "Zur Theorie der orientierten Ausscheidung von Ionenkristallen aufeinander," *Monatshefte für Chemie*, vol. 71, no. 1, pp. 351–364, 1937.
- [45] Y. Arakawa, "Progress in Growth and Physics of Nitride-Based Quantum Dots," *Phys. status solidi*, vol. 188, no. 1, pp. 37–45, 2001.
- [46] A. Salhi, G. Raino, L. Fortunato, V. Tasco, G. Visimberga, L. Martiradonna, M. T. Todaro, M. De Giorgi, R. Cingolani, A. Trampert, M. De Vittorio, and A. Passaseo, "Enhanced Performances of Quantum Dot Lasers Operating at  $1.3\ \mu\text{m}$ ," *IEEE J. Sel. Top. Quantum Electron.*, vol. 14, no. 4, pp. 1188–1196, 2008.
- [47] N. Kirstaedter, N. N. Ledentsov, M. Grundmann, D. Bimberg, V. M. Ustinov, S. S. Ruvimov, M. V. Maximov, P. S. Kop'ev, Z. I. Alferov, U. Richter, P. Werner, U. Gösele, and J. Heydenreich, "Low threshold, large To injection laser emission from  $(\text{InGa})\text{As}$  quantum dots," *Electron. Lett.*, vol. 30, no. 17, p. 1416, 1994.
- [48] N. N. Ledentsov, V. a Shchukin, M. Grundmann, N. Kirstaedter, J. Böhrer, O. Schmidt, D. Bimberg, V. M. Ustinov, Yu. A. E. Zhukov, P. S. Kop'ev, S. V. Zaitsev, Zh. A. I. Borovkov, A. O. Kosogov, S. S. Ruvimov, P. Werner, U. Gösele, J. Heydenreich, A. Y. Egorov, N. Y. Gordeev, and Z. I. Alferov, "Direct Formation of Vertically Coupled Quantum Dots in Stranski--Krastanov Growth," *Phys. Rev. B*, vol. 54, no. 12, pp. 8743–8750, 1996.
- [49] A. R. Kovsh, N. A. Maleev, A. E. Zhukov, S. S. Mikhlin, A. P. Vasil'ev, E. A. Semenova, Y. M. Shernyakov, M. V. Maximov, D. A. Livshits, V. M. Ustinov, N. N. Ledentsov, D. Bimberg, and Z. I. Alferov, "InAs/InGaAs/GaAs quantum dot lasers of  $1.3\ \mu\text{m}$  range with enhanced optical gain," *J. Cryst. Growth*, vol. 251, no. 1–4, pp. 729–736, 2003.
- [50] P. B. Joyce, T. J. Krzyzewski, P. H. Steans, G. R. Bell, J. H. Neave, and T. S. Jones, "Variations in

- critical coverage for InAs/GaAs quantum dot formation in bilayer structures," *J. Cryst. Growth*, vol. 244, no. 1, pp. 39–48, 2002.
- [51] F. Y. Chang, C. C. Wu, and H. H. Lin, "Effect of InGaAs capping layer on the properties of InAs/InGaAs quantum dots and lasers," *Appl. Phys. Lett.*, vol. 82, no. 25, p. 4477, 2003.
- [52] J. Oshinowo, M. Nishioka, S. Ishida, and Y. Arakawa, "Highly uniform InGaAs/GaAs quantum dots ( $\sim 15$  nm) by metalorganic chemical vapor deposition," *Appl. Phys. Lett.*, vol. 65, no. 11, pp. 1421–1423, 1994.
- [53] P. J. Poole, K. Kaminska, P. Barrios, Z. Lu, and J. Liu, "Growth of InAs/InP-based quantum dots for  $1.55\text{ }\mu\text{m}$  laser applications," *J. Cryst. Growth*, vol. 311, no. 6, pp. 1482–1486, 2009.
- [54] M. T. Crowley, N. A. Naderi, H. Su, F. Grillot, and L. F. Lester, "GaAs-Based Quantum Dot Lasers," in *Advances in Semiconductor Lasers*, J. J. Coleman, A. C. Bryce, and C. Jagadish, Eds. Academic Press, pp. 371–417, 2012.
- [55] L. F. Lester, A. Stintz, H. Li, T. C. Newell, E. A. Pease, B. A. Fuchs, and K. J. Malloy, "Optical characteristics of  $1.24\text{-}\mu\text{m}$  InAs quantum-dot laser diodes," *IEEE Photonics Technol. Lett.*, vol. 11, no. 8, pp. 931–933, 1999.
- [56] D. Bimberg, N. N. Ledentsov, M. Grundmann, N. Kirstaedter, O. G. Schmidt, M. H. Mao, V. M. Ustinov, A. Y. Egorov, A. E. Zhukov, P. S. Kopév, Z. I. Alferov, S. S. Ruvimov, U. Gösele, and J. Heydenreich, "InAs–GaAs Quantum Pyramid Lasers: In Situ Growth, Radiative Lifetimes and Polarization Properties," *Jpn. J. Appl. Phys.*, vol. 35, no. Part 1, No. 2B, pp. 1311–1319, 1996.
- [57] D. L. Huffaker, G. Park, Z. Zou, O. B. Shchekin, and D. G. Deppe, " $1.3\text{ }\mu\text{m}$  room-temperature GaAs-based quantum-dot laser," *Appl. Phys. Lett.*, vol. 73, no. 18, pp. 2564–2566, 1998.
- [58] T. C. Newell, D. J. Bossert, A. Stintz, B. Fuchs, K. J. Malloy, and L. F. Lester, "Gain and linewidth enhancement factor in InAs quantum-dot laser diodes," *IEEE Photonics Technol. Lett.*, vol. 11, no. 12, pp. 1527–1529, 1999.
- [59] S. Fathpour, Z. Mi, P. Bhattacharya, A. R. Kovsh, S. S. Mikhlin, I. L. Krestnikov, A. V. Kozhukhov, and N. N. Ledentsov, "The role of Auger recombination in the temperature-dependent output characteristics ( $T_0=\infty$ ) of p-doped  $1.3\text{ }\mu\text{m}$  quantum dot lasers," *Appl. Phys. Lett.*, vol. 85, no. 22, pp. 5164–5166, 2004.
- [60] I. R. Sellers, H. Y. Liu, K. M. Groom, D. T. Childs, D. Robbins, T. J. Badcock, M. Hopkinson, D. J. Mowbray, and M. S. Skolnick, " $1.3\text{ }\mu\text{m}$  InAs/GaAs multilayer quantum-dot laser with extremely low room-temperature threshold current density," *Electron. Lett.*, vol. 40, no. 22, p. 1412, 2004.
- [61] T. J. Badcock, R. J. Royce, D. J. Mowbray, M. S. Skolnick, H. Y. Liu, M. Hopkinson, K. M. Groom, and Q. Jiang, "Low threshold current density and negative characteristic temperature  $1.3\text{ }\mu\text{m}$  InAs self-assembled quantum dot lasers," *Appl. Phys. Lett.*, vol. 90, no. 11, pp. 1–4, 2007.
- [62] P. Crump, S. Patterson, S. Elim, S. Zhang, M. Bougher, J. Patterson, S. Das, W. Dong, M. Grimshaw, J. Wang, D. Wise, M. DeFranza, J. Bell, J. Farmer, M. DeVito, R. Martinsen, A. Kovsh, F. Toor, and C. F. Gmachl, "Extending the wavelength range of single-emitter diode lasers for medical and sensing applications:  $12\text{xx-nm}$  quantum dots,  $2000\text{-nm}$  wells,  $>5000\text{-nm}$  cascade lasers," in *Proceedings of SPIE*, vol. 6456, p. 64560E, 2007.
- [63] D. G. Deppe, K. Shavritranuruk, G. Ozgur, H. Chen, and S. Freisem, "Quantum dot laser diode with low threshold and low internal loss," *Electron. Lett.*, vol. 45, no. 1, p. 54, 2009.
- [64] T. Kageyama, K. Watanabe, Q. H. Vo, K. Takemasa, M. Sugawara, S. Iwamoto, and Y. Arakawa, "InAs/GaAs quantum dot lasers with GaP strain-compensation layers grown by molecular beam epitaxy," *Phys. status solidi*, vol. 213, no. 4, pp. 958–964, 2016.



- [65] a. E. Zhukov, M. V. Maksimov, and a. R. Kovsh, "Device characteristics of long-wavelength lasers based on self-organized quantum dots," *Semiconductors*, vol. 46, no. 10, pp. 1225–1250, 2012.
- [66] P. Zhou, F. Zhang, Q. Guo, and S. Pan, "Linearly chirped microwave waveform generation with large time-bandwidth product by optically injected semiconductor laser," *Opt. Express*, vol. 24, no. 16, p. 18460, 2016.
- [67] QDLaser Inc., "White Paper: New era of Quantum dot lasers with evolution history of semiconductor lasers." 2008.
- [68] K. Bergman, L. P. Carloni, A. Biberman, J. Chan, and G. Hendry, *Photonic Network-on-Chip Design*. Springer New York, 2013.
- [69] Intel, "The 50G Silicon Photonics Link," 2010.
- [70] S. L. Graham, M. Snir, C. A. Patterson, C. F. Supercomputing, C. S. T. Board, D. E. P. Sciences, and N. R. Council, *Getting Up to Speed: The Future of Supercomputing*. National Academies Press, 2005.
- [71] Gail Overton, "Ranovus launches 200G quantum-dot-laser-based datacenter interconnect platform," Available: <http://www.laserfocusworld.com/articles/2016/09/ranovus-launches-200g-quantum-dot-laser-based-datacenter-interconnect-platform.html>, 2016. [Online].
- [72] V. M. Ustinov, A. R. Kovsh, A. E. Zhukov, A. Y. Egorov, N. N. Ledentsov, A. V. Lunev, Y. M. Shernyakov, M. V. Maksimov, A. F. Tsatsul'nikov, B. V. Volovik, P. S. Kop'ev, and Z. I. Alferov, "Low-threshold quantum-dot injection heterolaser emitting at 1.84  $\mu\text{m}$ ," *Tech. Phys. Lett.*, vol. 24, no. 1, pp. 22–23, 1998.
- [73] K. Nishi, M. Yamada, T. Anan, A. Gomyo, and S. Sugou, "Long-wavelength lasing from InAs self-assembled quantum dots on (311) B InP," *Appl. Phys. Lett.*, vol. 73, no. 4, pp. 526–528, 1998.
- [74] R. H. Wang, A. Stintz, P. M. Varangis, T. C. Newell, H. Li, K. J. Malloy, and L. F. Lester, "Room-temperature operation of InAs quantum-dash lasers on InP [001]," *IEEE Photonics Technol. Lett.*, vol. 13, no. 8, pp. 767–769, 2001.
- [75] A. Lenz, F. Genz, H. Eisele, L. Ivanova, R. Timm, D. Franke, H. Künzel, U. W. Pohl, and M. Dähne, "Formation of InAs/InGaAsP quantum-dashes on InP(001)," *Appl. Phys. Lett.*, vol. 95, no. 20, p. 203105, 2009.
- [76] P. Miska, J. Even, C. Platz, B. Salem, T. Benyattou, C. Bru-Chevalier, G. Guillot, G. Bremond, K. Moumanis, F. H. Julien, O. Marty, C. Monat, and M. Gendry, "Experimental and theoretical investigation of carrier confinement in InAs quantum dashes grown on InP(001)," *J. Appl. Phys.*, vol. 95, pp. 1074–1080, 2004.
- [77] M. Z. M. Khan, T. K. Ng, and B. S. Ooi, "Self-assembled InAs/InP quantum dots and quantum dashes: Material structures and devices," *Prog. Quantum Electron.*, vol. 38, no. 6, pp. 237–313, 2014.
- [78] G. Elias, A. Létoublon, R. Piron, I. Alghoraibi, A. Nakkar, N. Chevalier, K. Tavernier, A. Le Corre, N. Bertru, and S. Loualiche, "Achievement of High Density InAs/GaInAsP Quantum Dots on Misoriented InP(001) Substrates Emitting at 1.55  $\mu\text{m}$ ," *Jpn. J. Appl. Phys.*, vol. 48, no. 7, p. 70204, 2009.
- [79] C. N. Allen, P. J. Poole, P. Barrios, P. Marshall, G. Pakulski, S. Raymond, and S. Fafard, "External cavity quantum dot tunable laser through 1.55  $\mu\text{m}$ ," *Phys. E Low-dimensional Syst. Nanostructures*, vol. 26, no. 1–4, pp. 372–376, 2005.
- [80] F. Lelarge, B. Rousseau, B. Dagens, F. Poingt, F. Pommereau, and A. Accard, "Room temperature continuous-wave operation of buried ridge stripe lasers using InAs-InP (100) quantum dots as

- active core," *IEEE Photonics Technol. Lett.*, vol. 17, no. 7, pp. 1369–1371, 2005.
- [81] S. Banyoudeh and J. P. Reithmaier, "High-density 1.54  $\mu\text{m}$  InAs/InGaAlAs/InP(100) based quantum dots with reduced size inhomogeneity," *J. Cryst. Growth*, vol. 425, pp. 299–302, 2015.
- [82] S. Banyoudeh, A. Abdollahinia, O. Eyal, F. Schnabel, V. Sichkovskiy, G. Eisenstein, and J. P. Reithmaier, "Temperature-Insensitive High-Speed Directly Modulated 1.55- $\mu\text{m}$  Quantum Dot Lasers," *IEEE Photonics Technol. Lett.*, vol. 28, no. 21, pp. 2451–2454, 2016.
- [83] S. Bhowmick, M. Z. Baten, T. Frost, B. S. Ooi, and P. Bhattacharya, "High Performance InAs/In<sub>0.53</sub>Ga<sub>0.23</sub>Al<sub>0.24</sub>As/InP Quantum Dot 1.55  $\mu\text{m}$  Tunnel Injection Laser," *IEEE J. Quantum Electron.*, vol. 50, no. 1, pp. 7–14, 2014.
- [84] H. Li, G. T. Liu, P. M. Varangis, T. C. Newell, A. Stintz, B. Fuchs, K. J. Malloy, and L. F. Lester, "150-nm tuning range in a grating-coupled external cavity quantum-dot laser," *IEEE Photonics Technol. Lett.*, vol. 12, no. 7, pp. 759–761, 2000.
- [85] P. Miska, J. Even, C. Paranthoen, O. Dehaese, H. Folliot, S. Loualiche, M. Senes, and X. Marie, "Optical properties and carrier dynamics of InAs/InP(113)B quantum dots emitting between 1.3 and for laser applications," *Phys. E Low-dimensional Syst. Nanostructures*, vol. 17, pp. 56–59, 2003.
- [86] P. Caroff, C. Paranthoen, C. Platz, O. Dehaese, H. Folliot, N. Bertru, C. Labbé, R. Piron, E. Homeyer, A. Le Corre, and S. Loualiche, "High-gain and low-threshold InAs quantum-dot lasers on InP," *Appl. Phys. Lett.*, vol. 87, no. 24, pp. 1–3, 2005.
- [87] I. Alghoraibi, T. Rohel, N. Bertru, a. Le Corre, a. Létoublon, P. Caroff, O. Dehaese, and S. Loualiche, "Self-assembled InAs quantum dots grown on InP (311)B substrates: Role of buffer layer and amount of InAs deposited," *J. Cryst. Growth*, vol. 293, pp. 263–268, 2006.
- [88] K. Akahane, N. Yamamoto, and T. Kawanishi, "The dependence of the characteristic temperature of highly stacked InAs quantum dot laser diodes fabricated using a strain-compensation technique on stacking layer number," in *International Semiconductor Laser Conference (ISLC)*, vol. 8277, pp. 82–83, 2012.
- [89] W. Guo, A. Bondi, C. Cornet, H. Folliot, A. Létoublon, S. Boyer-Richard, N. Chevalier, M. Gicquel, B. Alsahwa, A. Le Corre, J. Even, O. Durand, and S. Loualiche, "First step to Si photonics: Synthesis of quantum dot light-emitters on GaP substrate by MBE," *Phys. Status Solidi Curr. Top. Solid State Phys.*, vol. 6, no. 10, pp. 2207–2211, 2009.
- [90] T. Nguyen Thanh, C. Robert, C. Cornet, M. Perrin, J. M. Jancu, N. Bertru, J. Even, N. Chevalier, H. Folliot, O. Durand, and A. Le Corre, "Room temperature photoluminescence of high density (In,Ga)As/GaP quantum dots," *Appl. Phys. Lett.*, vol. 99, no. 14, pp. 2012–2015, 2011.
- [91] E. M. Sala, G. Stracke, S. Selve, T. Niermann, M. Lehmann, S. Schlichting, F. Nippert, G. Callsen, A. Strittmatter, and D. Bimberg, "Growth and structure of In<sub>0.5</sub>Ga<sub>0.5</sub>Sb quantum dots on GaP(001)," *Appl. Phys. Lett.*, vol. 109, no. 10, pp. 1–6, 2016.
- [92] M. Seimetz, "Laser linewidth limitations for optical systems with high-order modulation employing feed forward digital carrier phase estimation," *OFC/NFOEC Conf. Opt. Fiber Commun. Fiber Opt. Eng. Conf.*, pp. 2–4, 2008.
- [93] T. Kita, R. Tang, and H. Yamada, "Narrow Spectral Linewidth Silicon Photonic Wavelength Tunable Laser Diode for Digital Coherent Communication System," *IEEE J. Sel. Top. Quantum Electron.*, vol. 22, no. 6, pp. 23–34, 2016.
- [94] H. Olesen, B. Tromborg, H. E. Lassen, and X. Pan, "Mode instability and linewidth rebroadening in DFB lasers," *Electron. Lett.*, vol. 28, no. 5, p. 444, 1992.

- 
- [95] X. Pan, B. Tromborg, and H. Olesen, "Linewidth rebroadening in DFB lasers due to weak side modes," *IEEE Photonics Technol. Lett.*, vol. 3, no. 2, pp. 112–114, 1991.
  - [96] H. Wenzel, H. J. Wünsche, and U. Bandelow, "Linewidth rebroadening in semiconductor lasers due to lateral spatial holeburning," *Electron. Lett.*, vol. 27, no. 25, p. 2301, 1991.
  - [97] G. P. Agrawal, G.-H. Duan, and P. Gallion, "Influence of refractive index nonlinearities on modulation and noise properties of semiconductor lasers," *Electron. Lett.*, vol. 28, no. 19, p. 1773, 1992.
  - [98] F. Girardin, Guang-Hua Duan, and P. Gallion, "Linewidth rebroadening due to nonlinear gain and index induced by carrier heating in strained quantum-well lasers," *IEEE Photonics Technol. Lett.*, vol. 8, no. 3, pp. 334–336, 1996.
  - [99] T. Morioka, H. Takara, S. Kawanishi, K. Uchiyama, and M. Saruwatari, "Polarization-independent all-optical demultiplexing up to 200 Gbit/s using four-wave mixing in a semiconductor laser amplifier," in *Optical Fiber Communications, OFC.*, pp. 131–132, 2001.
  - [100] J. Qin, G.-W. Lu, T. Sakamoto, K. Akahane, N. Yamamoto, D. Wang, C. Wang, H. Wang, M. Zhang, T. Kawanishi, and Y. Ji, "Simultaneous multichannel wavelength multicasting and XOR logic gate multicasting for three DPSK signals based on four-wave mixing in quantum-dot semiconductor optical amplifier," *Opt. Express*, vol. 22, no. 24, p. 29413, 2014.
  - [101] Y. Long, J. Liu, X. Hu, A. Wang, L. Zhou, K. Zou, Y. Zhu, F. Zhang, and J. Wang, "All-optical multi-channel wavelength conversion of Nyquist 16 QAM signal using a silicon waveguide," *Opt. Lett.*, vol. 40, no. 23, p. 5475, 2015.
  - [102] G. I. Papadimitriou, S. Member, C. Papazoglou, and A. S. Pomportsis, "Optical switching: Switch fabrics, techniques, and architectures," *J. Light. Technol.*, vol. 21, no. 2, pp. 384–405, 2003.
  - [103] C. H. Lee, *Microwave Photonics, Second Edition*. Taylor & Francis, 2013.
  - [104] C.-W. Chow and Y. Liu, "Nonlinear Photonic Signal Processing Subsystems and Applications," in *Advances in Lasers and Electro Optics*, InTech, 2010.
  - [105] H. N. Tan, T. Inoue, and S. Namiki, "Highly cascadable all-optical wavelength conversions of DP-QPSK, DP-16QAM, and DP-64QAM signals," in *2015 European Conference on Optical Communication (ECOC)*, vol. 1, pp. 1–3, 2015.
  - [106] K. Weich, J. Hörer, and E. Patzak, "Fast all-optical switching using two-section injection-locked semiconductor lasers," *Electron. Lett.*, vol. 30, no. 6, pp. 493–494, 1994.
  - [107] L. Vivien and L. Pavesi, *Handbook of Silicon Photonics*. CRC Press, 2016.
  - [108] J.H. Lee, W. Belardi, K. Furusawa, P. Petropoulos, Z. Yusoff, T.M. Monro, and D.J. Richardson, "Four-wave mixing based 10-Gb/s tunable wavelength conversion using a holey fiber with a high SBS threshold," *IEEE Photonics Technol. Lett.*, vol. 15, no. 3, pp. 440–442, 2003.
  - [109] T. H. Tuan, T. Cheng, K. Asano, Z. Duan, W. Gao, D. Deng, T. Suzuki, and Y. Ohishi, "Optical parametric gain and bandwidth in highly nonlinear tellurite hybrid microstructured optical fiber with four zero-dispersion wavelengths," *Opt. Express*, vol. 21, no. 17, pp. 20303–20312, 2013.
  - [110] M. Ferrera, L. Razzari, D. Duchesne, R. Morandotti, Z. Yang, M. Liscidini, J. E. Sipe, S. Chu, B. E. Little, and D. J. Moss, "Low-power continuous-wave nonlinear optics in doped silica glass integrated waveguide structures," *Nat. Photonics*, vol. 2, no. 12, pp. 737–740, 2008.
  - [111] M. Ferrera, D. Duchesne, L. Razzari, M. Peccianti, R. Morandotti, P. Cheben, S. Janz, D.-X. Xu, B. E. Little, S. Chu, and D. J. Moss, "Low power four wave mixing in an integrated, micro-ring resonator with Q = 12 million," *Opt. Express*, vol. 17, no. 16, p. 14098, 2009.
  - [112] J. R. Ong, R. Kumar, R. Aguinaldo, and S. Mookherjee, "Efficient CW Four-Wave Mixing in Silicon-

- on-Insulator Micro-Rings With Active Carrier Removal," *IEEE Photonics Technol. Lett.*, vol. 25, no. 17, pp. 1699–1702, 2013.
- [113] G. Contestabile, A. Maruta, and K.-I. Kitayama, "Four Wave Mixing in Quantum Dot Semiconductor Optical Amplifiers," *IEEE J. Quantum Electron.*, vol. 50, no. 5, pp. 379–389, 2014.
- [114] C. Meuer, C. Schmidt-Langhorst, H. Schmeckeber, G. Fiol, D. Arsenijević, C. Schubert, and D. Bimberg, "40 Gb/s wavelength conversion via four-wave mixing in a quantum-dot semiconductor optical amplifier," *Opt. Express*, vol. 19, no. 4, p. 3788, 2011.
- [115] S. J. B. Yoo, "Wavelength conversion technologies for WDM network applications," *J. Light. Technol.*, vol. 14, no. 6, pp. 955–966, 1996.
- [116] H. Soto and D. Erasme, "Investigation of nondegenerate four wave mixing in semiconductor optical amplifier through bias current modulation," *Appl. Phys. Lett.*, vol. 68, no. 26, p. 3698, 1996.
- [117] T. Akiyama, H. Kuwatsuka, N. Hatori, Y. Nakata, H. Ebe, and M. Sugawara, "Symmetric highly efficient ( $\sim 0$  dB) wavelength conversion based on four-wave mixing in quantum dot optical amplifiers," *IEEE Photonics Technol. Lett.*, vol. 14, no. 8, pp. 1139–1141, 2002.
- [118] H. Schmeckeber and S. Theses, "Quantum-Dot-Based Semiconductor Optical Amplifiers for O-Band Optical Communication," Springer International Publishing, 2016.
- [119] D. Nielsen and S. L. Chuang, "Four-wave mixing and wavelength conversion in quantum dots," *Phys. Rev. B*, vol. 81, no. 3, p. 35305, 2010.
- [120] P. Borri, S. Schneider, W. Langbein, and D. Bimberg, "Ultrafast carrier dynamics in InGaAs quantum dot materials and devices," *J. Opt. A Pure Appl. Opt.*, vol. 8, no. 4, pp. S33–S46, 2006.
- [121] T. Akiyama, O. Wada, H. Kuwatsuka, T. Simoyama, Y. Nakata, K. Mukai, M. Sugawara, and H. Ishikawa, "Nonlinear processes responsible for nondegenerate four-wave mixing in quantum-dot optical amplifiers," *Appl. Phys. Lett.*, vol. 77, no. 12, p. 1753, 2000.
- [122] Z. G. Lu, J. R. Liu, S. Raymond, P. J. Poole, P. J. Barrios, D. Poitras, F. G. Sun, G. Pakulski, P. J. Bock, and T. Hall, "Highly efficient non-degenerate four-wave mixing process in InAs/InGaAsP quantum dots," *Electron. Lett.*, vol. 42, no. 19, p. 1112, 2006.
- [123] I. Tomkos, I. Zacharopoulos, E. Roditi, and D. Syvridis, "Experimental investigation of wavelength conversion based on four-wave mixing in a three-electrode distributed feedback laser," *Appl. Phys. Lett.*, vol. 75, no. 9, p. 1195, 1999.
- [124] S. Murata, A. Tomita, J. Shimizu, and A. Suzuki, "THz optical-frequency conversion of 1 Gb/s-signals using highly nondegenerate four-wave mixing in an InGaAsP semiconductor laser," *IEEE Photonics Technol. Lett.*, vol. 3, no. 11, pp. 1021–1023, 1991.
- [125] L. Li and K. Petermann, "Small-signal analysis of optical-frequency conversion in an injection-locked semiconductor laser," *IEEE J. Quantum Electron.*, vol. 30, no. 1, pp. 43–48, 1994.
- [126] Cisco, "Cisco Global Cloud Index : Forecast and Methodology , 2014–2019," *White Pap.*, pp. 1–41, 2014.
- [127] D. O'Brien, S. P. Hegarty, G. Huyet, and a. V. Uskov, "Sensitivity of quantum-dot semiconductor lasers to optical feedback," *Opt. Lett.*, vol. 29, no. 10, p. 1072, 2004.
- [128] K. Lüdge, *Nonlinear Laser Dynamics: From Quantum Dots to Cryptography*. Wiley, 2012.
- [129] F. Grillot, Cheng Wang, N. A. Naderi, and J. Even, "Modulation Properties of Self-Injected Quantum-Dot Semiconductor Diode Lasers," *IEEE J. Sel. Top. Quantum Electron.*, vol. 19, no. 4, pp. 1900812–1900812, 2013.
- [130] C. Wang, B. Lingnau, K. Ludge, J. Even, and F. Grillot, "Enhanced Dynamic Performance of

- Quantum Dot Semiconductor Lasers Operating on the Excited State," *IEEE J. Quantum Electron.*, vol. 50, no. 9, pp. 723–731, 2014.
- [131] B. J. Stevens, D. T. D. Childs, H. Shahid, and R. A. Hogg, "Direct modulation of excited state quantum dot lasers," *Appl. Phys. Lett.*, vol. 95, no. 6, p. 61101, 2009.
  - [132] D. Arsenijević, A. Schliwa, H. Schmeckeber, M. Stubenrauch, M. Spiegelberg, D. Bimberg, V. Mikhelashvili, and G. Eisenstein, "Comparison of dynamic properties of ground- and excited-state emission in p-doped InAs/GaAs quantum-dot lasers," *Appl. Phys. Lett.*, vol. 104, no. 18, p. 181101, 2014.
  - [133] D. Arsenijević and D. Bimberg, "Quantum-dot lasers for 35 Gbit/s pulse-amplitude modulation and 160 Gbit/s differential quadrature phase-shift keying," vol. 9892, pp. 1–10, 2016.
  - [134] M. A. Cataluna, W. Sibbett, D. A. Livshits, J. Weimert, A. R. Kovsh, and E. U. Rafailov, "Stable mode locking via ground- or excited-state transitions in a two-section quantum-dot laser," *Appl. Phys. Lett.*, vol. 89, no. 8, p. 81124, 2006.
  - [135] E. U. Rafailov, M. A. Cataluna, and E. A. Avrutin, *Ultrafast Lasers Based on Quantum Dot Structures: Physics and Devices*. Wiley, 2011.
  - [136] C. Mesaritakis, C. Simos, H. Simos, S. Mikroulis, I. Krestnikov, E. Roditi, and D. Syvridis, "Effect of optical feedback to the ground and excited state emission of a passively mode locked quantum dot laser," *Appl. Phys. Lett.*, vol. 97, no. 6, p. 61114, 2010.
  - [137] F. I. Zubov, M. V. Maximov, E. I. Moiseev, A. V. Savelyev, Y. M. Shernyakov, D. A. Livshits, N. V. Kryzhanovskaya, and A. E. Zhukov, "Observation of zero linewidth enhancement factor at excited state band in quantum dot laser," *Electron. Lett.*, vol. 51, no. 21, pp. 1686–1688, 2015.
  - [138] F. Grillot, N. A. Naderi, J. B. Wright, R. Raghunathan, M. T. Crowley, and L. F. Lester, "A dual-mode quantum dot laser operating in the excited state," *Appl. Phys. Lett.*, vol. 99, no. 23, p. 231110, 2011.
  - [139] M. Virte, S. Breuer, M. Sciamanna, and K. Panajotov, "Switching between ground and excited states by optical feedback in a quantum dot laser diode," *Appl. Phys. Lett.*, vol. 105, no. 12, 2014.
  - [140] M. A. Cataluna, D. I. Nikitichev, S. Mikroulis, H. Simos, C. Simos, C. Mesaritakis, D. Syvridis, I. Krestnikov, D. Livshits, and E. U. Rafailov, "Dual-wavelength mode-locked quantum-dot laser, via ground and excited state transitions: experimental and theoretical investigation," *Opt. Express*, vol. 18, no. 12, p. 12832, 2010.
  - [141] A. Röhm, B. Lingnau, and K. Lüdge, "Ground-state modulation-enhancement by two-state lasing in quantum-dot laser devices," *Appl. Phys. Lett.*, vol. 106, no. 19, pp. 1–6, 2015.
  - [142] Z. R. Lv, H. M. Ji, S. Luo, F. Gao, F. Xu, D. H. Xiao, and T. Yang, "Dynamic characteristics of two-state lasing quantum dot lasers under large signal modulation," *AIP Adv.*, vol. 5, no. 10, 2015.
  - [143] A. J. Zilkie, "High-Speed Properties of 1.55- $\mu$ m-wavelength Quantum Dot Semiconductor Amplifiers and Comparison with Higher-Dimensional Structures," University of Toronto, 2008.
  - [144] D. Bimberg, N. Kirstaedter, N. N. Ledentsov, Z. I. Alferov, P. S. Kop'ev, and V. M. Ustinov, "InGaAs-GaAs quantum-dot lasers," *IEEE J. Sel. Top. Quantum Electron.*, vol. 3, no. 2, pp. 196–205, 1997.
  - [145] M. Gioannini, "Analysis of the optical gain characteristics of semiconductor quantum-dash materials including the band structure modifications due to the wetting layer," *IEEE J. Quantum Electron.*, vol. 42, no. 3, pp. 331–340, 2006.
  - [146] C. Cornet, C. Platz, P. Caroff, J. Even, C. Labbé, H. Folliot, A. Le Corre, and S. Loualiche, "Approach to wetting-layer-assisted lateral coupling of InAs/InP quantum dots," *Phys. Rev. B*, vol. 72, no. 3, p. 35342, 2005.

- 
- [147] A. J. Zilkie, J. Meier, M. Mojahedi, P. J. Poole, P. Barrios, D. Poitras, T. J. Rotter, C. Yang, A. Stintz, K. J. Malloy, P. W. E. Smith, and J. S. Aitchison, "Carrier Dynamics of Quantum-Dot, Quantum-Dash, and Quantum-Well Semiconductor Optical Amplifiers Operating at 1.55  $\mu\text{m}$ ," *IEEE J. Quantum Electron.*, vol. 43, no. 11, pp. 982–991, 2007.
  - [148] A. J. Nozik, "Multiple exciton generation in semiconductor quantum dots," *Chem. Phys. Lett.*, vol. 457, no. 1–3, pp. 3–11, 2008.
  - [149] T. Chen and Y. Liu, *Semiconductor Nanocrystals and Metal Nanoparticles: Physical Properties and Device Applications*. Taylor & Francis, 2016.
  - [150] M. Virte, "Two-mode dynamics and switching in quantum dot lasers Martin Virte," Vrije Universiteit Brussel and Supélec, 2015.
  - [151] T. R. Nielsen, P. Gartner, and F. Jahnke, "Many-body theory of carrier capture and relaxation in semiconductor quantum-dot lasers," *Phys. Rev. B*, vol. 69, no. 23, p. 235314, 2004.
  - [152] J. Siegert, S. Marcinkevičius, and Q. X. Zhao, "Carrier dynamics in modulation-doped InAs/GaAs quantum dots," *Phys. Rev. B*, vol. 72, no. 8, p. 85316, 2005.
  - [153] B. Ohnesorge, M. Albrecht, J. Oshinowo, A. Forchel, and Y. Arakawa, "Rapid carrier relaxation in self-assembled In<sub>x</sub>Ga<sub>1-x</sub>As/GaAs quantum dots," *Phys. Rev. B. Condens. Matter*, vol. 54, no. 16, pp. 11532–11538, 1996.
  - [154] K. Veselinov, F. Grillot, C. Cornet, J. Even, A. Bekiarski, M. Gioannini, and S. Loualiche, "Analysis of the Double Laser Emission Occurring in 1.55- $\mu\text{m}$  InAs-InP (113)B Quantum-Dot Lasers," *IEEE J. Quantum Electron.*, vol. 43, no. 9, pp. 810–816, 2007.
  - [155] P. C. Sercel, "Multiphonon-assisted tunneling through deep levels: A rapid energy-relaxation mechanism in nonideal quantum-dot heterostructures," *Phys. Rev. B*, vol. 51, no. 20, pp. 14532–14541, 1995.
  - [156] P. C. Sercel, A. L. Efros, and M. Rosen, "Intrinsic Gap States in Semiconductor Nanocrystals," *Phys. Rev. Lett.*, vol. 83, no. 12, pp. 2394–2397, 1999.
  - [157] S. Marcinkevičius, "Dynamics of Carrier Transfer into In(Ga)As Self-assembled Quantum Dots," in *Self-Assembled Quantum Dots*, New York, NY: Springer New York, pp. 129–163, 2008.
  - [158] M. Lorke, T. R. Nielsen, J. Seebeck, P. Gartner, and F. Jahnke, "Influence of carrier-carrier and carrier-phonon correlations on optical absorption and gain in quantum-dot systems," *Phys. Rev. B - Condens. Matter Mater. Phys.*, vol. 73, no. 8, 2006.
  - [159] I. Magnusdottir, A. V. Uskov, S. Bischoff, B. Tromborg, and J. Mørk, "One- and two-phonon capture processes in quantum dots," *J. Appl. Phys.*, vol. 92, no. 10, pp. 5982–5990, 2002.
  - [160] I. Magnusdottir, S. Bischoff, A. V. Uskov, and J. Mørk, "Geometry dependence of Auger carrier capture rates into cone-shaped self-assembled quantum dots," *Phys. Rev. B*, vol. 67, no. 20, p. 205326, 2003.
  - [161] U. Bockelmann and G. Bastard, "Phonon scattering and energy relaxation in two-, one-, and zero-dimensional electron gases," *Phys. Rev. B*, vol. 42, no. 14, pp. 8947–8951, 1990.
  - [162] H. Benisty, C. M. Sotomayor-Torrès, and C. Weisbuch, "Intrinsic mechanism for the poor luminescence properties of quantum-box systems," *Phys. Rev. B*, vol. 44, no. 19, pp. 10945–10948, 1991.
  - [163] J. Urayama, T. B. Norris, J. Singh, and P. Bhattacharya, "Observation of phonon bottleneck in quantum dot electronic relaxation," *Phys. Rev. Lett.*, vol. 86, no. 21, pp. 4930–4933, 2001.
  - [164] X.-Q. Li, H. Nakayama, and Y. Arakawa, "Phonon bottleneck in quantum dots: Role of lifetime of the confined optical phonons," *Phys. Rev. B*, vol. 59, no. 7, pp. 5069–5073, 1999.

- 
- [165] O. Verzele, G. Bastard, and R. Ferreira, "Energy Relaxation in Quantum Dots," *Phys. Rev. B*, vol. 66, p. 081308(R), 2002.
  - [166] A. V. Uskov, J. McInerney, F. Adler, H. Schweizer, and M. H. Pilkuhn, "Auger carrier capture kinetics in self-assembled quantum dot structures," *Appl. Phys. Lett.*, vol. 72, no. 1, pp. 58–60, 1998.
  - [167] D. F. Schroeter, D. J. Griffiths, and P. C. Serce, "Defect-assisted relaxation in quantum dots at low temperature," *Phys. Rev. B*, vol. 54, no. 3, pp. 1486–1489, 1996.
  - [168] D. Bimberg, "Quantum dot based nanophotonics and nanoelectronics," *Electron. Lett.*, vol. 44, no. 5, p. 390, 2008.
  - [169] P. Blood, "Gain and recombination in quantum dot lasers," *IEEE J. Sel. Top. Quantum Electron.*, vol. 15, no. 3, pp. 808–818, 2009.
  - [170] H. Dery and G. Eisenstein, "The impact of energy band diagram and inhomogeneous broadening on the optical differential gain in nanostructure lasers," *IEEE J. Quantum Electron.*, vol. 41, no. 1, pp. 26–35, 2005.
  - [171] K. Akahane, N. Yamamoto, and M. Tsuchiya, "Highly stacked quantum-dot laser fabricated using a strain compensation technique," *Appl. Phys. Lett.*, vol. 93, no. 4, pp. 58–61, 2008.
  - [172] H. C. Schneider, W. W. Chow, and S. W. Koch, "Excitation-induced dephasing in semiconductor quantum dots," *Phys. Rev. B - Condens. Matter Mater. Phys.*, vol. 70, no. 23, pp. 1–4, 2004.
  - [173] H. Haug and S. W. Koch, *Quantum Theory of the Optical and Electronic Properties of Semiconductors*. World Scientific, 2009.
  - [174] H. H. Nilsson, J. Z. Zhang, and I. Galbraith, "Homogeneous broadening in quantum dots due to Auger scattering with wetting layer carriers," *Phys. Rev. B - Condens. Matter Mater. Phys.*, vol. 72, no. 20, pp. 1–8, 2005.
  - [175] A. Sakamoto and M. Sugawara, "Theoretical calculation of lasing spectra of quantum-dot lasers: Effect of homogeneous broadening of optical gain," *IEEE Photonics Technol. Lett.*, vol. 12, no. 2, pp. 107–109, 2000.
  - [176] P. Borri, W. Langbein, S. Schneider, U. Woggon, R. Sellin, D. Ouyang, and D. Bimberg, "Ultralong Dephasing Time in InGaAs Quantum Dots," *Phys. Rev. Lett.*, vol. 87, no. 15, p. 157401, 2001.
  - [177] K. Matsuda, K. Ikeda, T. Saiki, H. Tsuchiya, H. Saito, and K. Nishi, "Homogeneous linewidth broadening in a  $\text{In}_{0.5}\text{Ga}_{0.5}\text{As}/\text{GaAs}$  single quantum dot at room temperature investigated using a highly sensitive near-field scanning optical microscope," *Phys. Rev. B*, vol. 63, p. 121304, 2001.
  - [178] M. Bayer and A. Forchel, "Temperature dependence of the exciton homogeneous linewidth in  $\text{In}_{0.60}\text{As}_{0.40}/\text{GaAs}$  self-assembled quantum dots," *Phys. Rev. B*, vol. 65, no. 4, p. 41308, 2002.
  - [179] K. Veselinov, F. Grillot, M. Gioannini, I. Montrosset, E. Homeyer, R. Piron, J. Even, A. Bekiariski, and S. Loualiche, "Lasing spectra of  $1.55\ \mu\text{m}$  InAs/InP quantum dot lasers: Theoretical analysis and comparison with the experiments," *Opt. Quantum Electron.*, vol. 40, no. 2–4, pp. 227–237, 2008.
  - [180] D. Gready and G. Eisenstein, "Effects of homogeneous and inhomogeneous broadening on the dynamics of tunneling injection quantum dot lasers," *IEEE J. Quantum Electron.*, vol. 47, no. 7, pp. 944–949, 2011.
  - [181] C. Cornet, M. Hayne, P. Caroff, C. Levallois, L. Joulaud, E. Homeyer, C. Paranthoen, J. Even, C. Labbé, H. Folliot, V. V. Moshchalkov, and S. Loualiche, "Increase of charge-carrier redistribution efficiency in a laterally organized superlattice of coupled quantum dots," *Phys. Rev. B - Condens. Matter Mater. Phys.*, vol. 74, no. 24, pp. 1–10, 2006.

- 
- [182] C. Henry, "Theory of the linewidth of semiconductor lasers," *IEEE J. Quantum Electron.*, vol. 18, no. 2, pp. 259–264, 1982.
  - [183] W. W. Chow and S. W. Koch, *Semiconductor-Laser Fundamentals: Physics of the Gain Materials*. Springer Berlin Heidelberg, 1999.
  - [184] M. Osinski and J. Buus, "Linewidth broadening factor in semiconductor lasers--An overview," *IEEE J. Quantum Electron.*, vol. 23, no. 1, pp. 9–29, 1987.
  - [185] G. H. Duan, P. Gallion, and G. Debarge, "Analysis of the Phase-Amplitude Coupling Factor and Spectral Linewidth of Distributed Feedback and Composite-Cavity Semiconductor Lasers," *IEEE J. Quantum Electron.*, vol. 26, no. 1, pp. 32–44, 1990.
  - [186] G. Duan, P. Gallion, and G. Debarge, "Analysis of frequency chirping of semiconductor lasers in the presence of optical feedback," *Opt. Lett.*, vol. 12, no. 10, pp. 800–802, 1987.
  - [187] G. P. Agrawal, "Intensity dependence of the linewidth enhancement factor and its implications for semiconductor lasers," *IEEE Photonics Technology Letters*, vol. 1, no. 8, pp. 212–214, 1989.
  - [188] S. Wieczorek, B. Krauskopf, and D. Lenstra, "Multipulse Excitability in a Semiconductor Laser with Optical Injection," *Phys. Rev. Lett.*, vol. 88, no. 6, p. 63901, 2002.
  - [189] B. Haegeman, K. Engelborghs, D. Roose, D. Pieroux, and T. Erneux, "Stability and rupture of bifurcation bridges in semiconductor lasers subject to optical feedback," *Phys. Rev. E*, vol. 66, no. 4, p. 46216, 2002.
  - [190] C.-F. Chuang, Y.-H. Liao, C.-H. Lin, S.-Y. Chen, F. Grillot, and F.-Y. Lin, "Linewidth enhancement factor in semiconductor lasers subject to various external optical feedback conditions," *Opt. Express*, vol. 22, no. 5, p. 5651, 2014.
  - [191] M. Lax, "Classical Noise. V. Noise in Self-Sustained Oscillators," *Phys. Rev.*, vol. 160, no. 2, pp. 290–307, 1967.
  - [192] H. Haug and H. Haken, "Theory of noise in semiconductor laser emission," *Zeitschrift für Phys.*, vol. 204, no. 3, pp. 262–275, 1967.
  - [193] L.A.Coldren, S.W.Corzine, L. A. Coldren, S. W. Corzine, and M. L. Mashanovitch, *Diode Lasers and Photonic Integrated Circuits*, vol. 36, no. 2. Wiley, 1995.
  - [194] B. Dagens, A. Markus, J. X. Chen, J.-G. Provost, D. Make, O. Le Gouezigou, J. Landreau, A. Fiore, and B. Thedrez, "Giant linewidth enhancement factor and purely frequency modulated emission from quantum dot laser," *Electron. Lett.*, vol. 41, no. 6, p. 323, 2005.
  - [195] E. Rosencher and B. Vinter, *Optoelectronics*. Cambridge University Press, 2002.
  - [196] Z. Mi, P. Bhattacharya, and S. Fathpour, "High-speed 1.3  $\mu\text{m}$  tunnel injection quantum-dot lasers," *Appl. Phys. Lett.*, vol. 86, no. 15, pp. 1–3, 2005.
  - [197] B. Lingnau, K. Lüdge, W. W. Chow, and E. Schöll, "Failure of the  $\alpha$  factor in describing dynamical instabilities and chaos in quantum-dot lasers," *Phys. Rev. E - Stat. Nonlinear, Soft Matter Phys.*, vol. 86, no. 6, pp. 1–5, 2012.
  - [198] B. Lingnau, W. W. Chow, E. Schöll, and K. Lüdge, "Feedback and injection locking instabilities in quantum-dot lasers: A microscopically based bifurcation analysis," *New J. Phys.*, vol. 15, 2013.
  - [199] A. V. Uskov, E. P. O'Reilly, D. McPeake, N. N. Ledentsov, D. Bimberg, and G. Huyet, "Carrier-induced refractive index in quantum dot structures due to transitions from discrete quantum dot levels to continuum states," *Appl. Phys. Lett.*, vol. 84, no. 2, pp. 272–274, 2004.
  - [200] S. P. Hegarty, B. Corbett, J. G. McInerney, and G. Huyet, "Free-carrier effect on index change in 1.3  $\mu\text{m}$  quantum-dot lasers," *Electron. Lett.*, vol. 41, no. 7, p. 416, 2005.
  - [201] D. E. McCumber, "Intensity Fluctuations in the Output of cw Laser Oscillators. I," *Phys. Rev.*, vol.



- 141, no. 1, pp. 306–322, 1966.
- [202] A. Uchida, *Optical Communication with Chaotic Lasers: Applications of Nonlinear Dynamics and Synchronization*. Wiley, 2012.
- [203] E. Malic, M. J. P. Bormann, P. Hovel, M. Kuntz, D. Bimberg, A. Knorr, and E. Scholl, “Coulomb Damped Relaxation Oscillations in Semiconductor Quantum Dot Lasers,” *IEEE J. Sel. Top. Quantum Electron.*, vol. 13, no. 5, pp. 1242–1248, 2007.
- [204] P. Borri, W. Langbein, J. M. Hvam, F. Heinrichsdorff, M.-H. Mao, and D. Bimberg, “Spectral hole-burning and carrier-heating dynamics in InGaAs quantum-dot amplifiers,” *IEEE J. Sel. Top. Quantum Electron.*, vol. 6, no. 3, pp. 544–551, 2000.
- [205] Z. Bakonyi, H. Su, G. Onishchukov, L. F. Lester, A. L. Gray, T. C. Newell, and A. Tünnermann, “High-Gain Quantum-Dot Semiconductor Optical Amplifier for 1300 nm,” *IEEE J. Quantum Electron.*, vol. 39, no. 11, pp. 1409–1414, 2003.
- [206] M. Willatzen, A. Uskov, J. Mørk, H. Olesen, B. Tromborg, and A.-P. Jauho, “Nonlinear Gain Suppression in Semiconductor Lasers Due to Carrier Heating,” *IEEE Photonics Technol. Lett.*, vol. 3, no. 7, pp. 606–609, 1991.
- [207] J. Huang and L. W. Casperson, “Gain and saturation in semiconductor lasers,” *Opt. Quantum Electron.*, vol. 25, no. 6, pp. 369–390, 1993.
- [208] D. J. Klotzkin, *Introduction to Semiconductor Lasers for Optical Communications*. New York, NY: Springer New York, 2014.
- [209] G. Morthier, F. Libbrecht, K. David, P. Vankwikelberge, and R. G. Baets, “Theoretical investigation of the second-order harmonic distortion in the AM response of 1.55  $\mu\text{m}$  F-P and DFB lasers,” *IEEE J. Quantum Electron.*, vol. 27, no. 8, pp. 1990–2002, 1991.
- [210] G.-H. Duan, P. Gallion, and G. P. Agrawal, “Effective nonlinear gain in semiconductor lasers,” *IEEE Photonics Technol. Lett.*, vol. 4, no. 3, pp. 218–220, 1992.
- [211] R. H. Wentworth, “Large-scale longitudinal spatial-hole burning contribution to laser gain compression,” *IEEE J. Quantum Electron.*, vol. 29, no. 7, pp. 2145–2153, 1993.
- [212] F. Grillot, B. Dagens, J. Provost, H. Su, and L. F. Lester, “Gain Compression and Above-Threshold Linewidth Enhancement Factor in 1.3- $\mu\text{m}$  InAs-GaAs Quantum-Dot Lasers,” *IEEE J. Quantum Electron.*, vol. 44, no. 10, pp. 946–951, 2008.
- [213] M. Nakazawa, K. Kikuchi, T. Miyazaki, and D. Chowdhury, *High Spectral Density Optical Communication Technologies*, vol. 79. Berlin, Heidelberg: Springer Berlin Heidelberg, 2010.
- [214] J. Kahn, “Modulation and Detection Techniques for Optical Communication Systems,” in *Optical Amplifiers and Their Applications/Coherent Optical Technologies and Applications*, vol. 2, no. M, p. CThC1, 2006.
- [215] M. Fukuda, *Optical Semiconductor Devices*. Wiley, 1999.
- [216] T. W. Berg and J. Mørk, “Quantum dot amplifiers with high output power and low noise,” *Appl. Phys. Lett.*, vol. 82, no. 18, p. 3083, 2003.
- [217] S. Osborne, P. Blood, P. Smowton, J. Lutti, Y. C. Xin, A. Stintz, D. Huffaker, and L. F. Lester, “State filling in InAs quantum-dot laser structures,” *IEEE J. Quantum Electron.*, vol. 40, no. 12, pp. 1639–1645, 2004.
- [218] H. Su, “Dynamic Properties of Quantum Dot Distributed Feedback Lasers,” University of New Mexico, 2004.
- [219] E. Kapon, *Semiconductor Lasers I: Fundamentals*. Elsevier Science, 1999.
- [220] V. M. Ustinov, N. a. Maleev, a. E. Zhukov, a. R. Kovsh, a. Y. Egorov, a. V. Lunev, B. V. Volovik, I.

- L. Krestnikov, Y. G. Musikhin, N. a Bert, P. S. Kop'ev, Z. I. Alferov, N. N. Ledentsov, and D. Bimberg, "InAs/InGaAs quantum dot structures on GaAs substrates emitting at 1.3  $\mu\text{m}$ ," *Appl. Phys. Lett.*, vol. 74, no. 19, p. 2815, 1999.
- [221] M. V. Maximov, A. F. Tsatsul'nikov, B. V. Volovik, D. S. Sizov, Y. M. Shernyakov, I. N. Kaiander, A. E. Zhukov, A. R. Kovsh, S. S. Mikhlin, V. M. Ustinov, Z. I. Alferov, R. Heitz, V. A. Shchukin, N. N. Ledentsov, D. Bimberg, Y. G. Musikhin, and W. Neumann, "Tuning quantum dot properties by activated phase separation of an InGa(Al)As alloy grown on InAs stressors," *Phys. Rev. B*, vol. 62, no. 24, pp. 16671–16680, 2000.
- [222] P. Crump, J. Wang, T. Crum, S. Das, M. DeVito, W. Dong, J. Farmer, Y. Feng, M. Grimshaw, D. Wise, and S. Zhang, "360 W and 70% efficient GaAs-based diode lasers," *Proc. SPIE*, vol. 5711, no. 1, pp. 21–29, 2005.
- [223] D. Liang, D. C. Chapman, Y. Li, D. C. Oakley, T. Napoleone, P. W. Juodawlkis, C. Brubaker, C. Mann, H. Bar, O. Raday, and J. E. Bowers, "Uniformity study of wafer-scale InP-to-silicon hybrid integration," *Appl. Phys. A Mater. Sci. Process.*, vol. 103, no. 1, pp. 213–218, 2011.
- [224] N. N. Ledentsov, V. M. Ustinov, V. A. Shchukin, P. S. Kop'ev, Z. I. Alferov, and D. Bimberg, "Quantum dot heterostructures: Fabrication, properties, lasers (Review)," *Semiconductors*, vol. 32, no. 4, pp. 343–365, 1998.
- [225] J. E. Carroll, J. Whiteaway, and D. Plumb, *Distributed Feedback Semiconductor Lasers*, vol. 10. Institution of Electrical Engineers, 1998.
- [226] A. L. Schawlow and C. H. Townes, "Infrared and optical masers," *Phys. Rev.*, vol. 112, no. 6, pp. 1940–1949, 1958.
- [227] B. W. Hakki and T. L. Paoli, "cw degradation at 300°K of GaAs double-heterostructure junction lasers. II. Electronic gain," *J. Appl. Phys.*, vol. 44, no. 9, p. 4113, 1973.
- [228] C. Harder, K. Vahala, and A. Yariv, "Measurement of the linewidth enhancement factor  $\alpha$  of semiconductor lasers," *Appl. Phys. Lett.*, vol. 42, no. 4, pp. 328–330, 1983.
- [229] J.-G. Provost and F. Grillot, "Measuring the Chirp and the Linewidth Enhancement Factor of Optoelectronic Devices with a Mach-Zehnder Interferometer," *IEEE Photonics J.*, vol. 3, no. 3, pp. 476–488, 2011.
- [230] F. Devaux, Y. Sorel, and J. F. Kerdiles, "Simple measurement of fiber dispersion and of chirp parameter of intensity modulated light emitter," *J. Light. Technol.*, vol. 11, no. 12, pp. 1937–1940, 1993.
- [231] R. Hui, a. Mecozzi, A. D'Ottavi, and P. Spano, "Novel measurement technique of  $\alpha$  factor in DFB semiconductor lasers by injection locking," *Electron. Lett.*, vol. 26, no. 14, p. 997, 1990.
- [232] Y. Yu, G. Giuliani, and S. Donati, "Measurement of the Linewidth Enhancement Factor of Semiconductor Lasers Based on the Optical Feedback Self-Mixing Effect," *IEEE Photonics Technol. Lett.*, vol. 16, no. 4, pp. 990–992, 2004.
- [233] C.-H. Lin, H.-H. Lin, and F.-Y. Lin, "Four-wave mixing analysis of quantum dot semiconductor lasers for linewidth enhancement factor extraction," *Opt. Express*, vol. 20, no. 1, p. 101, 2012.
- [234] H. Nakajima and J.-C. Bouley, "Observation of power dependent linewidth enhancement factor in 1.55  $\mu\text{m}$  strained quantum well lasers," *Electron. Lett.*, vol. 27, no. 20, p. 1840, 1991.
- [235] K. Furuya, "Dependence of linewidth enhancement factor  $\alpha$  on waveguide structure in semiconductor lasers," *Electron. Lett.*, vol. 21, no. 5, p. 200, 1985.
- [236] L. D. Westbrook, "Dispersion of linewidth-broadening factor in 1.5  $\mu\text{m}$  laser diodes," *Electron. Lett.*, vol. 21, no. 22, p. 1018, 1985.

- 
- [237] G. P. Agrawal, "Effect of gain and index nonlinearities on single-mode dynamics in semiconductor lasers," *IEEE J. Quantum Electron.*, vol. 26, no. 11, pp. 1901–1909, 1990.
  - [238] A. J. Zilkie, J. Meier, M. Mojahedi, A. S. Helmy, P. J. Poole, P. Barrios, D. Poitras, T. J. Rotter, C. Yang, A. Stintz, K. J. Malloy, P. W. E. Smith, and J. S. Aitchison, "Time-Resolved Linewidth Enhancement Factors in Quantum Dot and Higher-Dimensional Semiconductor Amplifiers Operating at 1.55  $\mu\text{m}$ ," *J. Light. Technol.*, vol. 26, no. 11, pp. 1498–1509, 2008.
  - [239] M. Funabashi, H. Kawanishi, T. K. Sudoh, T. Nakura, D. Schmitz, F. Schulte, Y. Nakano, and K. Tada, "Comparision of InGaAs absorptive grating structures in 1.55  $\mu\text{m}$  InGaAsP/InP strained MQW gain-coupled DFB lasers," in *Conference Proceedings International Conference on Indium Phosphide and Related Materials*, pp. 292–295, 1997.
  - [240] K. E. Chlouverakis, K. M. Al-Aswad, I. D. Henning, and M. J. Adams, "Determining laser linewidth parameter from Hopf bifurcation minimum in lasers subject to optical injection," *Electron. Lett.*, vol. 39, no. 16, p. 1185, 2003.
  - [241] C. Wang, M. E. Chaibi, H. Huang, D. Erasme, P. Poole, J. Even, and F. Grillot, "Frequency-dependent linewidth enhancement factor of optical injection-locked quantum dot/dash lasers," *Opt. Express*, vol. 23, no. 17, p. 21761, 2015.
  - [242] R. Schimpe, J. E. Bowers, and T. L. Koch, "Characterisation of frequency response of 1.5  $\mu\text{m}$  InGaAsP DFB laser diode and InGaAs PIN photodiode by heterodyne measurement technique," *Electron. Lett.*, vol. 22, no. 9, p. 453, 1986.
  - [243] L. Olofsson and T. G. Brown, "Frequency dependence of the chirp factor in 1.55  $\mu\text{m}$  distributed feedback semiconductor lasers," *IEEE Photonics Technol. Lett.*, vol. 4, no. 7, pp. 688–691, 1992.
  - [244] B. Moller, E. Zeeb, U. Fiedler, T. Hackbarth, and K. J. Ebeling, "Linewidth enhancement factor of vertical-cavity surface-emitting laser diodes," *IEEE Photonics Technol. Lett.*, vol. 6, no. 8, pp. 921–923, 1994.
  - [245] M. E. Chaibi, H. T. Nguyen, C. Gosset, F. Grillot, and D. Erasme, "Time Resolved Chirp Measurement Based on a Polarization-Maintaining Fiber," *IEEE Photonics Technol. Lett.*, vol. 27, no. 14, pp. 1557–1560, 2015.
  - [246] H. Su, L. Zhang, a. L. Gray, R. Wang, P. M. Varangis, and L. F. Lester, "Gain compression coefficient and above-threshold linewidth enhancement factor in InAs/GaAs quantum dot DFB lasers," in *SPIE 5722, Physics and Simulation of Optoelectronic Devices XIII*, vol. 5722, pp. 72–79, 2005.
  - [247] C. Wang, F. Grillot, and J. Even, "Impacts of Wetting Layer and Excited State on the Modulation Response of Quantum-Dot Lasers," *IEEE J. Quantum Electron.*, vol. 48, no. 9, pp. 1144–1150, 2012.
  - [248] F. Aflatouni and H. Hashemi, "Light Source Independent Linewidth Reduction of Lasers - OSA Technical Digest," *Opt. Fiber Commun. Conf.*, p. OW1G.6, 2012.
  - [249] T. Wang, T. Yang, D. Jia, Z. Wang, and C. Ge, "Multi-wavelength lasers with suppressed spectral linewidth of 10 kHz," *Opt. Express*, vol. 22, no. 22, pp. 26862–26871, 2014.
  - [250] T. Okoshi, K. Kikuchi, and A. Nakayama, "Novel method for high resolution measurement of laser output spectrum," *Electron. Lett.*, vol. 16, no. 16, p. 630, 1980.
  - [251] P. Thompson, D. E. Cox, and J. B. Hastings, "Rietveld Refinement of Debye-Scherrer Synchrotron X-ray Data from A1203," *J. Appl. Crystallogr.*, vol. 20, no. 2, pp. 79–83, 1987.
  - [252] S. Borenstain and J. Katz, "Intersubband Auger recombination and population inversion in quantum-well subbands," *Phys. Rev. B*, vol. 39, no. 15, pp. 10852–10857, 1989.
  - [253] K. Takaki, T. Kise, K. Maruyama, N. Yamanaka, M. Funabashi, and A. Kasukawa, "Reduced

- linewidth re-broadening by suppressing longitudinal spatial hole burning in high-power 1.55- $\mu\text{m}$  continuous-wave distributed-feedback (CW-DFB) laser diodes," *IEEE J. Quantum Electron.*, vol. 39, no. 9, pp. 1060–1065, 2003.
- [254] S. Melnik, G. Huyet, and A. Uskov, "The linewidth enhancement factor  $\alpha$  of quantum dot semiconductor lasers," *Opt. Express*, vol. 14, no. 7, p. 2950, 2006.
- [255] S. Knappe, P. Schwindt, V. Shah, L. Hollberg, J. Kitching, L. Liew, and J. Moreland, "A chip-scale atomic clock based on 87Rb with improved frequency stability," *Opt. Express*, vol. 13, no. 4, pp. 1249–1253, 2005.
- [256] R. Lutwak, "The chip-scale atomic clock - Recent developments," *2009 IEEE Int. Freq. Control Symp. Jt. with 22nd Eur. Freq. Time Forum*, pp. 573–577, 2009.
- [257] R. A. Fisher, *Optical Phase Conjugation*. Elsevier Science, 1983.
- [258] C. Bohémond, T. Rampone, and A. Sharaiha, "Performances of a photonic microwave mixer based on cross-gain modulation in a semiconductor optical amplifier," *J. Light. Technol.*, vol. 29, no. 16, pp. 2402–2409, 2011.
- [259] H. Tsuchida, T. Simoyama, H. Ishikawa, T. Mozume, M. Nagase, and J. Kasai, "Cross-phase-modulation-based wavelength conversion using intersubband transition in InGaAs/AlAs/AlAsSb coupled quantum wells," *Opt. Lett.*, vol. 32, no. 7, pp. 751–3, 2007.
- [260] Ju Han Lee, W. Belardi, K. Furusawa, P. Petropoulos, Z. Yusoff, T. M. Monro, and D. J. Richardson, "Four-wave mixing based 10-Gb/s tunable wavelength conversion using a holey fiber with a high SBS threshold," *IEEE Photonics Technol. Lett.*, vol. 15, no. 3, pp. 440–442, 2003.
- [261] H. Su, H. Li, L. Zhang, Z. Zou, A. L. Gray, R. Wang, P. M. Varangis, and L. F. Lester, "Nondegenerate four-wave mixing in quantum dot distributed feedback lasers," *IEEE Photonics Technol. Lett.*, vol. 17, no. 8, pp. 1686–1688, 2005.
- [262] A. Mecozzi and R. Hui, "Nearly degenerate four-wave mixing in distributed feedback semiconductor lasers operating above threshold," *IEEE J. Quantum Electron.*, vol. 29, no. 6, pp. 1477–1487, 1993.
- [263] T. Simoyama, H. Kuwatsuka, and H. Ishikawa, "Cavity Length Dependence of Wavelength Conversion Efficiency of Four-wave Mixing in  $\lambda/4$ -shifted DFB Laser," *Fujitsu Sci. Tech. J.*, vol. 34, no. 2, pp. 235–244, 1998.
- [264] H. Su, H. Li, L. Zhang, Z. Zou, A. L. Gray, R. Wang, P. M. Varangis, and L. F. Lester, "Nondegenerate four-wave mixing in quantum dot distributed feedback lasers," *IEEE Photonics Technol. Lett.*, vol. 17, no. 8, pp. 1686–1688, 2005.
- [265] F. Grillot, "On the Effects of an Antireflection Coating Impairment on the Sensitivity to Optical Feedback of AR/HR Semiconductor DFB Lasers," *IEEE J. Quantum Electron.*, vol. 45, no. 6, pp. 720–729, 2009.
- [266] V. Roncin, "Contribution à l'étude de fonctions optiques à base d'amplificateurs optiques à semi-conducteurs pour la régénération des signaux de télécommunication à très haut débit," Université de Rennes I, 2008.
- [267] J. Zhou, N. Park, J. W. Dawson, K. J. Vahala, M. A. Newkirk, and B. I. Miller, "Terahertz four-wave mixing spectroscopy for study of ultrafast dynamics in a semiconductor optical amplifier," *Appl. Phys. Lett.*, vol. 63, no. 9, pp. 1179–1181, 1993.
- [268] H. Kuwatsuka, H. Shoji, M. Matsuda, and H. Ishikawa, "THz frequency conversion using nondegenerate four-wave mixing process in a lasing long-cavity  $\lambda/4$ -shifted DFB laser," *Electron. Lett.*, vol. 31, no. 24, pp. 2108–2110, 1995.

- [269] T. Sadeev, H. Huang, D. Arsenijević, K. Schires, F. Grillot, and D. Bimberg, "Highly efficient non-degenerate four-wave mixing under dual-mode injection in InP/InAs quantum-dash and quantum-dot lasers at 1.55  $\mu\text{m}$ ," *Appl. Phys. Lett.*, vol. 107, no. 19, p. 191111, 2015.
- [270] H. Ju, A. V. Uskov, R. Nötzel, Z. Li, J. M. Vázquez, D. Lenstra, G. D. Khoe, and H. J. S. Dorren, "Effects of two-photon absorption on carrier dynamics in quantum-dot optical amplifiers," *Appl. Phys. B Lasers Opt.*, vol. 82, no. 4, pp. 615–620, 2006.
- [271] S. Murata, A. Tomita, J. Shimizu, M. Kitamura, and A. Suzuki, "Observation of highly nondegenerate four-wave mixing ( $\geq 1$  THz) in an InGaAsP multiple quantum well laser," *Appl. Phys. Lett.*, vol. 58, no. 14, p. 1458, 1991.
- [272] H. Huang, K. Schires, P. J. Poole, and F. Grillot, "Non-degenerate four-wave mixing in an optically injection-locked InAs/InP quantum dot Fabry–Perot laser," *Appl. Phys. Lett.*, vol. 106, no. 14, p. 143501, 2015.
- [273] H. Huang, D. Arsenijević, K. Schires, T. Sadeev, D. Erasme, D. Bimberg, and F. Grillot, "Efficiency of four-wave mixing in injection-locked InAs/GaAs quantum-dot lasers," *AIP Adv.*, vol. 6, no. 12, p. 125105, 2016.
- [274] H. Kuwatsuka, H. Shoji, M. Matsuda, and H. Ishikawa, "Nondegenerate four-wave mixing in a long-cavity  $\lambda/4$ -shifted DFB laser using its lasing beam as pump beams," *IEEE J. Quantum Electron.*, vol. 33, no. 11, pp. 2002–2010, 1997.
- [275] R. Lang, "Injection Locking Properties of a Semiconductor Laser," *IEEE J. Quantum Electron.*, vol. 18, no. 6, pp. 976–983, 1982.
- [276] F. Mogensen, H. Olesen, and G. Jacobsen, "Locking conditions and stability properties for a semiconductor laser with external light injection," *IEEE J. Quantum Electron.*, vol. 21, no. 7, pp. 784–793, 1985.
- [277] A. Murakami, K. Kawashima, and K. Atsuki, "Cavity resonance shift and bandwidth enhancement in semiconductor lasers with strong light injection," *IEEE J. Quantum Electron.*, vol. 39, no. 10, pp. 1196–1204, 2003.
- [278] K. E. Chlouverakis and M. J. Adams, "Stability maps of injection-locked laser diodes using the largest Lyapunov exponent," *Opt. Commun.*, vol. 216, no. 4–6, pp. 405–412, 2003.
- [279] T. B. Simpson, J. M. Liu, and A. Gavrielides, "Bandwidth enhancement and broadband noise reduction in injection-locked semiconductor lasers," *IEEE Photonics Technol. Lett.*, vol. 7, no. 7, pp. 709–711, 1995.
- [280] C. Lin and F. Mengel, "Reduction of frequency chirping and dynamic linewidth in high-speed directly modulated semiconductor lasers by injection locking," *Electron. Lett.*, vol. 20, no. 25–26, p. 1073, 1984.
- [281] J. M. Liu, H. F. Chen, X. J. Meng, T. B. Simpson, and T. B. Thompson, "Modulation bandwidth, noise, and stability of a semiconductor laser subject to strong injection locking," *IEEE Photonics Technol. Lett.*, vol. 9, no. 10, pp. 1325–1327, 1997.
- [282] G. Yabre, H. De Waardt, H. P. A. van den Boom, and G.-D. Khoe, "Noise characteristics of single-mode semiconductor lasers under external light injection," *IEEE J. Quantum Electron.*, vol. 36, no. 3, pp. 385–393, 2000.
- [283] R. Hui and A. Mecozzi, "Phase noise of four-wave mixing in semiconductor lasers," *Appl. Phys. Lett.*, vol. 60, no. 20, pp. 2454–2456, 1992.
- [284] M. Gioannini and I. Montrosset, "Numerical Analysis of the Frequency Chirp in Quantum-Dot Semiconductor Lasers," *IEEE J. Quantum Electron.*, vol. 43, no. 10, pp. 941–949, 2007.

- 
- [285] T. Sadeev, D. Arsenijević, D. Franke, J. Kreissl, H. Künzel, and D. Bimberg, "1.55- $\mu\text{m}$  mode-locked quantum-dot lasers with 300 MHz frequency tuning range," *Appl. Phys. Lett.*, vol. 106, no. 3, 2015.
  - [286] D. Hadass, A. Bilenca, R. Alizon, H. Dery, V. Mikhelashvili, G. Eisenstein, R. Schwertberger, A. Somers, J. P. Reithmaier, A. Forchel, M. Calligaro, S. Bansropun, and M. Krakowski, "Gain and noise saturation of wide-band InAs-InP quantum dash optical amplifiers: model and experiments," *IEEE J. Sel. Top. Quantum Electron.*, vol. 11, no. 5, pp. 1015–1026, 2005.
  - [287] G. P. Agrawal, "Four-wave mixing and phase conjugation in semiconductor laser media.," *Opt. Lett.*, vol. 12, no. 4, pp. 260–262, 1987.
  - [288] A. Capua, V. Mikhelashvili, G. Eisenstein, J. P. Reithmaier, A. Somers, and A. Forchel, "Cross talk free multi channel processing of 10 Gbit/s data via four wave mixing in a 1550 nm InAs/InP quantum dash amplifier," *Conf. Dig. - IEEE Int. Semicond. Laser Conf.*, no. 1, pp. 119–120, 2008.
  - [289] D. Bimberg, C. Meuer, G. Fiol, H. Schmeckeber, and D. Arsenijević, "Four-wave mixing in 1.3  $\mu\text{m}$  quantum-dot semiconductor optical amplifiers," in *2010 12th International Conference on Transparent Optical Networks*, pp. 1–4, 2010.
  - [290] O. Karni, A. Capua, G. Eisenstein, D. Franke, J. Kreissl, H. Kuenzel, D. Arsenijević, H. Schmeckeber, M. Stubenrauch, M. Kleinert, D. Bimberg, C. Gilfert, and J. P. Reithmaier, "Nonlinear pulse propagation in a quantum dot laser," *Opt. Express*, vol. 21, no. 5, pp. 5715–36, 2013.
  - [291] A. Capua, G. Eisenstein, and J. P. Reithmaier, "A nearly instantaneous gain response in quantum dash based optical amplifiers," *Appl. Phys. Lett.*, vol. 97, no. 13, p. 131108, 2010.
  - [292] M. Usman, S. Heck, E. Clarke, P. Spencer, H. Ryu, R. Murray, and G. Klimeck, "Experimental and theoretical study of polarization-dependent optical transitions in InAs quantum dots at telecommunication-wavelengths (1300-1500 nm)," *J. Appl. Phys.*, vol. 109, no. 10, 2011.
  - [293] P. Ridha, L. H. Li, M. Mexis, P. M. Smowton, J. Andrzejewski, G. Sek, J. Misiewicz, E. P. O'Reilly, G. Patriarche, and A. Fiore, "Polarization properties of columnar quantum dots: Effects of aspect ratio and compositional contrast," *IEEE J. Quantum Electron.*, vol. 46, no. 2, pp. 197–204, 2010.
  - [294] M. Gioannini, A. Sevega, and I. Montrosset, "Simulations of Differential Gain and Linewidth Enhancement Factor of Quantum Dot Semiconductor Lasers," *Opt. Quantum Electron.*, vol. 38, no. 4–6, pp. 381–394, 2006.
  - [295] J. Ohtsubo, *Semiconductor Lasers: Stability, Instability and Chaos*, vol. 111. Berlin, Heidelberg: Springer Berlin Heidelberg, 2010.
  - [296] M. Sciamanna and K. A. Shore, "Physics and applications of laser diode chaos," *Nat. Photonics*, vol. 9, no. 3, pp. 151–162, 2015.
  - [297] F. Y. Lin and J. M. Liu, "Nonlinear dynamical characteristics of an optically injected semiconductor laser subject to optoelectronic feedback," *Opt. Commun.*, vol. 221, no. 1–3, pp. 173–180, 2003.
  - [298] M. Yousefi and D. Lenstra, "Dynamical behavior of a semiconductor laser with filtered external optical feedback," *IEEE J. Quantum Electron.*, vol. 35, no. 6, pp. 970–976, 1999.
  - [299] D. Kane and A. Shore, *Unlocking Dynamical Diversity*, vol. 1. Chichester, UK: John Wiley & Sons, Ltd, 2005.
  - [300] R. F. Broom, E. Mohn, C. Risch, and R. Salathé, "Microwave Self-Modulation of a Diode Laser Coupled to an External Cavity," *IEEE J. Quantum Electron.*, vol. 6, no. 6, pp. 328–334, 1970.
  - [301] C. Risch and C. Voumard, "Self-pulsation in the output intensity and spectrum of GaAs-AlGaAs cw diode lasers coupled to a frequency-selective external optical cavity," *J. Appl. Phys.*, vol. 48,

- no. 5, pp. 2083–2085, 1977.
- [302] I. Ikushima and M. Maeda, “Self-coupled phenomena of semiconductor lasers caused by an optical fiber,” *IEEE J. Quantum Electron.*, vol. 14, no. 5, pp. 331–332, 1978.
  - [303] T. Kanada and K. Nawata, “Injection laser characteristics due to reflected optical power,” *IEEE J. Quantum Electron.*, vol. 15, no. 7, pp. 559–565, 1979.
  - [304] R. Lang and K. Kobayashi, “External optical feedback effects on semiconductor injection laser properties,” *IEEE J. Quantum Electron.*, vol. 16, no. 3, pp. 347–355, 1980.
  - [305] K. Kikuchi and T. Okoshi, “Simple formula giving spectrum-narrowing ratio of semiconductor-laser output obtained by optical feedback,” *Electron. Lett.*, vol. 18, no. 1, p. 10, 1982.
  - [306] L. Goldberg, H. Taylor, A. Dandridge, J. F. Weller, and R. O. Miles, “Spectral Characteristics of Semiconductor Lasers with Optical Feedback,” *IEEE Trans. Microw. Theory Tech.*, vol. 30, no. 4, pp. 401–410, 1982.
  - [307] D. Lenstra, B. Verbeek, and A. Den Boef, “Coherence collapse in single-mode semiconductor lasers due to optical feedback,” *IEEE J. Quantum Electron.*, vol. 21, no. 6, pp. 674–679, 1985.
  - [308] C. Henry and R. Kazarinov, “Instability of semiconductor lasers due to optical feedback from distant reflectors,” *IEEE J. Quantum Electron.*, vol. 22, no. 2, pp. 294–301, 1986.
  - [309] R. W. Tkach and A. R. Chraplyvy, “Regimes of feedback effects in 1.5- $\mu\text{m}$  distributed feedback lasers,” *J. Light. Technol.*, vol. LT-4, no. 11, pp. 1655–1661, 1986.
  - [310] J. Mørk, B. Tromborg, and P. L. Christiansen, “Bistability and low-frequency fluctuations in semiconductor lasers with optical feedback: a theoretical analysis,” *IEEE J. Quantum Electron.*, vol. 24, no. 2, pp. 123–133, 1988.
  - [311] N. Schunk and K. Petermann, “Stability Analysis for Laser Diodes with Short External Cavities,” *IEEE Photonics Technology Letters*, vol. 1, no. 3, pp. 49–51, 1989.
  - [312] O. Nilsson and J. Buus, “Linewidth and feedback sensitivity of semiconductor diode lasers,” *IEEE J. Quantum Electron.*, vol. 26, no. 12, pp. 2039–2042, 1990.
  - [313] K. Petermann, “External optical feedback phenomena in semiconductor lasers,” *IEEE J. Sel. Top. Quantum Electron.*, vol. 1, no. 2, pp. 480–489, 1995.
  - [314] H. Olesen, J. H. Osmundsen, and B. Tromborg, “Nonlinear Dynamics and Spectral Behavior for an External Cavity Laser,” *IEEE J. Quantum Electron.*, vol. 22, no. 6, pp. 762–773, 1986.
  - [315] F. Favre, “Theoretical analysis of external optical feedback on DFB semiconductor lasers,” *IEEE J. Quantum Electron.*, vol. 23, no. 1, pp. 81–88, 1987.
  - [316] J. Wang and K. Petermann, “Noise Analysis of Semiconductor Lasers within the Coherence Collapse Regime,” *IEEE J. Quantum Electron.*, vol. 27, no. 1, pp. 3–9, 1991.
  - [317] J. Mørk, J. Mark, and B. Tromborg, “Route to chaos and competition between relaxation oscillations for a semiconductor laser with optical feedback,” *Phys. Rev. Lett.*, vol. 65, no. 16, pp. 1999–2002, 1990.
  - [318] A. A. Tager and B. B. Elenkrig, “Stability regimes and high-frequency modulation of laser diodes with short external cavity,” *IEEE J. Quantum Electron.*, vol. 29, no. 12, pp. 2886–2890, 1993.
  - [319] G. P. Agrawal, “Line Narrowing in a Single-Mode Injection Laser Due to External Optical Feedback,” *IEEE J. Quantum Electron.*, vol. 20, no. 5, pp. 468–471, 1984.
  - [320] F. Grillot, B. Thedrez, and G.-H. Duan, “Feedback Sensitivity and Coherence Collapse Threshold of Semiconductor DFB Lasers With Complex Structures,” *IEEE J. Quantum Electron.*, vol. 40, no. 3, pp. 231–240, 2004.
  - [321] G. Acket, D. Lenstra, A. Den Boef, and B. Verbeek, “The influence of feedback intensity on

- longitudinal mode properties and optical noise in index-guided semiconductor lasers," *IEEE J. Quantum Electron.*, vol. 20, no. 10, pp. 1163–1169, 1984.
- [322] F. Grillot, B. Thedrez, J. Py, O. Gauthier-Lafaye, V. Voiriot, and J. L. Lafragette, "2.5-Gb/s transmission characteristics of 1.3- $\mu\text{m}$  DFB lasers with external optical feedback," *IEEE Photonics Technol. Lett.*, vol. 14, no. 1, pp. 101–103, 2002.
- [323] Y. C. Chung and Y. H. Lee, "Spectral characteristics of vertical-cavity surface-emitting lasers with external optical feedback," *IEEE Photonics Technol. Lett.*, vol. 3, no. 7, pp. 597–599, 1991.
- [323] Y. C. Chung and Y. H. Lee, "Spectral characteristics of vertical-cavity surface-emitting lasers with external optical feedback," *IEEE Photonics Technol. Lett.*, vol. 3, no. 7, pp. 597–599, 1991.
- [324] F. Y. Lin and J. M. Liu, "Chaotic Lidar," *IEEE J. Sel. Top. Quantum Electron.*, vol. 10, no. 5, pp. 991–997, 2004.
- [325] O. Carroll, S. P. Hegarty, G. Huyet, and B. Corbett, "Length dependence of feedback sensitivity of InAs/GaAs quantum dot lasers," *Electron. Lett.*, vol. 41, no. 16, p. 911, 2005.
- [326] F. Grillot, "Lasers monomodes à faible sensibilité à la rétroaction optique pour les transmissions à 2,5 Gbit/s sans isolateur," Université de Franche-Comté, 2003.
- [327] H. Su, L. Zhang, A. L. Gray, R. Wang, T. C. Newell, K. J. Malloy, and L. F. Lester, "High external feedback resistance of laterally loss-coupled distributed feedback quantum dot semiconductor lasers," *IEEE Photonics Technol. Lett.*, vol. 15, no. 11, pp. 1504–1506, 2003.
- [328] M. W. Fleming and A. Mooradian, "Spectral Characteristics of External-Cavity Controlled Semiconductor Lasers," *IEEE J. Quantum Electron.*, vol. 17, no. 1, pp. 44–59, 1981.
- [329] R. Wyatt and W. J. Devlin, "10 kHz linewidth 1.5  $\mu\text{m}$  InGaAsP external cavity laser with 55 nm tuning range," *Electron. Lett.*, vol. 19, no. 3, p. 110, 1983.
- [330] H. Temkin, N. a. Olsson, J. Abeles, R. Logan, and M. Panish, "Reflection noise in index-guided InGaAsP lasers," *IEEE J. Quantum Electron.*, vol. 22, no. 2, pp. 286–293, 1986.
- [331] K. Petermann, *Laser Diode Modulation and Noise*. Springer Netherlands, 1991.
- [332] N. Schunk and K. Petermann, "Numerical analysis of the feedback regimes for a single-mode semiconductor laser with external feedback," *IEEE J. Quantum Electron.*, vol. 24, no. 7, pp. 1242–1247, 1988.
- [333] B. Tromborg, J. Osmundsen, and H. Olesen, "Stability analysis for a semiconductor laser in an external cavity," *IEEE J. Quantum Electron.*, vol. 20, no. 9, pp. 1023–1032, 1984.
- [334] J. Osmundsen and N. Gade, "Influence of optical feedback on laser frequency spectrum and threshold conditions," *IEEE J. Quantum Electron.*, vol. 19, no. 3, pp. 465–469, 1983.
- [335] A. M. Levine, G. H. M. van Tartwijk, D. Lenstra, and T. Erneux, "Diode lasers with optical feedback: Stability of the maximum gain mode," *Phys. Rev. A*, vol. 52, no. 5, pp. R3436–R3439, 1995.
- [336] S.-Y. Ye and J. Ohtsubo, "Experimental Investigation of Stability Enhancement in Semiconductor Lasers with Optical Feedback," *Opt. Rev.*, vol. 5, no. 5, pp. 280–284, 1998.
- [337] A. Uchida, *Optical Communication with Chaotic Lasers*. Weinheim, Germany: Wiley-VCH Verlag GmbH & Co. KGaA, 2012.
- [338] Y. Liu, N. Kikuchi, and J. Ohtsubo, "Controlling dynamical behavior of a semiconductor laser with external optical feedback," *Phys. Rev. E*, vol. 51, no. 4, pp. R2697–R2700, 1995.
- [339] J. Sacher, W. Elsässer, and E. O. Göbel, "Intermittency in the coherence collapse of a semiconductor laser with external feedback," *Phys. Rev. Lett.*, vol. 63, no. 20, pp. 2224–2227, 1989.
- [340] T. Heil, I. Fischer, W. Elsässer, and W. Elsässer, "Coexistence of low-frequency fluctuations and



- stable emission on a single high-gain mode in semiconductor lasers with external optical feedback," *Phys. Rev. A (Atomic, Mol. Opt. Physics)*, vol. 58, no. 4, pp. R2672–R2675, 1998.
- [341] T. Heil, I. Fischer, W. Elsässer, a Gavrielides, W. Elsässer, and a Gavrielides, "Dynamics of semiconductor lasers subject to delayed optical feedback: the short cavity regime.," *Phys. Rev. Lett.*, vol. 87, no. 24, p. 243901, 2001.
- [342] J. P. Toomey, D. M. Kane, C. McMahon, A. Argyris, and D. Syvridis, "Integrated semiconductor laser with optical feedback: transition from short to long cavity regime," *Opt. Express*, vol. 23, no. 14, p. 18754, 2015.
- [343] S. Donati and M. T. Fathi, "Transition from short-to-long cavity and from self-mixing to chaos in a delayed optical feedback laser," *IEEE J. Quantum Electron.*, vol. 48, no. 10, pp. 1352–1359, 2012.
- [344] A. Gavrielides, T. C. Newell, V. Kovanis, R. G. Harrison, N. Swanston, D. Yu, and W. Lu, "Synchronous Sisyphus effect in diode lasers subject to optical feedback," *Phys. Rev. A*, vol. 60, no. 2, p. 1577, 1999.
- [345] M. Sciamanna, A. Tabaka, H. Thienpont, and K. Panajotov, "Intensity behavior underlying pulse packages in semiconductor lasers that are subject to optical feedback," *J. Opt. Soc. Am. B*, vol. 22, no. 4, p. 777, 2005.
- [346] T. Heil, I. Fischer, W. Elsässer, B. Krauskopf, K. Green, and A. Gavrielides, "Delay dynamics of semiconductor lasers with short external cavities: Bifurcation scenarios and mechanisms," *Phys. Rev. E*, vol. 67, no. 6, p. 66214, 2003.
- [347] S. Azouigui, B. Dagens, F. Lelarge, J.-G. Provost, D. Make, O. Le Gouezigou, A. Accard, A. Martinez, K. Merghem, F. Grillot, O. Dehaese, R. Piron, S. Loualiche, Qin Zou, and A. Ramdane, "Optical Feedback Tolerance of Quantum-Dot- and Quantum-Dash-Based Semiconductor Lasers Operating at 1.55  $\mu\text{m}$ ," *IEEE J. Sel. Top. Quantum Electron.*, vol. 15, no. 3, pp. 764–773, 2009.
- [348] J. Helms and K. Petermann, "A simple analytic expression for the stable operation range of laser diodes with optical feedback," *IEEE J. Quantum Electron.*, vol. 26, no. 5, pp. 833–836, May 1990.
- [349] A. J. Williamson, L. W. Wang, and A. Zunger, "Theoretical interpretation of the experimental electronic structure of lens-shaped self-assembled InAs/GaAs quantum dots," *Phys. Rev. B*, vol. 62, no. 19, pp. 12963–12977, 2000.
- [350] M. Arahata and A. Uchida, "Inphase and Antiphase Dynamics of Spatially-Resolved Light Intensities Emitted by a Chaotic Broad-Area Semiconductor Laser," *IEEE J. Sel. Top. Quantum Electron.*, vol. 21, no. 6, pp. 522–530, 2015.
- [351] A. Karsaklian Dal Bosco, K. Kanno, A. Uchida, M. Sciamanna, T. Harayama, and K. Yoshimura, "Cycles of self-pulsations in a photonic integrated circuit," *Phys. Rev. E*, vol. 92, no. 6, p. 62905, 2015.
- [352] A. Tabaka, M. Sciamanna, I. Veretennicoff, and K. Panajotov, "Bifurcation study of regular pulse packages in laser diodes subject to optical feedback," *2003 Eur. Quantum Electron. Conf. EQEC 2003*, vol. 36211, p. 40, 2003.
- [353] C. Gosset, I. Aldaya, C. Wang, H. Huang, X. You, J. Even, G. Campuzano, and F. Grillot, "Self-referenced technique for monitoring and analysing the non-linear dynamics of semiconductor lasers," *Opt. Express*, vol. 22, no. 13, p. 16528, 2014.
- [354] L. Chen, C. Doerr, R. Aroca, S. Y. Park, J. C. Geyer, T. Nielsen, C. Rasmussen, and B. Mikkelsen, "Silicon Photonics for 100G-and-beyond Coherent Transmissions," *Opt. Fiber Commun. Conf.*, vol. 1, no. d, p. Th1B.1, 2016.

- [355] H. Schmeckeber, B. Lingnau, S. Koenig, K. Lüdge, C. Meuer, A. Zeghuzi, D. Arsenijević, M. Stubenrauch, R. Bonk, C. Koos, C. Schubert, T. Pfeiffer, and D. Bimberg, "Ultra-Broadband Bidirectional Dual-Band Quantum-Dot Semiconductor Optical Amplifier," in *Optical Fiber Communication Conference*, vol. 6, no. 6 1, p. Tu3I.7, 2015.
- [356] A. Karsaklian Dal Bosco, K. Kanno, A. Uchida, M. Sciamanna, T. Harayama, and K. Yoshimura, "Cycles of self-pulsations in a photonic integrated circuit," *Phys. Rev. E*, vol. 92, no. 6, p. 62905, 2015.
- [357] E. Agrell, M. Karlsson, A. R. Chraplyvy, D. J. Richardson, P. M. Krummrich, P. Winzer, K. Roberts, J. K. Fischer, S. J. Savory, B. J. Eggleton, M. Secondini, F. R. Kschischang, A. Lord, J. Prat, I. Tomkos, J. E. Bowers, S. Srinivasan, M. Brandt-Pearce, and N. Gisin, "Roadmap of optical communications," *J. Opt.*, vol. 18, no. 6, p. 63002, 2016.
- [358] A. Spott, J. Peters, M. L. Davenport, E. J. Stanton, C. D. Merritt, W. W. Bewley, I. Vurgaftman, C. S. Kim, J. R. Meyer, J. Kirch, L. J. Mawst, D. Botez, and J. E. Bowers, "Quantum cascade laser on silicon," *Optica*, vol. 3, no. 5, p. 545, 2016.
- [359] L. Jumpertz, K. Schires, M. Carras, M. Sciamanna, and F. Grillot, "Chaotic light at mid-infrared wavelength," *Light Sci. Appl.*, vol. 5, no. 6, p. e16088, 2016.





## Non-linéarités optiques dans les lasers à boîtes quantiques pour les communications à haut-débit

### RESUME :

L'évolution actuelle des systèmes de communications optiques est telle que la circulation d'information n'est plus exclusivement limitée par les liens longues distances transocéaniques ou par les réseaux cœurs. De nombreuses applications courtes distances comme les réseaux d'accès où les débits des systèmes amenant la fibre chez l'abonné doivent être maximisés et les connexions internes et externes des centres de données transportent un trafic de données important produit en partie par les applications de type « Big Data ». Les critères imposés par ces nouvelles architectures notamment en termes de coût et consommation énergétique doivent être pris en compte en particulier par le déploiement de nouveaux composants d'extrémités. Grâce au très fort confinement des porteurs, les lasers à boîtes quantiques constituent une classe d'oscillateurs présentant des caractéristiques remarquables notamment en termes de courant de seuil et de stabilité thermique. En particulier, l'application d'une perturbation optique externe permet d'exploiter les non-linéarités optiques des boîtes quantiques pour la réalisation de convertisseurs en longueur d'onde performants ou de transmetteurs à haut-débit fonctionnant sans isolateur optique. Ce dernier point est particulièrement critique dans les réseaux courtes distances où l'utilisation de sources modulées directement reste une solution technologique importante. Ce travail de thèse réalisé sur des structures lasers à base d'Arséniure de Gallium (GaAs) et de Phosphure d'Indium (InP) montre la possibilité d'améliorer l'efficacité de conversion non-linéaire par injection optique et de générer de nombreuses dynamiques dans des oscillateurs rétroactionnés et émettant sur différents états quantiques. Par ailleurs, le déploiement massif des systèmes cohérents mais également la conception des futures horloges atomiques sur puces nécessite l'utilisation de sources optiques à faible largeur de raie et ce afin de limiter la sensibilité de la réception au bruit de phase du transmetteur et de l'oscillateur local et induire un taux d'erreur binaire important. La conception de laser à faible largeur spectrale constitue un autre objectif de ce travail thèse. Les avantages de la technologie boîtes quantiques ont été mis à profit pour d'atteindre une largeur spectrale de 160 kHz (100 kHz en présence de rétroaction optique) ce qui est de première importance pour les applications susmentionnées.

**Mots clés :** lasers à semiconducteur, boîtes quantiques, mélange à quatre ondes, rétroaction optique, injection optique, dynamique non-linéaire, largeur de raie, communications optiques.

## Optical nonlinearities in quantum dot lasers for high-speed communications

**ABSTRACT:** The recent evolution of optical communication systems is such that the transfer of massive amounts of information is no longer limited to long-distance transoceanic links or backbone networks. Numerous short-reach applications requiring high data throughputs are emerging, not only in access networks, where upgrades of the bit rate of fiber-to-the-home systems need to be anticipated, but also in data center networks where huge amounts of information may need to be exchanged between servers, in part triggered by the rise of big data applications. The new requirements in terms of cost and energy consumption set by novel short-reach applications therefore need to be considered in the design and operation of a new generation of semiconductor laser sources. Owing to the tight quantum confinement of carriers, quantum dot lasers constitute a class of oscillators exhibiting superior characteristics such as a lower operating threshold, a better thermal stability as well as larger optical nonlinearities. The investigation of quantum dot lasers operating under external perturbations allows probing such optical nonlinearities in the view of developing all-optical wavelength-converters with improved performance as well as optical feedback-resistant transmitters. This last point is even more critical since it is expected that short-reach links making use of directly modulated sources will experience massive deployment in the near future, in contrast to conventional backbone links where the number of required optoelectronic interfaces remains relatively modest. In order to do so, the thesis reports on novel findings in GaAs- and InP-based quantum dot lasers such as improved bandwidth and conversion efficiency under optical injection and various complex dynamics with delayed quantum dot oscillators emitting on different lasing states. Last but not the least, the massive deployment of coherent systems as well as the realization of future chip-scale atomic clocks require the implementation of optical sources with narrow spectral linewidth otherwise the sensitivity to the phase noise of both transmitters and local oscillators can strongly affect the bit error rates at the receiver. This is another objective to be addressed in the thesis where the benefits of the quantum dot technology has allowed to reach a spectral linewidth as low as 160 kHz (100 kHz under optical feedback) which is of paramount importance not only regarding the aforementioned applications.

**Keywords:** semiconductor lasers, quantum dots, four wave mixing, optical feedback, optical injection, nonlinear dynamics, spectral linewidth, high-speed communications.